ABSTRACT

RHODES, CRISSY LYNETTE. Materials Science and Sensing Applications of Surface Plasmon Resonance in Conducting Metal Oxides. (Under the direction of Stefan Franzen.)

Surface plasmon resonance spectroscopy was developed for the conducting metal oxide, indium tin oxide (ITO). This technique detects changes in the refractive index of a substrate produced by a monolayer or biomolecule binding. To determine if effective monolayer binding occurred, many characterization techniques were employed including reflectance FT-IR, XPS, and near edge X-ray fine structure absorption (NEAXFS) spectroscopy. The reflectance FT-IR experimental data revealed not only confirmation of monolayer formation but evidence for the existence of the plasma frequency (ω_p) as predicted by the Drude Free Electron Model. The XPS data was primarily used as corroborating deposition evidence and NEXAFS spectroscopy was vital in recognizing the order or disorder of a deposition monolayer. Fundamental studies with Indium tin oxide revealed a strong dependence of the excitation of surface plasmons upon preparation conditions, crystal orientation, and skin depth. Complementary theoretical studies allowed for separation of the different plasmonic contributions in the thin film.

MATERIALS SCIENCE AND SENSING APPLICATIONS OF SURFACE PLASMON RESONANCE IN CONDUCTING METAL OXIDES

by
CRISSY LYNETTE RHODES

A dissertation submitted to the Graduate Faculty of
North Carolina State University
in partial fulfillment of the
requirements for the Degree of
Doctor of Philosophy

CHEMISTRY

Raleigh, North Carolina

2007

APPROVED BY:

_____
Dr. Stefan Franzen, Chair of Advisory Committee

_____ _____
Dr. Lin He Dr. Edmond F. Bowden

_____
Dr. Jan Genzer,
Graduate School Representative

BIOGRAPHY

Crissy Lynette Rhodes was born on June 25, 1972. She graduated Magma Cum Laude with a Bachelor of Science degree in Chemistry with a minor in Biology in 1994. She completed a Master of Science degree in Biochemistry at the University of Arkansas for Medical Sciences in 1996. After a series of laboratory and teaching positions, she returned to graduate school at North Carolina State University to pursue a Doctor of Philosophy degree in Chemistry. In 2007, she was awarded a Doctor of Philosophy degree in Physical Chemistry under the direction of Stefan Franzen.

TABLE OF CONTENTS

Page

LIST OF TABLES

Page

CHAPTER 2

CHAPTER 3

CHAPTER 5

CHAPTER 6

CHAPTER 7

CHAPTER 9

CHAPTER 10

LIST OF FIGURES

Page

CHAPTER 1

CHAPTER 2

CHAPTER 3

CHAPTER 6

CHAPTER 7

CHAPTER 8

CHAPTER 10

Chapter 1

Introduction

1.1 Motivation

The emergence of Material Science departments at universities around the country has signaled the importance of the fundamental study of substrates. The deposition of self-assembled monolayers (SAMs) upon materials has a variety of notable applications and has been shown to be highly dependent upon the optical and electronic properties of a surface; thus, necessitating these studies. [1-3] Within conductive thin films, material properties are the result of properties such as the mobility and density of electrons bound within a conduction band of the material. As will be shown, these electrons have the possibility of oscillating, absorbing radiation, or excitation into an excited state. Therefore, this research incorporated a variety of techniques designed to not only understand the origin of these fundamental material properties but also to observe their effect upon self-assembled monolayer deposition. The technological importance of these studies ranges from design of optics to monitor film quality control to biosensing.

1.2 The Drude Model and Plasmons

Conductivity in materials arises due to the mobility of the electrons within the conduction band, which is graphically displayed in figure 9 of Chapter 3. Specifically, electrical conductivity is measured by placing an electrical potential difference across a conductor with the movement of the charges (conduction electrons) results in a detectable electric current. In general, conductivity, σ (S/m), is determined by dividing the current density, J (amps/m^2) by the electric field strength, E (V/m). Metals are the typically

conductive materials and were the basis for the theoretical studies attempting to explain this phenomenon. The Drude Free Electron Model (FEM) is a classical theory of metallic conductivity that is widely employed to quantify the conductivity in terms of the density and mobility of charge carriers. The historical origins and derivation of this theory are found in Appendix 1. Essentially this theory approximates the transport properties of the electrons in a conducting material by portraying the conduction electrons as a noninteracting classical gas surrounding immobile positive ions. [1]

The interaction of light with conductors can also be derived from the Drude FEM. Assuming an electric field in which $E=E_o e^{-i\omega t}$, where E is the electric field and ω is the angular frequency, then the Drude theory calculates a plasma frequency as seen in equation 1 (derivation in appendix 1).

$$\omega_p^2 = \frac{ne^2}{m\varepsilon_o} \qquad (1)$$

In this equation, ω_p is the plasma frequency, n is the free charge carrier concentration, m is the free electron mass and ε_0 is the permittivity of vacuum. [1] This plasma frequency is a material property dependent on the charge carrier and dielectric constant of the conductor and represents the frequency of light that the conduction electrons will absorb. For typical metals, the plasma frequency predicts absorption in the ultraviolet region of the electromagnetic spectrum due the high charge carrier density ($n \geq 10^{21}$ electrons/cm^3) of metallic materials although this absorption is shifted in the visible region in metallic materials such as gold and silver due to the strong interactions of the d electrons in the outer shell. [1,2] This absorption is also dependent on the angle of the incident radiation

and thus, has a maximum absorption at a certain frequency and angle with a range of intensities.

The Drude Free Electron Model successfully explains optical absorption at the plasma frequency but it does not predict all of the electronic oscillations that may occur within conductors. Collective oscillations of conduction electrons result from the perturbation of the free conduction electrons by an impinging energy source and are known as plasmons. The literature survey that follows presents the current thinking about plasmons based principally on the experience using the noble metals, gold and silver. My research has revealed inconsistencies in the literature and a level of complication that was heretofore unrecognized. Definitions of plasmons have ranged from quasiparticle to oscillations within the bulk or the surface. [2-4] As soon as types of plasmons are discussed, the complication increases. Bulk Plasmons have been referred to as both bulk and volume plasmons and/or absorptions with excitable energy ranging from electromagnetic radiation to soft x-ray. [2,5,6] Surface plasmons or absorptions are also inconsistent in their defintions and understandings. The direction of propagation has not even been consistent with some papers mentioning a tranverse propagation while others claim longitudinal. In fact a recent 2007 report two different types of surface plasmons known as "ordinary" and "extraordinary". [5] Attempting to decipher and organize plasmon knowledge has been a challenge.

In the literature, two distinct types of plasmons are recognized, the bulk volume plasmons and surface plasmons. Bulk volume plasmons propagate longitundinally throughout the material and are excited into resonance by a high-energy source such as an

electron. These plasmons originate within the bulk of the material, hence the name, and are detected when high-energy electrons are transmitted through a material. Once the resonant frequency is attained and electron absorption occurs, detection ensues with a transmission electron microscope (TEM). This technique is known as electron energy loss spectroscopy (EELS). This typically occurs in the high energy ultraviolet or soft x-ray regime and is an electronic disturbance or oscillation of the conduction electrons that propagates longitudinally within the film. These oscillations, as with other plasmons, are related to the complex dielectric constant of the material and are a direct result of the real part of the dielectric constant going to zero. [6] The figure below shows a graphical representation of this relationship in which the real dielectric constant crosses the frequency axis at the resonant frequency while the imaginary part stays positive.

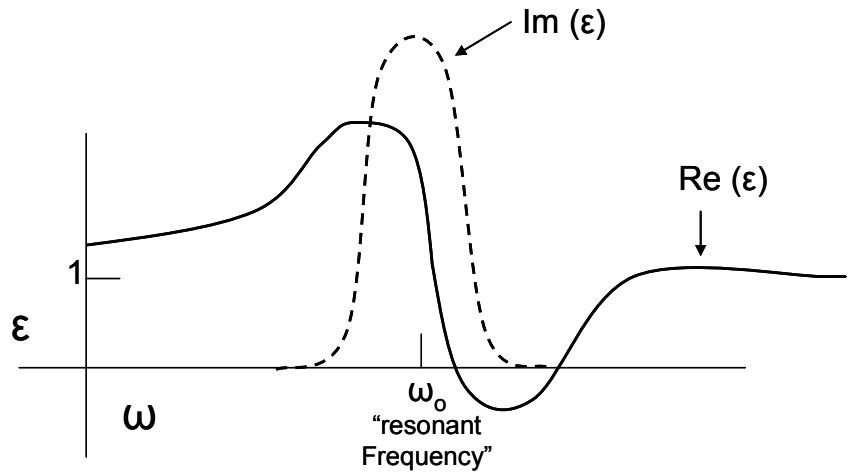

Figure 1.1 – An ideal Plasmon spectral graph of the dielectric versus the frequency. ω_o represents the resonant frequency of the ideal conductor. The solid (__) line represents the real part of the dielectric while the dashed line (---) represents the imaginary part.

The crossover of the real part of the dielectric constant may occur several times throughout the frequency range of the conductor, indicative of several different types of plasmons present within a typical material, which can be excited into their representative resonant states by different types of radiative forces including electrons (bulk plamson-EELS) and visible and/or infrared light (surface plasmons-SPR). .The range of values for bulk plasmons for conductors is typically lower in value than in either semiconductors or insulators. For instance, gold is reported as ~16 eV [7] while silicon dioxide is ~28 eV [8]. Intuitively, the more conduction electrons present, the greater the chance of the excitation of the bulk plasmon. Thus, other intermediate substrates such as conducting metal oxides which have charge carrier densities between metals and semiconductors, should have values between them. Experimental results comparing the bulk plasmon on a conductive surface (ITO) can be found within Chapter 4.

As a frame of reference for discussing plasmons, a 3-d Carteisan coordinate system (xyz-space) for the surface is used. In this coordinate system, all three axes are perpendicular to each other with all passing through a central origin. Following convention, the x axis is east/west, the y axis is north/south and the z axis is up/down. For the discussion of the plasmons within the thin film, only the z and x axes will be pertinent. Since the bulk plasmon is longitudinal, in the surface, its motion is primarily in the z diretion in a compression/expansion progression. The next type of plasmon to be discussed, the surface plasmon, has components in both the x and z direction and thus, the coordinate system becomes important.

Surface plasmons (SPs) are a distinct type of plasmon that propagates along an interface in response to electromagnetic waves of the appropriate energy and momentum (i.e. frequency and angle). Depending on the plasmon frequency the surface plasmon may be excited by light in the range from the ultraviolet (>4.5 eV, <275 nm, 36,300 cm^{-1}), visible (1.7-4.5 eV, 275-729 nm, 13,700-36,300 cm^{-1}) or infrared (0.5-1.7 eV, 739-2,480 nm, 4,000-13,700 cm^{-1}). Rather than a propagating longitudinal wave, the surface plasmons is a transverse oscillation in the x direction, that decays exponentially in the z-direction. Experimentally, these surface plasmons have been observed under conditions of total internal reflection as a sharp decrease in the intensity of reflected incident light. A specific resonant angle is required for maximum absorption, which is dependent upon the refractive index, thickness, and composition of the substrate as detailed in following chapters. The absorption at the plasma frequency as well as the oscillations of the surface plasmons typically appear in the visible spectral region for highly conductive metallic materials such as gold or silver. In this thesis, I show for the first time that surface plasmons are observed in the infrared spectral region for the semi-conductor or semi-metals such as conducting metal oxides.

Excitation of these surface plasmonic waves occurs through coupling of plane (p) polarized radiation near the plasma frequency (ω_p) of the conductor. Two phase dispersion relationships of p-polarized light can be derived that describe at which particular angle and frequency coupling can occur between two substrates of different refractive index.

A final related phenomenon is the appearance of a plasma absorption within a material. Conduction electrons are capable of absorbing radiation with a frequency at or below the plasma frequency (ω_p) of the material. Above this frequency, all the radiation would be transmitted through the material as the momentum of the conduction electrons is too low to match the momentum of the incoming radiation. Experimentally, this absorption is observed by a decrease in reflectance that is not angle-dependent. From the dispersion relationship detailed further in the chapter, it can be concluded that this absorption can be detected directly in air (without a prism). This absorption is predicted by the Drude Free Electron model as the plasma frequency (ω_p) as shown in equation 1. It is directly dependent on charge carrier density and thus, the higher the number of conduction electrons, ie. metals, the higher in frequency this absorption occurs. The bulk of my research is a direct result of the attempts to understand this plasma absorption in conducting metal oxides (CMO). As CMO's exhibit charge carrier densities approximately two orders magnitude less than gold, an observable change in the reflectance should be observable at a lower frequency. A key result from a previous graduate student, Dr. Scott Brewer, revealed this predicted change in reflectance in conducting metal oxides in the infrared spectral region {Brewer, 2002 #65 and it has been my goal to understand the properties and development of these plasmons and plasma absorptions within conducting metal oxides..

1.3 Surface Plasmon Resonance Spectroscopy

a. Fundamentals of surface plasmons and plasma absorptions

My thesis research has focused upon the fundamental understanding and technical adaptation of the lower energy oscillations of surface plasmons. The excitation of these plasmons using incident electromagnetic radiation in the infrared region is ideal for the possible development of multiplexed optical biosensors utilizing routine laboratory equipment such as an FT-IR coupled to an SPR attachment, revealing both chemical and material properties simultaneously.

As Fourier Transform Reflectance Infrared (FT-IR) spectroscopy has become a routine and well-understood technology, I will not detail its use other than to reveal that for this study, the spectrometer was utilized in an angle dependent reflectance mode. On the other hand, I will discuss in depth the development of the detection of surface plasmons in the infrared region of the electromagnetic spectrum and reveal fundamental understanding of their origins.

In order for surface plasmon resonance biosensing to occur, an interface between two opposing dielectrics such as a conductive surface (with a negative ε_m) and a dielectric such as air or water (with a positive ε_s) must be present. [4] The following equation therefore relates this dispersion relationship between the two surfaces

$$\kappa_{sp} = \frac{\omega}{c}\sqrt{\frac{\varepsilon_m(\omega)\varepsilon_s(\omega)}{\varepsilon_m(\omega)+\varepsilon_s(\omega)}} \qquad (2)$$

where ω is the plasma frequency investigated and κ_{sp} is the wave vector of the surface plasmons. This is the equation typically applied to plasmons although our experience revealed that this equation gives only a crude approximation of the coupling of the plasmons. The initial publication on surface Plasmon resonance [8] used this general dispersion relationship primarily to prove the existence of these plasmons and visualize the coupling points.

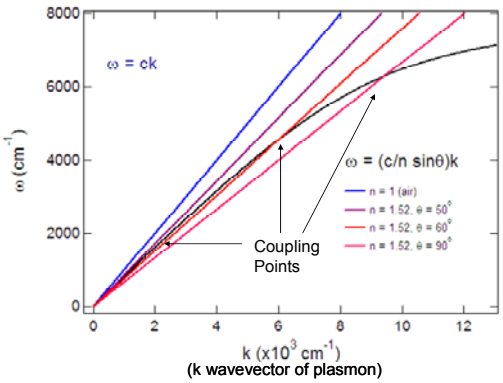

Figure 1.2 - Dispersion curve of surface plasmons over a metal-dielectric interface and that of the photons in a prism.

In this graphical representation, the blue line displaying the wavevector in which air is the interface does not cross the black wavevector of the electrons within the substrate. Thus, for coupling to occur, the refractive index of the material must be greater than air (n=1). This is accomplished with the use of a higher refractive index prism, typically made of glass such as BK7 (n=1.52) or SF10 (n=1.72) or even occasionally sapphire (n=1.8). As shown in figure 1, the coupling points are theoretical positions at specific wavenumbers with the corresponding angles at which surface plasmon oscillations should appear. Chapter 5 details the initial

attempts and success in the application of this dispersion relationship to a substrate other than a metal, a conducting metal oxide.

Recently, a collaborative effort with a physics professor resulted in a greater understanding of the fundamentals in electromagnetic properties, specifically plasmons. For a more thorough understanding of plasmonic origins, the complex dielectric function of the substrate must be taken into account for the dispersion relation as shown in equation 3

$$n_x = \sqrt{\frac{\varepsilon_a \varepsilon_s}{\varepsilon_s + \varepsilon_a}} = \sqrt{\frac{\varepsilon_a(\varepsilon_1 + i\varepsilon_2)}{(\varepsilon_a + \varepsilon_1 + i\varepsilon_2)}} \qquad (3)$$

where n is the refractive index and ε_a and ε_s refer to the two substrates at the two-phase interface (air and substrate, respectively) and ε_1 and ε_2 are the real and imaginary parts of the complex dielectric function of the substrate, respectively. This more complete definition of a dispersion relationship also takes into account that p-polarized radiation has both a x- and a z- component. Equation one relates the n_x which is the component responsible for the appearance of the surface plasmon as it traverse the interface in the x-direction. Placing this refractive index into equation 1 and realizing that $n=kc/\omega$ where k is the wavevector, c is the speed of light, and ω is the frequency, reveals a new dispersion equation specific for surface plasmons as shown in equation 4.

$$k_x = \frac{\omega}{c}\sqrt{\frac{\varepsilon_g(\varepsilon_1 + i\varepsilon_2)}{(\varepsilon_g + \varepsilon_1 + i\varepsilon_2)}} \qquad (4)$$

Conversely, for the plasma absorption, the wavevector traverses primarily in the z-direction (perpendicular) within the bulk of the material. This radiation

impinging on the surface in this direction exponentially decays. The effect of the addition of the imaginary dielectric constant is shown in equation 5.

$$n_z = \sqrt{\frac{-\varepsilon_s^2}{\varepsilon_s + \varepsilon_a}} = i\sqrt{\frac{(\varepsilon_1 + i\varepsilon_2)(\varepsilon_1 + i\varepsilon_2)}{(\varepsilon_a + \varepsilon_1 + i\varepsilon_2)}} \tag{5}$$

Replacing the real dielectric constant found in equation 1 with this complex form for the perpendicular component produces a dispersion relationship specific for the plasma absorption as shown in equation 6.

$$k_z = \frac{\omega}{c} i\sqrt{\frac{(\varepsilon_1 + i\varepsilon_2)(\varepsilon_1 + i\varepsilon_2)}{(\varepsilon_g + \varepsilon_1 + i\varepsilon_2)}} \tag{6}$$

Thus, these equations allowed for the separation of the plasmonic components within a two-phase p-polarized system by separation of the perpendicular and parallel wavevectors. Graphically, this separation is shown for a typical conducting metal oxide substrate in the following figure.

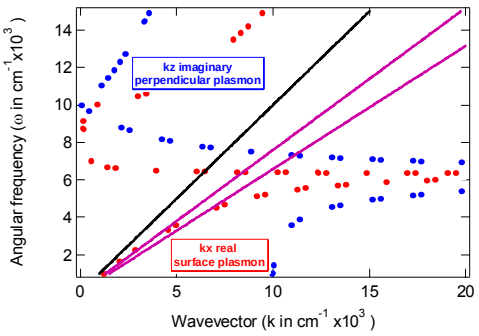

Figure 1.3- Theoretically determined dispersion relationship for a two phase boundary displayed as the wavevector (k) in terms of the angular frequency. The black line shown is the wavevector of light in vacuum while the two purple lines indicate calculated wavevectors at the boundary for two different angles (60° and 90°). The two theoretical plasmons are shown as red and blue lines.

The observation of this separation of the plasmonic components is an important step for fundamental understanding of the material properties of thin film substrates. It will be shown in further chapters that understanding of these component plasmons aids with the interpretation of actual experimental data.

1.4 Conducting Metal Oxides

Conducting metal oxides (CMOs) were studied because of the precedent in the research that indicated that they may possess surface plasmons. The material properties of the CMO's reveal not only the required property of conductivity but also infrared reflectivity. There are two primary types of CMO's, sp- and d-type. In sp-type conductors, the conduction electrons are found in either the s or p orbital such as in indium tin oxide (ITO), cadmium tin oxide (CTO) and aluminum-doped zinc oxide (AZO). In d-type conductors, the conduction electrons are donated from the d orbitals, allowing for d-d transitions and mixing. This is the case for metals such as gold and silver and semi-metallic materials such as iridium oxide (IrO_2) and ruthenium oxide (RuO_2). The d-d transitions are responsible for the energetic shift of gold and silver substrates and complicate spectra such that it may become difficult to theoretically model data as shown later in this thesis in chapter 10 (ruthenium oxide). Moreover, the sp-type conductors are typically transparent in the visible region while the d-type conductors seldom are, thus, allowing for various optical multiplexing possibilities. Typically, the charge carrier density of the CMO's are on the order of 10^{21} electrons/cm^3 while metals, such as gold and silver, usually have higher charge carrier densities on the order of 10^{23} electrons/cm^3 leading to a change

in skin depth and location of the plasma frequency as will be revealed in subsequent chapters.

1.5 Possible application: Biosensors

Surface Plasmon resonance spectroscopy has applications in many areas; thus, the fundamental understanding of it has relevance in many areas as well. For my personal interest, I chose to expand upon research in the area of biosensing. I feel it is an emerging field increasing in importance everyday and thus, deserves further explanation.

Biosensing research is an active area of investigation toward the development of analytical devices for the specific detection of any biological material such as oligonucleotides, carbohydrates, proteins, or even viruses and whole cells. A variety of sensing methods are available including electrochemical, optical, immobilized biomolecule detection, and micropatterning by photolithography, microcontact printing, or atomic force microscopy (AFM). [9-14] Therefore, with the wide variety of biomolecules and detection methods available, an accepted definition for a biosensor is "an analytical device composed of a biological recognition element directly interfaced to a signal transducer which together relate the concentration of an analyte (or group of related analytes) to a measurable response" as related by the Environmental Protection Agency. [9] Consequently, biosensors are involved in the most basic and essential human needs including risk assessment, environmental monitoring, drug discovery, and disease diagnosis and prognosis. [10-17] A schematic of possible biosensors displaying potential sensing biomolecules is shown in Figure 1.4.

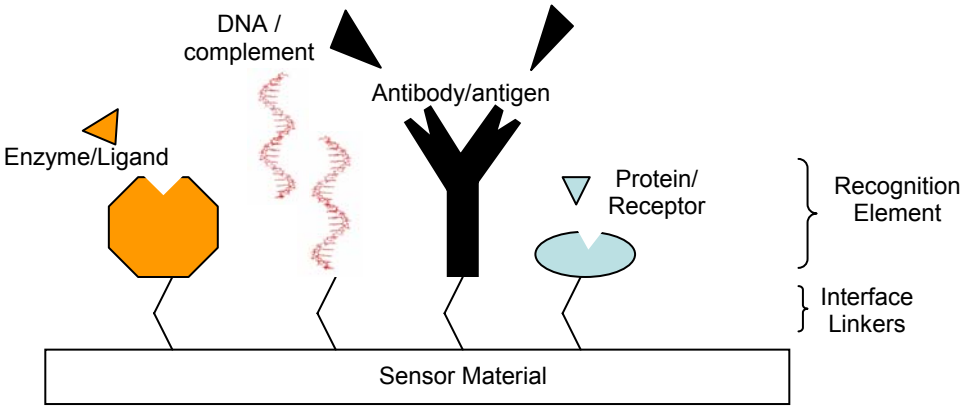

Figure 1.4. Schematic representing different types of biosensors with generic interfaces linkers coupled to four typical recognition elements: enzymes, DNA, antibodies, proteins.

A significant part of research in our laboratory involves development of spectroscopic techniques with the prospect of novel and unique biosensing capabilities. Endeavors have included the development of thermographic detection of DNA utilizing gold and silica-coated gold nanoparticles [18], chronocolumbic and electrochemical detection of nucleic acids [19], as well as various detection methods using fluorescently labeled biomolecules. Further routes of biosensor development include optical detection methods with multiplexing possibilities, thus SPR is a prime candidate. This for me has been the impetus of my research throughout this thesis work.

1.6 Introductory Summary

The remainder of this dissertation reveals my research I conducted into understanding the properties of thin films. Several of the chapters have resulted in publications while others divulge research attempts, which were either unsuccessful or not useful for publication. I have included nearly all of my trials and conclusions so that others in my group may learn from and possibly improve upon my efforts.

1.7. References

1. Wooten, F., *Optical Properties of Solids*. Academic Press, Inc.: San Diego, 1972.

2. Knoll, W., Interfaces and thin films as seen by bound electromagnetic waves. *Annual Review of Physical Chemistry* **1998,** 49, 569-638.

3. Kretschm.E, Determination of Optical Constants of Metals by Excitation of Surface Plasmons. *Zeitschrift Fur Physik* **1971,** 241, (4), 313-&.

4. Brockman, J. M.; Nelson, B. P.; Corn, R. M., Surface plasmon resonance imaging measurements of ultrathin organic films. *Annual Review of Physical Chemistry* **2000,** 51, 41-63.

5. Markel, V. A.; Sarychev, A. K., Propagation of surface plasmons in ordered and disordered chains of metal nanospheres. *Physical Review B* **2007,** 75, (8).

6. Egerton, R. F., *Electron Energy-Loss Spectroscopy in the Electron Microscope*. 2nd Edition ed.; Plenum Press: New York and London, 1986.

7. Fu, R. L., Xu, J. Z., Li, Y. R., Wei, Y. L., Zhu, J. J., *Frontiers in Bioscience* **2005,** 10, 2841-2847.

8. Rhodes, C. L. W., S.; Maria, J.P.; Losego, M.; Leonard, D.N.; Laughlin, B.; Duscher, G.; Franzen, S., Surface Plasmon Resonance in Conducting Metal Oxides. *Journal of Applied Physics* **2006,** 100, (1).

9. Rogers, K. R., Recent advances in biosensor techniques for environmental monitoring. *Analytica Chimica Acta* **2006,** 568, (1-2), 222-231.

10. Bagni, G.; Osella, D.; Sturchio, E.; Mascini, M., Deoxyribonucleic acid (DNA) biosensors for environmental risk assessment and drug studies. *Analytica Chimica Acta* **2006,** 573, 81-89.

11. Michelini, E.; Guardigli, M.; Magliulo, M.; Mirasoli, M.; Roda, A.; Simoni, P.; Baraldini, M., Bioluminescent biosensors based on genetically engineered living cells in environmental and food analysis. *Analytical Letters* **2006,** 39, (8), 1503-1515.

12. Kahru, A.; Ivask, A.; Kasemets, K.; Pollumaa, L.; Kurvet, I.; Francois, M.; Dubourguier, H. C., Biotests and biosensors in ecotoxicological risk assessment of field soils polluted with zinc, lead, and cadmium. *Environmental Toxicology and Chemistry* **2005,** 24, (11), 2973-2982.

13. Wang, J., Electrochemical biosensors: Towards point-of-care cancer diagnostics. *Biosensors & Bioelectronics* **2006,** 21, (10), 1887-1892.

14. Ferreira, A. A. P.; Colli, W.; da Costa, P. I.; Yamanaka, H., Immunosensor for the diagnosis of Chagas' disease. *Biosensors & Bioelectronics* **2005,** 21, (1), 175-181.

15. Potterat, O.; Hamburger, M., Natural products in drug discovery - Concepts and approaches for tracking bioactivity. *Current Organic Chemistry* **2006,** 10, (8), 899-920.

16. Simpson, P. B.; Wafford, K. A., New directions in kinetic high information content assays. *Drug Discovery Today* **2006,** 11, (5-6), 237-244.

17. Leifert, W. R.; Aloia, A. L.; Bucco, O.; Glatz, R. V.; McMurchie, E. J., G-protein-coupled receptors in drug discovery: nanosizing using cell-free technologies and molecular biology approaches. *Journal of Biomolecular Screening* **2005,** 10, (8), 765-779.

18. Cerruti, M. G.; Sauthier, M.; Leonard, D.; Liu, D.; Duscher, G.; Feldheim, D. L.; Franzen, S., Gold and silica-coated gold nanoparticles as thermographic labels for DNA detection. *Analytical Chemistry* **2006,** 78, (10), 3282-3288.

19. Moses, S.; Brewer, S. H.; Lappi, S. E.; Franzen, S., Factors affecting the DNA hybridization on surface. *Biophysical Journal* **2004,** 86, (1), 160A-160A.

Chapter 2

Deposition and Characterization Methodology

2.1 Deposition Techniques

In each of the subsequent chapters, specific deposition techniques for the particular experiment are described. This section provides an overview of the most common deposition and characterization strategies used in my thesis work

2.1.1 Thiolated Adlayer Deposition

Typically, these studies utilize long chain alkane thiols such as hexadecanethiol (C-16) and octadecanethiol.(C-18) since they are considered model systems due to their close packing and strong interaction with surfaces such as gold. [1] A submersion deposition technique was employed post-cleaning. For all the metal oxides examined, cleaning for this deposition technique consisted of a UVO-ozonolysis cleaning with optimal ozone-production time of 5-7 minutes for ITO and AZO and 20 minutes for CTO. Longer times resulted in surface degradation. For gold slides, a 20 minute ethanol soak followed by a 5-7 minute UVO cleaning was sufficient. Deposition concentrations and times varied for the substrates with the extreme case of ITO requiring neat solutions and a 12-16 hour soak in contrast to AZO which required only a 15 or 30 minute deposition of a 10 mM solution. CTO necessitated intermediate conditions of 50/50 v/v thiol/ethanol solution and a 30 minute deposition.

2.1.2 Oligonucleotide Surface Attachment

Many routes were investigated for successful nucleic acid deposition. Initially, a DNA coupling reaction scheme utilizing 1-ethyl-3-(3-dimethylaminopropyl)carbodiimide hydrochloride (EDC) was used in our laboratory. [2] The EDC coupling reagent linked a 12-PDA adlayer deposited onto an ITO surface through the –COOH moiety of the adlayer and the amino group of an amine terminated DNA oligomer. Part of the impetus for alteration of this coupling scheme was the lack of availability of the key compound 12-phosphonododecanoic (12-PDA). As with the EDC coupling, each method investigated for the deposition of the oligonucleotides onto the ITO surfaces involved a linker molecule. The rationale of the linker is to avoid nonspecific binding of the DNA to the surface by electrostatic interactions and is the usual reported attachment methodology [3]. Figure 2.1 shows a schematic of an idealized ITO/DNA surface based upon our attachment strategies.

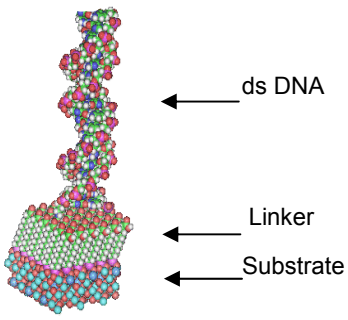

Figure 2.1. Schematic of idealized nucleic acid bonding to a substrate (ITO), with a specific linker and a 20-mer dsDNA attachment.

Several methodologies were examined, specifically with the aid of a post-doctoral research associate, Dr. Marta Cerruti. To date, the best methodology used in our laboratory employs a short chain methoxysilane linker for the attachment of DNA. The procedure for this method is described below.

A.. Silane Linker Attachment

Step 1. Pre-treat ITO in 0.1M NaOH overnight in order to protonate the oxides into hydroxyls on the surface of the thin film. Rinse with ethanol, dry with filtered high-purity nitrogen gas and UVO-ozonlysis for 5 minutes.

Step 2. Place 1% distilled tri-methoxypropylaminosilane into toluene for 5 minutes followed by sonication in absolute ethanol.

Step 3. Rinse with absolute or 95% ethanol and dry with filtered high-purity nitrogen gas.

B. DNA Deposition with Silane Linker

B1. Single-Stranded DNA Attachment

Step 1. Place the silane covered thin films into a container with SSMCC (sulfosuccinimidyl-4-(*N*-maleimidomethyl)cyclohexane-1-carboxylate) at concentration of 1 mg/ml 0.05M KP buffer pH 7.1 for 1 hour. Sonicate with same concentration KP buffer for 5 minutes, rinse with purified water and dry with filtered high-purity nitrogen gas.

Step 2. Select appropriate thiol-terminated DNA (T20 see appendix 2) for deposition and determine concentration using Beer's Law $A=\varepsilon bc$ where ε is the extinction coefficient of the DNA, b is the path length of the cell and c is the concentration of DNA. A simple UV-VIS spectrum with to determine absorption at 280 nm (absorption of the nitrogenous bases) is all that is needed.

Step 3 (if needed). Deprotect the thiolated DNA

1. Vortex well 1 ml of 100 mM dithiolthreitol (DTT) pH 8.4 and shake for ½ hour.

2. Rinse NAP 10 columns with 0.05 M KP buffer 3 times.

3. Add thiolated DNA sample and let drain completely

4. Add 0.05 KP buffer and collect the first 1.5 mL of solution.

5. Wash column 2 times and store for later use (can reuse for 3 cleanings).

Step 4. React 1 micromolar of the silane-SSMCC thin films in 0.05 M KP buffer for 4 hours at room temperature. Follow this with a 5 minute sonication in 0.05 M KP buffer, water rinse, and dry with filtered high-purity nitrogen gas.

B 2. Double-Stranded DNA

Step 1. Select appropriate complement oligonucleotide (termination linkage is not vital with either a biotin-terminated (B20) or thiol-terminated DNA (X20) utilized-see appendix 2) for

deposition and determine concentration as detailed in previous thesis [4] and mentioned above.

Step 2. React the complimentary strand for a final concentration of 1 micromolar in 0.2 M KP buffer overnight (12-16 hours) at room temperature. Follow this with a 5 minute sonication in 0.2 M KP buffer, water rinse, and dry with filtered high-purity nitrogen gas.

2.1.3. Carboxylate Adlayer Deposition

Step 1. Clean the thin film by UVO-ozonlysis for 5 minutes.

Step 2. Place 10mM carboxylate (malonic acid) in absolute ethanol overnight (16-20 hours).

Step 3. Rinse with absolute or 95% ethanol and dry with filtered high-purity nitrogen gas.

2.2 Characterization Techniques

2.2.1. NEXAFS Spectroscopy

A primary characterization technique used for the examination of the orientation of the self-assembled monolayers (SAMs) is near edge x-ray fine structure spectroscopy (NEXAFS). This type of spectroscopy relies upon resonant x-ray excitation of a K or L shell electron into an antibonding molecular orbital of either σ or π symmetry (σ^* or π^*) in order to provide element specific bonding information. [5] The specificity of this technique includes elemental and chemical bond selectivity as well as monolayer

orientation and depth information. The initial excitation of the specific K or L shell allows for elemental and chemical bond specificity, i.e., carbon K-shell excitation of ~290 eV while the nitrogen K-shell excitation is ≈400 eV[6] and a C-H 1s→σ* transition occurs at ≈287 eV while a C-C 1s→σ* transition takes place at ≈294 eV. Surface monolayer orientation information is provided by the angular dependence of the unoccupied molecular orbitals as shown in detail further in this thesis. [7] The depth information is a by-product of the detection method in which scattering from auger electrons are collected by a partial electron yield detector (PEY) representing the top 10 nm of the surface. A complementary technique involved detection of fluorescent photons which encompasses the top 100 nm of the surface using a full electron yield detector (FY). A general schematic of the NEXAFS technique is shown below.

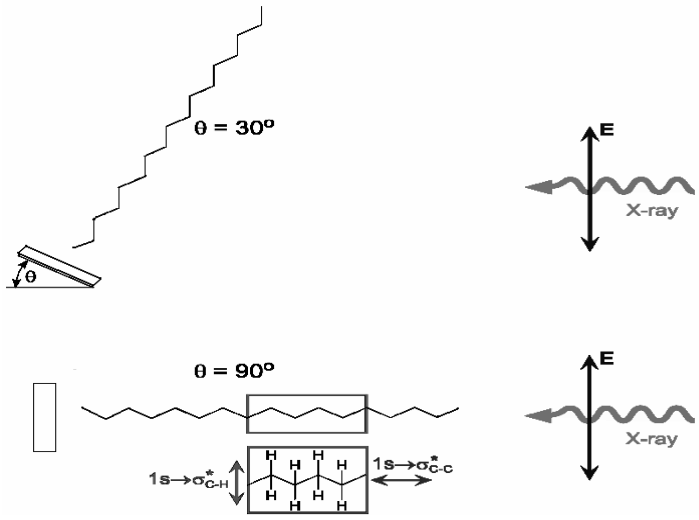

Figure 2.2. Schematic of the Angular Dependence of the Samples in a NEXAFS Experiment.

In figure 2.6, orientation information is obtained from the dependence of the antibonding orbital on the polarization vector of the x-ray beam. For a well-ordered monolayer, selective excitation of bonds occurs, with those bonds aligned to the electric vector of the x-ray beam displaying the highest intensity while those perpendicular to the beam having the lowest intensity. This angular dependence is a function of the fact that at a fixed geometry the excitations, $1s \rightarrow \sigma^*$ and $1s \rightarrow \pi^*$, are governed by dipole selection rules and thus, the resonance intensities vary as a function of the electric vector of the incident polarized x-ray relative to the axis of the σ^* and π^*. This technique is very useful for examining orientations of monolayers containing carbon, nitrogen, oxygen, or fluorine since these elements have sharp core level excitations that occur in the soft x-ray spectral region. [8] The technique has been used for a variety of adlayers and substrates with early studies focusing on Langmuir-Blodgett monolayers on silica [9] and thiols deposited on gold [10, 11] then progressing to other materials such as rare earth sol-gel films in silica-titania matrices [12], semi-fluorinated polymers on silica[13-15] and novel substrates such as vanadium pentoxide (V_2O_5) [16], humic acid europium (III) [17] and DNA nucleobases [18].

I performed NEXAFS on the soft x-ray materials characterization facility located at the NIST/DOW U7A VUV beam-line at NSLS. The materials characterization end station at the U7A beam line is equipped with detectors for simultaneous PEY and FY detection as well as a computer controlled heating/cooling

stage. The sample is mounted on the 4 degree-of-freedom stage. When possible, the PEY NEXAFS spectra was collected at several sample orientations, θ, typically 20°-90°, although we routinely dismissed the data collected at 20° due to irregularities observed as result of the large footprint of the impinging x-rays at that glancing angle arrangement. The orientation was determined using standard procedures reported in the literature [5] and will be discussed in detail in chapter 8.

2.2.2 Instrumentation and Techniques for SPR spectroscopy

By definition, surface plasmon resonance (SPR) spectroscopy is an optical technique used to measure and monitor biomolecular interactions occurring on conductive thin films and was first demonstrated by Liedberg in 1983 with the detection of various gases onto specific substrates as well as antibody detection upon a silver surface. [19] This technique detects changes in the refractive index in a self-assembled monolayer or liquid in contact with the film and has been widely used to study binding interactions of biomolecules including antigen/antibody, complementary DNA probes, enzyme/substrate, and receptor/ligand interactions. [20] [21, 22] [23-30] Although the theoretical principles underlying the SPR effect are applicable to any conductive material, until this thesis research, only silver and gold thin films have been studied for practical use in SPR instrumentation.

Instrumentation for surface plasmon resonance biosensing requires a source emitting radiation within the range of the plasma frequency and a detector to measure a change in the absorption. Commercially available SPR biosensors utilize a gold substrate and hence a visible light source and

extended range InGaAs detector. In order to alter the substrate choice for metal oxide detection, an infrared source and detector was necessitated. Initially, attempts were made to design an adaptable prism holder for an existing FT-IR spectrometer followed by an attempt to create a theta/2-theta stage for a home-built SPR. In the meantime, commercial development of instrumentation for FT-SPR technology was developed by GWC in collaboration with Thermo Electron Corporation. With this instrumentation, the angle dependence of the surface plasmons could be observed for a range of frequencies in the mid-infrared region. A schematic for this attachment, which is coupled to an FTIR spectrometer, is shown below.

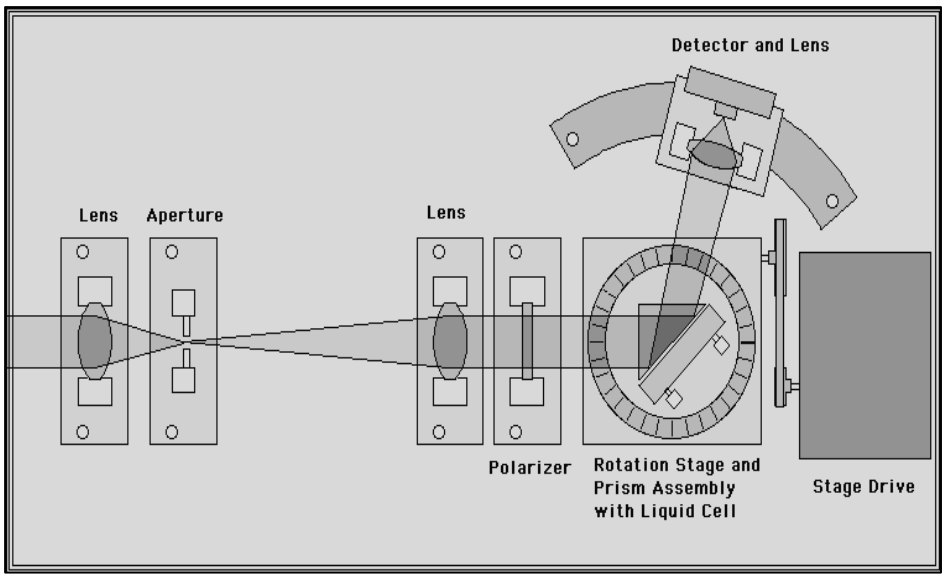

Figure 2.3. Schematic of the GWC FT-SPR module. The shaded rays incoming through the lens and aperture assembly represent infrared source radiation from a coupled FT-IR spectrometer.

As shown in the figure above, radiation from an infrared source is collimated through lenses in a GWC-patented design into a prism (refractive index 1.52 or 1.72) in which the radiation is transmitted through the backside of the thin film sample and reflected back through the prism to the infrared detector. The amount of reflected light reaching the detector changes as a function of the frequency of light as described above. The theta/2theta guarantees examination of a wide variety of angles of 25 to 40 depending on the model. The prism requirement is a direct result of the theoretical dispersion curve shown above. The figure clearly shows that the momentum of a free photon propagating is always smaller than the momentum of the surface plasmon mode since the momentum of the photon is only directly proportional to ε_s. Therefore, the two differing momentums must be matched. This is typically accomplished by a prism or grating-coupling. Patskovsky et. al. detailed a typical SPR prism coupling arrangement in the following figure. [31]

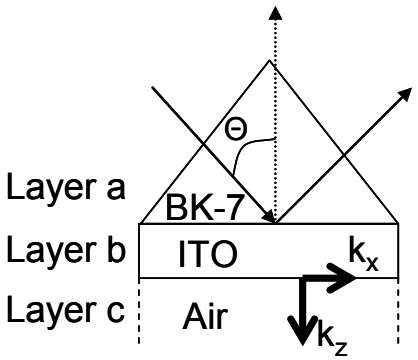

Figure 2.4. A three layer system {BK7 prism-ITO (metal/conductor)-air(testing medium)) in a Kretschmann-Raether prism coupling arrangement.

In the Kretschmann-Raether configuration, the prism is in direct contact with the substrate with only a small layer of refractive index matching fluid between. The other possible configuration is the Otto configuration in which there the impinging radiation passes through the prism into a less dense dielectric (typically air) before reflecting off the surface of the thin film. [32] In this configuration, the radiation is not transmitted through the glass but is reflected off the thin film on the topside. Thus, the substrate is in the reverse arrangement as the Kretschmann configuration. To date, more studies employ the Kretschmann configuration, due to the technical problems of fabricating extremely smooth prism elements and substrates to obtain the ideal proximity between them. A final excitation configuration is a grating coupling device. This is any device with a reflection diffraction grating with a periodicity similar to the wavelength. It was this type of setup that was the basis for the initial documentation of plasmons by R. W. Wood in 1902 [33].

For this thesis work on surface plasmons, the Kretschmann configuration was utilized with an FT-SPR attachment built by GWC, Incorporated. Substrate choice and monolayer deposition and characterization techniques will be discussed in subsequent chapters.

2.2.3 Other Characterization Techniques

A. X-ray Photoelectron Spectroscopy (XPS)

X-ray photoelectron spectroscopy is a relatively old technique developed in the mid-1960's by K. Siegbahn [34]. The photoelectric effect,

which was discovered in 1887 by Heinrich Hertz and explained by Albert Einstein, is the foundation upon the XPS theory. In general, this effect describes the ejection of an electron, using the concept of the photon when its radiant energy impinges upon a surface. Reference photon energy lines typically chosen are Al K alpha at 1486.6 eV or Mg K alpha at 1253.6 eV or at times Ti K alpha. [35] I typically utilized XPS solely as a conformational technique and used Mg K alpha photon energies. This technique is an elementally specific measurement in which the energy of the photoelectrons ejected from the surface is characteristic of the particular element. For instance, this energy known as the binding energy is ~285 eV for carbon. All elements with the exception of helium and hydrogen exhibit identifiable peaks of binding energy, which are readily available in reference books such as *X-ray Photoelectron Spectroscopy*. Examination of peak area and shape can also reveal additional information of the chemical environment of the element as both are highly dependent upon the bonding environment of the surface.

B. Atomic Force Microscopy (AFM)

Scanning probe microscopes are a class of instrumentation utilized for surface studies ranging from the atomic to the micron level. [36] Atomic force microscopy is a powerful characterization technique. Many theses have been derived using primarily this tool in many various capacities. However, I only utilized this tool briefly and solely for surface roughness

measurements, thus, I will only focus on this small utility of the apparatus. A schematic of a typical AFM is shown below.

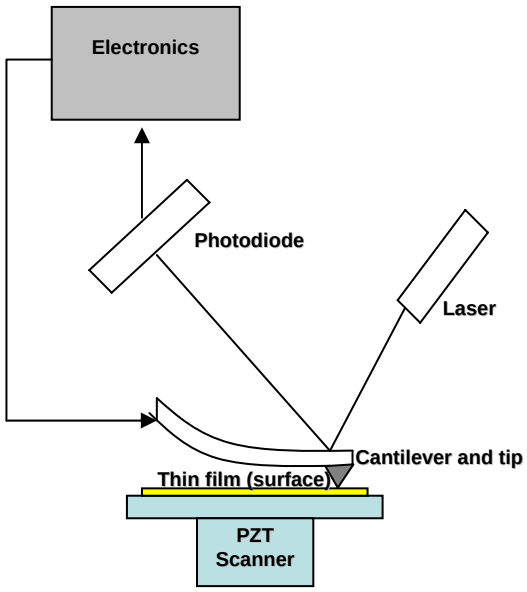

Figure 2.5. Schematic of a typical Atomic Force Microscope showing the main components of the device including the microscope (PZT scanner), the cantilever, and the photodiode detector.

The atomic force microscope (AFM) developed in 1986 is a surface technique that probes the features with a sharp tip that has a diameter less than 100 angstroms and a length less than 2 microns. This tip is attached to the free end of a flexible cantilever that is 100-200 microns long. The deflection of the cantilever is detected and as it is directly dependent of the surface topography, reveals the surface morphology of the material regardless of whether it is a conductor or

insulator. [36] The traditional force causing the deflection of the AFM cantilever is van der Waals force which the force between two atoms (the interatomic force). This curve is responsible for the 3 primary modes of AFM, the contact mode, and intermittent (tapping) mode, and non-contact mode. This is shown in the figure below.

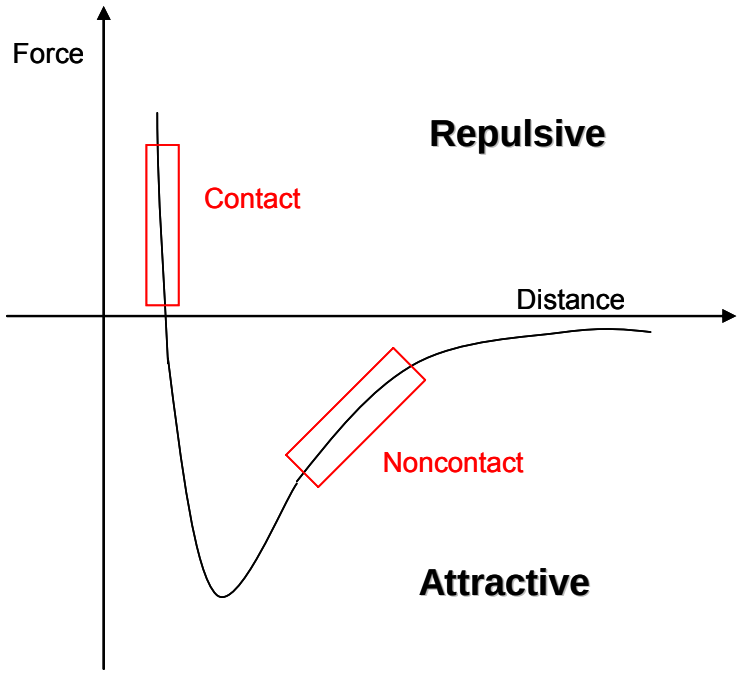

Figure 2.6. Graphical representation of the van der Waals curve and the regimes for different methods of performing AFM analysis (red boxes).

As shown, the contact mode is in the repulsive regime of the van der Waals curve, while the non-contact mode is used in the region in which attractive forces dominant. In contact mode AFM, the tip physically makes contact with the surface of the sample and due to the atomic repulsive forces on the surface, the cantilever tip bends in response to the topography rather than bringing the tip closer to the sample. In this mode,

other forces involved include the capillary force of the thin water layer typically present at room temperature and the force of the cantilever itself exerted onto the surface. For most applications, the capillary force is considered to be constant, and thus, the variable force that must match the atomic repulsion is the cantilever force. The movement of the cantilever is typically detected with the use of a laser beam reference allowing for subangstrom measurements. In the constant AFM mode,.either constant-height or constant-force detection is possible with constant-height having a fixed scan height and constant-force having constant cantilever deflection.

In noncontact mode, the cantilever does not contact the surface, instead it oscillates above the adsorbed fluid layer, typically water, that is present on the surface. The frequency of the oscillation is typically above the cantilever's resonance frequency and occurs with an amplitude of less than 10 nm to facilitate the development of an AC signal originating from the cantilever. [37] For detection purposes, the cantilever's resonant frequency is decreased by the van der Waal's forces and other long range forces resulting in the decrease of the amplitude of the oscillation. In order for a constant oscillation to occur, the scanner must move vertically for each x,y data point and thus, a topographic image of the surface is produced.

The third and final type of AFM is the intermittent or "tapping" mode. This mode is similar to noncontact AFM in that the cantilever tip is vibrated with an oscillation although it occurs at or slightly below the resonance frequency with a larger amplitude between 20-100 nm. The vibrating cantilever tip is brought closer to the sample so that it just barely "taps" the surface during scanning, contacting the surface during the bottom of its swing. A constant "setpoint" amplitude is desired and again vertical repositioning of the scanner accomplishes this. The topographical image of the surface is formed as the scanner moves to maintain this constant tip-sample interaction. Tapping AFM can examine both liquid and room temperature solid films and thus, is extremely versatile for surface characterization.

C. Reflectance Fourier Transform Infrared Spectroscopy (FT-IR)

Fourier Transform Infrared Spectroscopy (FT-IR) is another mainstay of any modern spectroscopy laboratory including undergraduate laboratories. For my research, this tool was utilized throughout as a monitoring and conformational technique for monolayer deposition. FT-IR is a vibrational spectroscopic technique based upon the excitation of stretching and bending modes of chemical bonds. Infrared spectra reveal much about not only the chemical composition of the analyte but also the surrounding chemical environment. For instance, hydrogen bonding is apparent as well as differentiation between monolayer and multilayer

deposition. The term “fourier transform” refers simply to the mathematical conversion of data from an interference pattern (time dependent) to a spectrum (frequency dependent). Thus, unlike a dispersive instrument, all frequencies are gathered at once making this type of detection more sensitive and much faster. Nearly all the infrared spectrometers in use today are FT based and thus, I will assume a familiarity with this instrument.

D. Resistivity

Intrinsic resistivity, ρ, is a material parameter measured experimentally with a four point probe. The resistivity of a material is related to the resistance of a material through equation 1

$$R = \rho * \frac{L}{A} \qquad (1)$$

where R is resistance in ohms, ρ is the resistivity in ohms/cm, L is the length of the film in cm and A is the area in cm^2 calculated from multiplying the thickness by the width (t*w). For an area in which the width equals the length (w=L), then the resistance is known as the “sheet resistance” as shown in equation 2

$$R_S = \frac{\rho}{t} \qquad (2)$$

where t is the thickness of cm and R_s is the sheet resistance in ohm/square. This variable becomes invaluable in the further understanding of surface plasmons as revealed in later chapters.

2.3 Development of a Phenomenological DFT model

Density Functional Theory (DFT) calculations have been used in our group to model the optical and electronic properties of conductive materials for the last several years. [38-40] For all of the DFT calculations discussed within this thesis, single point energy calculations were carried out with the use of the quantum chemical software DMol3 (Accelrys, Inc.). [41]. The double numerical polarized function (DNP) basis set with an atomic cutoff at 5.49Å. was used for all the conducting metal oxides modeled and the Perdew and Wang GGA functional applied. [42] The DFT calculations utilized the grand canonical ensemble approach which allows for partial electron occupation which is needed for the charge carrier calculations. [43] Periodic boundary conditions were employed in all the calculations of the optical and electronic properties of the materials.

Initially, as shown in the Ruthenium oxide chapter (Chapter 10), DFT calculations were carried out in the THERMAL option of DMol3. These calculations were performed at the arbitrary value of 0.02 Hartrees (6300K) and then temperature were increased and decreased until SCF convergence was no longer possible. Typically, a room temperature value at 300 K was impossible to reach. [39, 44] In this option only the electron populations are affected since the nuclear temperature is absolute zero.

The methodology of the DFT calculation was subsequently altered after the breakdown of the model for ruthenium oxide and cadmium tin oxide (CTO). Currently, the analysis is based upon oxygen depletion studies in which the removal of oxygen atoms is responsible for the conductivity of the material similar to one mechanism proposed for ITO [45]. This alternate methodology was first tried with CTO with the random removal of eight oxygen atoms from the unit cell. The energy levels of the CTO were determined from the calculation and then the electron populations are modeled using the Fermi-Dirac distribution function $f(\varepsilon_i) = 1/(1 + \exp[(\varepsilon_i - \varepsilon_F)/k_BT]$, (eqn. 3) where the ε_i are the discrete energies of bands with index i above ε_F. The charge carrier concentration was determined by summing the electrons in the conduction band of cadmium tin oxide divided by the unit cell volume calculated from the lattice constants as shown in the following equation

$$n = \frac{\sum_{i=n_{Fermi}}^{\infty} f(\varepsilon_i)}{V_{cell}} \qquad (4)$$

where n_{Fermi} is the quantum number of the energy level corresponding to the Fermi energy. This approach to determining the charge carrier density is a phenomenological method used to estimate the effects of doping, which is accomplished in CTO by depletion of oxygen atoms. The resulting charge carrier concentrations from this altered approach not only correlate better with experimental values but more importantly, are calculated at room temperature [46]. The following table shows the resultant calculations of CTO.

Table 2.1. The calculated electronic properties of Fermi energy, band gap and charge carrier concentration as a function of the stoichiometry of the oxygen-depleted CTO species.

Stoichiometry	Fermi level	Band Gap	Charge Carrier Density
	ε_F (eV)	ε_G (eV)	n (elec./cm^3) at 300 K
$Cd_{16}Sn_8O_{32}$	-5.03	1.28	3.11×10^{12}
$Cd_{16}Sn_8O_{31}$	-4.93	0.65	9.36×10^{12}
$Cd_{16}Sn_8O_{30}$	-4.78	0.69	2.49×10^{14}
$Cd_{16}Sn_8O_{29}$	-4.81	0.69	1.53×10^{18}
$Cd_{16}Sn_8O_{28}$	-4.80	0.57	4.83×10^{19}
$Cd_{16}Sn_8O_{27}$	-4.68	0.42	3.15×10^{19}
$Cd_{16}Sn_8O_{26}$	-4.71	0.22	1.49×10^{18}

These values are in comparison to the experimental Hall effect measurement of the charge carrier concentration of 1.1×10^{20} electrons/cm^3. As the oxygen is depleted, the better the correlation between experiment and theory appears. The calculated band gap of $Cd_{16}Sn_8O_{32}$ shown in Table 2, is 1.5 eV, which is a factor of two smaller than the experimentally reported values of ~3 eV. [47, 48] The discrepancy of roughly a factor of two between DFT calculations and experiment is well known in the semi-conductor literature. [41 49-51]

This work has resulted in one submitted publication shown in Chapter 9 for cadmium tin oxide. This chapter reveals additional details on the DFT methodology including graphical representations of the electronic populations. Future work in which the revision of the ruthenium oxide takes place may also result in a possible publication submission and further details of those calculations are found in Chapter 10.

2.4 Conclusions

This chapter briefly summarized some of the characterization techniques utilized throughout this thesis work. Each subsequent chapter further details the specific methodology used within it and shows the data collected upon application of the particular method. As will be discussed in each subsequent chapter, some of these methodologies are not yet optimal. I have placed the most updated version of the method within this document to be of use to those working to improve them.

2.5. References

1. Bain, C. D.; Biebuyck, H. A.; Whitesides, G. M., Comparison of Self-Assembled Monolayers on Gold - Coadsorption of Thiols and Disulfides. *Langmuir* **1989**, 723-727.

2. Moses, S.; Brewer, S. H.; Lowe, L. B.; Lappi, S. E.; Gilvey, L. B. G.; Sauthier, M.; Tenent, R. C.; Feldheim, D. L.; Franzen, S., Characterization of single- and double-stranded DNA on gold surfaces. *Langmuir* **2004,** 20, (25), 11134-11140.

3. Bain, C. D.; Evall, J.; Whitesides, G. M., Formation of Monolayers by the Coadsorption of Thiols on Gold - Variation in the Head Group, Tail Group, and Solvent. *Journal of the American Chemical Society* **1989**, 7155-7164.

4. Moses, S. Characterization and functionalization of substrates and nanoparticles for detection of surface binding events of biomolecules. Dissertation, North Carolina State Univeristy, Raleigh, 2005.

5. Stohr, J., *NEXAFS Spectroscopy*. Springer: Berlin, 1992.

6. Ade, H. U., S.G.; , *Chemical Applications of Synchrotron Radiation*. World Scientific Publishing: Singapore, 2002; Vol. 12, p 285-355.

7. Fischer, D.; Efimenko, K.; Bhat, R.; Sambasivan, S.; Genzer, J., Mapping Surface Chemistry and Molecular Orientation with Combinatorial Near-Edge X-Ray Absorption Fine Structure Spectroscopy. *Macromolecular Rapid Communications* **2004,** 25, 141-149.

8. Genzer, J.; Kramer, E. J.; Fischer, D. A., Accounting for Auger yield energy loss for improved determination of molecular orientation using soft x-ray absorption spectroscopy. *Journal of Applied Physics* **2002,** 92, (12), 7070-7079.

9. Outka, D. A.; Stohr, J.; Rabe, J. P.; Swalen, J. D., The Orientation of Langmuir-Blodgett Monolayers Using Nexafs. *Journal of Chemical Physics* **1988,** 88, (6), 4076-4087.

10. Hahner, G., Kinzler, M., Thummler, C., Woll, Ch., Grunze, M., Structure of self-organzing organic films: A near edge x-ray absorption fine structure investigation of thiol layers adsorbed on gold. *Journal of Vacuum Science & Technology A* **1992,** 10, (4), 2758-2763.

11. Hahner, G.; Woll, C.; Buck, M.; Grunze, M., Investigation of Intermediate Steps in the Self-Assembly of N-Alkanethiols on Gold Surfaces by Soft-X-Ray Spectroscopy. *Langmuir* **1993,** 9, (8), 1955-1958.

12. Almeida, R. M.; Vasconcelos, H. C.; Goncalves, M. C.; Santos, L. F., XPS and NEXAFS studies of rare-earth doped amorphous sol-gel films. *Journal of Non-Crystalline Solids* **1998,** 234, 65-71.

13. Genzer, J.; Efimenko, K.; Fischer, D. A., Molecular orientation and grafting density in semifluorinated self-assembled monolayers of mono-, di-, and trichloro silanes on silica substrates. *Langmuir* **2002,** 18, (24), 9307-9311.

14. Genzer, J.; Sivaniah, E.; Kramer, E. J.; Wang, J. G.; Korner, H.; Xiang, M. L.; Char, K.; Ober, C. K.; DeKoven, B. M.; Bubeck, R. A.; Chaudhury, M. K.; Sambasivan, S.; Fischer, D. A., The orientation of semifluorinated alkanes attached to polymers at the surface of polymer films. *Macromolecules* **2000,** 33, (5), 1882-1887.

15. Genzer, J.; Sivaniah, E.; Kramer, E. J.; Wang, J. G.; Xiang, M. L.; Char, K.; Ober, C. K.; Bubeck, R. A.; Fischer, D. A.; Graupe, M.; Colorado, R.; Shmakova, O. E.; Lee, T. R., Molecular orientation of single and two-armed monodendron semifluorinated chains on "soft" and "hard" surfaces studied using NEXAFS. *Macromolecules* **2000,** 33, (16), 6068-6077.

16. Kolczewski, C.; Hermann, K., Ab initio DFT cluster studies of angle-resolved NEXAFS spectra for differently coordinated oxygen at theV(2)O(5)(010) surface. *Surface Science* **2004,** 552, (1-3), 98-110.

17. Plaschke, M.; Rothe, J.; Denecke, M. A.; Fanghanel, T., Soft X-ray spectromicroscopy of humic acid europium(III) complexation by comparison to model substances. *Journal of Electron Spectroscopy and Related Phenomena* **2004,** 135, (1), 53-62.

18. Fujii, K.; Akamatsu, K.; Yokoya, A., Near-edge X-ray absorption fine structure of DNA nucleobases thin film in the nitrogen and oxygen K-edge region. *Journal of Physical Chemistry B* **2004,** 108, (23), 8031-8035.

19. Liedberg, B., Nylander, C., Lundstrom, I., Surface plasmon resonance for gas detection and biosensing. *sensors and Actuators B* **1983,** 4, 299-304.

20. Vareiro, M. L. M.; Liu, J.; Knoll, W.; Zak, K.; Williams, D.; Jenkins, A. T. A., Surface plasmon fluorescence measurements of human chorionic gonadotrophin: Role of antibody orientation in obtaining enhanced sensitivity and limit of detection. *Analytical Chemistry* **2005,** 77, (8), 2426-2431.

21. Ekgasit, S.; Tangcharoenbumrungsuk, A.; Yu, F.; Baba, A.; Knoll, W., Resonance shifts in SPR curves of nonabsorbing, weakly absorbing, and strongly absorbing dielectrics. *Sensors and Actuators B-Chemical* **2005,** 105, (2), 532-541.

22. Fujii, E.; Shimizu, K.; Kurokawa, Y.; Endo, A.; Sasaki, S.; Kurihara, K.; Citterio, D.; Yamazaki, H.; Suzuki, K., Determination of glycosylated albumin using surface plasmon resonance sensor. *Bunseki Kagaku* **2003,** 52, (5), 311-317.

23. Englebienne, P.; Van Hoonacker, A.; Verhas, M., Surface plasmon resonance: principles, methods and applications in biomedical sciences. *Spectroscopy-an International Journal* **2003,** 17, (2-3), 255-273.

24. Morrill, P. R.; Millington, R. B.; Lowe, C. R., Imaging surface plasmon resonance system for screening affinity ligands. *Journal of Chromatography B-Analytical Technologies in the Biomedical and Life Sciences* **2003,** 793, (2), 229-251.

25. Nelson, B. P.; Liles, M. R.; Frederick, K. B.; Corn, R. M.; Goodman, R. M., Label-free detection of 16S ribosomal RNA hybridization on reusable DNA arrays using surface plasmon resonance imaging. *Environmental Microbiology* **2002,** 4, (11), 735-743.

26. Shumaker-Parry, J. S.; Zareie, M. H.; Aebersold, R.; Campbell, C. T., Microspotting streptavidin and double-stranded DNA Arrays on gold for high-throughput studies of protein-DNA interactions by surface plasmon resonance microscopy. *Analytical Chemistry* **2004,** 76, (4), 918-929.

27. Smith, E. A.; Erickson, M. G.; Ulijasz, A. T.; Weisblum, B.; Corn, R. M., Surface plasmon resonance imaging of transcription factor proteins: Interactions of bacterial response regulators with DNA arrays on gold films. *Langmuir* **2003,** 19, (5), 1486-1492.

28. Soh, N.; Tokuda, T.; Watanabe, T.; Mishima, K.; Imato, T.; Masadome, T.; Asano, Y.; Okutani, S.; Niwa, O.; Brown, S., A surface plasmon resonance immunosensor for detecting a dioxin precursor using a gold binding polypeptide. *Talanta* **2003,** 60, (4), 733-745.

29. Wegner, G. J.; Lee, H. J.; Corn, R. M., Characterization and optimization of peptide arrays for the study of epitope-antibody interactions using surface plasmon resonance imaging. *Analytical Chemistry* **2002,** 74, (20), 5161-5168.

30. Yu, F.; Tian, S. J.; Yao, D. F.; Knoll, W., Surface plasmon enhanced diffraction for label-free biosensing. *Analytical Chemistry* **2004,** 76, (13), 3530-3535.

31. Patskovsky, S.; Kabashin, A. V.; Meunier, M.; Luong, J. H. T., Properties and sensing characteristics of surface-plasmon resonance in infrared light. *Journal of the Optical Society of America a-Optics Image Science and Vision* **2003,** 20, (8), 1644-1650.

32. Otto, A., A New Method for Exciting Nonradiant Plasma Surface Vibration. *Physica Status Solidi* **1968,** 26, (2), K99-&.

33. Wood, R. W., A suspected case of the electrical resonance of minute metal particles for light-waves. A new type of absorption. *Philosophical Magazine* **1902,** 3, (13-18), 396-410.

34. Fahlman, A.; Hamrin, K.; Hedman, J.; Nordberg, R.; Nordling, C.; Siegbahn, K., Electron Spectroscopy and Chemical Binding. *Nature* **1966,** 210, (5031), 4-&.

35. Wagner, C. D.; Gale, L. H.; Raymond, R. H., 2-Dimensional Chemical-State Plots - Standardized Data Set for Use in Identifying Chemical-States by X-Ray Photoelectron-Spectroscopy. *Analytical Chemistry* **1979,** 51, (4), 466-482.

36. Howland, R., Benatar, L., *A Practical Guide to Scanning Probe Microscopy*. Park Scientific Instruments: 1997.

37. *SPM Training Notebook*. Version 3.0 ed.; Veeco Instruments Incorporated: 2003.

38. Brewer, S. H.; Franzen, S., Indium tin oxide plasma frequency dependence on sheet resistance and surface adlayers determined by reflectance FTIR spectroscopy. *Journal of Physical Chemistry B* **2002,** 106, (50), 12986-12992.

39. Brewer, S. H.; Franzen, S., Calculation of the electronic and optical properties of indium tin oxide by density functional theory. *Chemical Physics* **2004,** 300, (1-3), 285-293.

40. Franzen, S., Density functional calculation of a potential energy surface for alkane thiols on Au(111) as function of alkane chain length. *Chemical Physics Letters* **2003,** 381, (3-4), 315-321.

41. Delley, B., An all-electron numerical-method for solving the local density functional for polyatomic molecules. *Journal of Chemical Physics* **1990,** 92, (1), 508-517.

42. Perdew, J. P.; Chevary, J. A.; Vosko, S. H.; Jackson, K. A.; Pederson, M. R.; Singh, D. J.; Fiolhais, C., Atoms, molecules, solids and surfaces - Applications of the generalized gradient approximation for exchange and correlation. *Phys. Rev. B* **1992,** 46, 6671-6687.

43. Mermin, N. D., Thermal Properties of Inhomogeneous Electron Gas. *Physical Review* **1965,** 137, (5A), 1441-1443.

44. Brewer, S. H.; Wicaksana, D.; Maria, J. P.; Kingon, A. I.; Franzen, S., Investigation of the electrical and optical properties of iridium oxide by reflectance FTIR spectroscopy and density functional theory calculations. *Chemical Physics* **2005,** 313, (1-3), 25-31.

45. Gonzalez, G. B.; Mason, T. O.; Quintana, J. P.; Warschkow, O.; Ellis, D. E.; Hwang, J. H.; Hodges, J. P.; Jorgensen, J. D., Defect structure studies of bulk and nano-indium-tin oxide. *Journal of Applied Physics* **2004,** 96, (7), 3912-3920.

46. Rhodes, C. L. B., S.H.; Folmer, J.; Li,X., Coutts, T.J.; Franzen, S. , Investigation of an Alkane Thiol Adlayer on Cadmium Tin Oxide Thin Films. *Thin Solid Films* **Accepted**.

47. Mamazza, R.; Morel, D.; Ferekides, C., Transparent conducting oxide thin films of Cd2SnO4 prepared by RF magnetron co-sputtering binary oxides. *Thin Solid Films* **2005,** 484, (1-2), 26-33.

48. Metz, A. W.; Ireland, J. R.; Zheng, J. G.; Lobo, R.; Yang, Y.; Ni, J.; Stern, C. L.; Dravid, V. P.; Bontemps, N.; Kannewurf, C. R.; Poeppelmeier, K. R.; Marks, T. J., Transparent conducting oxides: Texture and microstructure effects on charge carrier mobility in MOCVD-derived CdO thin films grown with a thermally stable, low-melting precursor. *Journal of the American Chemical Society* **2004,** 126, (27), 8477-8492.

49. Hohenberg, P.; Kohn, W., Inhomogeneous Electron Gas. *Physical Review B* **1964,** 136, (3B), B864-&.

50. Kohn, W.; Sham, L. J., Self-Consistent Equations Including Exchange and Correlation Effects. *Physical Review* **1965,** 140, (4A), 1133-&.

51. Sham, L. J.; Kohn, W., 1-Particle Properties of an Inhomogeneous Interacting Electron Gas. *Physical Review* **1966,** 145, (2), 561-&.

Chapter 3

Theoretical Approaches to Understanding Conductivity in Conducting Metal Oxides

3.1. Theoretical Section

3.1.1. Band Structure Definition

In the early twentieth century, Neils Bohr developed his model of the atom in which discrete energy levels of the electrons existed. The energy of these levels is given in equation (1).

$$E_n = -\left(\frac{me^4}{8h^2\varepsilon_o^2}\right)\frac{1}{n^2} \qquad (1)$$

where n is an integer indicating the numeric of the energy level, m is the mass of the electron, e is the charge on the electron, h is Planck's constant, and ε_o is the permittivity of free space. [1] This model was the basis for the theory of solid band structure put forth by Felix Bloch in 1928, which depicts the probability of the location of an electron within a solid. As the electron energy levels defined by Bohr and others are brought in close contact with each other in the solid structure, a broadening occurs. In a more simplistic view, this is attributed primarily to the Pauli Exclusion principle, which does not allow for identical electronic states and thus, the electron energies shift relative to each other. [1] A more complete description includes the concept of periodicity. The crystal may contain delocalized levels over the entire structure leading to continuous band of energies. Conversely, a crystal

structure may contain nodes due to orbital symmetry which shift the energy bands into more discrete units. The Pauli Exclusion principle allows each level to have only two electrons and thus, creating the concept of energy bands [2]. The amount of shift and broadening of these energy levels into "bands" is highly dependent on the type and number of atoms found within the solid. For clarification, Figure 3.1 shows the energy levels for the allowed states in the case of the free electron such as those found in an ideal metal (a), the bound electrons within the nodes of a solid such as those within a semi-metal or semiconductor (b), and an insulator (c).

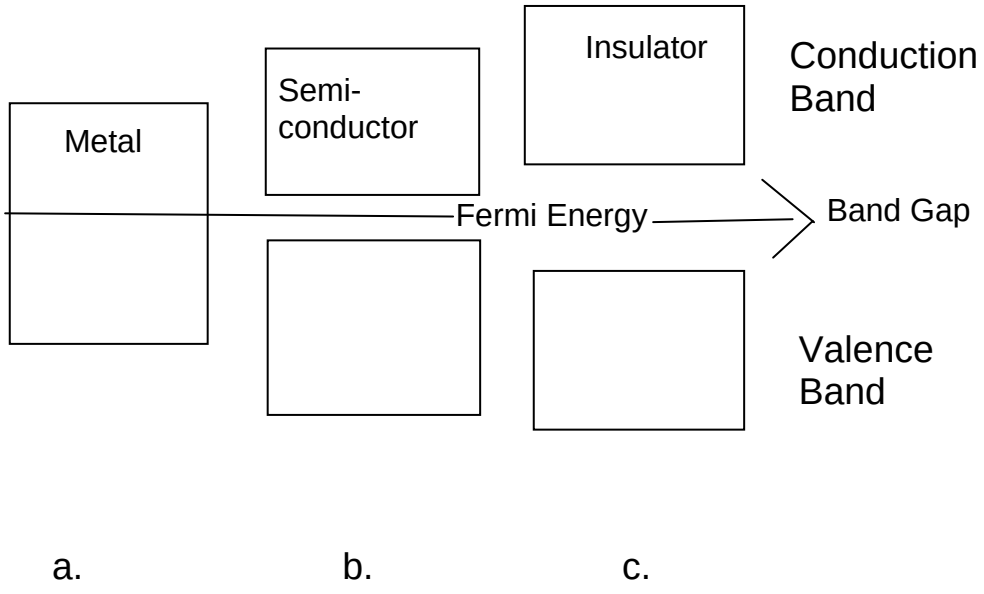

Figure 3.1. Graphical representation of the separation of energy levels for the electronic allowed states in an ideal metal (a), a semi-metal or semiconductor (b), and an insulator (c). The Fermi Level separating the valence and conduction bands is shown. The band gap is depicted as the gap between these levels.

This modification of energy levels into energy bands is known as the "tight-binding approximation" due to the fact that the model is based upon the modification of tightly bound electrons in an atom. This is in contrast to the other popular theory known as the "free-electron approximation", in which free electrons are converted into periodic potentials within a solid. Both models are valid; but they differ in their approach. Since their inception, intermediate models have since been developed that utilize concepts from both models. [1]

In this energy band approximation discussed above, the highest occupied electronic energy band is the "valence band". The lowest unoccupied energy level at ground state is the "conduction band". The Fermi level separates the valence band from the conduction band and it is this level that defines the differences between semi-conductors, insulators, and metals. Specifically, the Fermi energy, ε_f, is the energy of the highest filled level in the ground state of the N electron system as shown in equation 2.

$$\mathcal{E}_f = \frac{\hbar^2}{2m}\left(\frac{n_f \pi}{L}\right)^2 \qquad (2)$$

where n_f is the highest filled energy level, m is the mass of an electron that is confined to length L. Thus, the location of the Fermi energy level with regard to the allowed energy states is essential for this determination of the electrical properties. The figure below displays this electronic occupancy of a metal, semiconductor and insulator in solids. [3]

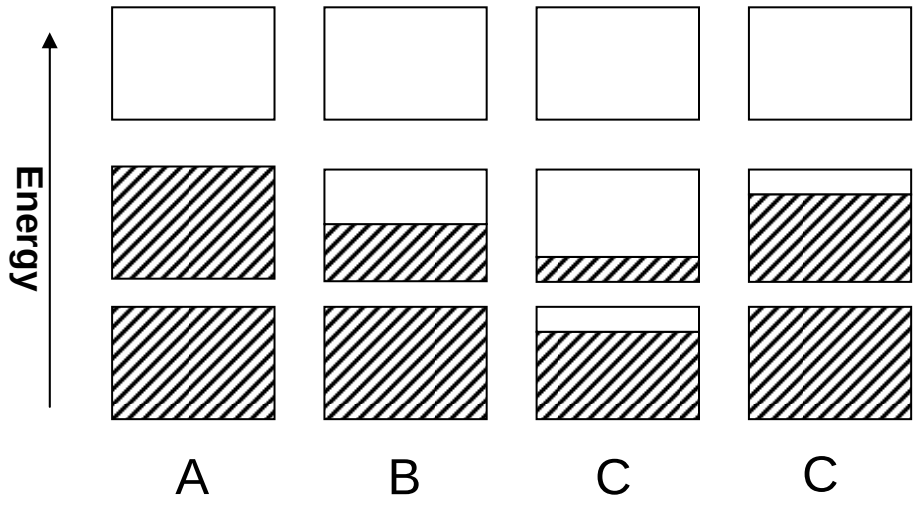

Figure 3.2. The energy bands of an insulator (A), a metal (B) and two types of semiconductors (C). The position of these bands are directly related to the observed conductivity of these materials.

As shown in equation 2 and Figure 3.2, these levels are a direct function of the electron occupancy of the conduction electrons. The response of the electrons to an applied electric field is the basis for conductivity in solids. As shown, an insulator (A) has all the possible energy bands either filled or empty, thus the electrons do not show a response to an electric field and are therefore, not conductive. Conversely, a metal (B) has partially filled bands and thus, displays a large response to an applied electric field in the form of electrical conductivity. Semiconductors (C) exhibit an intermediate response as they possess one or two bands that are either slightly filled or slightly empty.

The ground state discussed above is at absolute zero and is thus, not applicable for standard conditions. The solution for distribution of the electron with a rise in temperature is known as the Fermi-Dirac distribution. As shown below in equation 3, this function gives the probability that in an ideal gas at thermal equilibrium, an orbital at energy ε will be occupied.

$$f(\varepsilon) = \frac{1}{\exp[(\varepsilon - \mu)/k_B T] + 1} \qquad (3)$$

The quantity μ is a function of temperature that is equivalent to N; therefore, μ equals ε_f at absolute zero. [3]

Furthermore, a more complete understanding arose with the revision of the rival model, the free electron model (see appendix 1), which extended the model to include periodic lattices of the solid. Additionally, at this point, it is prudent to mention the concept of "effective mass" (m*) in which the presence of an electric field, the mass of the electron may become larger or smaller than the free electron mass depending on their conductivity-it is only the effective mass that is considered herein. Effective mass is thus an adjustable parameter that accounts for the experimental observation that electron mobility is affected by the occupancy of the energy bands.

This revised Nearly Free Electron model adequately explains the physical origins of the energy gaps. In crystals, the wavefunctions have approximately the same dimension as the lattice. Once a periodic potential is introduced, if the potential barrier is electron energy barrier then the wave

function will be reflected. These reflections are known as Bragg reflections. The condition for this reflection is $2a(\sin\theta)=n\lambda$ where a is the lattice parameter, θ is the angle of reflection, and λ is the wavelength of the electrons. This relationship is also knows as "Bragg's Law". These reflections are related to wave propagation in the lattice and are responsible for the observed energy gaps in the crystal. The description of the energy gaps determines whether a solid is an insulator or conductor. The physical description of the energy is shown in the figure below in Figure 3.3.

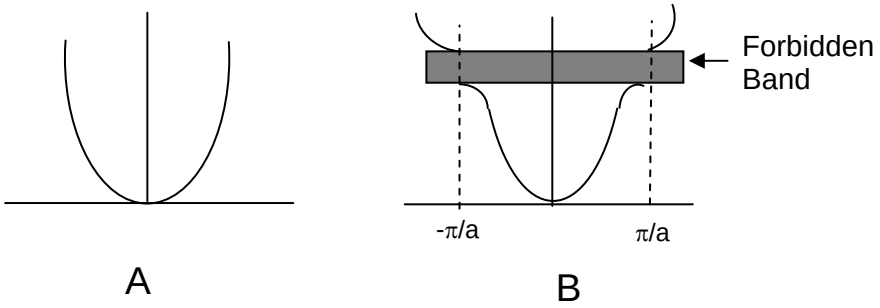

Figure 3.3. Physical depiction of the "Free Electron" model (A) assuming ideal noninteracting electrons within the metal and the "Nearly Free Electron" model (B) which includes a periodic perturbation to take into account interactions between conduction electrons and ions in a crystal. Neither model takes into account electron-electron interactions.

The comparison between the two plots displays the differences between the free electron model and the nearly free electron model in which an energy gap is apparent at the first Bragg reflection shown (first Brillouin zone). The Brillouin zone is thus the boundary, at which the reflections of the electron wavefunction occur. In a linear solid with a lattice constant of a, the

wavevector, k becomes k=± nπ/a. It is at this point that the first energy gap forms, with more gaps formed at subsequent values of n. These wavefunctions are not traveling waves as in the free electron model but are standing waves composed of equal parts of right- and left-directed traveling waves. The result is that rather than a constant charge density found in free electrons, the standing waves of the wavevector k have different values of the potential energy and form energy gaps. This gap is equal to the Fourier component of the potential of the crystal.

As stated above, Bloch was instrumental in fundamental understanding of energy bands. [4] In the form of localized wave packets, the Bloch functions represent electrons that propagate freely through the potential field. The solutions of the wave equation in a periodic lattice are shown in the following equation [3]

$$\psi_K(r) = e^{ik\cdot r} u_k(r) \qquad (4)$$

where k is the wavevector and $u_k(r)$ is an invariant function having the period of the crystal lattice. It is these functions that allow for the existence of forbidden regions of energy to exist, thus, creating gaps and differentiating between insulators and conductors.

The conductivity classification of a material is dependent upon the number of valence electrons in a primitive cell. In an insulator, this number must be even, leading to bands that are completely filled. Alkali and noble metals have one valence electron leading to their good conductivity. Alkaline

metals have two electrons in overlapping bands therefore they are not insulators, but they are also not very good conductors. Thus, these theories of the bands lead to a graphical representation of a material as shown in the following Figure 3.4.

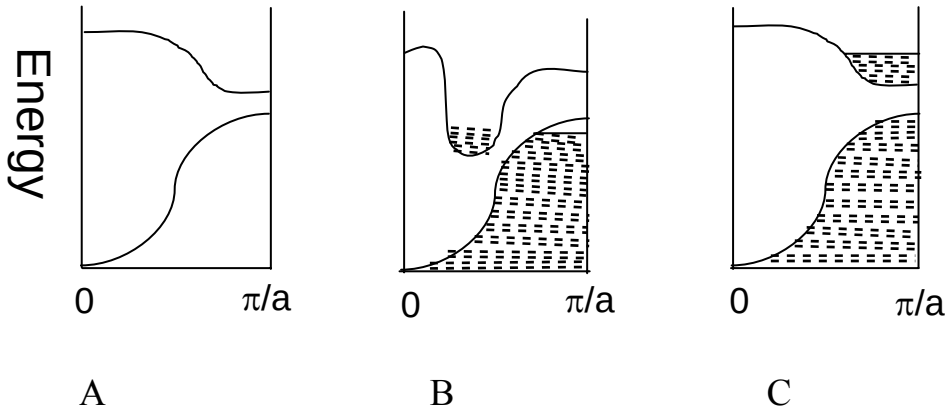

Figure 3.4. Graphical depiction of the valence electrons in a primitive cell of an insulator (A), an alkali or noble metal (B), and an alkaline metal (C).

3.1.2. Calculation of the Band Structure of Indium Tin Oxide

Band structure diagrams describe the theoretical regions within a solid that an electron is allowed or forbidden to inhabit. As part of my thesis research, I attempted to calculate the band structure of indium tin oxide using a theoretical real space code developed by Professor Bernholc's group Lu at North Carolina State University. For band structure calculations, two primary models exist based upon either 1) plane waves or 2) real space. The advantage to the plane wave approach is ease of developing a band structure. Many downloadable programs including Quantum Expresso exist and are relatively user friendly. The primary disadvantage is the limitations associated with both computational time as well as the numerical limit of

atoms present in the model. In contrast, the real space code, although less user friendly and less commercialized, is useful for larger structures (especially those with more than 200 atoms) and is time saving since it can be placed in a parallel computing system.

Computation was conducted on a 4.5 TF IBM pSeries System operated by the NCCS for the Joint Institute for Computational Sciences (JICS). The compute partition includes 27 p690 nodes, each with thirty-two 1.3 GHz Power4 processors. Most of the compute nodes have 32 GB of memory, five have 64 GB of memory and two have 128 GB of memory.

In general, this real space code requires the use of materials comprised of elements in which the pseudopotential values have been previously determined. The real space source code needs to be within the framework of the supercomputer. The result of the computations is the eigenvalues of the plane waves in real space of the band structure for the user-defined k points (typically ~15). The projects along Γ→xyz of 000, ½00, 0½0, 00½, ½½½ were chosen. The values of the output files received (in the form of wave.out) are the k points related to the effective mass (m*) by the following equation

$$m^* = \hbar^2 \left[\frac{d^2 \varepsilon}{dk^2} \right]^{-1} \tag{5}$$

where k is the wave vector and $\varepsilon(k)$ is the energy as a function of k, or the dispersion relation. For a free particle, the effective mass is equal to the real

mass as a result of a quadratic dispersion relation. Yet in solids the dispersion relation is not quadratic effective mass differs from the free electron mass. The concept of the effective mass can be useful wherever a minimum occurs in the dispersion relation, the minimum can be approximated by a quadratic curve in the small region around that minimum. Therefore, for electrons, which have energy close to a minimum, effective mass is a useful concept. In general, energy bands with high curvature lead to a low effective mass, flat energy bands lead to high effective mass and for an electron near the top of an energy band, ie, a "hole", the effective mass is negative. A negative effective mass suggests deceleration in the presence of an electric field possibly to due momentum transfer to the lattice. For ITO, the concept of holes is not an issue.

As shown in the following figures, the band structures determination reveals the effective masses of the substrate in question. These figures depict band structures determined using this real space code for indium tin oxide substrates with either zero tins (indium oxide) or one tin (ITO). The k points were calculated from gamma to 0.5 and mirror spectra over this range were generated.

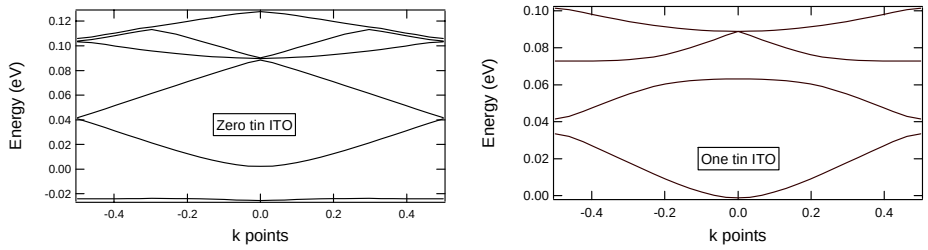

Figure 3.5. Theoretical band structure of indium oxide (zero tin ITO) and indium tin oxide (one tin ITO) calculated from real space pseudopotential code.

For calculation of the effective mass, a mathematical quadratic fit of the band structure is shown below with an accompanying table of calculated effective masses of various ITO substrates. For each of the substrates, a more accurate effective mass was determined using a smaller subset of the points as shown in the small graphs.

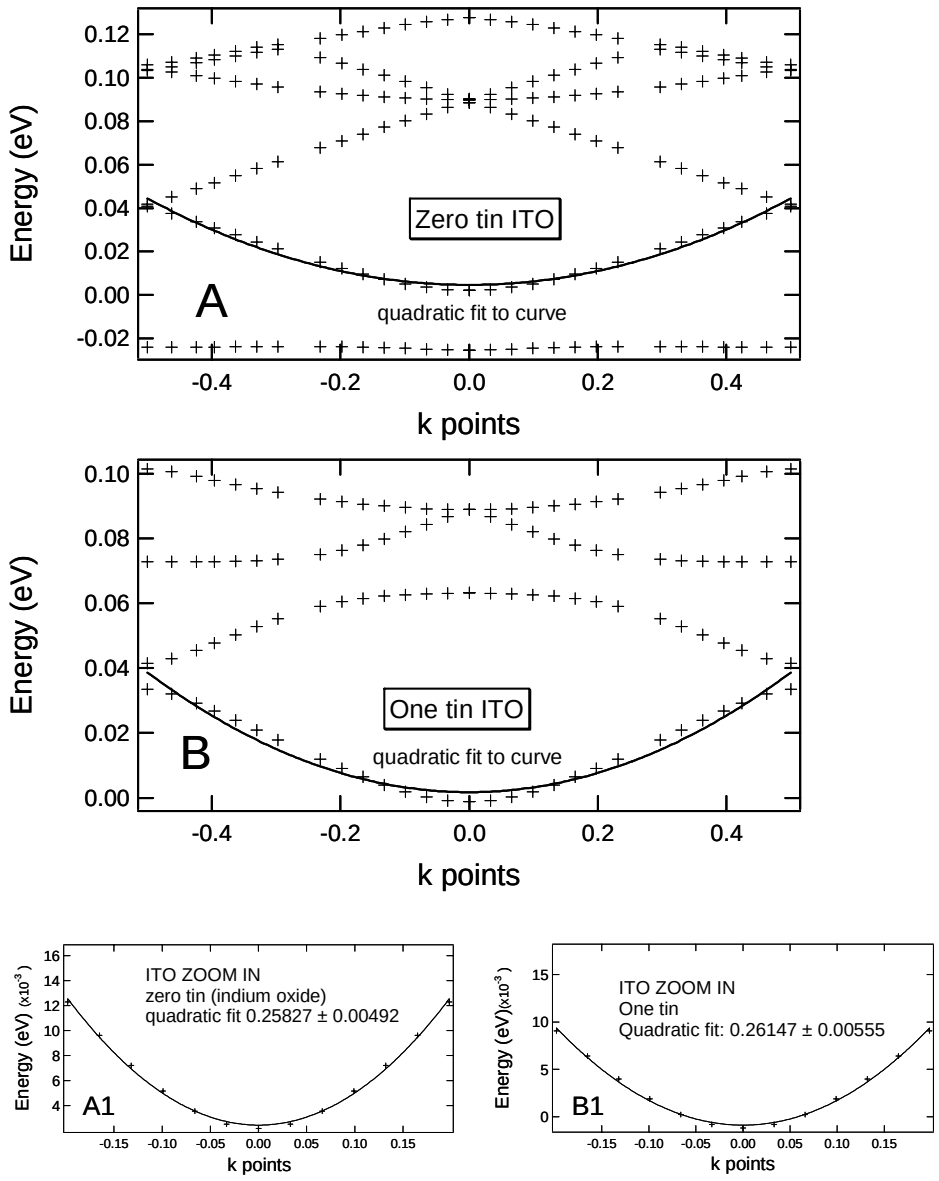

Figure 3.6. Determination of effective mass from a quadratic fit of the band structure for indium oxide (A) and indium tin oxide (B). Zoomed in sections of each graph (A1,B1) were used for the calculation.

Table 1- Effective mass (m_e) calculations of ITO ranging from 0 - 9.375% tin doping.

Substrate	Number of Tins	Calculated Effective Mass
Indium Oxide	Zero	0.25827 ± 0.00492
Indium Tin Oxide One tin – 3.125%	One	0.26147 ± 0.00555
Indium Tin Oxide Two tin – 6.25%	Two - 1st Electron	0.26609 ± 0.00639
	Two - 2nd Electron	0.30042 ± 0.0272
Indium Tin Oxide Three tin – 9.375%	Three – 1st Electron	0.2533 ± 0.00723
	Three – 2nd & 3rd Electrons	0.2611 ± 0.0326

The theoretical and experimental effective mass of ITO previously reported by our laboratory and others is ~0.3-0.4 m_e [5] which is in reasonable agreement with the results obtained here.

For this research, the ultimate goal was both the confirmation of earlier more simplistic theoretical calculations of the effective mass and the determination of a charge carrier density for ITO. Confirmation of the effective mass was accomplished although the methodology used utilized only full or empty orbitals, partial occupation was not an option. This limitation did not allow for any reasonable calculation of a charge carrier concentration and thus, the study did produce all the anticipated results.

3.1.3: Computational aspect of Effective Mass Determination

1. Two input files are prepared, a typical input file with all controls and commands for the myriad of possible variations available for the band structure calculations. The second file is the pseudopotential file for

the elements in use for the band structure calculations. See Appendix 3. A Makefile command assists in determination of which platform to use and then compilation of the code must take place.

3.2. Experimental Determination of Resistivity of Conducting Metal Oxides

I will begin discussion of the material properties of two conducting metal oxides, indium tin oxide (ITO) and aluminum-doped zinc oxide (AZO) in the regime of experimental resistivities and infrared data. This resultant experimental data gave me the first indication of the wide variability in the material properties of different CMO's. It lead directly to my interest in other techniques such as NEXAFS to further explore and understand this vast range of possible material properties within this class of thin film substrates.

3.2.1. Indium Tin Oxide

Initially, the studies performed on ITO had been conducted at room temperature; thus, as an extension to these original studies, I began examining the temperature dependence of the electronic and optical properties of the metal oxide. [5] For the electronic properties, the experimental resistivity was examined followed by the theoretical calculation of it's band structure (see 1.3). In pure metals, such as gold or silver, the temperature dependence of the resistivity is related by the Drude free electron model as given in equation 6

$$\sigma = \frac{\eta e^2 \tau}{m} = \frac{1}{\rho} \qquad (6)$$

where σ is the conductivity and ρ is the resistivity, η is the density of conduction electrons, *e* is the electron charge, *m* is the electron effective mass and τ is the scattering time *τ*. Thus, to investigate the similarities and/or differences of the electronic properties of the ITO substrates to pure metals, the resistivity was studied with a four point probe using the Van de Pauw method. [6] This study involved development of a temperature dependent four point probe capable of measurement within the range of liquid nitrogen (85K to 460K). The figure below shows the results of this study.

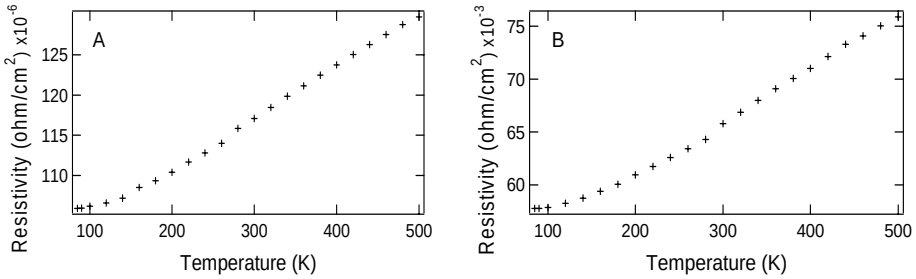

Figure 3.7 A,B. Resistivity spectra of 2 ITO slides of the same manufacturer as a function of temperature in the range of 85K to 460K in ~20K increments.

The measured resistivity from 85 K to 460 K are indicative of both metallic as well as semiconductor character in the thin film. The resistivity of an ideal metallic film is directly proportional to the temperature (ρ~T) with an initial residual resitivity due to impurity scattering. In figures 3.7A,B this residual resistivity is not apparent nor is the resistivity response directly proportional to the temperature. In an ideal semiconductor, the charge carrier density is proportional to the conductivity, thus, leading to an exponential relationship between conductivity and temperature. [1] Therefore, the curvatures observed

in the above plots may be due to a nonmetallic, possibly semiconductor-type behavior. However, this increase in resistivity correlates well with previous studies of the conductance of indium tin oxide performed by Popplemeir. [7] The measurements in both laboratories indicate that ITO is an excellent conductor, however, it is quite different from typical metals. The charge carrier density is lower and there is a significant band gap. ITO is known as a degenerate semiconductor whose conducting properties depend on n-type doping due to Sn atoms and oxygen deficiencies. I examined the temperature dependent shifts of the plasmon band of ITO from 5 K to 460 K and correlated these shifts with the resistivity measurements from 85K to 460 K shown above. Figures 8A and 8B show the temperature dependent transmission FTIR spectra of two ITO thin films at an angle of normal incident using a helium-cooled cryostat. There is a significant shift in the region of the plasmon frequency with a change in temperature. As the change in temperature increases, the spectrum shifts to higher wavenumbers. This is indicative of a change in the electronic scattering time as defined by the Drude model. [8]

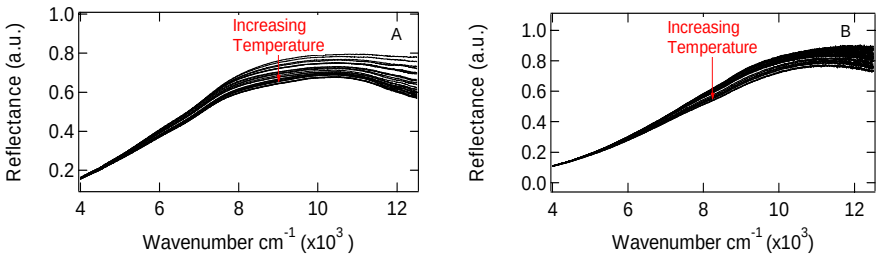

Figure 3.8A,B FTIR Transmission spectra of two different ITO slides manufactured by Delta technologies as a function of temperature in the range of 5-460K in ~20K increments.

The relative magnitude of the frequency shift is different for the two spectra, thus indicating the variability between electrodes from the same lot and manufacturer of ITO slides. The properties of this conducting metal oxide were directly compared to another sp-type conducting metal oxide to investigate the differences between the class of conducting metal oxides.

3.2.2. Aluminum-doped (2%) Zinc Oxide

For comparison, the temperature dependence of the resistivity and transmission FT-IR spectra of aluminum-doped (2%) zinc oxide was studied to examine the relationship of the intrinsic properties to near-infared spectra. Resistivity measurements were conducted on the ZnO:Al thin films with the same temperature dependent 4-point probe as described above. Similar to metals, the resistivity of the ZnO:Al thin films are nearly constant at low temperatures, signifying very little phonon scattering occurring in this region. As the temperature increases, the resistivity also increases but unlike a metal, it does not follow a quadratic rate increase. This is shown in figure 3.9 below.

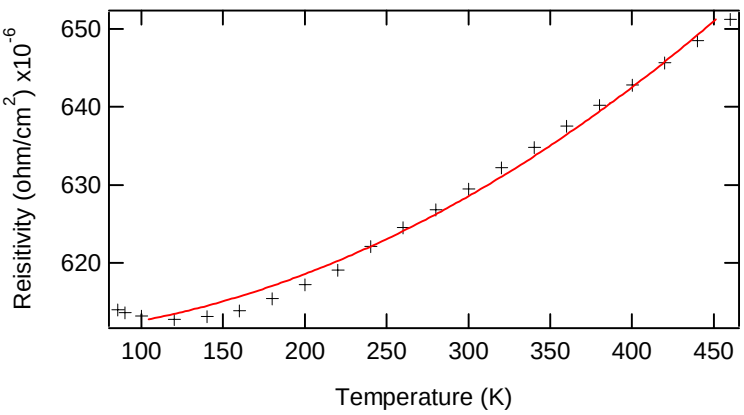

Figure 3.9. Resistivity spectra of the ZnO thin film as a function of temperature in the range of 85K to 440K in ~20K increments. The markers (+) indicate the experimental resistivity. The red line compares the typical quadratic increase for a metal with the experimental data of the AZO.

Therefore, AZO does have metallic character but it is not a pure metal. This resistivity is in sharp contrast to ITO which more closely resembles the resistivity of a semiconductor above room temperature. Theoretically, it is proposed that the addition of the aluminum dopant (2-5%) decreases the resistvity and increases the conductivity as compared to zinc oxide by the replacement of Zn^{+2} with Al^{+3} ions. [9] [10] [11] This research on conducting doped ZnO shows the need for a better understanding of the nature of the metal oxide properties.

The optical properties of this conducting metal oxide were examined by studying the temperature dependence of the transmission FTIR spectra. Figure 9 reveals the temperature dependence of these spectra of the AZO thin film at an angle of normal incident using a helium-cooled cryostat with a temperature range of 5 K to 440 K. This figure reveals a significant shift in the region of the plasmon frequency with a change in temperature.

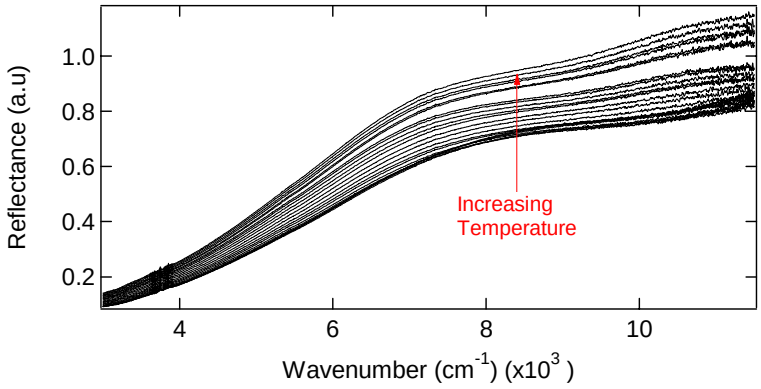

Figure 3.10. FTIR transmission spectra of a ZnO thin film deposited onto a CaF window as a function of temperature in the range of 5-440K in ~20K increments.

As temperature increases, the spectra shift to lower wavenumbers. This is indicative of a change in the material properties of ITO, such as the in the electron mobility or the charge carrier density. More recent data has supported this claim with a controlled change in the charge carrier density causing a shift in the surface plasmon resonance spectra (data not shown). In comparison with the temperature dependence study of Indium Tin Oxide (see figure 3.7 A,B), the trend is exactly the reverse with increasing temperature increasing the wavemenumbers. Thus, there is a wide variability within the class of sp-type conducting metal oxides allowing for the exploitation of many different properties in the area of biosensing.

3.3. References

1. Jiles, D., *Introduction to the Electronic Properties of Materials*. Chapman & Hall: London, 1994.

2. Canadell, E.; Whangbo, M. H., Conceptual Aspects of Structure Property Correlations and Electronic Instabilities, with Applications to Low-Dimensional Transition-Metal Oxides. *Chemical Reviews* **1991,** 91, (5), 965-1034.

3. Kittel, C., *Introduction to Solid State Physics*. Seventh Edition ed.; John Wiley & Sons: New York, 1996.

4. Bloch, F., *Z. Phsik* **1928,** 52, 555.

5. Brewer, S. H.; Franzen, S., Optical properties of indium tin oxide and fluorine-doped tin oxide surfaces: correlation of reflectivity, skin depth, and plasmon frequency with conductivity. *Journal of Alloys and Compounds* **2002,** 338, (1-2), 73-79.

6. Van der Pauw, L. J., A Method of Measuring Specific Resistivity and Hall Effect of Discs of Arbitrary Shape. *Philips Research Reports* **1958,** 13, (1), 1-9.

7. Ambrosini, A.; Duarte, A.; Poeppelmeier, K. R.; Lane, M.; Kannewurf, C. R.; Mason, T. O., Electrical, optical, and structural properties of tin-doped In2O3-M2O3 solid solutions (M = Y, Sc). *Journal of Solid State Chemistry* **2000,** 153, (1), 41-47.

8. Wooten, F., *Optical Properties of Solids*. Academic Press, Inc.: San Diego, 1972.

9. Suh, K. J.; Okada, H.; Wakahara, A.; Kim, H. J.; Chang, H. J.; Yoshida, A., Transparent conducting ZnO films on polymer substrates by pulsed laser deposition. In *Advances in Nondestructive Evaluation, Pt 1-3*, 2004; Vol. 270-273, pp 878-883.

10. Jeong, W. J.; Park, G. C., Electrical and optical properties of ZnO thin film as a function of deposition parameters. *Solar Energy Materials and Solar Cells* **2001,** 65, (1-4), 37-45.

11. Park, K. C.; Ma, D. Y.; Kim, K. H., The physical properties of Al-doped zinc oxide films prepared by RF magnetron sputtering (vol 305, pg 201, 1997). *Thin Solid Films* **1998,** 320, (2), 329-329.

Chapter 4

Surface Plasmon Resonance in Conducting Metal Oxides

(Adaptation from Publication *Journal of Applied Physics* 100 (5) 2006)

4.1. Abstract

We report the initial observation of surface plasmon resonance (SPR) in a conducting metal oxide thin film. The SPR phenomenon has been observed by attenuated total reflection of near-infrared radiation and is in agreement with electron energy loss spectroscopy measurements. To date, only metals are known to exhibit surface plasmon resonance and only noble metals have practical application. According to theory SPR should be observable in any conductor. This theoretical prediction is verified in the present study. The compositions of many conducting metal oxides are systematically variable, suggesting a significant advance in thin film characterization and novel possibilities for versatile and sensitive chemical sensing applications.

4.2 Introduction

Surface plasmon resonance (SPR) spectroscopy is an optical technique used to measure changes in the index of refraction in a self-assembled monolayer or liquid in contact with a conducting thin film. SPR has been widely used to study binding interactions of biomolecules including antigen/antibody, complementary DNA probes, enzyme/substrate, and receptor/ligand interactions. [1-12] Although the theoretical principles underlying the SPR effect are applicable to any conductive material, only silver and gold thin films have been used in practical SPR instrumentation. Gold has been the metal of choice for SPR applications because its plasma resonance is observed in the visible part of the electromagnetic spectrum giving rise to its yellowish luster. There are isolated reports of SPR on other transition metals such as copper [13-15], aluminum [16], or nickel [17], however, most metals have surface plasmon frequencies in the ultraviolet region > 8 eV. In contrast, gold and silver have surface plasmon frequencies of 2.5 eV and 3.9 eV, respectively [18,19], due to the fact that the d-electron bands of gold and silver are lower in energy than the conduction bands in these metals. Consequently, silver and gold have been the primary substrates for SPR research in over three decades of investigation [20,21]. A recent innovation in SPR sensing applications using gold substrates has been the use of a Fourier-transform infrared (FTIR) spectrometer equipped with a θ-2θ stage for the detection of surface plasmons in the near-infrared [22,23]. We have used this instrumentation to identify SPR, for the first time, in the well-known thin film conductor indium tin oxide ($In_{1-x}Sn_xO_3$). Our data suggest that this observation

extends to the full range of sp- and d-type conducting metal oxide materials (CMOs), better elucidating the fundamental physics of SPR as a general phenomenon in conductors.

The observation of SPR in a conducting metal oxide has implications for materials science as well as optical applications in sensing and analysis. The frequency of surface plasmons is related to the charge carrier density, which can be correlated with reflectance measurements as a novel probe of the surface conductance of thin films. Unlike noble or base metals, many conducting metal oxides (CMOs) exhibit a systematic range of composition due to differences in metal atom doping and oxygen content. The ability to tune the SPR frequency by changing the thin film preparation has exciting application in the study of the electronic and optical properties of novel materials. The observations reported here extend the SPR method to materials that span a range of surface chemistries [24-26]. The basic experimental observation of the SPR effect in a well-known thin film material, indium tin oxide (ITO), has implications for a vast domain in solid state and surface chemistry, namely, thin film conducting metal oxides.

SPR behavior is explained by the Drude Free Electron model, which describes the transport properties of electrons in any conducting material by portraying the conduction electrons as a non-interacting classical gas surrounding immobile positive ions [18]. In response to electromagnetic waves, the conduction electrons oscillate and create an electric field on the surface that has a limited penetration depth (skin depth). The collective response of the conduction electrons to the alternating electric field can

be compared to a forced harmonic oscillator. The restoring force is the Coulombic attraction of the electrons with the nuclei in the lattice. The resonant frequency of the forced harmonic oscillator is also known as the plasma frequency. Figure 1 shows a conducting thin film surface, which has a plasma frequency (ω_p) described by the Drude Free Electron model as

$$\omega_p = \sqrt{\frac{ne^2}{\mu\varepsilon_0}} \qquad (1)$$

where n is the charge carrier density, ε is the charge on the electron, μ is the effective mass and ε_0 is the permittivity of vacuum.

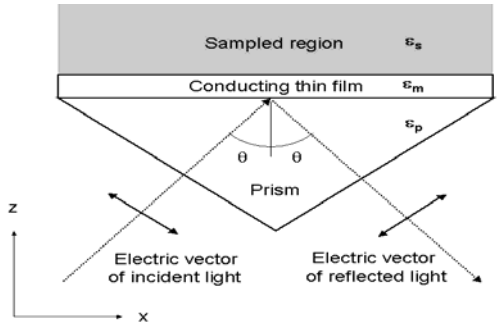

Figure 4.1. The Kretschmann configuration for detection of surface plasmons in conducting thin films. The angle θ must be greater than the critical angle so that the light is totally internally reflected. The incident light is p-polarized so that the x-component can drive an oscillation of conduction electrons (plasmon) while the z-polarized component is an evanescent wave that penetrates into the sampled region.

Below the plasma frequency incident radiation is reflected as shown in Figure 4.1 giving rise to the shiny appearance of metals and the reflective properties of conducting metal oxides in the infrared. At the plasma frequency the incident radiation is absorbed giving rise to the plasma absorption responsible for the SPR effect. A longitudinal surface plasmon can be excited at $\omega_{sp} = \omega_p/\sqrt{(1 + \varepsilon_s)}$ [18], where ε_s

is the dielectric constant of the sample region in contact with the conducting film shown in Figure 4.1. The measurements reported here consist of air contact with the ITO film so that $\varepsilon_s \sim 1$ and $\omega_{sp} = \omega_p/\sqrt{2}$. Above the plasma frequency incident radiation is transmitted in transparent conducting oxides like ITO or absorbed by interband transitions in d-type semi-conductors and metals.

The initial demonstration of surface plasmon resonance in conducting metal oxide thin films focuses on indium tin oxide as a novel SPR substrate. ITO is a member of the class of materials known as conducting metal oxides (CMOs), which encompasses both degenerate wide band gap semi-conductors (sp-type doped materials such as tin-doped indium oxide, fluorine-doped tin oxide, aluminum-doped zinc oxide) and semi-metals (d-type materials such as iridium oxide, ruthenium oxide). Typically, the charge carrier densities of CMOs are in the range $10^{20} < n < 10^{22}$ conduction electrons per cubic centimeter [27] intermediate between metals such as gold or aluminum ($n \sim 10^{23}$) or typical semi-conductors such as doped silicon ($n \sim 10^{19}$). Based on these values, Eqn. 1 indicates that the plasma frequency of conducting metal oxides would be expected to appear at ~1 eV, in the near-infrared region of the spectrum.

There have been a number of studies that led to the expectation that CMOs such as ITO should show the SPR effect [27-32]. Studies of ITO and other CMOs using variable angle reflectance FT near-infrared reflectance spectroscopy demonstrated a consistent surface sensitive decrease in the reflectivity of the substrate for both sp-type and d-type CMOs [29,30,32]. Based on the correlation of the plasma frequency and

reflectivity, it was suggested that this decrease was the result of a surface plasmon phenomenon [30]. Study of adlayer (self-assembled monolayer) formation led to the observation of consistent shifts in the decrease of the reflectance of the substrates [31]. Based on these observations, we predicted that a SPR effect similar to that observed on silver and gold would be observed on ITO and other CMOs using the appropriate geometry for coupling light into the conductor [29,30,32]. The Kretschmann configuration shown in Figure 4.1 permits coupling of incident light into the thin conducting film, provided the wavenumber and angle are matched to the surface plasmon frequency (ω_{sp}) and wavevector (k_{sp}) of the thin film [33].

4.3 Results

The prediction of SPR optical signals is well understood using optical constants obtained from reflectance data fit to multi-layer Fresnel equations [34]. Figure 4.2 shows a dispersion curve generated using optical constants for ITO (n the index of refraction and κ the absorption coefficient) obtained from reflectance measurements [29].

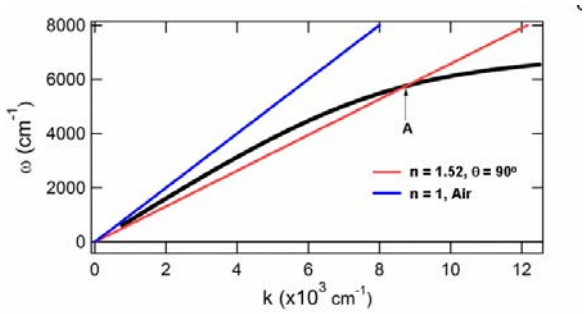

Figure 4.2. Dispersion curve for indium tin oxide calculated based on the optical constants n and κ. Point A represents the theoretical coupling regions of an ITO glass slide at an incident angle of 90° with coupling predicted to occur below 6000 cm^{-1} (0.74 eV).

Dispersion curves using the equation

$$k_{sp} = \frac{\omega_{sp}}{c}\sqrt{\frac{\varepsilon_m \varepsilon_p}{\varepsilon_m + \varepsilon_p}} \qquad (2)$$

are well-known for gold [35], but the curve shown in Figure 4.2 is the first one for ITO. For coupling to occur, both the energy ($h\omega_i$) and the momentum (hk_i) of the incident light must match the energy ($h\omega_{sp}$) and momentum (hk_{sp}) of the surface plasmons. This requirement is fulfilled when p-polarized light impinges on the surface under the condition of total internal reflection at the appropriate angle, as shown in Figure 4.1. Point A in Figure 4.2 indicates that surface plasmons will be observed at wavenumbers below ~6000 cm^{-1}. Given the simplicity of the three-phase model, this agrees with the incident energy and angle of observed surface plasmons.

The coupling of the optical infrared radiation into the oscillations of the conduction electrons is demonstrated by a scanning angle SPR experiment shown in left panel of Figure 4.3. Figure 4.3 compares the three-dimensional SPR image of gold and indium tin oxide.

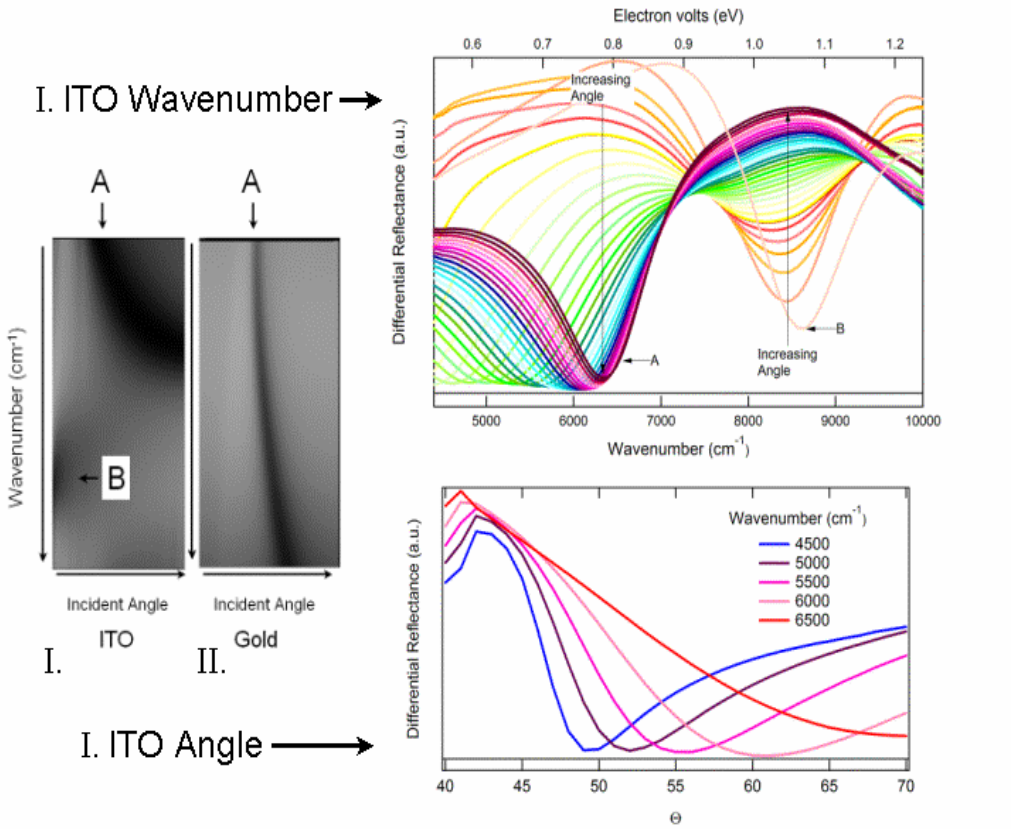

Figure 4.3. Three-dimensional reflectivity map of I.) indium tin oxide and II.) gold as a function of incident angle 40º-70º and 41º-43º and wavenumber ranging from 4200 cm^{-1} (0.52 eV) to 10,000 cm^{-1} (1.24 eV) and 6000 cm^{-1} (0.74 eV) to 11,000 cm^{-1} (1.36 eV) for I. and II., respectively. The grayscale represents the reflectivity changes with the darkest region representing the least reflectivity or most absorbance by the substrate. The wavenumber and angular dependence of reflected light are reported as the Difference Reflectance, which results from the subtraction of the reflectance of s-polarized light from p-polarized light. The sample geometry consists of the incident infrared light entering through a prism in the so-called Kretchmann geometry in a θ-2θ stage designed by GWC attached to a ThermoElectron FTIR spectrometer.

For both thin films, arrow A refers to the reflectivity loss indicative of the surface plasmon resonance, ω_{sp}. The position of minimum reflectivity is sensitive to both incident light angle and excitation frequency and follows a contour as indicated in the images. The reflectivity image in Figure 3 reveals that the SPR effect in ITO ranges

in wavenumbers from ~4200 cm^{-1} (~0.52 eV) to ~6,300 cm^{-1} (~0.78 eV) and angle from 40 to 70 degrees. The lower right panel in Figure 3 shows that the angle dependence of the plasmon absorption in ITO becomes sharper at lower wavenumber. Although the current experiment is limited to wavenumbers greater than 4,200 cm^{-1} (0.52 eV), the calculated plasmon absorption for ITO in the mid-infrared region is narrower than the features observed here, which is a trend that is also suggested by the data in Figure 4.3. The same effect is observed in gold as seen in Figure 4.3. In fact, the sharper angle dependence of surface plasmon on gold thin films was the original motivation for the design of the θ-2θ stage, which was used in our study to measure the SPR effect on ITO [36]. The B arrow in the ITO reflectivity map indicates the appearance of the critical angle of the indium tin oxide. The absorption that is observed above the critical angle is ω_p, while that below the critical angle is ω_{sp}. The direct observation of ω_p is consistent with the fact that the thin films of ITO are transparent above the plasma frequency. The situation is quite different for gold where interband transitions are observed above the plasma frequency [18] masking the optical signature of ω_p.

The behavior ITO surface plasmons in the wavenumber dimension are analogous to gold thin films. The top right panel of Figure 3 shows the cross sectional spectral view of indium tin oxide from 40^o to 70^o. Two regions are apparent where the reflected intensity is reduced. The lower wavenumber intensity reduction labeled **A**, corresponds to the surface plasmon, ω_{sp}. The surface plasmon ω_{sp} is observed from the detector cutoff at 4,200 cm^{-1} (0.52 eV) to 6,300 cm^{-1} (0.78 eV). A second

reduction in reflected intensity, **B**, corresponds to the plasma frequency, ω_p ~8,700 cm^{-1} (1.08 eV) for light incident below the critical angle ($\theta < 41^o$). With appropriate coupling obtained from the Kretschmann configuration the surface plasmon should be $\omega_{sp} = \omega_p/\sqrt{2} \sim 6{,}100\ cm^{-1}$ (0.76 eV), which agrees well with the data shown in Figure 4.3. Above the critical angle, light is totally internally reflected and only the lower energy surface plasmon band (ω_{sp}) is observed. The primary plasma band (ω_p) in ITO has been measured to be ~0.8 eV using high-resolution energy loss spectroscopy [37], which agrees well with the optical signatures measured using FTIR reflectance spectroscopy.

The relationship between optical plasmons and bulk plasmons studied by Valence Electron Energy Loss Spectroscopy (VEELS) provides further information on the nature of the conduction electrons in metal oxide thin films. The two methods provide complementary information on the propagation of longitudinal plasmons (SPR) and transverse plasmons (VEELS). VEELS has enhanced spatial resolution with an energy resolution of ~ 1 eV [38]. In Figure 4.4, the volume plasmons of ITO are compared with a pure elemental semi-metal, silicon and an insulator, silicon dioxide.

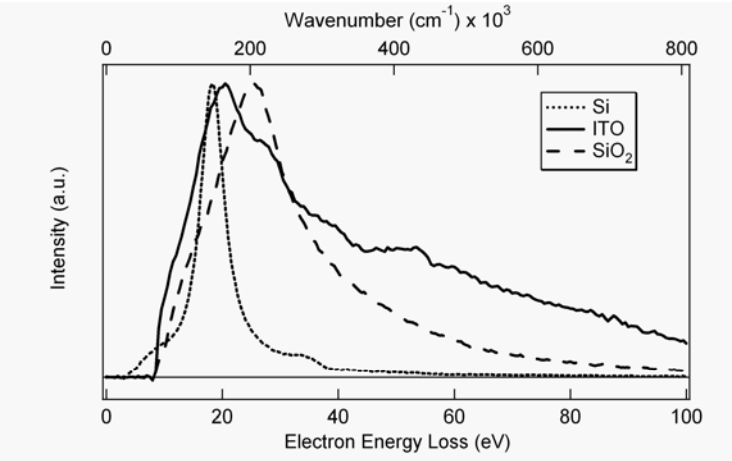

Figure 4.4. ITO bulk (volume) plasmons as determined by VEELS with an energy value given on the x-axis and intensity on the y-axis in terms of both energy (eV) and wavenumber (cm^{-1}). The volume plasmon energy values of ITO, silicon, and silicon dioxide are shown with an energy resolution of 2.5 eV.

This plasmon energy is calculated from the difference between the zero loss energy peak (not shown) and the low loss energy peak. As shown, silicon (B), has a volume plasmon energy of ~16 eV as compared to ~19 eV for ITO (A) and ~28 eV for silicon dioxide (C). The trend in the volume plasmon measured by VEELS is consistent with the ordering of conductors, semi-conductors and metals. The energy required to excite an electron into the conduction band in the volume plasmon increases in the order metal < semi-metal < semi-conductor < insulator. For example, the volume plasmon of gold is a broad band peaked at ~16 eV (*39*). The contrast of the energy range in Figure 4.4 for the volume plasmons and the energy observed in Figure 4.3 for the surface plasmons demonstrates that the optical signals observed do not arise from volume plasmons.

4.4. Conclusions

The observation of an SPR effect on ITO extends the application of optical plasmons to an entirely new range of materials, the conducting metal oxides. Although data are presented only for ITO, the results are relevant to the entire class of CMOs, both sp- and d-type. Using a simple optical method the physical consequences of methodical changes in charge carrier density, film thickness, and composition of matter can be systematically tested in hundreds of thin film materials. Applications can be enhanced by development of thin film technology in porous, machinable, and optically tunable substrates. ITO is already widely used in applications such as heat shields on windows from oven doors to spacecraft windows [40]. ITO is also widely used as a Faraday coating on computer monitors. Doped tin and indium oxides have application as conductimetric sensors [39,40]. The electrochemical stability of the conducting metal oxides compared to gold and silver presents another new set of possibilities [41]. While gold is electrochemically oxidized at 0.8 V, ITO can withstand voltages of greater than 1000 V in solution or polymer films. Other conducting metal oxides such as iridium oxide and ruthenium oxide that can be deposited on silicon semi-conductors as thin electrode surfaces also show optical properties indicative of surface plasmons in the near-infrared region [32]. The optical methods outlined here are also useful as a surface conductivity probe since reflectivity and charge carrier density can be simultaneously monitored during the annealing step of a thin film using optical methods. From a fundamental point of view, it is of great interest to

have a new class of materials to test the effects of surface plasmons, which have been area of intense investigation and some controversy for the past 30 years.

Acknowledgements. Thanks to Robert Corn for the use of a motorized θ-2θ stage used in part of this work.

4.5. References

[1] M. L. M. Vareiro, J. Liu, W. Knoll, K. Zak, D. Williams, and A. T. A. Jenkins, Analytical Chemistry **77,** 2426-2431 (2005).

[2] S. Ekgasit, C. Thammacharoen, F. Yu, and W. Knoll, Applied Spectroscopy **59,** 661-667 (2005).

[3] E. Fujii, K. Shimizu, Y. Kurokawa, A. Endo, S. Sasaki, K. Kurihara, D. Citterio, H. Yamazaki, and K. Suzuki, Bunseki Kagaku **52,** 311-317 (2003).

[4] E. A. Smith, W. D. Thomas, L. L. Kiessling, and R. M. Corn, Journal of the American Chemical Society **125,** 6140-6148 (2003).

[5] E. A. Smith, M. G. Erickson, A. T. Ulijasz, B. Weisblum, and R. M. Corn, Langmuir **19,** 1486-1492 (2003).

[6] B. P. Nelson, M. R. Liles, K. B. Frederick, R. M. Corn, and R. M. Goodman, Environmental Microbiology **4,** 735-743 (2002).

[7] G. J. Wegner, H. J. Lee, and R. M. Corn, Analytical Chemistry **74,** 5161-5168 (2002).

[8] P. R. Morrill, R. B. Millington, and C. R. Lowe, Journal of Chromatography B-Analytical Technologies in the Biomedical and Life Sciences **793,** 229-251 (2003).

[9] N. Soh, T. Tokuda, T. Watanabe, K. Mishima, T. Imato, T. Masadome, Y. Asano, S. Okutani, O. Niwa, and S. Brown, Talanta **60,** 733-745 (2003).

[10] P. Englebienne, A. Van Hoonacker, and M. Verhas, Spectroscopy-an International Journal **17,** 255-273 (2003).

[11] J. S. Shumaker-Parry, M. H. Zareie, R. Aebersold, and C. T. Campbell, Analytical Chemistry **76,** 918-929 (2004).

[12] F. Yu, B. Persson, S. Lofas, and W. Knoll, Analytical Chemistry **76,** 6765-6770 (2004).

[13] R. J. Bussjager and H. A. Macleod, Applied Optics **35,** 5044-5047 (1996).

[14] A. Hatta, S. Suzuki, and W. Suetaka, Applied Surface Science **40,** 9-18 (1989).

[15] S. Hussain, R. K. Roy, and A. K. Pal, Journal of Physics D-Applied Physics **38,** 900-908 (2005).

[16] K. J. Krane and H. Raether, Physical Review Letters **37,** 1355-1357 (1976).

[17] F. Yang, G. W. Bradberry, and J. R. Sambles, Thin Solid Films **196,** 35-46 (1991).

[18] F. Wooten, *Optical Properties of Solids* (Academic Press, New York, 1972).

[19] H. Raether, Optics Communications **42,** 217-222 (1982).

[20] E. Kretschmann, Japanese Journal of Applied Physics**,** A862-A862 (1974).

[21] A. J. Haes and R. P. V. Duyne, Anal. Bioanal. Chem. **379,** 920-930 (2004).

[22] R. W. Nelson, J. R. Krone, and O. Jansson, Analytical Chemistry **69,** 4363-4368 (1997).

[23] R. W. Nelson, J. R. Krone, and O. Jansson, Analytical Chemistry **69,** 4369-4374 (1997).

[24] S. Herrwerth, T. Rosendahl, C. Feng, J. Fick, W. Eck, M. Himmelhaus, R. Dahint, and M. Grunze, Langmuir **19,** 1880-1887 (2003).

[25] E. L. Bruner, A. R. Span, S. L. Bernasek, and J. Schwartz, Langmuir **17,** 5696-5702 (2001).

[26] D. Lavrich, S. Wetterer, S. Bernasek, and G. Scoles, Journal of Physical Chemistry B **102,** 3456-3465 (1998).

[27] S. H. Brewer and S. Franzen, Chemical Physics **300,** 285-293 (2004).

[28] I. Hamberg and C. G. Granqvist, Appl. Phys. Lett. **44,** 721-723 (1984).

[29] S. H. Brewer and S. Franzen, J. Phys. Chem. B **106,** 12986-12992 (2002).

[30] S. H. Brewer and S. Franzen, J. Alloys and Comp. **338,** 73-79 (2002).

[31] S. H. Brewer, D. A. Brown, and S. Franzen, Langmuir **18,** 6857-6865 (2002).

[32] S. H. Brewer, D. Wicaksana, J. P. Maria, A. I. Kingon, and S. Franzen, Chemical Physics **313,** 25-31 (2005).

[33] E. D. Kretschmann and M. W. Williams, Bulletin of the American Physical Society **22,** 1269-1269 (1977).

[34] B. Johne, K. Hansen, E. Mork, and J. Holtlund, Journal of Immunological Methods **183,** 167-174 (1995).

[35] J. M. Brockman, B. P. Nelson, and R. M. Corn, Annual Review of Physical Chemistry **51,** 41-63 (2000).

[36] B. P. Nelson, A. G. Frutos, J. M. Brockman, and R. M. Corn, Analytical Chemistry **71,** 3928-3934 (1999).

[37] J. A. Chaney, S. E. Koh, C. S. Dulcey, and P. E. Pehrsson, App. Surf. Sci. **218,** 258-266 (2003).

[38] R. H. French, H. Müllejans, D. J. Jones, G. Duscher, R. M. Cannon, and M. Rühle, Acta Mater. **46,** 2271-2287 (1998).

[39] R. L. Fu, J. Z. Xu, Y. R. Li, Y. L. Wei, and J. J. Zhu, Frontiers in Bioscience **10,** 2841-2847 (2005).

[40] Y. X. Zhou, B. Yu, and K. Levon, Biosensors & Bioelectronics **20,** 1851-1855 (2005).

[41] P. Armistead and H. Thorp, Analytical Chemistry **72,** 3764-3770 (2000).

Chapter 5

The Simultaneous Observation of a Plasma Frequency Absorption and Surface Plasmon Resonance

(Currently, in preparation for publication)

5.1. Introduction

Plasmons are the collective oscillations of free conduction electrons that traverse a conductive surface with wavevectors within the bulk and along the surface. The understanding of the properties and surface interactions of these plasmons is essential for many applications such as surface enhanced raman spectroscopy (SERS) and surface plasmon resonance spectroscopy (SPR). [1-3] Within the bulk, intrinsic plasmons are observed through radiation absorption at a specific plasma frequency (ω_p) as predicted by the Drude Model where $\omega_p = \sqrt{ne^2/\mu\varepsilon_0}$, with n representing the charge carrier density, e, the charge of an electron, μ, the effective mass of a particle and ε_0, the permittivity of vacuum. [4] This frequency ω_p is known as a plasma absorption and is experimentally detected by an attenuation of the reflectance at this wavelength. At the surface interface, another distinct plasmonic phenomenon occurs under a condition of total internal reflection, a surface plasmon (SP). SPs propagate transversely in response to electromagnetic waves of the appropriate energy and momentum (i.e. frequency and angle) resonating at the frequency known as ω_{sp} and also detected as a decrease in reflectance.

Schematically, the relationship between the plasma frequencies (ω_p and ω_{sp}) and the development of plasmons is depicted in Figure 5.1.

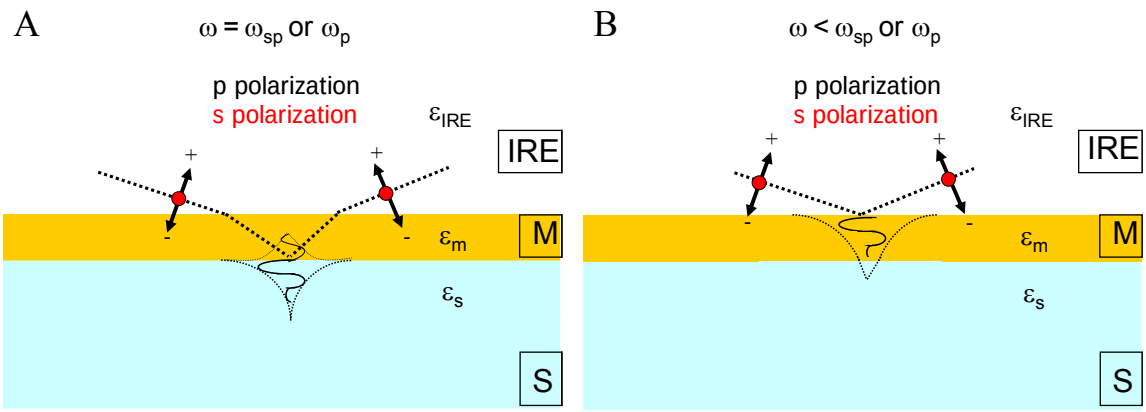

Figure 5.1. Schematic of radiation passing through an internally reflective optical element (layer 'IRE') and impinging on a metal (layer 'M') in contact with a substrate (layer 'S') where $\varepsilon_{IRE}>\varepsilon_s$ and $\varepsilon_{IRE}<\varepsilon_M$ Figure 1B: condition of incident radiation with ω below ω_p or ω_{sp} in which the ideal conductor (layer 'M') is completely reflective and the evanescent wave is localized at the metal/substrate (IRE/M) boundary. Figure 1A: condition of incident radiation with ω equal to ω_p or ω_{sp} in which the index of refraction of the metal is greater than that of the optical element resulting in the refraction of the light into the metal and localization of the evanescent wave at the metal/substrate boundary (M/S).

This figure shows two cases in which incident radiation impinges through an internally reflective element (IRE), such as a prism, a surface which in this case is a metal (m) overlaid onto a substrate (s) which in this is air. When the incident electromagnetic radiation is resonant with either ω_p or ω_{sp}, it is absorbed as shown in Figure 5.1A. Under this resonant condition, the index of refraction of the metal is greater than that of the optical element, in this case a prism, and the evanescent wave extends into the substrate. For incident radiation below $\omega_{p,}$ an ideal conductor is completely reflective within the appropriate surface selection rules as shown in Figure 1B.[5] The light is refracted into the thin film and the evanescent wave is

primarily within the boundary of the metal. When electromagnetic radiation above ω_p impinges on an ideal conductor, it is transmitted (not shown).

Theoretically, the frequency of the surface plasmon depends on the dielectric constant of the substrate, $\varepsilon_{s,}$ as $\omega_{sp} = \omega/\sqrt{(1 + \varepsilon_s)}$. [4] In air, $\varepsilon_s \sim 1$ thus, simplifying the equation to $\omega_{sp} = \omega/\sqrt{2}$. It has been hypothesized that the "ω"within this equation is actually the Drude predicted plasma frequency within the bulk, $\omega_{p.}$ [6] As for the presence of SPs in a thin film, dispersion calculations reveal that optical coupling of the plasmons with impinging incident radiation is prohibited in free space by the momentum mismatch of the wave vectors on either side of the interface and is governed by equation 1 [3]

$$\kappa_{sp} = \frac{\omega}{c}\sqrt{\frac{\varepsilon_m(\omega)\varepsilon_s(\omega)}{\varepsilon_m(\omega) + \varepsilon_s(\omega)}} \qquad (1)$$

where κ_{sp} is the wave vector of the surface plasmons and ε_m and ε_s are the dielectric constants of the metallic or metal oxide conductive surface and the substrate, respectively. Optical coupling of the absorption of incident electromagnetic radiation by surface plasmons is accomplished by the use of a prism in a Kretschmann configuration [7] resulting in a change in the detectable transmitted intensity. The detection and analysis of this reflectance change is known as surface plasmon resonance (SPR) spectroscopy.

Historically, surface plasmons have been studied using gold and silver thin films because their plasmon oscillations are detectable in the visible region.

However, as shown previously [6], a particular conducting metal oxide, indium tin oxide, is well-suited to discern the plasmonic properties on account of the origination of conduction electrons within the s and p orbitals This origin of the charge carriers within ITO helps to eliminate contributions by the d-d inter- and intraband mixing that experimentally results in additional reflectance changes not due to the primary ω_p. Additionally, the material properties of visible transparency, infrared reflectivity, and electrical conductivity, [8 9, 10 11] along with crystallographic stability make ITO not only a commercially viable substrate but also of great research interest. Commercially, this substrate has been used for a variety of applications including heat shields [12 13, 14] and solar cell electrodes while research applications include organic-light emitting diodes (OLEDs) and biosensors. [15 16 17 18] Thus, the preparation of ITO is well-studied, allowing for in-depth experimental examination of ITO thin films at different thicknesses and preparation conditions and corresponding theoretical studies. For this study, a series of well-controlled thicknesses of ITO were used to examine the excitable plasmonic components of the substrate including the plasma absorption and the surface plasmon.

5.2. Materials and Methods

5.2.1. Chemicals and Substrates.

Absolute ethanol was used as received from Aaper Alcohol and Chemical Co. The gold electrodes were obtained from Evaporated Metal Films, Inc.

5.2.2. Indium Tin Oxide Film Preparation.

A series of ITO films of varying thickness (~30 nm – 120 nm) were prepared on 1.0 mm thick BK7 glass (Schott Glass, Inc.) by RF magnetron sputtering from a 1" ceramic target (90 wt% In_2O_3 / 10 wt% SnO_2; Super Conductor Materials, Inc.). Films were sputtered at 20 W in an Argon atmosphere of 6.5 mTorr and at a distance of 6 cm. The observed deposition rate was ~6.4 nm/min. To improve crystallinity and activate dopants, the ITO films were annealed at 500°C in a reducing atmosphere (5% H_2 / 95% N_2; $pO_2 \sim 10^{-17}$ atm) for 30 min. Film thickness was evaluated by profilometry (Detak). Crystallinity was examined by x-ray diffraction (Bruker AXS D-5000 equipped with an area detector) while film resistivity was evaluated by standard four-point-probe measurements. Prior to spectroscopic analysis, the ITO electrodes were cleaned via 20 minutes of UV-Ozoneolysis (UVO-60, model number 42, Jelight Co. Inc.) to yield a clean hydrophilic surface and remove any adventitious carbon present.

5.2.3. Reflectance FTIR Spectroscopy.

The variable angle reflectance FTIR spectra were recorded by a Digilab FTS3000 spectrometer using p-(vertically) polarized IR radiation and a Varian Universal variable angle reflectance attachment. A near IR source, quartz beamsplitter, and liquid nitrogen cooled indium antimonide (InSb) detector were used in the spectral range of 4,000-12,000 cm^{-1}. All of the IR spectra were performed at room temperature with an incident angle of 70 degrees

relative to the surface normal. To obtain the ITO thin film reflectance spectra, a ratio of the single beam spectra of the metal oxide thin film on the glass substrate to the single beam spectra of a gold surface was made. These IR spectra were averaged over 16 scans at a resolution of 2 cm^{-1}.

5.2.4. Surface Plasmon Resonance.

SPR spectra were recorded on a Nicolet 6700 FTIR bench equipped with a GWC Technologies Surface Plasmon Resonance attachment. A white light source, polarizer, and extended range indium antimony detector were used in the spectral range of 4200-10,000 cm^{-1}. All of the SPR spectra were performed at room temperature with the incident angle varying from ~42° to 78° from the surface normal. The SPR reflectance spectra were obtained by subtracting the s-polarized background spectra from the p-polarized sample spectra for 32 scans with a resolution of 32 cm^{-1}. Theoretical calculations for SPR spectra were carried out using WinSpall© V. 2.20 (Max Planck Institute)

5.3. Computational Methods

5.3.1. Drude Free Electron Model and Fresnel three-phase Equations of Reflection.

The Drude free-electron model describes the dielectric function ε as a function of the frequency ω as: [19]

$$\varepsilon(\omega) = \varepsilon_{\infty} - \omega_p^2 \frac{1}{\omega^2 + i\omega\Gamma} \qquad (1)$$

where ε_∞ is the high-frequency dielectric constant, Γ is the damping constant and ω_p is the plasma frequency as defined in equation 2. [4]

$$\omega_p^2 = \frac{ne^2}{m^* \varepsilon_o} \qquad (2)$$

In this equation, n is the charge carrier concentration, e is the electron charge, ε_o is the permittivity of vacuum, and m^* is the effective mass of indium tin oxide (approximately 0.3) [20]. With these equations, theoretical modeling of the experimental data (see supporting information) yields an empirical average plasma frequency of ~17,700 cm^{-1} and damping constant of 892 cm^{-1}.

Theoretical reflectance spectra were calculated using a MATLAB© programming code by implementing the three-phase Fresnel equations of reflection as shown in the schematic below.

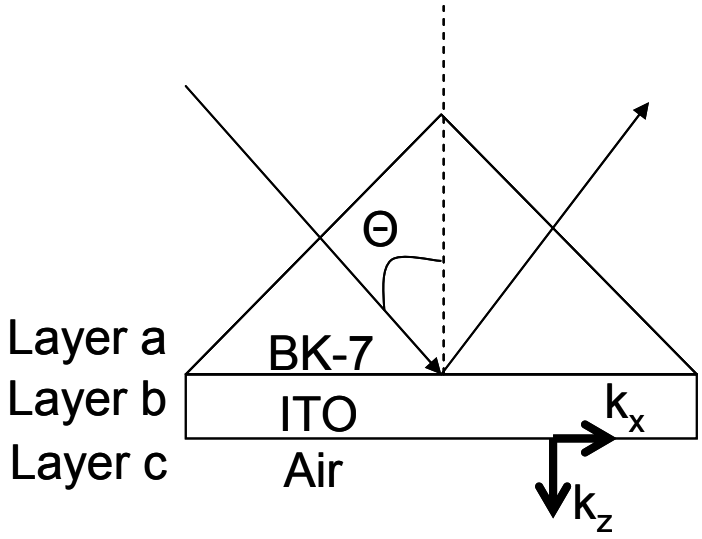

Figure 5.2. Schematic of the layers used in the calculation of the three-phase Fresnel equations of reflections with layer a referring to the BK7 prism, layer b as an ITO thin film, and layer c depicts the infinite layer of air. The directionality of the two dispersion wavevectors are also shown as k_x and k_z.

The calculation theoretically determined the reflectance from incident radiation passing through three layers, a, b, and c which in this case correspond to BK-7 glass prism, ITO, and air, respectively. The refractive indices of the three layers are shown in equation 3

$$n\_a = \sqrt{\left(\varepsilon_a - \sin\theta^2 * \varepsilon_a\right)}$$
$$n\_b = \sqrt{\left(\varepsilon_b - \sin\theta^2 * \varepsilon_a\right)}$$
$$n\_c = \sqrt{\left(\varepsilon_c - \sin\theta^2 * \varepsilon_a\right)} \qquad (3)$$

where a, b, and c refers to the BK7 glass, ITO, and air layers, respectively, theta (Θ) is the angle of incidence as shown above and ε is the complex dielectric function of the substrates. Only the real component of the complex dielectric function for BK7 glass and air is considered and is defined as 1.52 and 1.0 for glass and air respectively. The complex dielectric function for ITO is frequency dependent and given by equation 1 as shown above. The empirical damping constant and plasma frequency are used in the calculation.

The reflectance of the radiation as determined by the three-phase Fresnel equation is defined as the ratio of the reflected and incident radiation. A general form of this ratio is given in equation 4 [21]

$$r = \frac{r_{ab} + r_{bc}e^{2i\beta}}{1 + r_{ab}r_{bc}e^{2i\beta}} \qquad (4)$$

where r is the reflected radiation and the numerical subscripts (a,b,c) refer to the three phases of BK7 glass, ITO, and air. At each of the boundaries between the layers, the reflectance is considered. In addition, the reflectances,

r, between these boundaries, a-b and b-c, are determined separately for both the s-polarization component (r_x) and p-polarized (r_p) as shown in the following equations.

$$r_{a/b} = \frac{n_a - n_b}{n_a + n_b} \qquad \text{for s-polarization}$$

$$r_{a/b} = \frac{\varepsilon_b n_a - \varepsilon_a n_b}{\varepsilon_b n_a + \varepsilon_a n_b} \qquad \text{for p-polarization} \qquad (5)$$

where a/b represent a boundary between two of the layers a and b, extendable to the boundary of b-c. -Furthermore a final constant to be defined for equation 4 is β, which is film thickness dependent value as defined in equation 6

$$\beta = 2\pi\left(\frac{h}{\lambda}\right) * n_b \qquad (6)$$

where h is the thickness of ITO ranging from 30 to 315 nm, λ is the wavelength of radiation, and n_b is the complex index of refraction (equation 3).

The calculated reflectance, R, of either the p or s-polarized radiation is thus defined in equation 7.

$$R = |r|^2 \qquad (7)$$

In order to compare with our experimental results, the ratio of the p-polarized reflectance to the s-polarized reflectance was calculated.

5.3.2. Skin Depth Calculations.

The skin depth of the indium tin oxide thin films within the metal was calculated using the theoretical values of the real and imaginary dielectric constants, ε_1 and ε_2 respectively, as shown in equation 4

$$Z_1 = \frac{\lambda}{2\pi}\left(\frac{\varepsilon_1 + \varepsilon_2}{\varepsilon_1^2}\right)^{1/2} \qquad (8)$$

where λ is the wavelength (Å) examined and z_1 is the skin depth within the metal and is defined as $z = (|k_{zi}|)^{-1}$ where k_{zi} is the imaginary wave vector perpendicular to the surface that causes the exponential decay of the field E_z. [22]

5.3.3. Dispersion Relationship Calculations.

The general dispersion relationship for surface plasmons has been given by equation 1. Within the thin film, the excitation occurs along the x- and z-directions as defined by the coordinate system in Figure 5.2. The dispersion equations for excitation along each of these directions are given below for a two-phase boundary between the conducting metal oxide (CMO) and the glass prism. The fact that the CMO actually contains both imaginary and real parts ($\varepsilon_m = \varepsilon_1 + i\varepsilon_2$), is reflected in the equations.

$$k_x = \frac{\omega}{c}\sqrt{\frac{\varepsilon_g(\varepsilon_1 + i\varepsilon_2)}{(\varepsilon_g + \varepsilon_1 + i\varepsilon_2)}} \qquad (9)$$

$$k_z = \frac{\omega}{c} i \sqrt{\frac{(\varepsilon_1 + i\varepsilon_2)(\varepsilon_1 + i\varepsilon_2)}{(\varepsilon_g + \varepsilon_1 + i\varepsilon_2)}} \qquad (10)$$

Equation 9 and 10 represent the wavevectors of the p-polarized light in the x and z direction (k_x, k_z), ε_g in this case represents the BK7 prism of the SPR attachment and is comparable to the ε_s of the substrate in equation 1.

5.4. Results and Discussion

In order to systematically test the properties of surface plasmons of ITO, thin film samples of controlled thickness were prepared. Table 1 shows some of the material properties of the 8 ITO thin films studied. The thicknesses ranged from 30 nm to 318 nm with an overall deposition rate ranging from ~6.4 to ~8.3 nm/min. A range of sheet resistances from 6.1 to 51.6 ohms/□ was achieved with the samples displaying relatively similar intrinsic resistivities. While the resisitivity is relatively constant as function of the film thickness, the sheet resistance decreases approximately exponentially with a constant of 47.4 nm^{-1}.

Table 5.1. The thickness, sheet resistance and resistivity of the ITO thin films.

Thickness (nm ± 5%)	Sheet Resistance (ohm/□)	Resistivity (ohm-cm)
30.0 ± 1.5	51.6	1.55×10^{-4}
40.0 ± 2.0	34.5	1.38×10^{-4}
54.5 ± 2.7	28.6	1.56×10^{-4}
71.0 ± 3.6	24.0	1.70×10^{-4}
83.0 ± 4.2	20.2	1.68×10^{-4}
97.5 ± 4.9	17.4	1.70×10^{-4}
112 ± 5.6	16.0	1.79×10^{-4}
121 ± 6.1	15.8	1.91×10^{-4}
161 ± 8.1	9.7	1.56×10^{-4}
200 ± 10	8.3	1.66×10^{-4}
251 ± 12.6	6.8	1.71×10^{-4}
272 ± 13.6	6.1	1.66×10^{-4}
318 ± 15.9	6.3	2.00×10^{-4}

The surface plasmon is evident as an angle-dependent reflectance attenuation as shown in Figure 3. Figure 3 A-M reveals the variable angle reflectivity curves on the eight ITO samples acquired with a FT-SPR recorded with a range of incident angles from ~42 to ~78 degrees.

Figure 5.3. SPR spectra collected at different incident angles on ITO films with increasing thickness as indicated in the top corner of each quadrant. All the spectra have been collected as ratio between p-polarized and s-polarized light. In each graph, the different colors correspond to spectra collected at different angles ranging from 42 degrees (orange spectra) to 78 degree (purple spectra). The bottom X-axis scale is expressed in wavenumbers (cm^{-1}), whereas on the top it has been converted in energy units (eV).

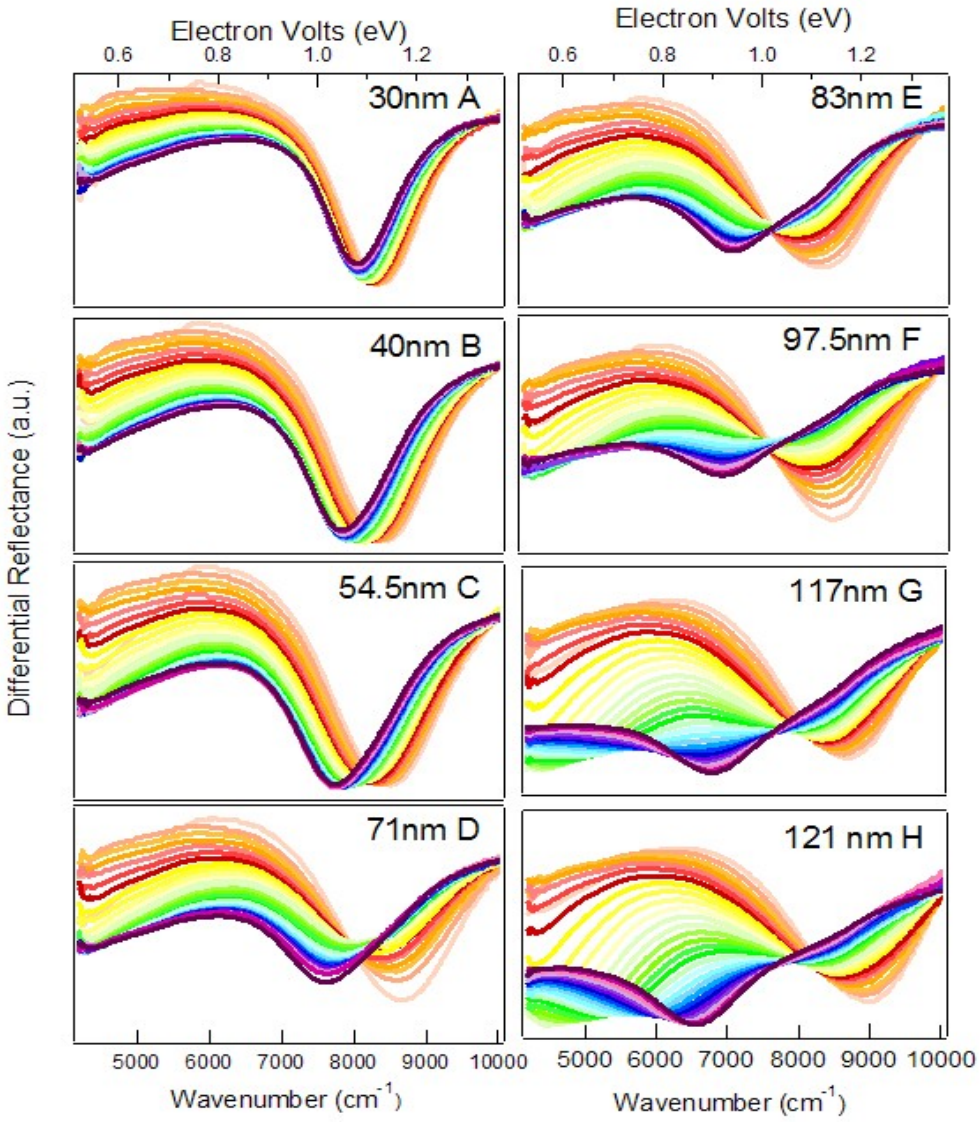
Electron Volts (eV)
0.6
0.8
1.0
1.2
30nm A
40nm B
54.5nm C
71nm D
Electron Volts (eV)
0.6
0.8
1.0
1.2
83nm E
97.5nm F
117nm G
121 nm H
Differential Reflectance (a.u.)
5000
6000
7000
8000
9000
10000
Wavenumber (cm-1)
5000
6000
7000
8000
9000
10000
Wavenumber (cm-1)

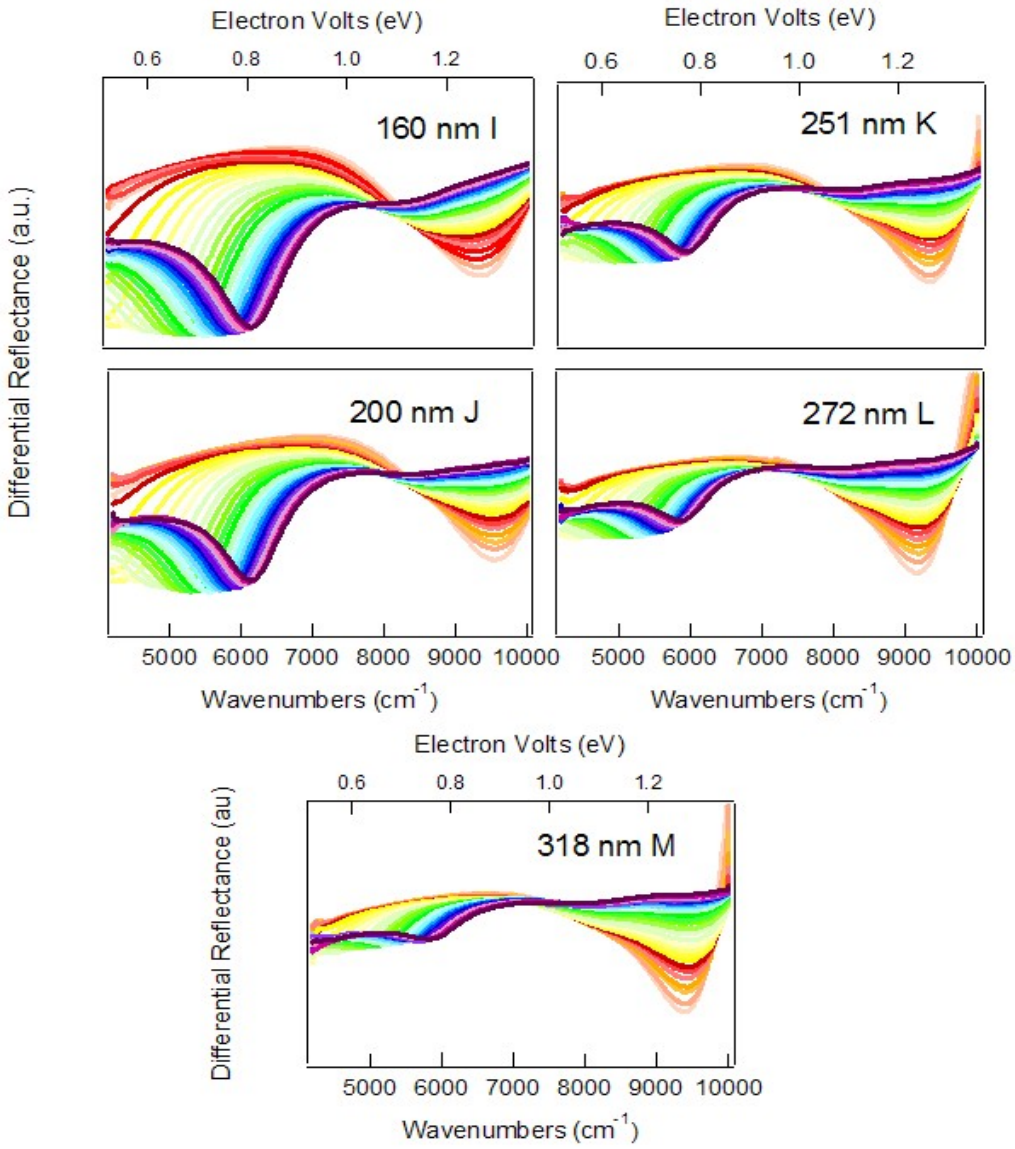
Electron Volts (eV)
0.6
0.8
1.0
1.2
160 nm I
251 nm K
200 nm J
272 nm L
Differential Reflectance (a.u.)
5000 6000 7000 8000 9000 10000
Wavenumbers (cm-1)
Electron Volts (eV)
318 nm M
Differential Reflectance (au)
Wavenumbers (cm-1)

Two different minima are observed in the spectra. A first minimum occurs at ~9,000 cm^{-1}, and it corresponds to the absorption predicted by the Drude free electron model, also shown experimentally in the reflectance spectra in the supporting information. Thus, we will call this "plasma absorption", ω_p. This peak appears at first in the thinner films ranging from 30 – 55 nm, shown in Figures 5.3A-C, and do not have a strong angle dependence (i.e. the frequency of the minimum does not shift much when the angle of the incident light changes). With film thicknesses ranging from 71 – 98 nm, as shown in Figures 5.3D-F, a new minimum is observed at ~6,500-7,000 cm^{-1} when the angle of incidence is greater than 50°. The position of this minimum shifts towards lower energy with increasing angle, but this decrease in reflectance appears to be qualitatively different from ω_p with a much broader peak shape. This second absorption transforms into a real surface plasmon when the film thickness ranges between 100 nm and ~200 nm as shown in Figure 5.3G to 5.3J. On these samples, the surface plasmon frequency (ω_{sp}) is lower than 6,400 cm^{-1} and is highly dependent on the angle of the incident light as predicted by theory. The maximum SPR effect is observed at ~160 nm (Fig. 5.3I). As shown in the subsequent figures of 3K to 3M, as the thickness is further increased, the intensity of the surface plasmon observed at $\omega_{sp,}$ steadily diminishes as the intrinsic plasma absorption, ω_p reemerges.

To understand the appearance of two peaks within the detectable spectral range, examination of the material properties of the ITO was performed. One

property, the skin depth, had a direct correlation with the appearance and disappearance of these peaks. Skin depth is a property of conductors in which the applied current through a material falls to 1/e of its original value. Figure 4 shows the calculated skin depth at 5,000, 6,000 and 7,000 cm^{-1} of the ITO thin films as a function of the conducting film thickness.

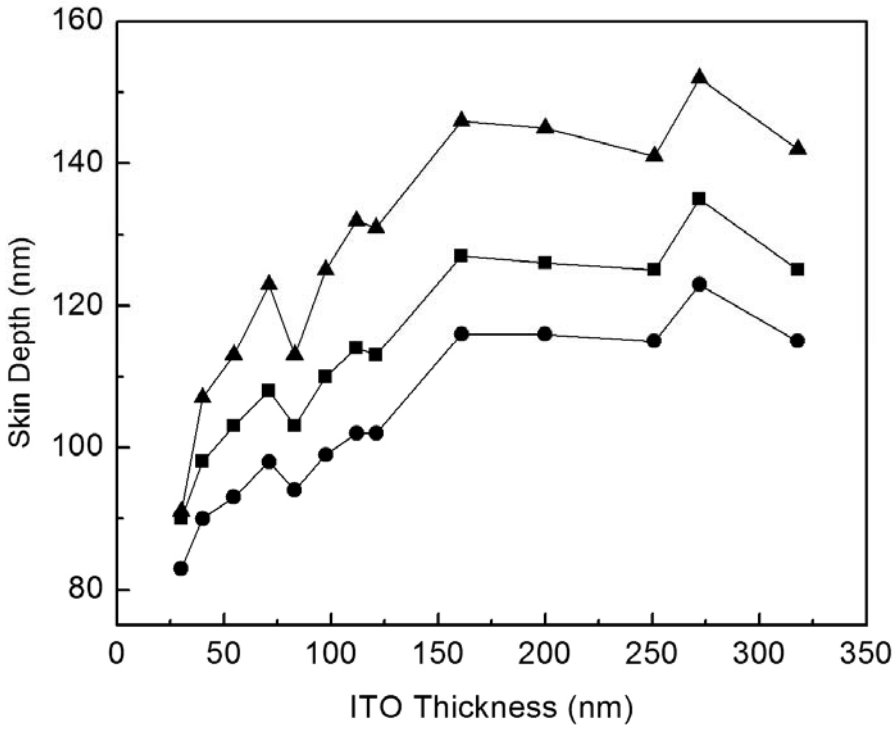

Figure 5.4. Calculated skin depth at different radiation frequency for the thirteen ITO thin films. In particular, solid squares, circles, and triangles represent skin depth calculated for radiation impinging at 7000 cm^{-1}, 6000 cm^{-1}, and 5000 cm^{-1}, respectively. The skin depth, was calculated using equation 8 with the dielectric constants, ε_1 and ε_2, obtained from the Drude free electron modeling of the experimental FTIR spectral data.

In general, as the thickness is increased, the skin depth increases, although there is a sharp attenuation at 83 nm, the same thickness at which the FTIR reflectance spectra exhibit a qualitative shift in slope of the reflectance change. (supporting information, Figure 5.7). The skin depth reaches a plateau for an ITO thickness of ~160 nm with only minor deviations. The plateau value for the skin depth is in the range of ~110-140 nm, which is the ITO film thickness around which observable SPR appears. However, even for the thinnest films the skin depth is always greater than 80 nm, which is the thin film thickness at which the spectra appears to losing features in the region of the ω_p and gaining them in the ω_{sp} spectral regime. These observations seem to indicate that SPR can be observed only when the thickness of the thin film sample is greater than the skin depth.

Figure 5 A-M displays the calculated reflectance spectra obtained from the Fresnel three phase equations of reflection.

Figure 5.5. Calculated SPR spectra at different angles on ITO samples of increasing thickness, analogous to the experimental spectra shown in Figure 2. The X-axis displays the frequency in both wavenumber (bottom scale) and in electron volts (top scale), while the Y-axis is the theoretical reflectance calculated from the Fresnel model.

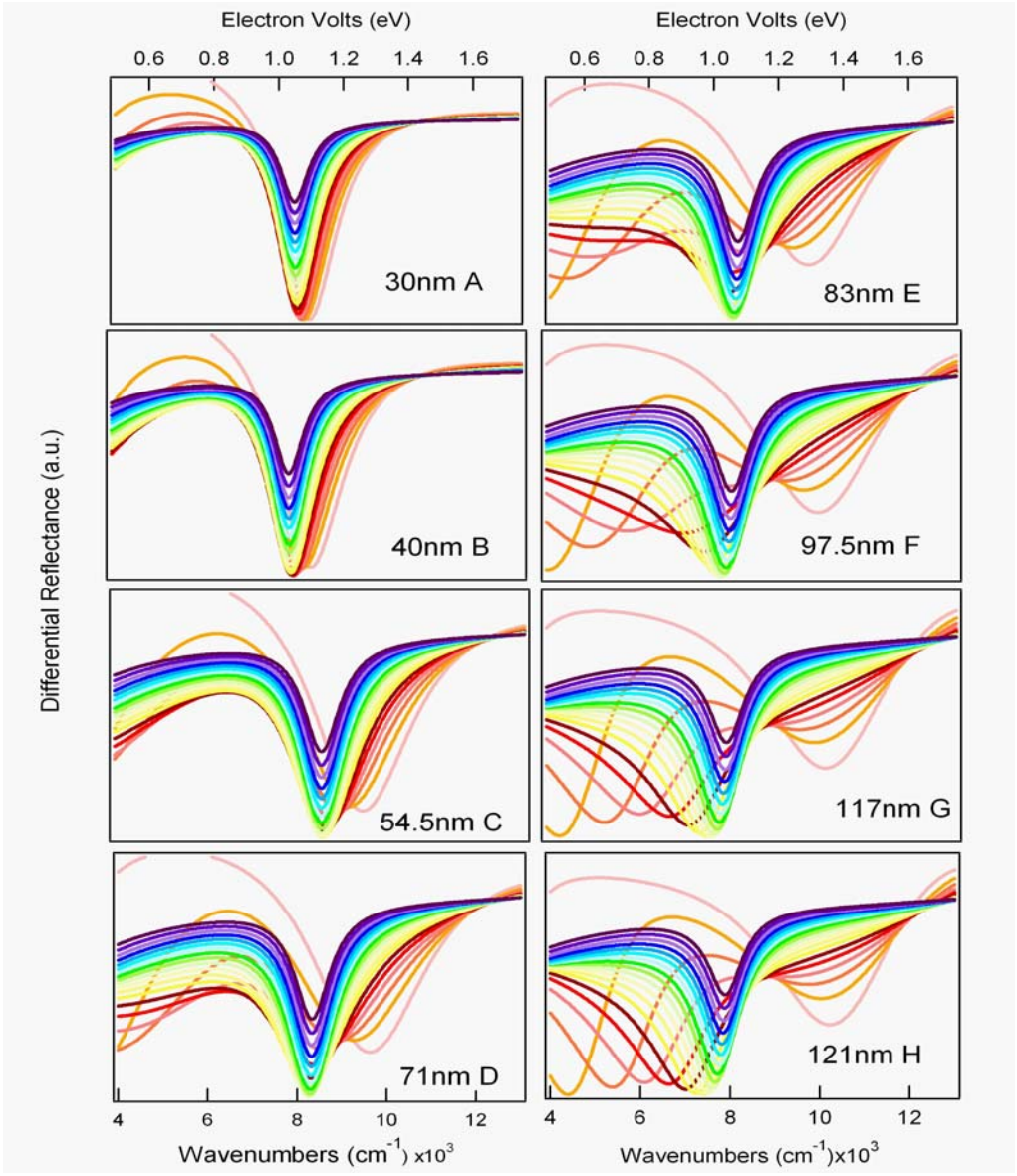
Electron Volts (eV)
0.6 0.8 1.0 1.2 1.4 1.6
Electron Volts (eV)
0.6 0.8 1.0 1.2 1.4 1.6
30nm A
83nm E
40nm B
97.5nm F
54.5nm C
117nm G
71nm D
121nm H
Differential Reflectance (a.u.)
4 6 8 10 12
Wavenumbers (cm-1) x10^3
4 6 8 10 12
Wavenumbers (cm-1)x10^3

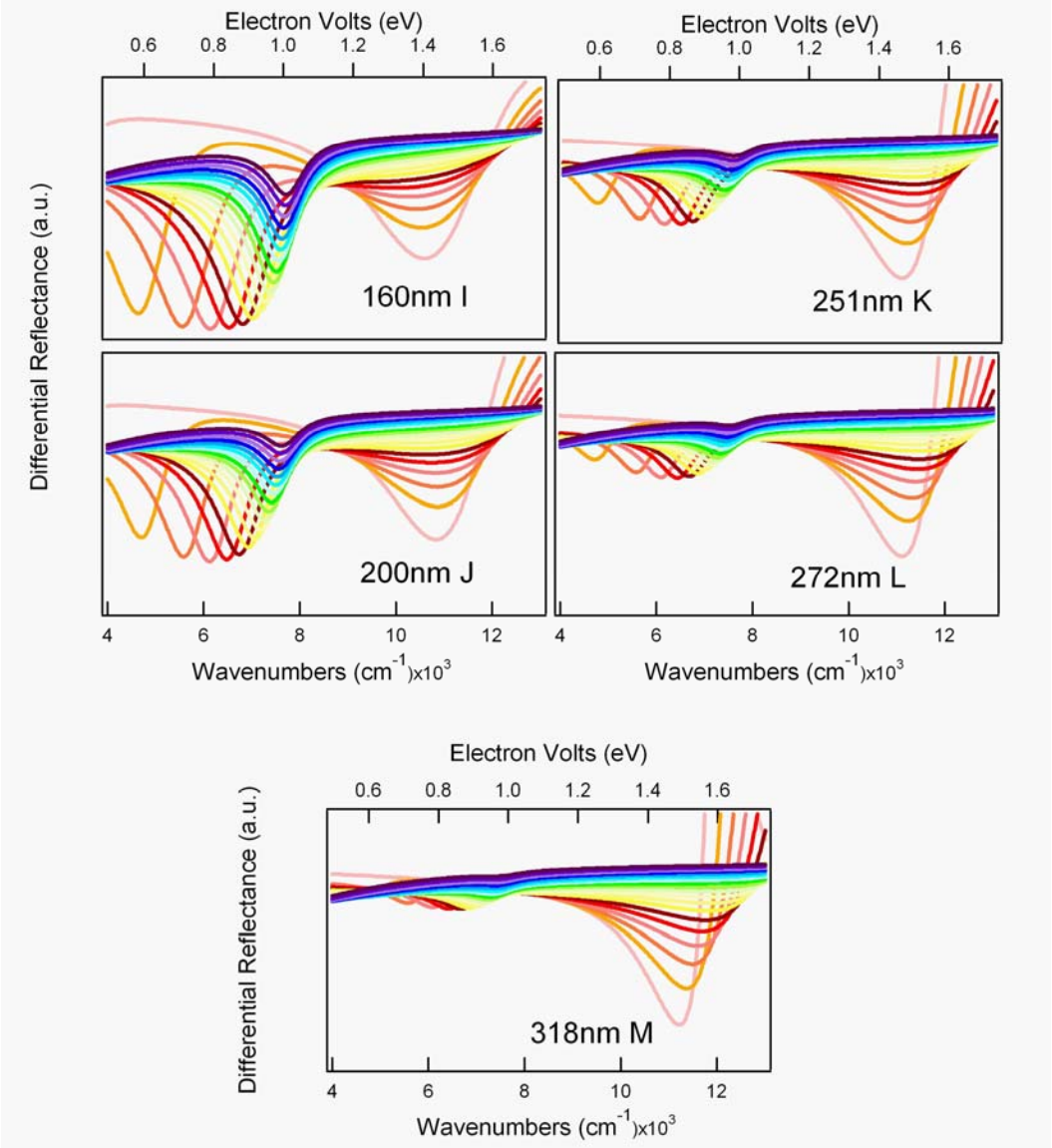
Electron Volts (eV)
0.6
0.8
1.0
1.2
1.4
1.6
Differential Reflectance (a.u.)
160nm I
251nm K
200nm J
272nm L
318nm M
4
6
8
10
12
Wavenumbers (cm-1)x10^3

Equivalent angles ranging from 42-78 degrees in a similar mid-infrared frequency regime were examined in order to compare with the experimental spectra shown in Figure 3. The resulting calculated spectra corresponded remarkably well with experimental. As with experimental, the thin samples ranging from 30 to 54.5 nm only showed a single absorbance, presumed to be the plasma absorption. Once a critical thickness was reached, a second spectral feature began appearing. This thicknesses of ~70-80 nm again corresponded well with the predicted skin depth of the material. This second peak at ~6500cm^{-1} appears to be a surface plasmon (SP) resonance as predicted and shown previously in ITO.[6] Consistent with Figure 5.3, the SP is highly angle dependent (the SPR frequency increases with increasing angle of incidence) and displays the greatest reflectance attenuation at 160 nm.. Additional increases in thickness (5.5J-5.5M) also show less of a surface plasmon and more of a plasma absorption, in agreement with Figures 5.3J-5.3M. The only divergence between the theoretical and the experimental calculation is a shift in the frequency of the plasmons with the plasma absorption appearing at roughly 1,500 more wavenumbers than in the experimentally observed.

The two dispersion relations in Eqns. 9 and 10 present the dielectric response parallel and perpendicular to the interface, respectively, as an extended in-phase oscillation (surface plasmon wave) and a damped out-of-phase absorption (plasma absorption). Theoretically, equations 9 and 10 can be used to plot dispersion curves for each of the component wavevectors. Figure 5.6 displays these calculations and

predicts the appearance of two different plasmons as shown by the two different coupling regions for exciting light.

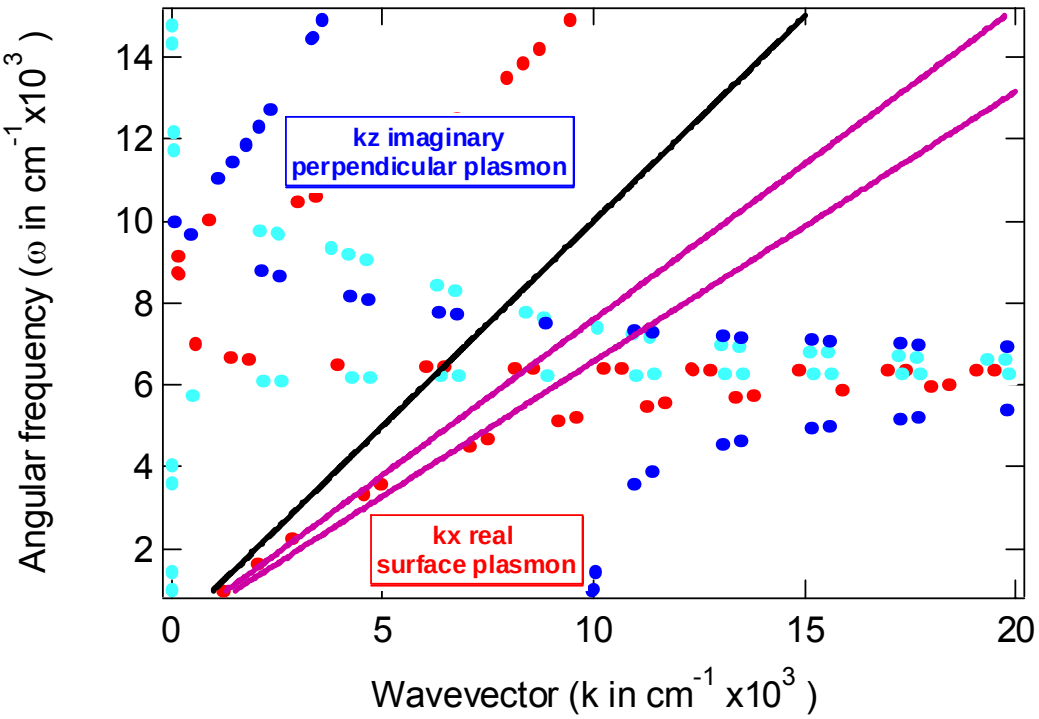

Figure 5.6. Theoretically determined dispersion relationship for ITO/BK7 glass boundary displayed as the wavevector (k) in terms of the angular frequency. The black line shown is the wavevector of light in vacuum while the two purple lines indicate calculated wavevectors at the boundary for the two different incident angles of 60 and 90 degrees. The two theoretical plasmons are shown as red and dark blue lines. The aqua line displays the imaginary portion of the kx wavevector (evanescent wave).

While the Drude model predicts a resonant (plasma) frequency for a conductor, it does not make a specific prediction for how this wave will be excited at a dielectric boundary. The dispersion relations in Eqns. 9 and 10 result from an application of the boundary conditions of Maxwell's equations and can provide a means to predict the interfacial behavior of the Drude model. The kz-component, perpendicular to the surface, shown in Figure 6 as the blue curve displays only a slight decrease in the wavevector with an increase in angular frequency. The real portion of the kx-component, parallel to the surface, is a collective oscillation of the conduction electrons known as a surface Plasmon while the imaginary portion of the kx wavevector appears as the evanescent wave. The surface plasmon is shown with the red curve and displays an initial sharp increase of the wavevector with an increase in angular frequency. As with typical dispersion curves, a k wavevector can be drawn for the sample both placed in air (black line) and in conjunction with a momentum changing material such as a prism (purple lines) at various incident angle. The points where the light lines intersect the dispersion curves reveal coupling regions of the sample. Theoretically, the plasma absorption wavevector is predicted to couple with the conductor in air (n=1.00) at ~7,600 cm^{-1} and with the conductor paired with a BK7 glass prism (n=1.52) at 60 and 90 degrees at ~ 7,400 cm^{-1} and ~7,300 cm^{-1}. On the other hand, the surface plamson is unable to couple to the conductor while it is in air but couples with the conductor/prism combination at ~3,200 cm^{-1} at 60 degrees and at 4,400 cm^{-1} at 90 degrees. As shown in the figure, the coupling of the surface plasmon wavevector to the sample is highly angle dependent and predicts a shift to

higher wavenumbers with in an increase in angle. The theoretical plasma absorption is less angle dependent and predicts a lower energy shift in with increasing angles. Both of these theoretical predictions corroborate experimental data shown in Figure 5.3, and thus, lends credence to this theoretical dispersion calculation.

5.5. Conclusions

Film consistency and parameter optimization in ITO film preparation is currently an area of concern and thus, understanding the interdependence of the material properties is paramount. With this motivation, we examined the relationship of film thickness upon the intrinsic material property of electromagnetic absorption as predicted by the Drude theory. This theory predicts the absorption of impinging radiation at a specific frequency but does not take into account the phenomenon of excitation of oscillations of the surface plasmons. With the available FT-SPR technology, we observed two peaks hypothesized to be the plasma absorption and the surface plasmon oscillation, both simultaneously and individually by varying the film thickness. The observation of the plasma absorption at the plasma frequency, ω_p, of the thinnest and thickest samples followed by the appearance and disappearance of the surface plasmon absorption ω_{sp}, at ideally thick samples is unique for materials such as this conducting metal oxide. Thickness studies such as these have not been feasible for gold due to small skin depth and the interference of the d-d band mixing and thus, this dependence of the plasma absorption and SPR on skin depth was not recognized until now.

5.6. Supporting Information

To illustrate the relationship between reflectivity and thickness, FTIR reflectance spectra were obtained. Figure 5.7 displays the variable angle FTIR reflectance spectra for all of the samples deposited on BK7 glass with thicknesses ranging from 30 nm to 318 nm .

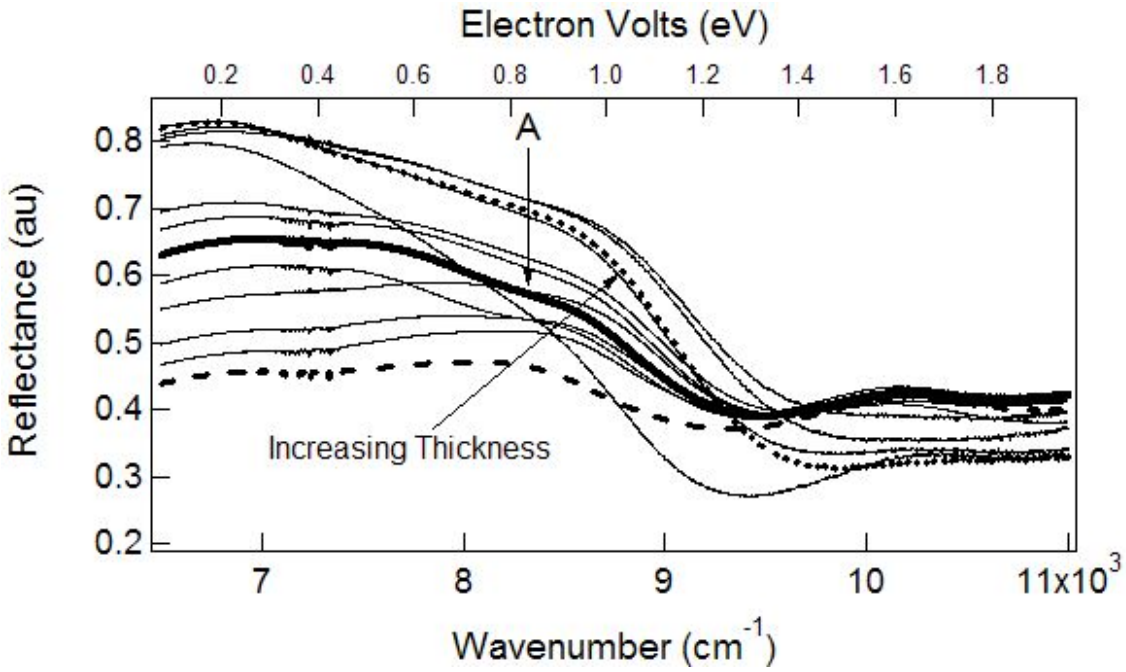

Figure 5.7. Experimental variable angle reflectance FTIR spectra of a thickness series of ITO thin films with a dashed line representing the thinnest sample (30 nm), a dotted line representing the thickest sample (318 nm) and all other thicknesses represented with solid lines. The emboldened solid line indicates 83 nm, the point at which the slope changes. The samples were on BK7 glass substrates and measured relative to a gold surface in the near-IR region with an incident angle of 70° with p-polarized radiation.

These spectra were recorded with an incident angle of 70 degrees, using p-polarized radiation. All of the reflectance spectra show a decrease in reflectance at ~9,000 cm^{-1} indicative of the surface plasmon resonance. In general, the increase in reflectivity

below 9,000 cm^{-1} is larger for thicker samples. There is a qualitative difference in the slope of reflectance curve at point A for films thicker than 83 nm. The thinner samples plateau at lower wavenumbers with little change occurring in the spectra below 8,000 cm^{-1}, whereas the thicker samples (83-318 nm) exhibit a steadily increasing reflectivity with decreasing wavenumbers.

Corroboration of the existence of a SPR is established through calculation of theoretical SPR reflectance spectra for each of the samples. These spectra, shown in Figures 8(A2-G2), were calculated using Winspall © with computations for the theoretical reflectivity curves based upon the resulting refractive index values of the Drude free electron model.

Figure 5.8. Figure 8(A1-G1) reveals the experimental angle dependence of the SPR reflectance at six wavenumbers from 4500 cm^{-1} to 7000 cm^{-1} in increments of 500 cm^{-1}. The dashed lines (---) represent the thinnest and the thickest samples 30 nm and 318 nm, respectively. The emboldened solid line (-) represents the ITO thickness of 160 nm which typically displays the maximum SPR effect. All intermediate thicknesses are shown with faint solid lines. Figure 8(A2-G2) displays the theoretical angle dependence of the SPR reflectance calculated by Winspall© for the same six wavenumbers (4500 – 7000 cm^{-1}) as shown in Figures 8(A1-G1). The graphical representations of the film thickness in Figures A2-G2 again utilizes dashed lines for the thinnest and thickest samples as well as a bold solid line for the 160 nm thin film with more diffuse solid lines representing all other thicknesses.

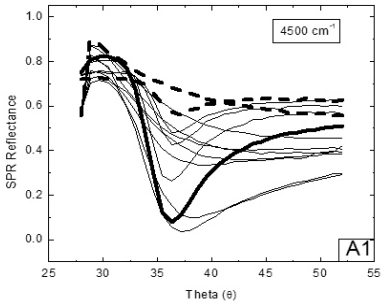
4500 cm-1
A1
SPR Reflectance
Theta (θ)

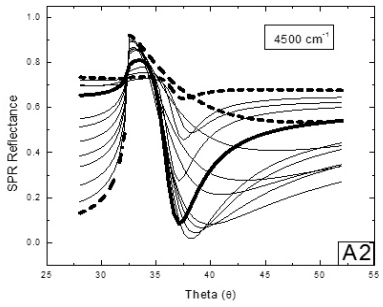
4500 cm-1
A2
SPR Reflectance
Theta (θ)

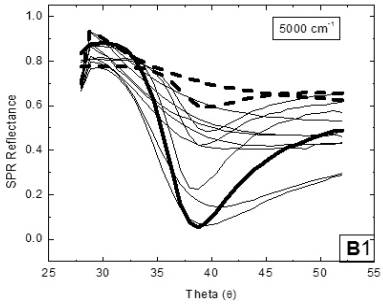
5000 cm-1
B1
SPR Reflectance
Theta (θ)

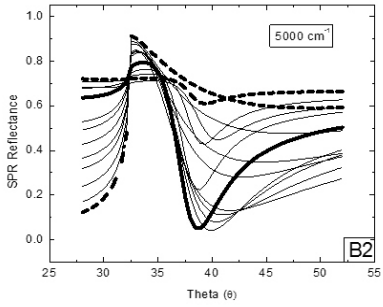
5000 cm-1
B2
SPR Reflectance
Theta (θ)

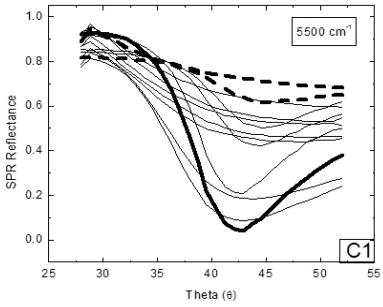
5500 cm-1
C1
SPR Reflectance
Theta (θ)

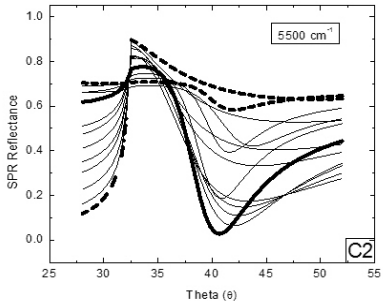
5500 cm-1
C2
SPR Reflectance
Theta (θ)

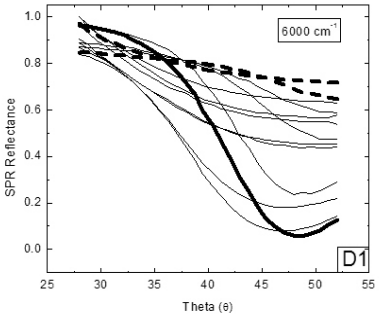
6000 cm-1
SPR Reflectance
Theta (θ)
D1

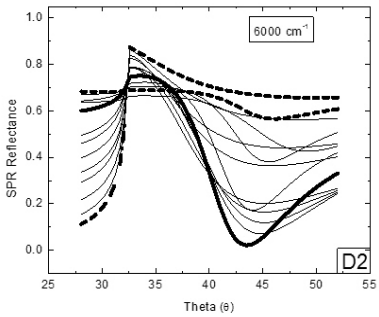
6000 cm-1
SPR Reflectance
Theta (θ)
D2

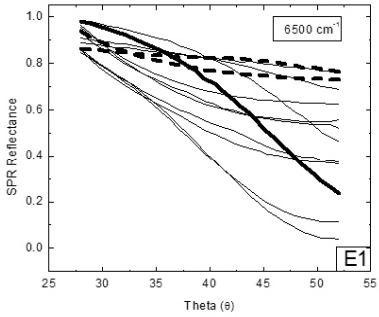
6500 cm-1
SPR Reflectance
Theta (θ)
E1

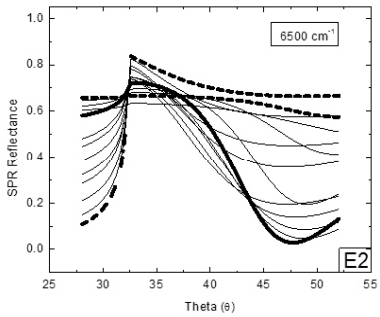
6500 cm-1
SPR Reflectance
Theta (θ)
E2

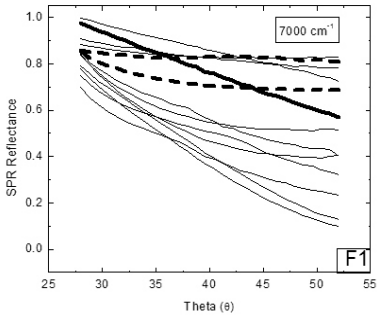
7000 cm-1
SPR Reflectance
Theta (θ)
F1

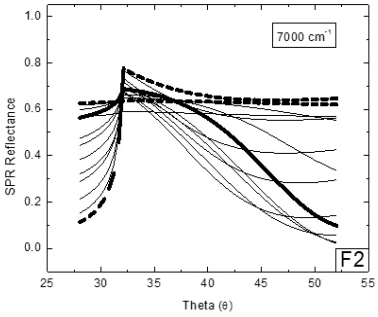
7000 cm-1
SPR Reflectance
Theta (θ)
F2

As shown above, an intermediate thickness sample of 160 nm possesses the sharpest and most narrow SPR reflectance dip. Thinner or thicker samples show less of a SPR effect, and only a large broadening of the spectra is seen with both the thinnest and thickest ITO films. In agreement with the experimental data, the sample of 160 nm retains the largest extinction with a reflectance minimum shift from $\theta \approx 60$ at 4,500 cm^{-1} to $\theta \approx 73$ at 6,000 cm^{-1}.

Figure 9 displays the X-ray diffraction analysis for four representative thickness samples (121, 97.5, 40, 30 nm).

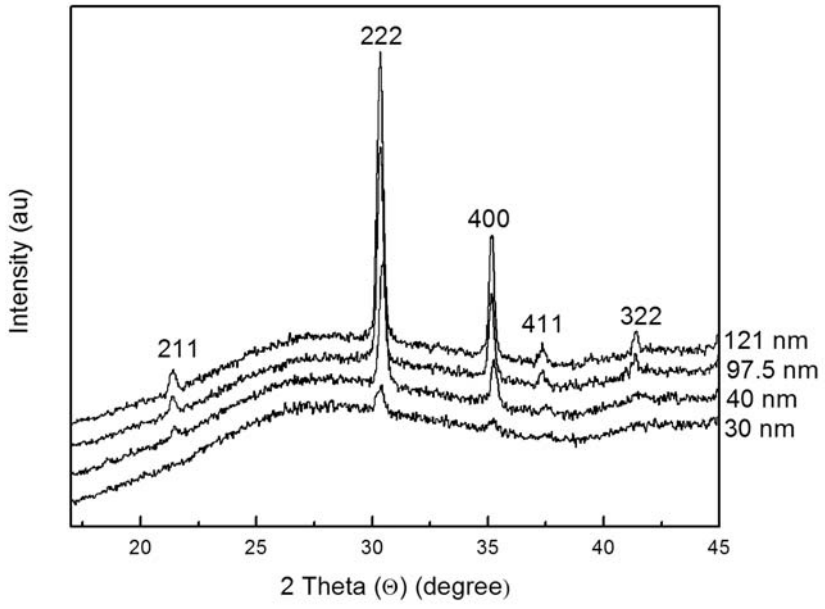

Figure 5.9. XRD spectra of 4 representative thickness samples at 30, 40, 97.5, and 121nm for 2-theta of 16-46 degrees.

This figure revealed that the ratio of the diffraction peaks was equivalent on all samples. Therefore, this data substantiates the assertion that the thickness change and not a change in the intrinsic crystallographic structure is solely responsible for the observed spectral changes.

5.7. Results of Atomic Force Microscopy Studies

For my studies, I was concerned with the surface roughness of the custom designed indium tin oxide thin films as this may have an effect upon monolayer deposition. To perform my simple surface roughness studies, experts suggested utilizing an AFM in the intermittent or "tapping" mode setup as previously described. Atomic force micrographs were obtained on a Digital Instruments Nanoscope IIIa using Al-coated tips (BS-Tap300, Budget Sensors) with the instrument in tapping mode. These tips were chosen as they are relatively stiff so that they will not break as easily over somewhat rough surfaces. Images shown below were 2^{nd} order flattened with the root-mean square (RMS) roughness calculated using the AFM software. ITO samples for AFM analysis were sonicated for 20 minutes in EtOH and dried under a N_2 stream immediately prior to examination. The table below details the overall results obtained from the AFM studies. As shown, there are not significant differences between the samples.

Table 5.2. Surface roughness results from AFM studies on an ITO thickness series.

Sample Thickness	Surface Roughness
A- 30 nm	1.114 nm
B - 40 nm	1.574 nm
C - 54.5 nm	0.802 nm
D - 71 nm	1.307 nm
E - 83 nm	2.288 nm
F - 97.5 nm	1.263 nm
G - 112 nm	1.194 nm
H - 121 nm	NA

Below the actual AFM images of the prepared samples are shown in Figure 5.10.

Figure 5.10. The AFM images of the thickness series with A-G displaying 30 nm-112 nm corresponding with the table labels. Note that the image F (97.5 nm) had a faulty tip resulting in the blurred image and that image H is not present.

A.

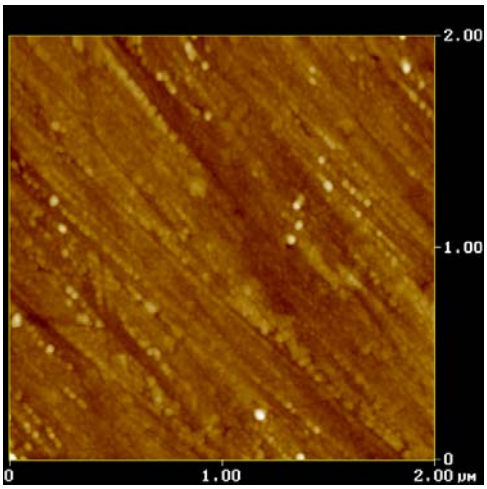
2.00
1.00
0
0
1.00
2.00 µm

B.

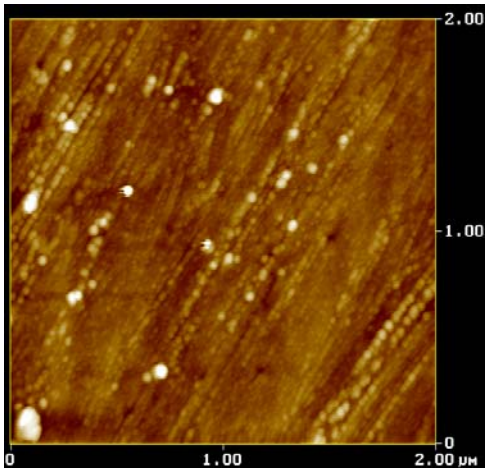
2.00
1.00
0
0
1.00
2.00 µm

C.

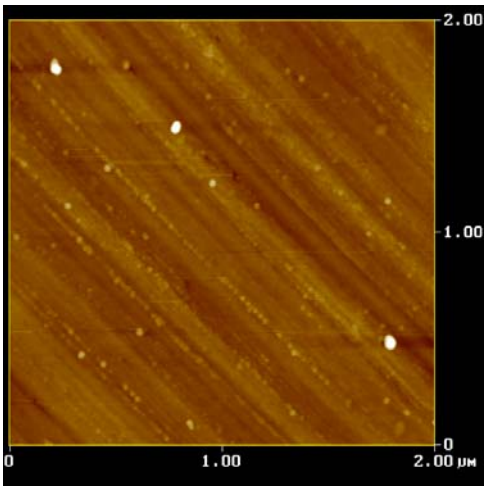
2.00
1.00
0
0
1.00
2.00 µm

D.

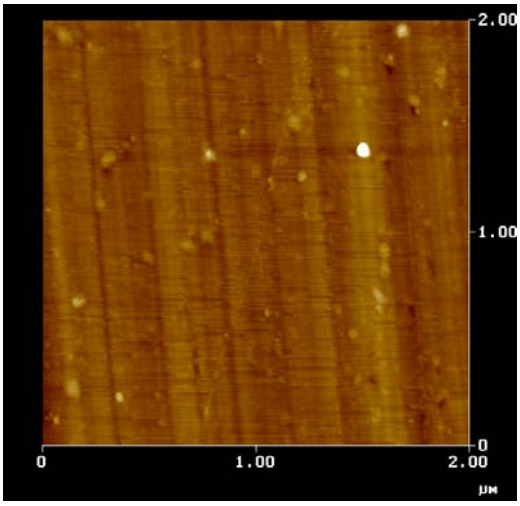
2.00
1.00
0
0
1.00
2.00
µm

E.

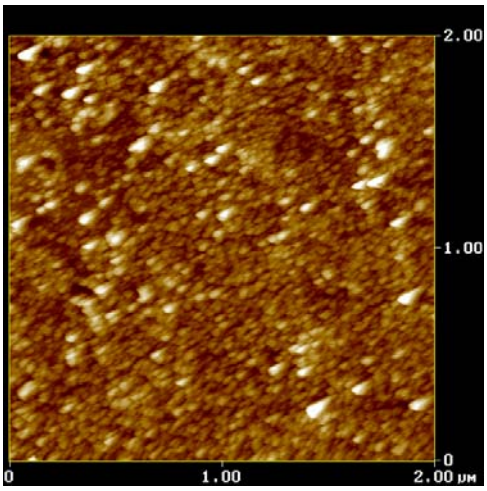

F.

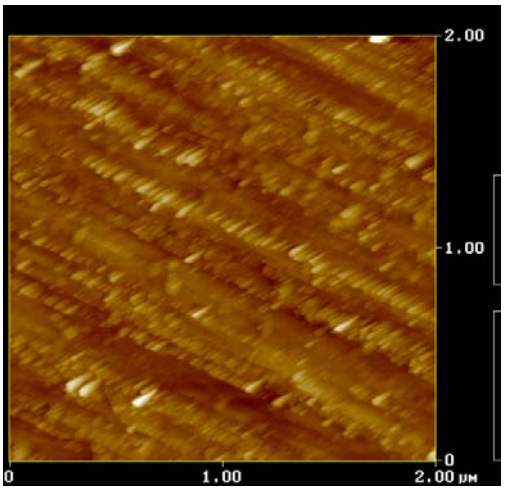

G.

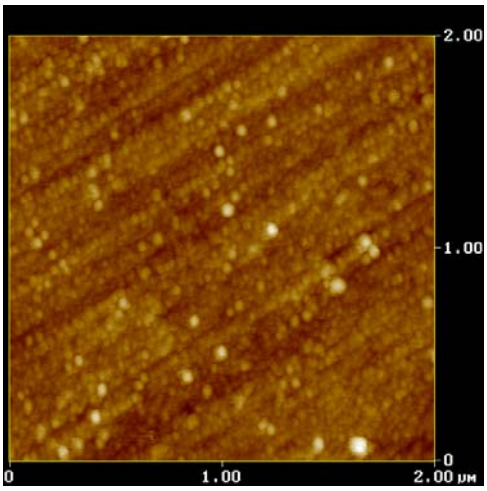

These images display the resultant flattened representation of the surfaces. The apparent white "spots" on the surface is assumed to be dust. All images are similar with the exception of the 97.5 nm sample in which the higher surface roughness resulting in several broke tips. As very little difference between the samples were detected, at this point, the study was halted due to the financial cost of the tips versus the useful data obtained and the last 121 nm sample was not examined. Therefore, for these samples in particular, surface roughness does not appear to be a variable that will affect the deposition of monolayers or the effectiveness of the excitation of the SPR effect.

5.8 References

1. Brandl, D.; Oubre, C.; Norlander, P., Plasmon Hybridization in Nanoshell Dimers. *The Journal of Chemical Physics* **2005,** 123, 0247011-02470111.

2. Norlander, P.; Le, F., Plasmonic Structure and Electromagnetic Field Enhance,ents in the Metallic Nanoparticle-film system. *Applied Physics B* **2006,** 84, 35-41.

3. Knoll, W., Interfaces and thin films as seen by bound electromagnetic waves. *Annual Review of Physical Chemistry* **1998,** 49, 569-638.

4. Wooten, F., *Optical Properties of Solids*. Academic Press, Inc.: San Diego, 1972.

5. Moskovits, M., Surface Selection-Rules. *Journal of Chemical Physics* **1982,** 77, (9), 4408-4416.

6. Rhodes, C., Weibel, S., Maria, J.P., Losego, M., Leonard, D.L., Laughlin, B., Duscher, G., Franzen, S., Surface Plasmon Resonance in Conducting Metal Oxides. *Journal of Applied Physics* **2006,** 100, (1), 1-5.

7. Kretschm.E; Raether, H., Radiative Decay of Non Radiative Surface Plasmons Excited by Light. *Zeitschrift Fur Naturforschung Part a-Astrophysik Physik Und Physikalische Chemie* **1968,** A 23, (12), 2135-&.

8. Oh, S.; Han, S., Ionic Charge-Selective Electron Transfer at Fullerene-Multilayered Architecture on an Indium-Tin Oxide Surface. *Langmuir* **2000,** 16, 6777-6779.

9. Neufeld, A. K.; O'Mullane, A. P., Effect of the mediator in feedback mode-based SECM interrogation of indium tin-oxide and boron-doped diamond electrodes. *Journal of Solid State Electrochemistry* **2006,** 10, (10), 808-816.

10. Lattante, S.; Romano, F.; Caricato, A. P.; Martino, M.; Anni, M., Low electrode induced optical losses in organic active single layer polyfluorene waveguides with two indium tin oxide electrodes deposited by pulsed laser deposition. *Applied Physics Letters* **2006,** 89, (3).

11. Purvis, K.; Lu, G.; Schwartz, J.; Bernasek, S., Surface Characterization and Modification of Indium Tin Oxide in Ultrahigh Vacuum. *The Journal of the American Chemical Society* **2000,** 122, 1808-1809.

12. Kim, K. Y.; Park, S. B., Preparation and property control of nano-sized indium tin oxide particle. *Materials Chemistry and Physics* **2004,** 86, (1), 210-221.

13. Hamberg, I.; Hjortsberg, A.; Granqvist, C., High Quality Transparent Heat Reflectors of Reactively Evaporated Indium Tin Oxide. *Applied Physics Letters* **1982,** 40, (5), 362-364.

14. Hjortsberg, A.; Hamberg, I.; Granqvist, C., Transparent and Heat-Reflecting Indium Tin Oxide Films Prepared by Reactive Electron Beam Evaporation. *Thin Solid Films* **1982,** 90, 323-326.

15. Hara, K.; Sayama, K.; Arakawa, H., Semiconductor-sensitized solar cells based on nanocrystalline In2S3/In2O3 thin film electrodes. *Solar Energy Materials and Solar Cells* **2000,** 62, (4), 441-447.

16. Zhu, B.; Eurell, T.; Gunawan, R.; Leckband, D., Chain-length dependence of the protein and cell resistance of oligo(ethylene glycol)-terminated self-assembled monolayers on gold. *Journal of Biomedical Materials Research* **2001,** 56, (3), 406-416.

17. Kim, J., Voltammetric studies of guanine and its derivatives by Ru(bpy)(2+/3+) mediator on indium tin oxide electrode. *Bulletin of the Korean Chemical Society* **2000,** 21, (7), 709-711.

18. Comini, E.; Cristalli, A.; Faglia, G.; Sberveglieri, G., Light enhanced gas sensing properties of indium oxide and tin dioxide sensors. *Sensors and Actuators B-Chemical* **2000,** 65, (1-3), 260-263.

19. Solieman, A.; Aegerter, M. A., Modeling of optical and electrical properties of In2O3 : Sn coatings made by various techniques. *Thin Solid Films* **2006,** 502, (1-2), 205-211.

20. Brewer, S. H.; Franzen, S., Optical properties of indium tin oxide and fluorine-doped tin oxide surfaces: correlation of reflectivity, skin depth, and plasmon frequency with conductivity (vol 338, pg 73, 2002). *Journal of Alloys and Compounds* **2002,** 343, (1-2), 244-244.

21. Hansen, W., Electric Fields Produced by the Propagation of Plane Coherent Electromagnetic Radiation in a Stratified Medium. *Journal of the Optical Society of America* **1968,** 58, (3), 380-390.

22. Raether, H., *Surface Plasmons on Smooth and Rough Surfaces and on Gratings*. Springer-Verlag: Berlin, 1988.

Chapter 6

Surface Plasmon Resonance Detection of Monolayer/Nucleic Acid Deposition onto Indium Tin Oxide Substrates

6.1. Monolayer Formation

Although Langmuir-Blodgett (LB) films of organic monolayers were discovered in the early 1900's, it was not until the early 1990's that fundamental understanding of the formation of these self assembled monolayers (SAMs) began. [1] Initially for these studies, gold was the substrate of choice due to its chemical inertness, strong specific bonding with sulfur, and the known dense packing of long-chain alkanethiols. [1] Through these and other studies, it was discovered that gold surfaces arrange in an hexagonal closest packed arrangement with three binding sites on the Au(111) face [2] when bonded to a long chain alkanethiol with an optimal chain length of least 10-carbons. [3] Therefore, initial studies of monolayer deposition within our group mimicked earlier SAM studies and focused primarily on long chain alkane thiol SAMs,.specifically hexadecanethiol (HDT) on the typical substrate of choice, ITO. Early studies with FTIR and XPS seem to suggest a thiolate adlayer does form on the CMO. [4.] A logical extension to this research has thus been to apply additional characterization techniques to the study of the formation of the SAMs, to not only verify the existence of an adlayer formation but also to attempt to understand factors affecting this formation. This chapter details my attempts to study the SAM formation of various substrates on ITO in a concise manner with both successes and failures represented.

Deposition parameters for hexadecanethiol discussed in detail in Chapter 1 were followed in the studies described in this chapter. Surface plasmon resonance (SPR) was performed both before and after deposition on three ITO substrates of similar material properties. The figures below detail the outcomes of these preliminary examinations.

A. B.

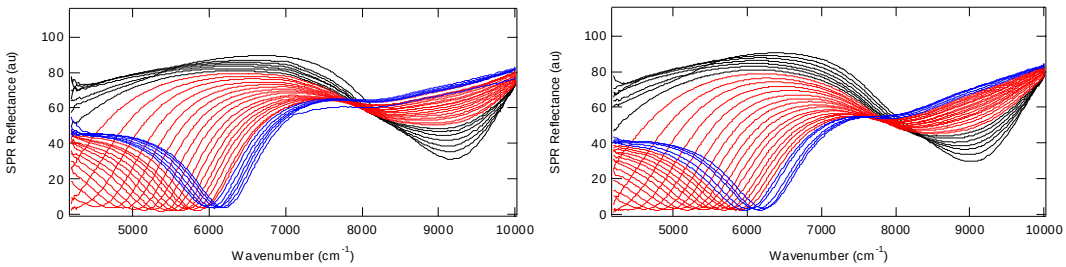

Figure 6.1A,B. The surface plasmon resonance spectra of the predeposition spectra of 2 ITO substrates prepared with equivalent processing parameters (~150nm, ~14 ohms/square). The angle of incidence ranged from ~42-77°. The range of the angles with the blue color is 73.6° to 77.2°, the range of the angles with the black shading is 40.2° to 52.1°, while the remaining angles are shown in red.

Subsequently, another straightforward experiment involved examination of one of the ITO substrates post-ultraviolet ozonlysis cleaning and post-sonication for the purpose of ensuring the integrity of the thin films under typical cleaning procedures.

A. B.

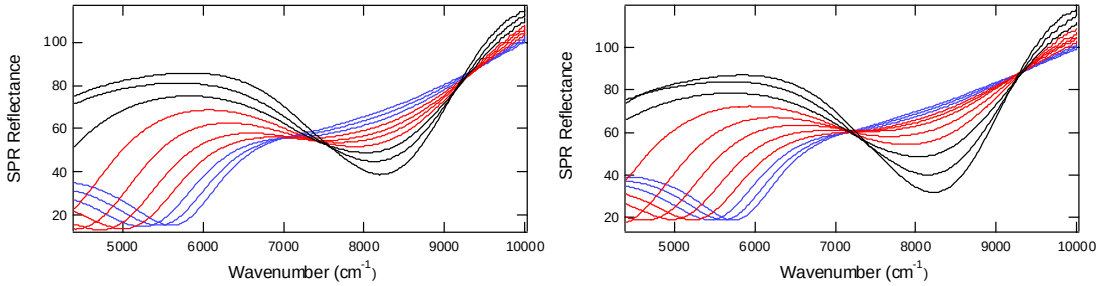

Figure 6.2 A,B. The SPR spectra of the post-cleaning procedures of UVO ozonlysis cleaning (A) and sonication (B) of the ITO substrate shown in Figure 1A. The angle of incidence ranged from ~30-52°. The range of the angles with the blue color is 47.0° to 52.05°, the range of the angles with the black shading is 29.6° to 34.6°, while the remaining angles are shown in red.

Figure 6.2 revealed that the cleaning methods utilized throughout the deposition did not significantly change the material properties of the thin film. This was shown by the lack of a shift in the SPR spectra between Figure 6.1A,B (predeposition and precleaning) and Figure 6.2A,B (post-cleaning). Fewer angles were examined to minimize the absorption of adventitious carbon to the surface.

The hexadecanethiol (HDT) deposition followed the procedure listed in the introduction. The deposition of the two substrates was performed simultaneously and in an analogous fashion.

A. B.

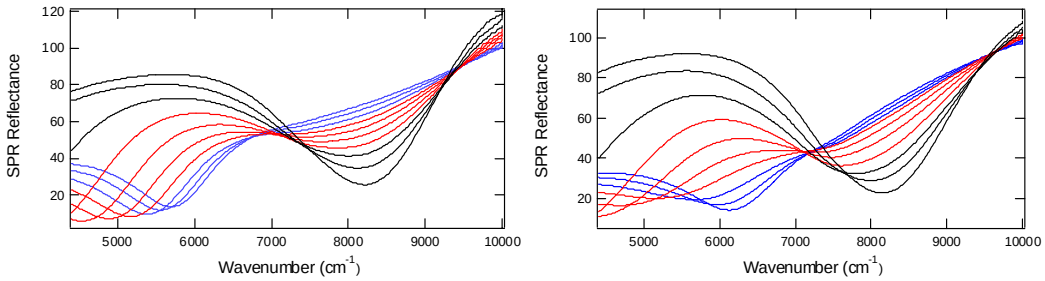

Figure 6.3 A,B. The SPR spectra of the post-deposition of hexadecanethiol (HDT) of the two ITO substrates shown in Figure 1A. The angle of incidence ranged from ~46-77°. The range of the angles with the blue color is 72.8° to 77.2°, the range of the angles with the black shading is 44.5° to 55.4°, while the remaining angles are shown in red.

The following figure further details the observed SPR shift of the HDT deposition.

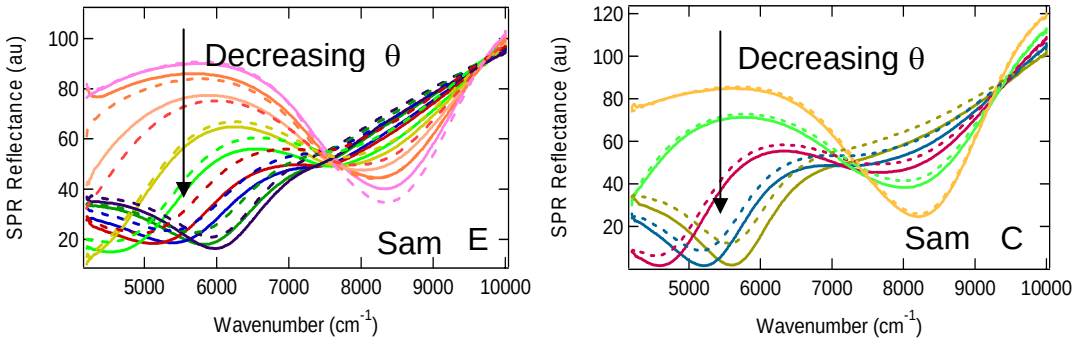

Figure 6.4 A,B. The SPR spectra of the post-deposition of hexadecanethiol (HDT) for representative angles. The hexadecanethiol (HDT) deposition is the dashed line (- -) while the predeposition sample is the solid line (__). The angle of incidence ranged from ~30-52°. The sample E shows 9 displayed angles while the sample C shows 6.

Figure 6.4 shows that the deposition of hexadecanethiol does affect the position of the SPR reflectance. For Sample E, the largest shift occurred at 68.2° with a wavenumber shift of nearly 500 cm^{-1} (red line). Simarily, there is a large shift in the sample C, with the maximum frequency shift occurring at 75.1° of over 300 cm^{-}

[1](olive line) This is indicative of a material property change in the ITO thin film such as a change in the conductivity.

Further studies within this area would include concentration studies to investigate whether a quantitative shift in the SPR exists as well as other surfaces chemistries to reveal if any chemical-specific spectral shifts occur. In the next section, I was able to extend the study to the deposition of nucleic acids.

6.2. Nucleic Acid Deposition

The coverage of an ITO thin film with a 20-mer oligonucleotide has been previously explored [Moses, 2004 #9; Moses, 2005 #1; Moses, 2004 #11] in our laboratory through FTIR, electrochemical, and photoelectrochemical techniques. [5, 6, 7, Moses, 2007 #19] The underlying motivation for this type of experiment is further development of a functional biosensor utilizing ITO as the substrate. The novel approach I took to this particular experimental design was the extension of surface plasmon resonance (SPR) spectroscopy. SPR spectroscopy has been previously utilized for observation of DNA deposition on gold surfaces primarily in the visible spectral region. [Brockman, 2001 #4; Brockman, 2001 #5; Brockman, 1999 #6; Corn, 2000 #7; Corn, 2001 #8] The deposition of the nucleic acids RNA and DNA are grayscale imaged at each step with the GWC FT-SPR Module© as described the methods chapter (2) of this thesis. My intention thus was to perform equivalent SPR experimentation in the near-IR spectral region with an Indium Tin Oxide substrate and utilize XPS as a conformational technique.

The DNA deposition strategy was described in detail in the Introduction. As shown in Figure 6.5, the ITO substrate is layered initially with a silane monolayer followed by reaction with SSMCC linker which then bonds the ssDNA to the substrate. Hybridization to the dsDNA is the final end product.

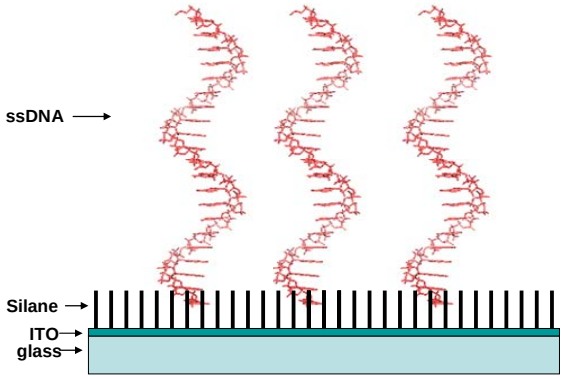

Figure 6.5 – Schematic of the ssDNA/ITO substrate. The ~150nm ITO thin film is deposited on BK7 glass. An adlayer of trimethoxyaminopropyl silane is deposited followed by the ssDNA. The orientation of the layers as shown is an idealized representation.

An abundance of linkers are possible for this deposition methodology. The rational for the utilization of the SSMCC linker chosen is for stability within the pH range of interest. The advantages to this crosslinker is that is contains an amine-reactive N-hydroxysuccinimide (NHS ester) and a sulfhydryl-reactive maleimide group. Both of which are stable at the neutral pH 7.1 at which our buffers are prepared. This stability

arises from the cyclohexane bridge in the spacer arm. Additionally, the solubility of SSMCC is unusually high, up to ~10mM in aqueous solutions. The reaction used with the SSMCC is detailed in Figure 6.3. This figure shows the crosslinking that theoretically occurs between the silane monolayer and the nucleic acid. The linker molecule, sulfo-SMCC, utilizes two crosslinking mechanisms with the attachment of the trimethoxyaminopropylsilane by a NHS-ester bond and a maleimide reaction scheme bonding the 20-mer oligonucleotide to the opposite end of the molecule.

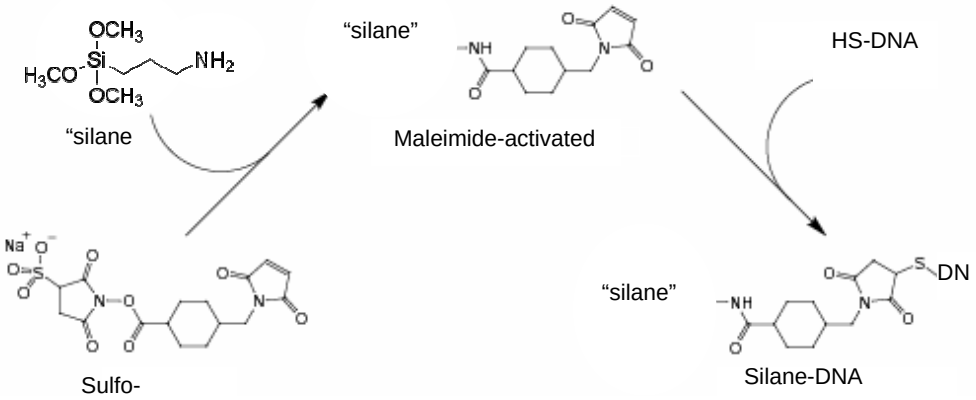

Figure 6.6. The crosslinking chemical reaction between sulfo-SMCC and the trimethoxyaminopropyl silane.

Thus, with my research, the deposition methodology of nucleic acids changed dramatically from previous work within the Franzen group. [Moses, 2005 #1] As I had encountered nonreproducibility issues, it was thought that a linker stable over a larger pH range may improve results. Literature searches had revealed an apparent pKa of 3.2 suggesting to me possible decreased efficiency at the higher pH's used for

the deposition buffers. [8] To date, this methodology has also not led to highly reproducible results, leading me to believe that new linking methodology should be examined in the future now that reproducible customized substrates are available.

6.3. Surface Plasmon Resonance (SPR) Spectroscopy of Oligonucleotides

For this initial study using the SPR detection method, four ITO/BK7 glass substrates of ~150 nm were prepared by the Materials Science and Engineering Department at NC State University. At each step, a SPR spectrum was acquired and compared with both the control sample and previous steps to assess the deposition. Subsequently, XPS spectroscopy was performed for 5 samples; a blank control sample, a silane monolayer sample, 2 ssDNA deposition and 1 dsDNA deposition samples. The following figures detail these results. The section begins with Figure 6.7, which shows the SPR of the four samples of equivalent deposition parameters prior to any deposition step to obtain a baseline spectra for subsequent comparison..

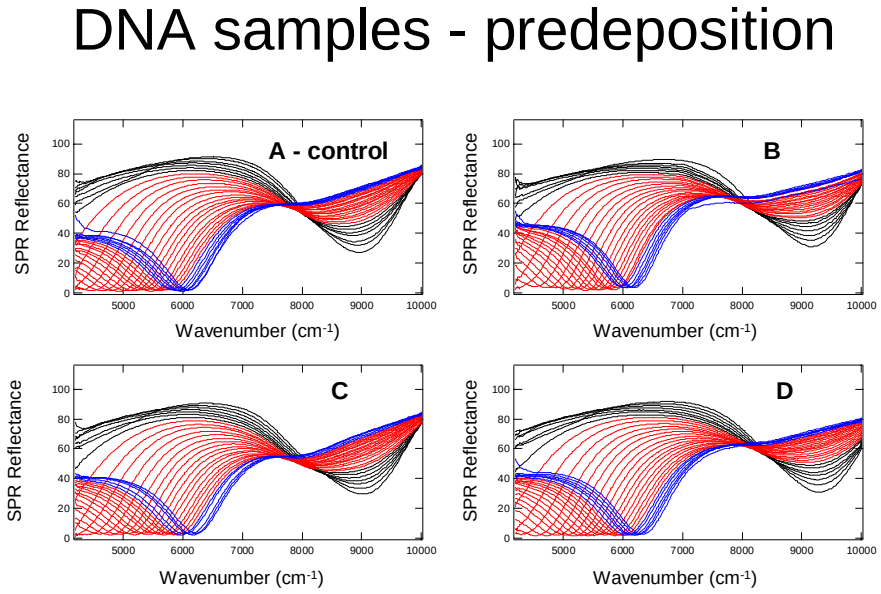

Figure 6.7. SPR of samples prior to deposition. The angle of incidence ranged from ~42-77°. The range of the angles with the blue color is the larger angles with ~72.8-77..2°, the range of the angles with the black shading is the smaller angles ~28-31°, while the remaining angles are shown in red.

Figure 6.8 shows the results of the SPR spectroscopy after silane deposition. Due to time constraints of the experiment so that only a modest amount of time elapsed between deposition steps, only every other angle was examined by SPR. Again, these are the identical samples shown in Figure 6.7 and were prepared with equivalent processing parameters.

DNA samples silane

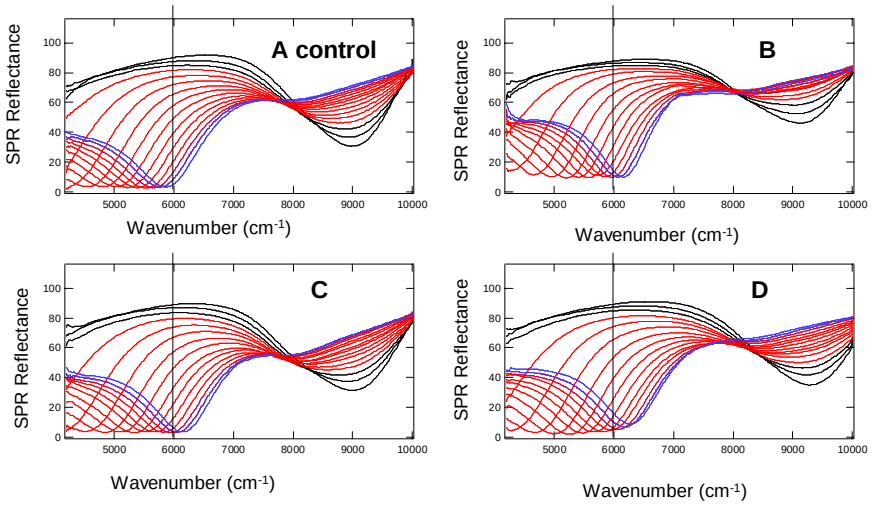

Figure 6.8. SPR of samples after deposition of trimethoxyaminopropylsilane as described in the introduction. The angle of incidence ranged from ~42-77° with the same color scheme as shown previously. For ease of comparison, a sight line has been drawn at 6000 cm^{-1}as an arbitrary value for comparison close to the observed surface plasma reflectance.

As shown in Figure 6.8, there is a slight shift in the SPR spectrum after the deposition of the silane, although it would be extremely difficult to use this methodology for quantitation.

Figure 6.9 details the ITO substrate after the 1 hour submersion in a solution of SSMCC. Due to even tighter time constraints with the surface modified by the crosslinker only 6 or 7 representative angles of the samples were taken.

DNA samples SSMCC

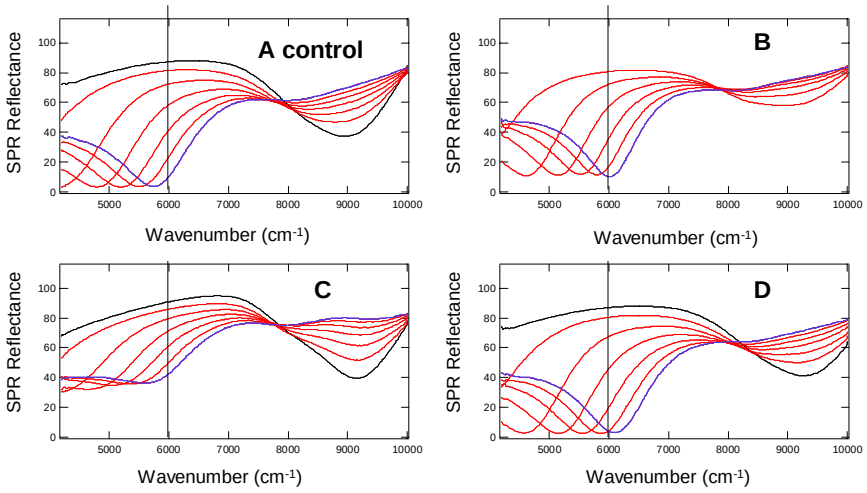

Figure 6.9. The SPR spectra of the ITO substrates layered with silane/SSMCC as described in the introduction. A sight line has been drawn at 6000 cm^{-1} for comparison of the shift in the SPR spectra. Angle of incidence ranged from ~47-76° with the blue angle depicting the largest angle while blue reveals the smallest with mid-range angles shown in red.

As shown in Figure 6.9, there is not a great deal of additional shift after the liguid deposition with the crosslinker. The discrepancies observed with sample C were further examined with the XPS spectroscopy.

Figure 6.10 shows the SPR of the ITO substrates post deposition of a 20-mer ssDNA.

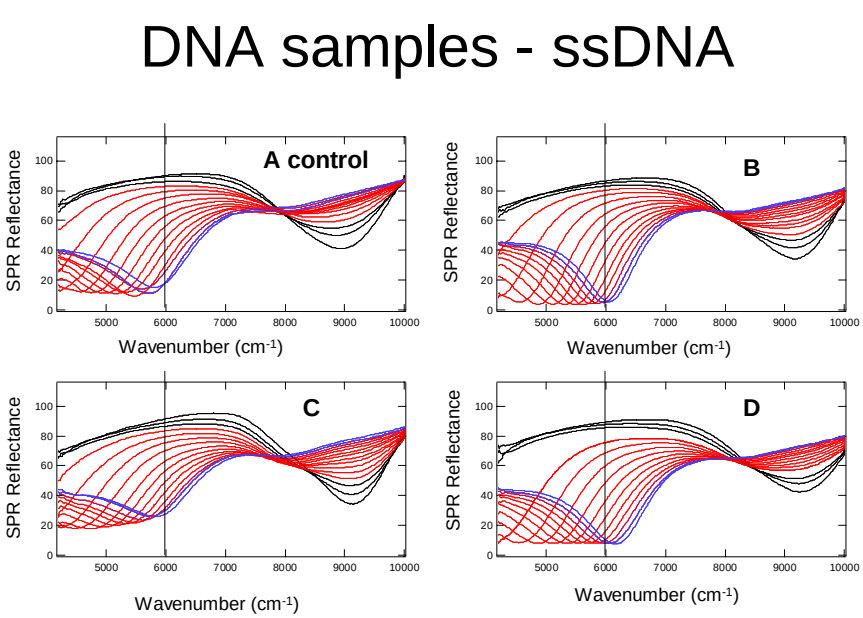

Figure 6.10. The SPR spectra of the ITO substrates deposited with 1μM ssDNA. Ideally the substrates are layered as ITO/silane/ssDNA. The sight line drawn at 6000 cm^{-1} differentiates the control ITO substrate from those undergoing the deposition. Angle of incidence ranged from ~42-77° with the original color scheme.

As with Figure 6.10, every other angle was examined so that samples were not left for an extended period of time exposed to atmosphere. Once again there is no large SPR shift, although the similarity between samples B and D suggests that something unexpected occurred on the surface of sample C, making it ineffectual for deposition. Additionally, all the samples appear different from the blank control sample, indicating that some type of adlayer formation has been accomplished.

Another route taken to attempt to quantify the effect of the adlayers on SPR was to mathematically determine difference spectra as shown in Figure 6.10.

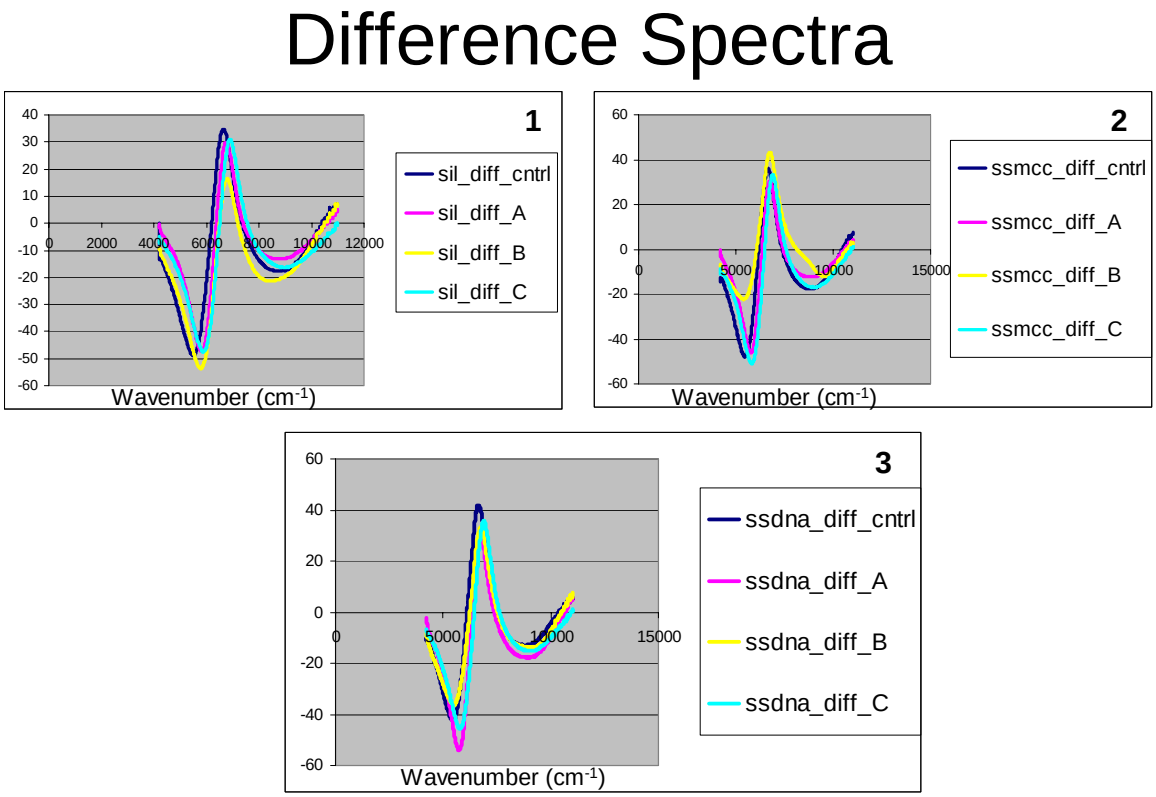

Figure 6.11. Difference spectra of the four ITO samples for each deposition step beginning with the silane deposition (1), followed by the SSMCC linker (2) and finally the ssDNA (3). All difference spectra were calculated for 72.8° by subtraction of the predeposition spectra from the adlayer deposition.

As shown in Figure 6.10, there is a shift in the SPR of the samples with the adlayer (A,B,C) as compared to the control but the shift is not consistent within the samples. More repetitions are needed of these deposition studies.

Figure 6.12 is the final stage of the nucleic acid deposition with the hybridization of 1 μM DNA to form dsDNA. Only one sample underwent this transformation.

dsDNA

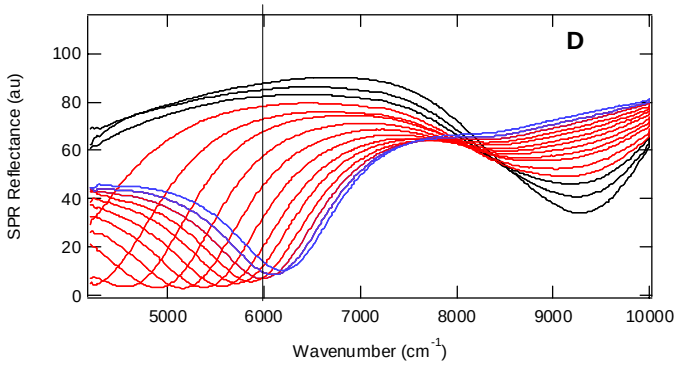

Figure 6.12. The SPR spectra of the ITO substrate hybridized with 1μM dsDNA. The sight line is drawn at 6000 cm^{-1} for comparison with the ssDNA SPR shift. Angle of incidence ranged from 40-77° with the original color scheme.

Figure 6.12 revealed very little SPR shift with the hybridization of 1 μM dsDNA. This is indicative that hybridization methodology was not successful and therefore, possibly needs to further investigation in the future.

6.4. XPS Spectroscopy

XPS spectroscopy was used to confirm the SPR spectroscopic results. Specifically the binding of ssDNA and hybridization to form dsDNA were studied. In order to examine the various deposition samples, the substrates were first examined as the blank, the two ssDNA and the single dsDNA. A trimethoxyaminopropyl silane monolayer was deposited onto the blank sample for subsequent examined by XPS. The following figures show the various elements chosen for analysis by this

spectroscopic technique. A more detailed description of the technique is found within the introduction as well as other chapters in which publications were submitted with more technical descriptions. The table below first details the rational of chosen elements.

Table 1. Photoelectron energy of elements chosen for XPS analysis.

Element	Energy (eV)		Locale
Carbon	1s	285 eV	1-Adventitious 2-Hydrocarbon Backbone
Indium	$3d_{5/2}$ $3d_{3/2}$	444 eV 452 eV	ITO substrate
Oxygen	1s	531 eV	1-ITO Substrate 2-Nucleic Acid 3-Silane
Nitrogen	1s	398 eV	1-Nucleic Acid 2-Silane
Phosphorus	$2p_{3/2}$ $2p_{1/2}$	130 eV 131 eV	Nucleic Acid
Sulfur	$2p_{3/2}$ $2p_{1/2}$	164 eV 165 eV	Nucleic Acid
Silicon	2p	103 eV	Silane

Note: This table assumes complete rinsing of the SSMCC.

The following figures depict each of these elements as analyzed for the 5 samples. Equivalent experimental conditions were used for all of the substrates and all were analyzed on the same day with the exception of the trimethoxyaminopropyl silane.

The first figure shown below, Figure 9, shows the carbon XPS spectra of the five substrates overlaid.

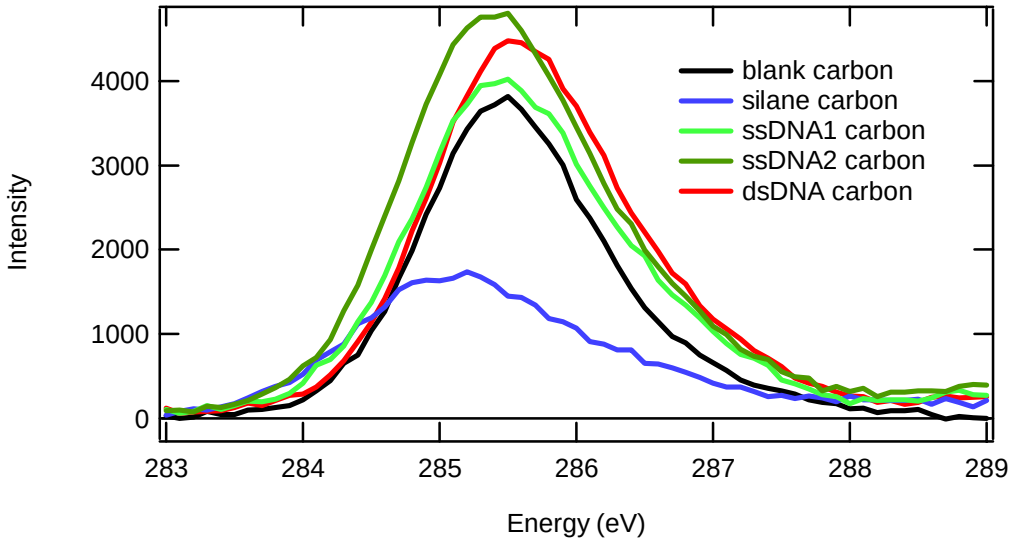

Figure 6.13.. XPS spectra of Carbon 1s of the control deposition (black), the dsDNA deposition (red), silane deposition (blue) and the 2 ssDNA depositions (light and dark green) on ITO.

Figure 6.13 reveals a large amount of adventitious carbon present on the surface as the control sample contains nearly the same amount of carbon as the nucleic acid depositions. The smaller observed intensity of the silane is possibly indicative of either the packing of the silane in which the hydrocarbon backbone is not accessible to the surface or else the surface has been cleaned more thoroughly with this deposition methodology.

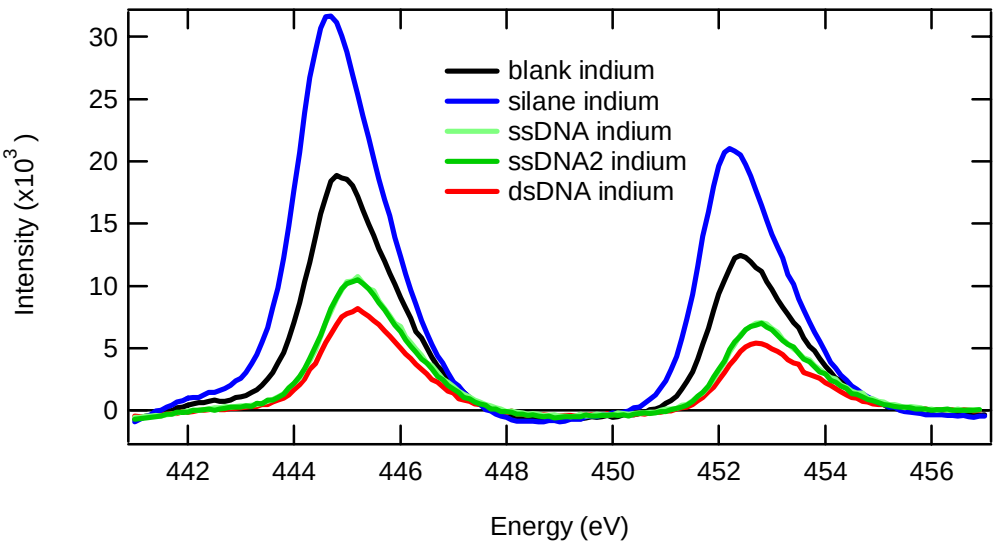

Figure 6.14 XPS spectra of Indium $3d_{3/2}$ and $3d_{5/2}$ of the control deposition (black), the dsDNA deposition (red), silane deposition (blue) and the 2 ssDNA depositions (light and dark green) on ITO.

Figure 6.14 reveals that as the nucleic acid monolayers are deposited, the surface is covered as shown by the decrease in indium. The increase of the indium with silane monolayer may again be due to the deposition conditions used in which the indium is more rigorously cleaned. This leads to the question of whether our ITO cleaning procedures are sufficient or if this too needs to be another area of investigation.

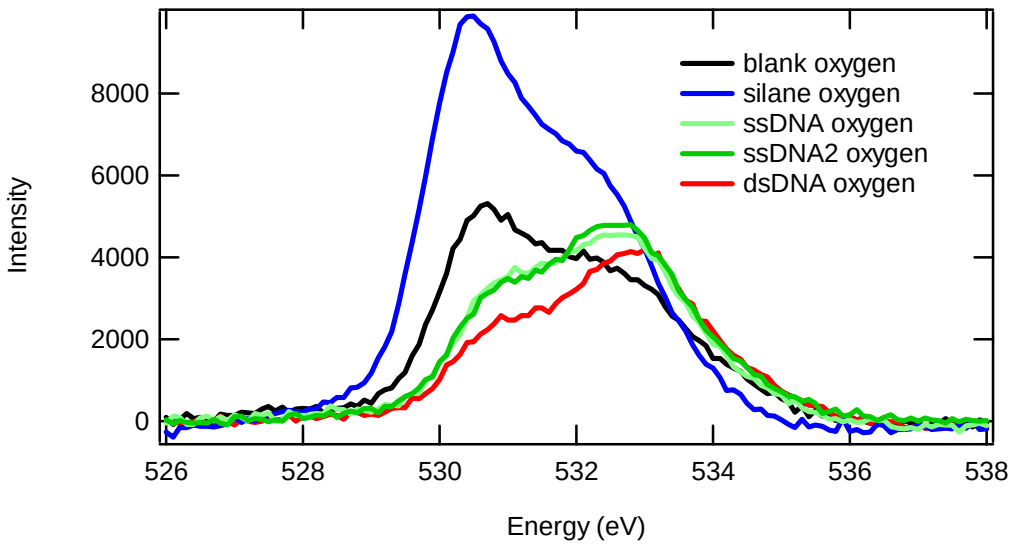

Figure 6.15. XPS spectra of Oxygen 1s of the control deposition (black), the dsDNA deposition (red), silane deposition (blue) and the 2 ssDNA depositions (light and dark green) on ITO.

Figure 6.15 shows the change in the environment of the oxygen once nucleic acid deposition has occurred. The ssDNA deposition samples appear equivalent and contain more oxygen than the dsDNA sample. Again, a discrepancy arises with the silane possibly indicating that the methoxy is located at the surface.

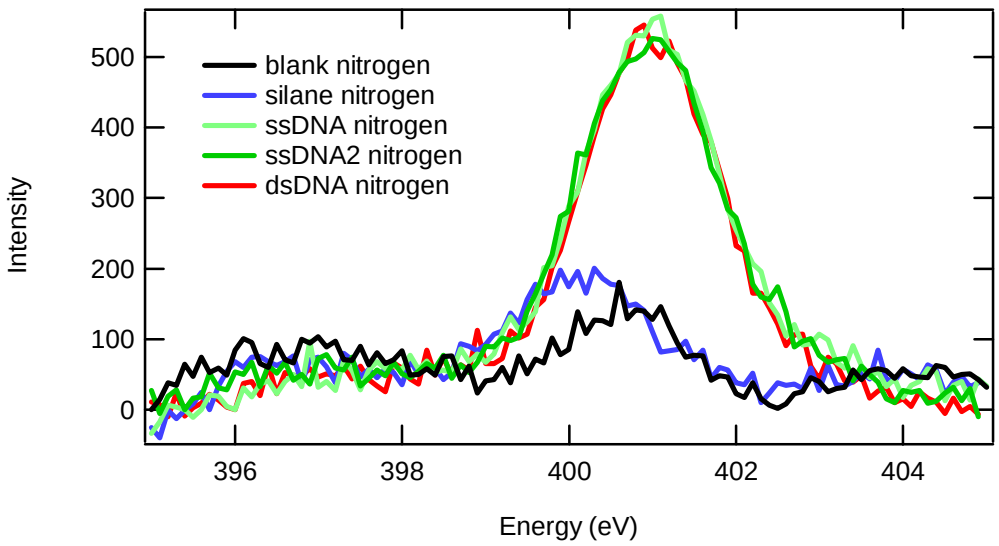

Figure 6.16. XPS spectra of Nitrogen 1s of the control deposition (black), the dsDNA deposition (red), silane deposition (blue) and the 2 ssDNA depositions (light and dark green) on ITO.

Figure 6.16 reveals the increase in nitrogen once nucleic acid deposition occurs. This is an expected result, which confirms that DNA is at least physisorbed with the ITO surface. The silane sample appears to possess slightly more nitrogen than the blank sample indicating some type of adlayer has formed on the surface.

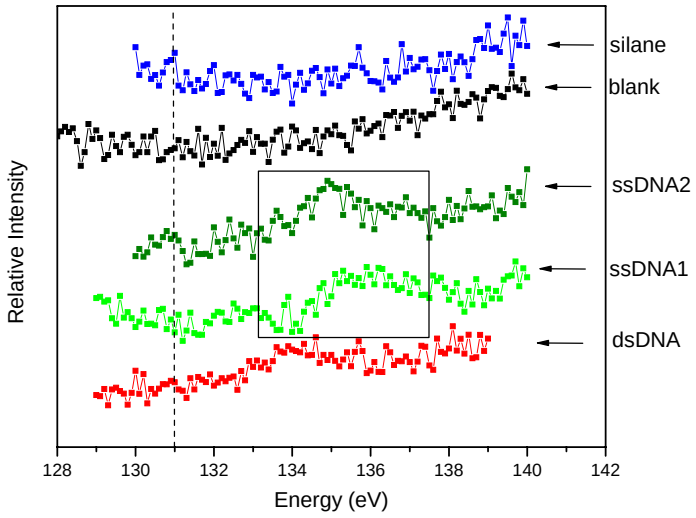

Figure 6.17. XPS spectra of Phosphorus $2p_{3/2}$ and $2p_{1/2}$ of the control deposition (black), the dsDNA deposition (red), silane deposition (blue) and the 2 ssDNA depositions (light and dark green) on ITO. The dotted line is placed at the position of the typical phosphorus peaks in an ideal environment. The boxed area refers to the region for which a phosphorus in phosphate environment would reside.

Figure 6.17 above reveals the phosphorus levels in the samples. Although the cross-section of the phosphorus is inherently low, we tried to compensate with more scans and longer dwell times. Even with these measures, the resulting intensity was still very low. A slight peak is apparent in both of the ssDNA samples at ~135 eV, which corresponds to the shift that phosphorus may experience when in a phosphate environment. Thus, this suggests that at least with the ssDNA deposition, some of the nucleic acid was bonded to the ITO surface, although I am doubtful of either full coverage or an ordered surface.

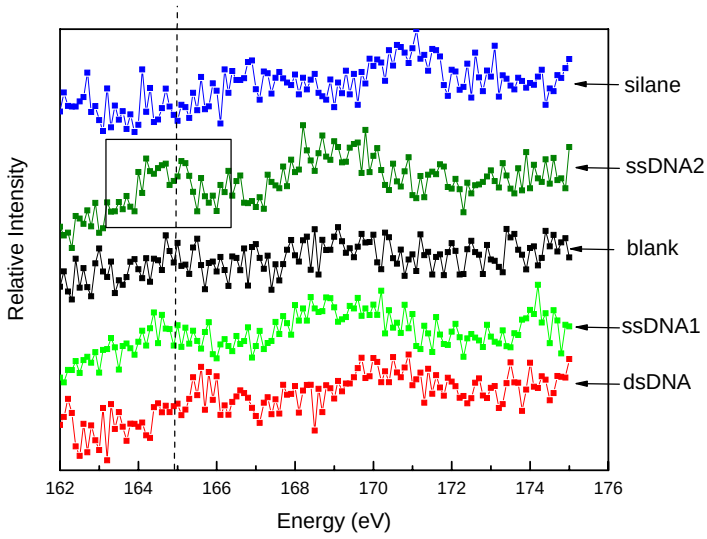

Figure 6.18. XPS spectra of Sulfur $2p_{3/2}$ and $2p_{1/2}$ of the control deposition (black), the dsDNA deposition (red), silane deposition (blue) and the 2 ssDNA depositions (light and dark green) on ITO. The dotted line is placed at the position of the typical sulfur peaks in an ideal environment. The boxed area highlights the small peak shown in one of the ssDNA deposition samples.

Figure 6.18 reveals the XPS spectra of the sulfur peaks. As with phosphorus, inherently the cross-section is quite low, although again longer dwell times and increased scan numbers were used in an attempt to compensate. As shown in the figure above, the intensity of sulfur peak is still very low and actually detectable only in the ssDNA2 sample. This is suggestive that the amount of DNA deposited on the surface is quite low.

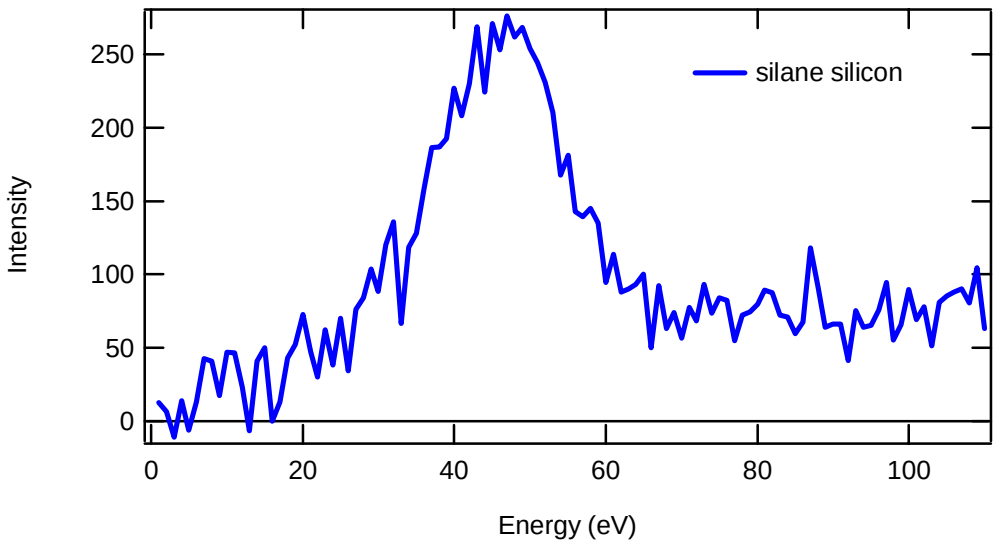

Figure 6.19 XPS spectra of Silicon 2p of an ITO thin film sample deposited with trimethoxyaminopropyl silane.

Figure 6.19 reveals a silicon peak in a silane environment for the sample on which trimethoxyaminopropyl silane was deposited. This confirms deposition did occur although it does not give any indication as to amount deposited or to the ordering of the deposited adlayers.

Overall, I believe the current methodology of DNA deposition needs more investigation. Possibly the silane adlayer concentrations are not optimal for a close-packed ordered base or else, the DNA deposition conditions need changing. In my opinion, both areas require further investigation for this type of research experimentation to proceed.

6.5. References

1. Bain, C. D.; Biebuyck, H. A.; Whitesides, G. M., Comparison of Self-Assembled Monolayers on Gold - Coadsorption of Thiols and Disulfides. *Langmuir* **1989**, 723-727.

2. Franzen, S., Density functional calculation of a potential energy surface for alkane thiols on Au(111) as function of alkane chain length. *Chemical Physics Letters* **2003,** 381, (3-4), 315-321.

3. Bain, C. D.; Evall, J.; Whitesides, G. M., Formation of Monolayers by the Coadsorption of Thiols on Gold - Variation in the Head Group, Tail Group, and Solvent. *Journal of the American Chemical Society* **1989**, 7155-7164.

4. Brewer, S. H.; Brown, D. A.; Franzen, S., Formation of thiolate and phosphonate adlayers on indium-tin oxide: Optical and electronic characterization. *Langmuir* **2002,** 18, (18), 6857-6865.

5. Moses, S.; Brewer, S. H.; Lowe, L. B.; Lappi, S. E.; Gilvey, L. B. G.; Sauthier, M.; Tenent, R. C.; Feldheim, D. L.; Franzen, S., Characterization of single- and double-stranded DNA on gold surfaces. *Langmuir* **2004,** 20, (25), 11134-11140.

6. Cerruti, M. G.; Sauthier, M.; Leonard, D.; Liu, D.; Duscher, G.; Feldheim, D. L.; Franzen, S., Gold and silica-coated gold nanoparticles as thermographic labels for DNA detection. *Analytical Chemistry* **2006,** 78, (10), 3282-3288.

7. Lowe, L. B.; Brewer, S. H.; Kramer, S.; Fuierer, R. R.; Qian, G. G.; Agbasi-Porter, C. O.; Moses, S.; Franzen, S.; Feldheim, D. L., Laser-induced temperature jump electrochemistry on gold nanoparticle-coated electrodes. *Journal of the American Chemical Society* **2003**, 14258-14259.

8. Williams, A.; Ibrahim, I. T., A New Mechanism Involving Cyclic Tautomers for the Reaction with Nucleophiles of the Water-Soluble Peptide Coupling Reagent 1-Ethyl-3-(3-(Dimethylamino)Propyl)Carbodiimide (Edc). *Journal of the American Chemical Society* **1981,** 103, (24), 7090-7095.

Chapter 7

Characterization of Monolayer Formation on Aluminum-doped Zinc Oxide Thin Films

(In preparation for publication)

7.1. Abstract

The optical and electronic properties of aluminum-doped zinc oxide (AZO) thin films on a glass substrate are investigated experimentally and theoretically. Optical studies with coupling in the Kretschmann configuration reveal an angle-dependent plasma frequency in the mid-IR for p-polarized radiation suggestive of the detection of a Drude plasma frequency. These studies are complemented by oxygen depletion density functional theory studies for the calculation of the charge carrier concentration and plasma frequency for bulk AZO. In addition, we report on the optical and physical properties of thin film adlayers of n-hexadecanethiol (HDT) and n-octadecanethiol (ODT) self-assembled monolayers (SAMs) on AZO surfaces using variable angle reflectance FTIR spectroscopy, x-ray photoelectron spectroscopy (XPS), and near-edge x-ray absorption fine structure (NEXAFS) spectroscopy. Our characterization of the SAM deposition onto the AZO thin film reveals a range of possible applications for this conducting metal oxide.

7.2. Introduction

The development of biosensing applications of thin films has been dependent upon the development of robust self-assembled monolayers (SAMs) for the attachment of biomolecules to such surfaces. For this reason, there has been an enormous interest in SAM technology in the past few years. [1-6] The applications of SAM technology have focused primarily on gold as the substrate using a wide range of techniques, including, electrochemistry, surface plasmon resonance (SPR), scanning tunneling microscopy, variable

angle reflectance Fourier transform infrared (FTIR) spectroscopy and x-ray photoelectron spectroscopy (XPS). [7-13] These studies have shown that alkane thiolates produce stable reproducible monolayers on gold substrates [6, 13-16]. Conducting metal oxides present a number of interesting properties, such as optical transparency, a wide range of surface-attachment chemistries, stability at high voltage, and stability in the presence of ions that solubilize metals, such as gold. . The stability of conducting metal oxide films to dissolution by acid is an important factor that must be considered a disadvantage in most applications. Fundamental study of the properties of self-assembled monolayers on optically transparent substrates is a key step in the development of multiplexing of sensing techniques, such as optical spectroscopy or microscopy coupled to electrochemistry. The potential advantage of dual sensing capabilities and tunability requires the study of both the SAMs and optical properties of the thin layer conducting metal oxides.

Transparent conducting metal oxides (TCOs) are materials that are visibly transparent and infrared reflecting [17]. These materials have been used widely in optoelectrical devices such as solar cells, and flat panel displays due to the need for high electrical conductivity paired with high transmittance in the visible region [18]. Indium tin oxide and fluorine-doped tin oxide are two such materials that have been studied in the past [19, Lowe, 2003 #33, 20, Brewer, 2001 #36]. In addition to these applications, indium tin oxide (ITO) has been shown to provide other novel applications such as thermographic sensing, photothermal electrochemistry, and photoelectrochemistry, all of which are important in the development of biosensing applications [20-24]. Yet a major limitation for the development of technology based on ITO is that indium is only found in minute amounts in the earth's crust and typically is extracted as a residue of ore processing, primarily zinc. [25]. Therefore due to the prohibitive cost,

availability, and environmental concerns of ITO, other materials with similar properties are being investigated for applications that require optical transparency combined with moderate conductivity [26].

One such alternative is zinc oxide (ZnO). Typical ZnO films are transparent n-type conducting metal oxides. The useful electro-optical properties, stability, and band gap of ZnO is primarily due to intrinsic defects, such as oxygen vacancies and zinc interstitials. For instance, in the presence of hydrogen plasma, chemisorbed oxygen can form a protective layer of surface hydroxyls (-OH) that resists reduction of the thin film surface [27]. Since the conductivity of the zinc interstitials within pure ZnO is not enough for use as transparent semiconductors dopants are added. The addition of a higher valence element such as an aluminum dopant (2-5%) to ZnO increases the conductivity by the replacement of the Zn^{+2} ions with Al^{+3} [17]. Additionally, conductivity is highly dependent on the deposition and post-deposition parameters, which permit either the desorption or absorption of oxygen in the film; thus, both routes of increasing conductivity are important areas of research[28-31]. ZnO films have previously shown application in the areas of photosensors [32], solar cells [33] and nanotechnology applications [34-36].

The resulting aluminum-doped zinc oxide (AZO) thin films are wide-band gap (3.4 eV) transparent conducting metal oxides that present numerous advantages over traditional transparent conductive oxides (TCOs). Unlike indium tin oxide (ITO) and cadmium tin oxide (CTO), AZO is non-toxic, relatively inexpensive, stable in hydrogen plasma atmosphere, and requires lower deposition temperatures. Yet, it still maintains the characteristic properties of ITO and CTO thin films by exhibiting high optical transparency in the visible region and low electrical resistance. [37-40] AZO films have been prepared by

spray pyrolysis (SP),[18] sol-gel method,[41] reactive and non-reactive radio frequency-magnetron sputtering, [42] pulsed magnetron sputtering,[43] and pulsed laser deposition.[18]. The resulting hexagonal close-packed structures are highly oriented with a "c axis" normal to the substrate with crystalline faces of (002) and (101). [44-46]

As an alternate biosensing substrate, AZO requires further investigations into various the sesnsing properties, specifically spectroscopic qualities and monolayer formation. The optical properties and electrical conductivity are similar to ITO, thus, similar sensing characteristics may be apparent in AZO. Observed reflectivity changes as a result of plasmon oscillations have been repeatedly demonstrated in ITO by FTIR and SPR spectroscopy; [23, 47, 48]; therefore, similar investigations are warranted in AZO. In addition, studies of SAM formation on conducting metal oxides have also been previously described in the literature for TCO's such as ITO and CTO [20, 47]. Here we report the deposition of n-hexadecanethiol- and n-octadecanethiol-based SAMs onto the surface of a 2% aluminum-doped zinc oxide thin film. Variable angle reflectance infrared spectroscopy, x-ray photoelectron spectroscopy (XPS), and near edge x-ray fine structure spectroscopy (NEXAFS) are used to characterize the SAM formation. These studies are complemented by density functional theory calculations of the charge carrier concentration and the plasma frequency of oxygen depleted substrates to increase understanding of the material properties of the AZO,

7.3. Materials and Methods

7.3.1. Chemicals and Substrates.

n-Hexadecanethiol (HDT) and n-Octadecanethiol (ODT) were obtained from Sigma Aldrich and used as received. Absolute ethanol was used as received from Aaper

Alcohol and Chemical Co. The gold electrodes were obtained from Evaporated Metal Films, Inc.

7.3.2. Aluminum-doped Zinc Oxide Thin Film Preparation.

Aluminum-doped zinc oxide (AZO) electrodes were fabricated by the National Renewable Energy Laboratory (NREL) at room temperature by RF sputtering with the MRC 603 side/vertical sputter system using a 5'' x 15" (nominal) Planar Magnetron ceramic target with a pure argon flow of 50 sccm. The film thickness was determined by a stylus profilometer (Dektak3). The carrier concentration and electron mobility were measured using Hall Effect measurements (van der Pauw technique, BioRad Model HL5500). The composition of the films was analyzed by an electron probe microanalysis (EPMA, JEOL 8900 Electron Microprobe), and crystal properties were assessed using x-ray diffraction (XRD, Sintag Model PTS). Under 5 mTorr pressure deposition, the AZO thin films were determined to have a thickness of 120 nm. The substrate for the AZO electrodes was 0.5 mm Corning 1737 borosilicate glass.

7.3.3. Deposition on Aluminum-doped Zinc Oxide Thin Films.

The AZO electrodes were cleaned via 20 minutes of UV-Ozonolysis (model number 42, Jelight Co. Inc.) to yield a clean hydrophilic surface and remove any adventitious carbon present [48]. The clean AZO electrode was subsequently immersed in the deposition solution of ODT or HDT (10 mM) in absolute ethanol for up to 30 minutes. The electrodes were rinsed with 95% ethanol followed by drying with N_2 gas.

7.3.4. Reflectance FTIR Spectroscopy.

All reflectance spectra were collected using a Digilab FTS-3000 Fourier Transform infrared (FT-IR) spectrometer using a Varian Universal variable grazing angle reflectance attachment. An infrared polarizer was used to obtain p-(vertically) polarized light. The infrared light is generated by a globar source, it then passes through a potassium bromide (KBr) beamsplitter and then focused onto the photodiode of a liquid nitrogen-cooled, narrow band mercury-cadmium-telluride (MCT/A) linearized detector with a normal spectral response of 650-7000 cm^{-1}. The angle of incidence used was 70° with respect to the surface normal. In order to obtain the AZO thin film reflectance spectra, a ratio of the single beam spectra of the metal oxide thin film on the glass substrate to the single beam spectra of a gold surface was made. The IR spectra presented are an averaged of 32 scans taken at a resolution of 2 cm^{-1}. The spectra of the thiolated adlayers on the AZO electrode were obtained by taking a ratio of the single beam spectra of the p-polarized spectra of the deposited material (HDT or ODT) on AZO to the s-polarized spectra of the same aluminum doped zinc oxide thin film. All SAM IR spectra are an average of 256 scans at a resolution of 2 cm^{-1}.

7.3.5. X-ray Photoelectron Spectroscopy.

XPS spectra were recorded on a VG CLAM II surface analysis system (100 mm mean radius) with MgK α X-rays ($h\upsilon$ = 1253.6 eV, takeoff angle = 90°) operated at 13 kV and 20 mA emission current. The elemental scans had a resolution of 1 eV as determined from the full width half maximum (FWHM) of a gold $4f_{7/2}$ spectral peak with 3 scans performed for zinc and 7 scans for sulfur.

7.3.6. Near Edge X-Ray Fine Structure Spectroscopy (NEXAFS).

The NEXAFS experiments were performed on the NIST/DOW soft x-ray materials characterization facility located at U7A beamline at the National Synchrotron Light Source at Brookhaven National Laboratory with a resolution of ≈0.15 eV at the carbon K-edge. The monochromator energy resolution was calibrated by setting a graphite carbon K-edge transition of C(1s)→π* to 285.35 eV [49]. The partial electron yield (PEY) signal was collected with a channeltron electron multiplier (50 mm diameter entrance cone) with an adjustable entrance grid bias (EGB), set to EGB=-150V, allowing rejection of low-energy inelastic auger electrons from below the surface. To account for fluctuations in the beamline x-ray intensity, the NEXAFS spectra were normalized with the incident beam intensity (I_o) from the photo yield of a clean in situ gold-coated grid. A computer controlled-stepping motor directed the orientation of the sample holder with respect to the polarization vector of the incoming x-ray beam for incident angles between the x-ray beam and the sample surface of 30 degrees (near glancing geometry) to 90 degrees (normal geometry). The cartoon in Figure 5 depicts the schematic of the performed NEXAFS experiments. The NEXAFS spectra were collected in the PEY mode for analysis of Auger electrons with photon energy ranging from 240 to 400 eV. The PEY NEXAFS spectra were normalized by adjusting the pre-edge and post-edge signals respectively to 0 and 1 [50].

7.3.7. Tilt Angle Calculations.

Tilt angle calculations were performed by the method reported by Outka et.al [51]. The intensity of the NEXAFS spectrum represents a molecular orbital transitioning from

the bonding to the antibonding state of a X-Y sigma bond ($1s \rightarrow \sigma^{*}_{X-Y}$) and is related by equation (1) [51]:

$$I_{X\text{-}Y} = A\left[PI^{\parallel}_{X\text{-}Y} + (1-P)I^{\perp}_{X\text{-}Y}\right] \quad , \tag{1}$$

where A is a prefactor constant, P is the polarization factor of the X-ray beam, and $I^{\parallel}_{X-Y}$ and $I^{\perp}_{X-Y}$ gives the resonance intensities of the parallel and perpendicular component of the X-ray beam **E** vector, respectively. The expressions for $I^{\parallel}_{X-Y}$ and $I^{\perp}_{X-Y}$ are given by equations (2) and (3) [51]:

$$I^{\parallel}_{X-Y} = B\left[\cos^2(\theta)\cos^2(\alpha_{X-Y}) + \frac{1}{2}\sin^2(\theta)\sin^2(\alpha_{X-Y})\right] \tag{2}$$

$$I^{\perp}_{X-Y} = \frac{B}{2}\sin^2(\alpha_{X-Y}) \quad , \tag{3}$$

where B is a prefactor that is a function of the bond absorption cross-section and instrumental parameters, θ is the angle between the substrate normal and the **E** (electric field vector) of the polarized X-ray beam, and $\alpha_{X\text{-}Y}$ is the angle between the surface normal and the X-Y bond of the antibonding orbital. Equation (4) relates the combination of the above equations (1)-(3):

$$I_{X\text{-}Y} = C\left[P\left(\cos^2(\theta)\cos^2(\alpha_{X-Y}) + \frac{1}{2}\sin^2(\theta)\sin^2(\alpha_{X-Y})\right) + \frac{(1-P)}{2}\sin^2(\alpha_{X-Y})\right] \quad , \tag{4}$$

where C is a constant.

The tilt angle and orientation of the monolayer alkane chain is calculated using the "tilted chain" model related by Stöhr et.al. [50] [52] where $\alpha_{C\text{-}C}$ and $\alpha_{C\text{-}H}$ are equated to the tilt angle and assuming bond angles of the C-H backbone as shown in equations (5) and (6);

$$\alpha_{C-C} = \arcsin\left[\sqrt{\frac{1+\cos(\delta_{C-C-C})\cos(2\tau)}{2}}\right] \quad (5)$$

$$\alpha_{C-H} = \arcsin\left[\sqrt{1-\frac{\sin^2(\tau)}{1+\tan^2\left(\frac{\delta_{H-C-H}}{2}\right)}}\right] \quad (6)$$

where $\delta_{C\text{-}C\text{-}C}$ and $\delta_{H\text{-}C\text{-}H}$ are the assumed bond angle of 115° between neighboring carbon atoms [51] and the bond angle of 110° of the hydrogen-carbon-hydrogen sequence [51], respectively and τ is the tilt angle of the chain with respect to the surface normal.

Comparison of the combination of equations (4) and (5) of the calculated $I_{C\text{-}C}$ to the experimental data leads to modeling of the tilt angle (τ) as the value of the constant C in equation (4) is adjusted until an adequate fit is obtained. In an analogous fashion, the tilt angle can be calculated by a comparison of the $I_{C\text{-}H}$ experimental data to the computed intensities, equations (4) and (6), and adjusting the constant C for an optimal fit. The reported tilt angles of the hydrocarbon chains represent an average over the two tilt chain angles calculated by the different approaches using comparison with both the $I_{C\text{-}H}$ and $I_{C\text{-}C}$ experimental and computed values.

7.3.8. Density Functional Theory Calculations.

The single point energy calculation of the molecule was carried out with the use of the quantum chemical software DMol3 (Accelrys, Inc.). [53] Density functional theory calculations were performed on an aluminum-doped zinc oxide unit cell containing 32 hexagonal formula units that comprise a total of 64 atoms with an

overall orthorhombic structure. The unit cell parameters for this orthorhombic cell (a = 6.50 Å. b = 11.26 Å. c = 10.41 Å) were expanded to find the unit cell parameters of minimum energy. The equilibrium geometry was found at 1.07a , 1.07b and 1.07c (see Supporting Information for details). This $Zn_{32}O_{32}$ orthorhombic cell (a = 6.95 Å, b = 12.05 Å, c= 11.14 Å) was used in order to study oxygen depletion as the n-type conduction mechanism as previously described for cadmium tin oxide and doping. [47, Brewer, 2002 #81] Oxygen depletion stoichiometries ranging from $Zn_{32}O_{32}$ to $Zn_{32}O_{26}$ were studied by random removal of oxygen atoms from random positions as previously described [Rhodes, Accepted #77] for un-doped and aluminum-doped (1.6%, 3.1%, 4.7%) zinc oxide structures. Periodic boundary conditions were used to determine the bulk electronic and optical properties of the metal oxide thin film. The double numerical plus p-function (DNP) basis set used was O(1s),2(2s),2(2p),2(3d), Zn(4s),(4p),2(4d) for the atoms with an atomic cutoff of 5.5 Å. The Perdew and Wang GGA functional was used for the DFT calculations. [54] The DFT calculations utilized the grand canonical ensemble approach, which allows for partial electron occupation needed for the charge carrier calculations. [55] In our experience, the effective electronic temperature of 0.02 Hartrees or ≈6300 K has been sufficient to guarantee self-consistent field (SCF) convergence. However, AZO thin film calculations, in which a layer thin film model is used for the AZO along its 001 axis with an ethane thiolate overlayer in a $(\sqrt{3} \times 3)R30^{o}$ hexagonal lattice required an electronic temperature of 0.04 Hartrees. The molecules in the adlayer where found to have a remarkable resemblance to the adlayer on Au(111) surfaces. In that case, as well the surface can be modeled using an orthorhombic unit cell.

The number of conduction electrons was determined from the energy bands above the Fermi energy, ε_F, at an electronic temperature of 300 K. The charge carrier concentration value was determined by summing the electrons in the conduction band of aluminum-doped zinc oxide divided by the unit cell volume calculated from the lattice constants. The plasma frequency was determined using equation (7): [56]

$$\omega_p^2 = \frac{ne^2}{m^* \varepsilon_o} \tag{7}$$

where ω_p is the plasma frequency, n is the charge carrier concentration, e is the charge of a conduction electron, εo is the permittivity of space, and m* is the effective mass of aluminum doped zinc oxide of approximately 0.28. [57] Thus, the plasma frequency is calculated directly from first principles using the Drude free-electron model. All of the DFT calculations were performed at the high performance computing Linux cluster at the North Carolina State University.

7.4. Results and Discussion

Both the formation of SAMs and the reflectivity of aluminum-doped zinc oxide (AZO) were measured experimentally by variable-angle Fourier transform infrared (FTIR) reflectance spectroscopy. Figure 7.1 reveals an angle-dependent reflectance change occurring at ≈8,500 cm^{-1}.

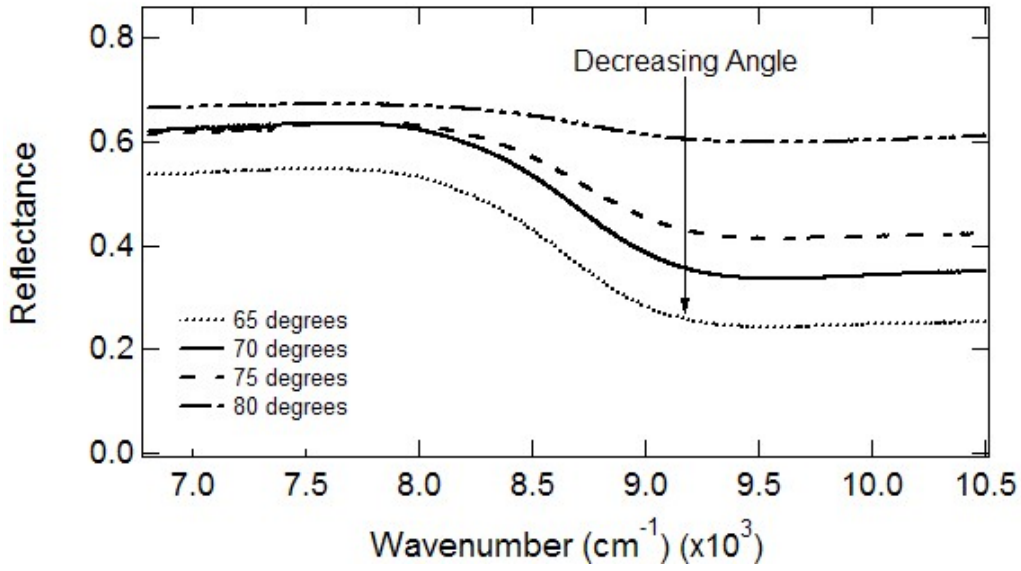

Figure 7.1. Experimental variable angle reflectance FTIR spectra of a thin film of AZO (80 Ω/sq, $4.7x10^{20}$ e- /cm) on a glass substrate relative to a gold surface in the mid-IR region for incident angles ranging from 65° to 80° with p-polarized light.

At wavenumbers below 8,500 cm^{-1}, the reflectance of the thin film varies between ≈55-65 % reflectance depending on the angle of incident, whereas, above 8,500 cm^{-1} the reflectance drops to ≈30 %. All of the incident angles follow this trend with the lowest incident angles of 65 and 70 degrees having the greatest reflectance change as shown by the wavenumber position in figure 7.1. The slight frequency shift in the reflectance is attributed to experimental factor including film inhomogeneity. The reduction in reflectivity coincides with the plasmon resonance frequency, which is the resonant absorption frequency for the conduction electrons as described in the Drude model. Below the plasma frequency of AZO at 8,500 cm^{-1}, the conduction electrons oscillate in phase with the incident radiation, which leads to reflection. When the incident radiation is matched to the resonant plasma frequency, the resonance condition leads to a sharp decrease in the reflectivity of the film. Above the plasma frequency, the AZO conduction electrons can no longer be driven in phase by the

incident radiation and the electromagnetic radiation is no longer efficiently reflected and is transmitted. In sp-type conductors, such as AZO, there is an increase in optical transparency of the film at wavenumbers higher than the plasma frequency, which is due to an absence of absorption bands in this region.

Figure 7.2 depicts both the experimental reflectance spectrum of a bare AZO thin film as well as the theoretical model spectrum calculated from a Drude free-electron model [56].

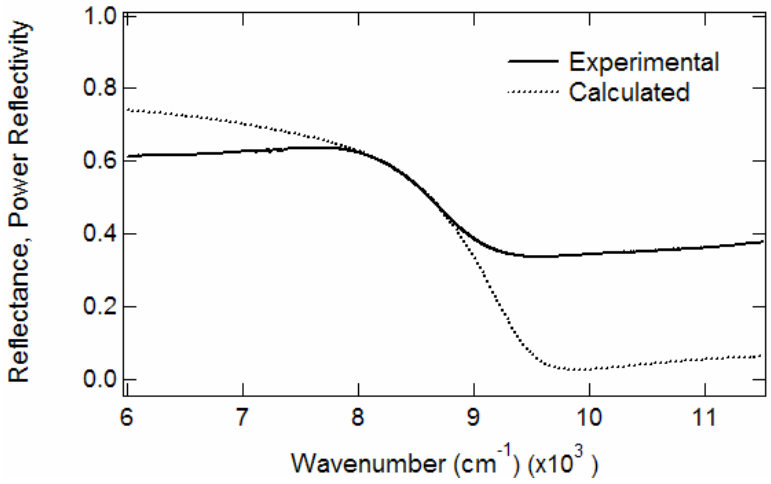

Figure 7.2. Experimental variable angle reflectance FTIR spectra (solid line) of a thin film of AZO on a glass substrate relative to a gold surface in the mid-IR region for an incident angle of 70° with p-polarized radiation. A theorectical FTIR spectra (dashed line) is calculated using the three-phase (air/glass/CTO) Fresnel equations of reflection and a dielectric index value of 1.8.

The dielectric function of AZO was determined by using the three-phase Fresnel equations of reflection (air/glass/AZO) [58]. Theoretically, the Drude free-electron model describes the dielectric function (ε(ω)) as a function of the plasma frequency (ω_p) and the scattering time (τ):

$$\varepsilon(\omega) = \varepsilon_\infty - \omega_p^2 \frac{1}{\omega^2 + \frac{i\omega}{\tau}} \quad , \qquad (8)$$

where ε_∞ is the high-frequency dielectric constant, ω_p is the plasma frequency as previously defined in equation (7), ω is the frequency, and τ is the electronic scattering time. Using the high frequency dielectric constant of the AZO substrate as 3.24 [59], an empirical scattering time of 6.7×10^{-15} s and a plasma frequency of 14,600 cm^{-1} were determined. These values were used in three-phase Fresnel equation of reflection to model a system comprised of two dielectric interfaces. Only the real components of the refractive index of air (η=1, κ=0) were included in the model. The complex refractive index for the AZO films was determined from the Drude free-electron as expressed in equation (9).

$$\varepsilon(\omega)^{\frac{1}{2}} = N(\omega) = n(\omega) + ik(\omega) \quad , \tag{9}$$

where N is the complex refractive index, n is the real, dispersive component and k is the imaginary, absorptive component of the refractive index. These equations relate the plasma frequency (ω_p) to both the charge carrier density (n) and the effective electron mass (m).

The formation of SAMs by alkanethiolates on conducting thin films is of fundamental and technological interest. Figures 7.3 A and B show experimental variable angle reflectance FTIR reflectance spectra for a bare AZO thin film and an AZO thin film with a thiolate adlayer of either HDT (A) or ODT (B).

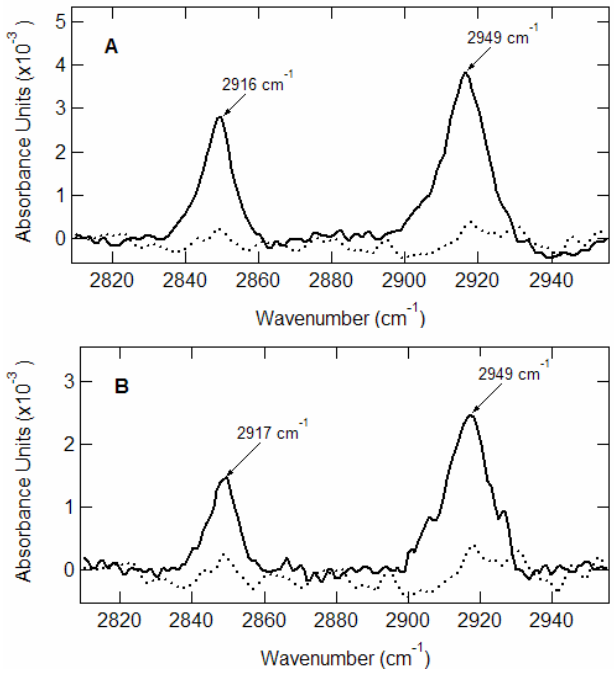

Figure 7.3A,B Baseline corrected reflectance FTIR spectra obtained from a ratio of p-polarized light of 1-hexadecanethiol and 1-octadecanethiol on AZO to s-polarized light of a bare AZO slide. The spectra shown are for an incident angle of 70°. The reference AZO (dashed line) was cleaned via 20 minutes of UVO. The adlayer (solid line) deposition time was for 30 minutes and 15 minutes for the octadecanethiol and hexadecanthiol solutions, respectively.

The dashed line displays the bare aluminum-doped zinc oxide thin film while the solid line reveals the spectra of the AZO with a thiolate adlayer. The vibrational symmetric and antisymmetric C-H stretching peaks are centered at 2949 cm^{-1} and 2916 cm^{-1}, respectively. The symmetric peak centered at 2949 cm^{-1} is lower than the peak corresponding to the vibrational stretching mode in neat liquid found at 2951 cm^{-1}. [16, 20, 60, 61]. This shift is indicative of an ordered adlayer on the surface. Additionally, as shown with other CMOs deposited on glass substrates, [20, 62] these spectra also displayed bands from the glass substrate onto which the aluminum-doped zinc oxide was deposited with the longitudinal optical (LO) and transverse optical (TO) Si-O-Si stretching modes observed at 1248 and 1064 cm^{-1} (data not shown). The FTIR data revealed that both the HDT (16-

carbon) and ODT,(18 carbon) successfully deposited, therefore AZO surface appears well-suited for deposition of long chain alkane molecules.

Although previous studies with the deposition of HDT on ITO thin films [20] revealed analogous peak positions of the C-H stretching modes, the intensities were lower than those reported for alkanethiolates SAMs on gold, indicative of a greater disorder or a lower packing density for SAMs deposited on ITO than on gold. Specifically, the absorbance units of a SAM on an ITO substrate are typically less than 0.001 a.u. [20] while thiolated SAMs on gold range from 0.002 to 0.006 a.u. [16, 60, 63]. Both the formation of alkanethiolate SAMs and the lower order parameter on ITO have been corroborated by NEXAFS [64] On the other hand, HDT SAMs on CTO had absorbances ranging from 0.002 to 0.003. [65] For the HDT SAM on AZO, the total absorbance was in the range from ≈0.003 to 0.004, while the ODT SAM that absorbance ranged from ≈0.0015 to 0.0025. This is indicative of a thiolate adlayer on AZO that is better ordered than alkanethiolate adlayers on ITO. Most likely the stability of the zinc-sulfur bond is responsible for this difference. Additionally, deposition parameters for the AZO were similar to gold using a 10 mM solution with either a 15 minute deposition time (HDT) or 30 minute deposition time (ODT). This is in contrast to the neat thiolate overnight deposition solution required for SAMs on ITO. In addition, the stability of the AZO thin films was tested by acquiring FTIR spectra one year post-preparation and –deposition. These data reveal that the surface morphology of the bare AZO thin film changes slightly as shown by shifts in the plasma frequency. However, the thiolate SAMs appear to be stable after one year as evidenced by the presence of distinct C-H stretching modes although the intensity is somewhat diminished indicating adlayer degradation. Extended washing with an aqueous solvent such as ethanol for several minutes, also does not destroy

the SAMs as shown by the presence of the CH stretching modes in a FTIR spectrum although a slight reduction of the intensity of peaks occurs as well as an observed small shift in the stretching peaks indicative of an entropic effect by the solvent as well (data not shown).

X-ray photoelectron spectroscopy (XPS) was also used to confirm the presence of the thiolated adlayers.

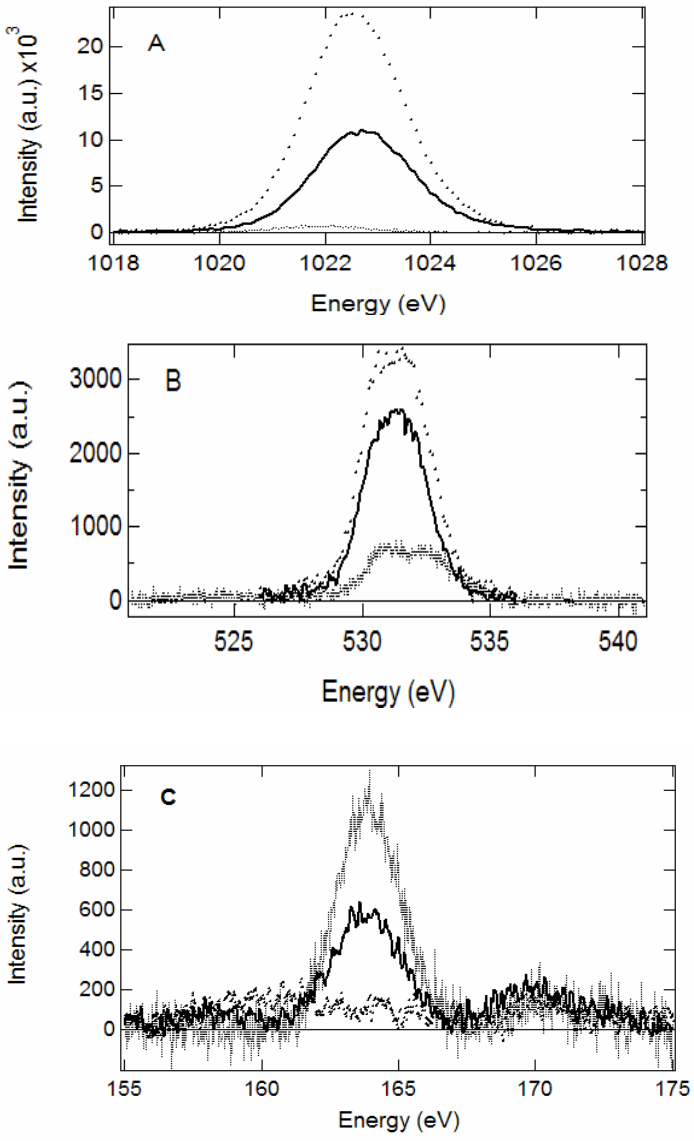

Figure 7.4A,B,C. XPS spectra corresponding to an adlayer of 1-hexadecanethiol (small dashes) and 1-octadeanethiol (solid line) on AZO compared to a bare reference AZO (large dots). A) The zinc $2p_{3/2}$region is shown. B) The oxygen 1s region is shown. C) The sulfur $2p_{3/2,1/2.}$region is shown.

Figure 7.4A shows the XPS spectra of zinc $2p_{3/2}$ of bare aluminum doped zinc oxide (dots), an adlayer of HDT (dashed line), and an adlayer of ODT (solid line) on AZO at a peak position of 1022 eV originating from the Zn^{+2} atoms in the exposed substrate. The observed attenuation of the zinc peak is indicative of adlayer formation on the AZO, although the different attenuations between the two adlayers indicate different surface coverages. The HDT and ODT SAMs demonstrate attenuations of the zinc $2p_{3/2}$ band of ≈97% and ≈50%, respectively, possibly as a result of different packing densities. Figure 7.4B reveals the XPS spectra of oxygen for the same substrate thin films. A similar attenuation of the 1s peak of oxygen (532 eV) provides additional evidence for the formation of an adlayer on AZO and follows a similar trend with attenuations or 75% and 30% observed for the HDT and the ODT monolayer, respectively. Figure 7.4C reveals the sulfur $2p_{3/2,1/2}$ XPS spectra of bare AZO, and an adlayer of both HDT and ODT on AZO using base AZO as a reference. These peaks, occurring at 162 and 163.7 eV, appear to coalesce into one indistinct peak centered at 164 eV. This position is in agreement with reported position of thiolates on gold. [15, 61] The intensity of the sulfur peak is similar to those previously reported in cadmium tin oxide and ITO. [20, 65] The intensity of the sulfur $2p_{3/2,1/2}$ XPS peak is 50% greater for HDT than ODT suggesting a difference in the bonding for thiolates of different chain lengths to AZO. This is in agreement to previous studies of functionalized thiolated species in gold [63, Nuzzo, 1987 #109]

The HDT and ODT adlayers on AZO were also investigated using NEXAFS, a surface sensitive technique capable of examination of the molecular organization of SAMs on substrates. In NEXAFS, core electrons from the K or L shell ground state of SAM are excited to their corresponding antibonding molecular orbitals (σ^* or π^*) as a result of the

interaction with incoming x-rays; the energy required for this excitation to occur is ≈290 eV for carbon K-shell. [66] Bonding differences are detectable as well; for instance, a C-H 1s→σ* transition occurs at ≈287 eV while a C-C 1s→σ* transition takes place at ≈294 eV [50]. As shown in the scheme in Figure 7.5, orientation information is obtained from the angular dependence of the antibonding orbital to the polarization vector of the x-ray beam.

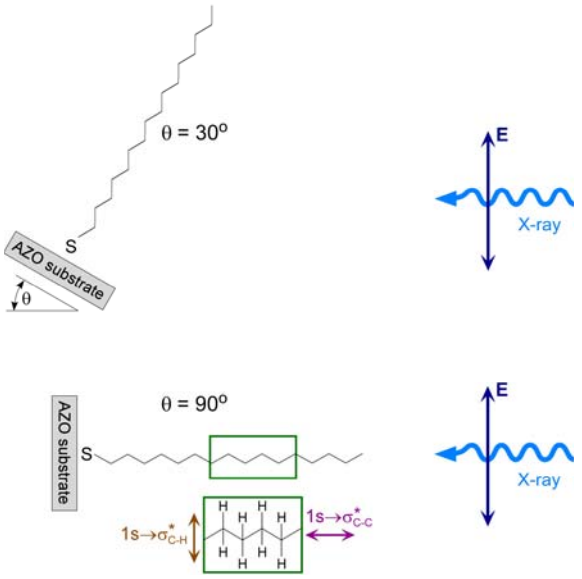

Figure 7.5. Illustration of the relationship between the electric vector of the x-ray beam and the monolayer orientation on the AZO thin film. The sample geometry is depicted with an incident photon angle of 30 and 90 degrees, respectively. A) The 30° geometry is shown. B) The 90° geometry is shown. The orientation of the antibonding orbitals corresponding to the C-H and C-C bonds is shown in the inset

For a well-ordered SAM, selective excitation of bonds occurs, with those bonds aligned to the electric vector of the x-ray beam displaying the highest intensity while those perpendicular to the beam having the lowest intensity. As the cartoon in Figure 5 depicts, for a well-ordered hydrocarbon backbone, the C-H sigma bond is perpendicular to the C-C bond and thus the transition of 1s→σ* for each of the bonds is inversely related. As the intensity of the C-H bond increases, the C-C bond decreases; the process reverses once the incident

angle of the x-ray beam changes from glancing to normal incidence as shown in the Figure 7.5.

These NEXAFS spectra were collected at θ ranging from 30 to 90^{o} in 10^{o} increments, where θ is the angle of incidence between the sample normal and the electric vector of the x-ray beam. The PEY NEXAFS spectra were normalized by setting the pre-edge and post-edge signal to 0 and 1, respectively, as described previously. [67] Figures 6A and B reveal the carbon K-edge partial electron yield (PEY) near-edge fine structure (NEXAFS) spectra collected from HDT and ODT SAM samples, respectively, deposited on 2% aluminum-doped zinc oxide thin films.

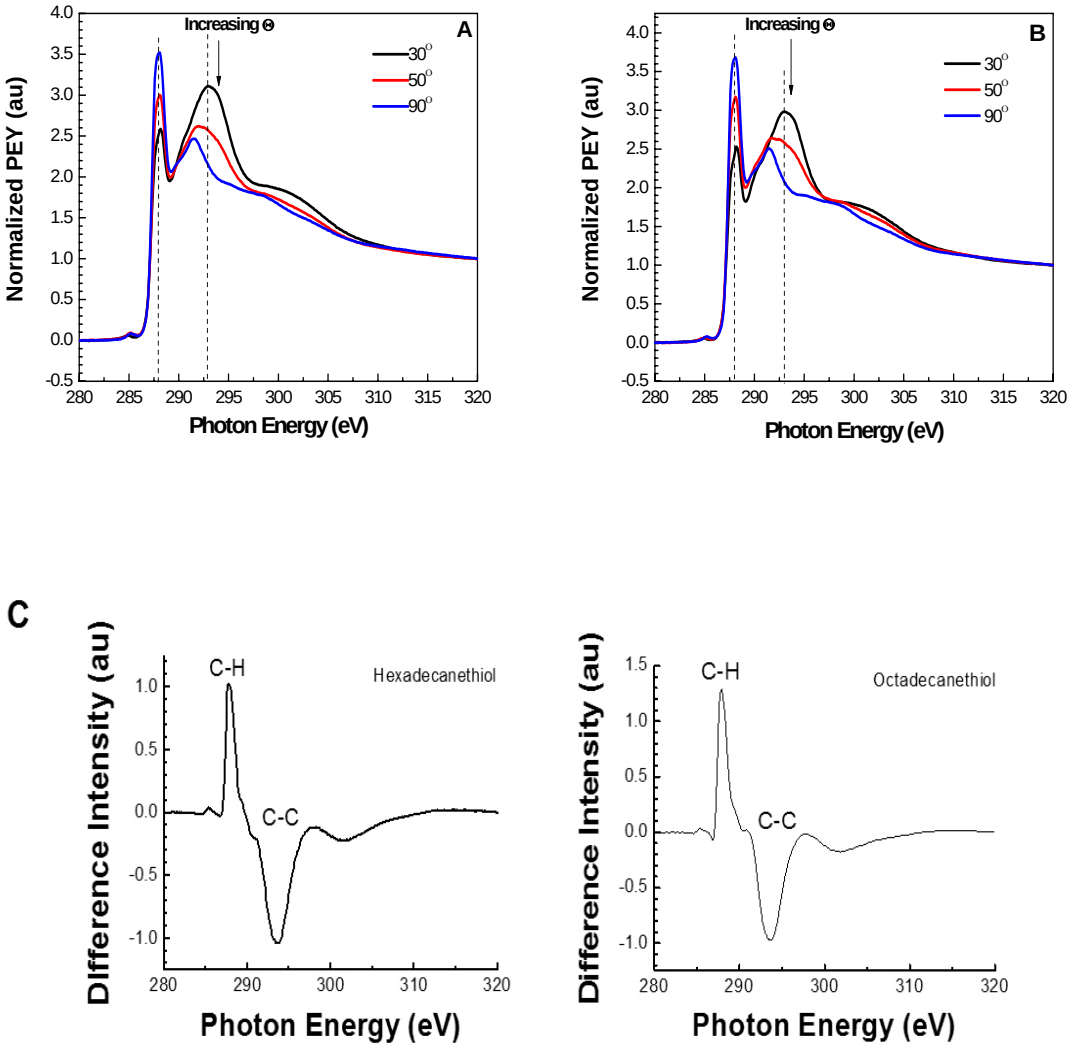

Figure 7.6 A,B,C. Normalized carbon K-edge PEY NEXAFS spectra of a monolayer of 1-hexadecanethiol (A) and 1-octadeanethiol (B) on AZO collected at θ from 30 to 90 degrees in increments of 10 degrees where θ is the incident angle between the sample and X-ray beam. The vertical dashed lines denote the $1\sigma \rightarrow \sigma^*$ transition for the C-H and C-C at 288 eV and 291 eV, respectively. Figure 6C represents the difference spectrum obtained by subtracting the intensity of the 30 degree angle PEY NEXAFS spectrum from the PEY NEXAFS spectrum taken at 90 degrees.

The vertical dashed lines in Figures 6A and B correspond to the positions of the two primary peaks observed in the spectra. A peak observed at ≈288.2 eV is attributed to the $1s \rightarrow \sigma^*$

transition into the Rydberg states of the C-H bond in a saturated alkane chain. [68] A second peak located at ≈291-293 eV is ascribed to the 1s→σ* excitation of the C-C bond in a saturated alkane chain [69].

The orientation of the SAM is inferred from the angle dependence of these bonds. As θ increases, the intensity of the peak corresponding to the 1s→σ* C-H transition increases while the intensity of the peak indicative of the 1s→σ* C-C transition decreases. This is indicative that both of the thiolated SAMs are well-organized. [50].

The difference in the molecular ordering between the HDT and ODT SAMs is not considerable as shown by the NEXAFS difference spectra (calculated from the subtraction of the $\theta=30^{o}$ spectra from the $\theta=90^{o}$) shown in Figures 7.6C.

The magnitude of the difference intensity reveals a qualitative measure of ordering in the two SAMs. The greater the peak height of the C-H and C-C peaks on the difference intensity scale, the more closely are the SAM molecules oriented towards the surface normal in the SAM; thus, relative to the HDT SAM, the molecules in ODT SAM appear to have a smaller tilt angle. The robustness of the films was examined by SAM reproduction as well as reanalysis of samples (data not shown). Both the HDT and the ODT were exceptionally reproducible, regardless of humidity or environmental temperature. Additionally, samples analyzed 3 months post deposition showed nearly identical NEXAFS spectra (data not shown). Thus, this evidence reveals long chain thiolated SAMs on AZO thin films form both well-organized and robust SAMs.

Figure 7.7A,B relates the intensity of the NEXAFS spectra for the two specific peaks of C-H (≈288 eV, square symbol) and C-C (≈294 eV, triangle symbol) to the $\sin^2\theta$.

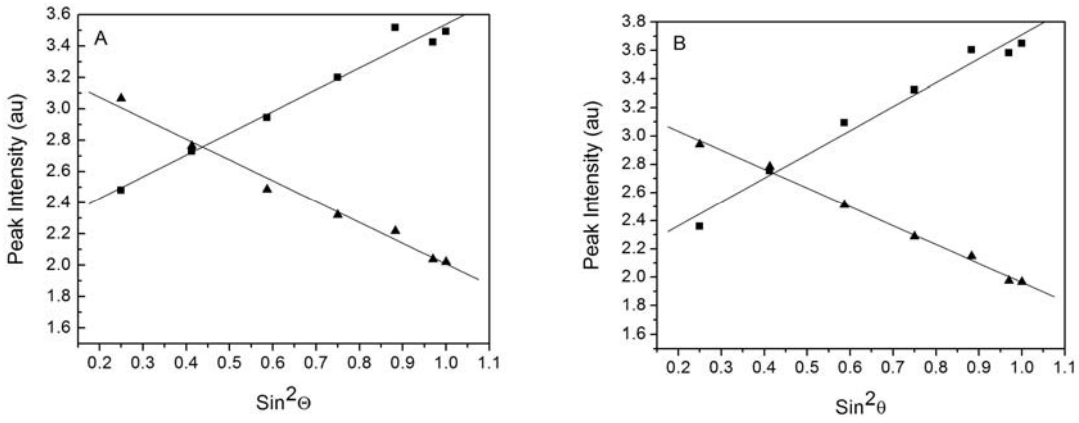

Figure 7.7A, B. Normalized carbon K-edge PEY NEXAFS spectra as a function of $\sin^2\theta$ for $1s\rightarrow\sigma^*_{C\text{-}C}$ (triangles) and $1s\rightarrow\sigma^*_{C\text{-}H}$ (squares). The linear fits are meant to guide the eye.

This type of plot is another qualitative indicator of the ordering of the thiolated monolayers. A steady decrease in the intensity of the C-C peaks in relation to the steady increase shown in the intensity of the C-H peaks is indicative of ordering of the SAMs. More detailed information about chain tilt can be obtained by performing an analysis using the method described previously by Outka et. al. [51], detailed in the *Materials and Methods* section. The tilt angle values were determined from a comparison of the experimental and calculated intensities of the C-H and C-C peak at the different incident angles. Table 1 details the tilt angle values defined as the angle between the surface normal and the alkyl chain in the SAM. As shown, the average tilt angle was ≈40 degrees for HDT and ≈35 degrees for ODT.

Table 7.1. Calculated tilt angles from the NEXAFS spectra for the two different self-assembled monolayers deposited onto the AZO thin films.

Monolayer	Bond	Tilt Angle (deg)[a)]
Hexadecanethiol	C-H	50
	C-C	30
	Average Tilt	**40 ± 10**
Octadecanethiol	C-H	45
	C-C	25
	Average Tilt	**35 ± 10**

a) The tilt angle is defined as the angle formed between the alkyl chain of the SAMs and the normal to the ITO surface.

These values are in close agreement with the reported tilt angles of 35 degrees for thiolates deposited on clean gold surfaces [70], which is indicative of well organized thiolated SAMs formed on AZO similar to those found on gold. The individual tilt angles of each of the bonds were ≈10 degrees different. We attribute this behavior to the approximations invoked in the "titled chain" model. The slight difference between the tilt angle values for the different types of SAMs indicates the SAMs formed differ structurally. Thus, although both long chain thiolates form well-organized and highly ordered SAMs on AZO, the molecular organization in the two SAMs is different.

Furthermore, these experimental results were complemented by density functional theory (DFT) calculations. Tables 2 and 3 reveal the results of the density functional theory (DFT) calculation of the charge carrier concentration and the plasma frequency of AZO and oxygen-depleted AZO.

Table 7.2. Charge carrier densities for various compositions of aluminum doped and oxygen depleted ZnO. The calculation used a unit cell of $Zn_{32}O_{32}$.

	No Al	**1 Al**	**2 Al**	**3Al**
All O	3.79E-07	2.59E+02	4.95E+07	3.40E+11
-1 O	4.92E+02	1.78E+05	2.26E+09	3.12E+15
-2 O	1.68E+12	5.26E+08	2.53E+12	2.50E+16
-3 O	1.87E+04	2.12E+09	4.52E+11	1.65E+15
-4 O	1.45E+13	5.67E+08	1.25E+13	2.01E+15
-5 O	9.50E+17	3.70E+11	3.06E+14	2.40E+16
-6 O	4.68E+13	2.45E+15	7.00E+18	7.01E+20
-7 O	5.97E+14	4.47E+15	2.35E+17	6.41E+19
-8 O	5.25E+15	8.83E+15	4.90E+17	5.25E+15

As shown in Table 2, in general increasing oxygen depletion results in increased charge carrier concentrations indicative that the depletion produces vacancies available for conduction electrons. The table also reveals that the amount of aluminum doping is an additional factor in the charge carrier density with another trend of increasing dopant levels leading to increasing charge carrier density. As stated earlier, this is due to the fact that the increased aluminum charge donates more conduction electrons to the substrate than a corresponding zinc atom. Experimentally, Hall effect measurements determined the charge carrier concentration value to be 4.7 x 10^{20} electrons/cm^3.for a 2% aluminum-doped zinc oxide thin film. This in reasonable agreement with the calculated oxygen deficient for the 3.1% doped (2 Al) samples as shown in Table 2. The calculated plasma frequencies are given in Table 3.

Table 7.3. Calculated plasma frequencies (ω_p) for various compositions of aluminum doped and oxygen depleted ZnO. The calculation used a unit cell of $Zn_{32}O_{32}$.

	No Al	**1 Al**	**2 Al**	**3Al**
All O	3.42E-10	8.93E-06	3.90E-03	3.23E-01
-1 O	1.23E-05	2.34E-04	2.64E-02	3.10E+01
-2 O	7.19E-01	1.27E-02	8.82E-01	8.76E+01
-3 O	7.59E-05	2.55E-02	3.73E-01	2.25E+01
-4 O	2.11E+00	1.32E-02	1.96E+00	2.49E+01
-5 O	5.41E+02	3.37E-01	9.71E+00	8.59E+01
-6 O	3.80E+00	2.75E+01	1.47E+03	1.47E+04
-7 O	1.35E+01	3.71E+01	2.69E+02	4.44E+03
-8 O	4.02E+01	5.21E+01	3.88E+02	4.02E+01

As observed in previous calculations for IrO_2 and $CdSn_2O_4$, [47, 62] the resulting plasma frequencies reveal a strong dependence on the oxygen depletion level in which increased oxygen depletion levels lead to higher energy plasma frequencies. The dependence on dopant level is not as strong although a trend of increasing dopant level shifting the plasma frequency to higher energy is apparent. The DFT calculated plasma frequencies exhibit a wide variation but in general, the oxygen deficient doped samples show a closer agreement to the Drude-model plasma frequency of 14,600 cm^{-1} or the experimental reflectance change at 8,500 cm^{-1}.

DFT investigations of the strength of the zinc sulfur bond provide further insight into the experimental observations of high surface density and order of alkane thiolates SAMS. Figure 8 shows the DFT calculated potential energy curve for a ZnO substrate for the binding of an ethane thiolate SAM using periodic boundary conditions. The ethane thiolates molecules were placed in a $(\sqrt{3} \times 3)R30^o$ lattice superposed on the orthorhombic unit cell of

the ZnO substrate. As shown in the figure, the maximum binding energy is reached at an atomic distance of 2.2 Å at which point a binding energy of nearly 430 kJ/mol is calculated. For comparison, a comparable ethane alkane thiol layer on gold (111) has been calculated to have a maximum binding energy of ~160 kJ/mol [71] while a hexadecanethiol monolayer on ITO was estimated to be ~30 kJ/mol. [20] As stated above, the thiolated monolayers appear both robust and ordered and thus, this calculation provides a possible explanation for some of these observed properties.

7.5. Conclusions

This present study explores the capacity of aluminum-doped zinc oxide, to form well-ordered, reproducible, and robust thiolates SAMs as well as the optical response of thin films of AZO.. The three methods employed, reflectance FTIR spectroscopy, XPS, and NEXAFS spectroscopy, provided complementary information on the formation of adlayers on AZO. The data substantiate that AZO. The data provide a comparison with similar measurements on ITO.[20, 64]. The order and stability of thiolates adlayers on AZO compares favorably to ITO. Optical properties studied with the FTIR suggests similar optical properties of AZO and ITO, although the CH stretching mode associated with the adlayer in AZO was present up to a year post-deposition suggesting a much longer lifetime than those typically observed with ITO. XPS spectra of both ITO and AZO confirmed the presence of a thiolated adlayer through the appearance of a sulfur peak. On the other hand, NEXAFS spectroscopy confirmed the existence of the adlayer and also provided information about the organization and molecular tilt angle of the constructed SAM on the surface. The ordering and tilt angle of the thiolated monolayers on AZO determined from the NEXAFS data are similar to those reported for gold. [70] This illustrates the diversity of conducting metal oxides with substrates

ranging from those, such as AZO, exhibiting properties similar to metals to those whose properties more closely resembles semi-conductors, such as ITO. [72]

A possible explanation for this diversity is the strength of the substrate-sulfur bond which attaches the thiolated adlayer to the surface. The zinc-sulfur bond in zinc sulfide is extremely stable and naturally occuring while the indium-sulfur bond in indium sulfide is not very stable. [73, 74] Natural zinc sulfide is prepared by the replacement of a divalent metal with a trivalent metal while indium sulfide is not a naturally occurring compound (Lu, 2005 #103}. In fact, the strength of the interaction of the zinc oxide and sulfur bond is such that immobilized ZnO has been used to scavenge hydrogen sulfide at concentrations ranging from 50 ppmv (parts per million by volume) to 20,000 ppmv [73]. Hydrothermal vent worms have evolved to use zinc ions to chealate the sulfide ions from hydrogen sulfide in these harsh environments [74]. On the other hand, indium sulfide only needs an oxygen annealing atmosphere to convert to indium oxide, which suggests it is innately unstable [75] [76]. In addition, experimental evidence has shown that the ITO sulfur bond is extremely dependent on film thickness, and annealing conditions with complicated chemical deposition conditions required for film reproducibility. [64] DFT calculations of potential energy curve for the Zn-S bond substantiated that the bond strength is not only stronger than ITO-S but also gold-S. Thus, the stability of the well-ordered SAM's formed on the AZO implies a possible biosensing aspect to this CMO.

Acknowledgements

The authors would like to thank Accelrys, Inc. for access to the DFT computing program DMol3. The NEXAFS experiments were performed at the National Synchrotron Light Source at Brookhaven National Laboratory which is funded by the US Department of Energy, Division of Materials Sciences and Division of Chemical Sciences. The AZO thin films were graciously provided by the National Center for Photovoltaics.at the National Renewable Energy laboratory.

7.6. References

1. Boozer, C.; Chen, S. F.; Jiang, S. Y., Controlling DNA orientation on mixed ssDNA/OEG SAMs. *Langmuir* **2006,** 22, (10), 4694-4698.

2. Hoque, E.; DeRose, J. A.; Hoffmann, P.; Mathieu, H. J.; Bhushan, B.; Cichomski, M., Phosphonate self-assembled monolayers on aluminum surfaces. *Journal of Chemical Physics* **2006,** 124, (17).

3. Lee, S.; Park, J.; Ragan, R.; Kim, S.; Lee, Z.; Lim, D. K.; Ohlberg, D. A. A.; Williams, R. S., Self-assembled monolayers on Pt(111): Molecular packing structure and strain effects observed by scanning tunneling microscopy. *Journal of the American Chemical Society* **2006,** 128, (17), 5745-5750.

4. Schreiber, F., Structure and growth of self-assembling monolayers. *Progress in Surface Science* **2000,** 65, (5-8), 151-256.

5. Ulman, A., Formation and structure of self-assembled monolayers. *Chemical Reviews* **1996,** 96, (4), 1533-1554.

6. Ulman, A., *Thin Films: Self-assembled Monolayers of Thiols (Thin Films).* Academic Press: 1998.

7. Kitagawa, K.; Morita, T.; Kimura, S., Observation of single helical peptide molecule incorporated into alkanethiol self-assembled monolayer on gold by scanning tunneling microscopy. *Journal of Physical Chemistry B* **2004,** 108, (39), 15090-15095.

8. Liu, Y. J.; Kalambur, A. T.; Rabolt, J. F.; Chase, D. B., Time-resolved IR studies of monolayer self-assembly on a gold substrate using planar array infrared (PA-IR) spectroscopy. *Langmuir* **2004,** 20, (3), 816-822.

9. Kontturi, E.; Thune, P. C.; Niemantsverdriet, J. W., Cellulose model surfaces-simplified preparation by spin coating and characterization by X-ray photoelectron spectroscopy, infrared spectroscopy, and atomic force microscopy. *Langmuir* **2003,** 19, (14), 5735-5741.

10. Yuge, R.; Miyazaki, A.; Enoki, T.; Tamada, K.; Nakamura, F.; Hara, M., Fabrication of TTF-TCNQ charge-transfer complex self-assembled monolayers: Comparison between the coadsorption method and the layer-by-layer adsorption method. *Journal of Physical Chemistry B* **2002,** 106, (27), 6894-6901.

11. Han, S. W.; Joo, S. W.; Ha, T. H.; Kim, Y.; Kim, K., Adsorption characteristics of anthraquinone-2-carboxylic acid on gold. *Journal of Physical Chemistry B* **2000,** 104, (50), 11987-11995.

12. Corn, R. M.; Hurtt, G.; Smith, E.; Nelson, B.; Grimsrud, T., Surface plasmon resonance imaging measurements of DNA, RNA, and protein adsorption onto DNA monolayer arrays. *Abstracts of Papers of the American Chemical Society* **2000,** 220, U272-U272.

13. Davis, F.; Higson, S. P. J., Structured thin films as functional components within biosensors. *Biosensors & Bioelectronics* **2005**, 1-20.

14. Bain, C. D.; Biebuyck, H. A.; Whitesides, G. M., Comparison of Self-Assembled Monolayers on Gold - Coadsorption of Thiols and Disulfides. *Langmuir* **1989**, 723-727.

15. Bain, C. D.; Troughton, E. B.; Tao, Y. T.; Evall, J.; Whitesides, G. M.; Nuzzo, R. G., Formation of Monolayer Films by the Spontaneous Assembly of Organic Thiols from Solution onto Gold. *Journal of the American Chemical Society* **1989,** 111, (1), 321-335.

16. Nuzzo, R. G.; Zegarski, B. R.; Dubois, L. H., Fundamental-Studies of the Chemisorption of Adsorbates on Well-Defined Organic-Surfaces. *Journal of the Electrochemical Society* **1987**, C110-C110.

17. Wu, X.; Coutts, T. J.; Mulligan, W. P., Properties of transparent conducting oxides formed from CdO and ZnO alloyed with SnO2 and In2O3. *Journal of Vacuum Science & Technology a-Vacuum Surfaces and Films* **1997,** 15, (3), 1057-1062.

18. Suh, K. J.; Okada, H.; Wakahara, A.; Kim, H. J.; Chang, H. J.; Yoshida, A., Transparent conducting ZnO films on polymer substrates by pulsed laser deposition. In *Advances in Nondestructive Evaluation, Pt 1-3*, 2004; Vol. 270-273, pp 878-883.

19. Bhaumik, S.; Barua, A. K., Growth and characterization of indium tin oxide films grown on polymer substrates by DC magnetron sputtering. *Japanese Journal of Applied Physics Part 1-Regular Papers Short Notes & Review Papers* **2003,** 42, (6A), 3619-3620.

20. Brewer, S. H.; Brown, D. A.; Franzen, S., Formation of thiolate and phosphonate adlayers on indium-tin oxide: Optical and electronic characterization. *Langmuir* **2002,** 18, (18), 6857-6865.

21. Lowe, L. B.; Brewer, S. H.; Kramer, S.; Fuierer, R. R.; Qian, G. G.; Agbasi-Porter, C. O.; Moses, S.; Franzen, S.; Feldheim, D. L., Laser-induced temperature jump electrochemistry on gold nanoparticle-coated electrodes. *Journal of the American Chemical Society* **2003**, 14258-14259.

22. Appleyard, S.; Day, S.; Pickford, R.; Willis, M., Organic electroluminescent devices: enhanced carrier injection using SAM derivatized ITO electrodes. *Journal of Material Chemistry* **2000,** 10, 169-173.

23. Brewer, S.; Franzen, S., **Optical properties of indium tin oxide and fluorine doped tin oxide surfaces: correlation of plasmon frequency, reflectivity and skin depth with conductivity**. *Jounal of Alloys and Compounds* **2001,** in press.

24. Zotti, G.; Schiavon, G.; Zecchin, S.; Berlin, A.; Pagani, G., Adsorption of Ferrocene Compounds on Indium-TIn-Oxide Electrodes. Enhancement of Adsorption by Decomposition of Ferrocenium Molecules by Oxygen. *Langmuir* **1998,** 14, 1728-1733.

25. Coutts, T. J., A Review of and Impressions from the 3rd European-Communities Conference on Photo-Voltaic Solar-Energy, Cannes, October 27-31, 1980. *Solar Cells* **1981,** 3, (4), 375-386.

26. Ginley, D.; Roy, B.; Ode, A.; Warmsingh, C.; Yoshida, Y.; Parilla, P.; Teplin, C.; Kaydanova, T.; Miedaner, A.; Curtis, C.; Martinson, A.; Coutts, T.; Readey, D.; Hosono, H.; Perkins, J., Non-vacuum and PLD growth of next generation TCO materials. *Thin Solid Films* **2003,** 445, (2), 193-198.

27. Major, S.; Chopra, K. L., Indium-Doped Zinc-Oxide Films as Transparent Electrodes for Solar-Cells. *Solar Energy Materials* **1988,** 17, (5), 319-327.

28. Jeong, W. J.; Park, G. C., Electrical and optical properties of ZnO thin film as a function of deposition parameters. *Solar Energy Materials and Solar Cells* **2001,** 65, (1-4), 37-45.

29. Jeong, W. J.; Kim, S. K.; Park, G. C., Preparation and characteristic of ZnO thin film with high and low resistivity for an application of solar cell. *Thin Solid Films* **2006,** 506, 180-183.

30. Kang, D. J.; Kim, J. S.; Jeong, S. W.; Roh, Y.; Jeong, S. H.; Boo, J. H., Structural and electrical characteristics of RF magnetron sputtered ZnO films. *Thin Solid Films* **2005,** 475, (1-2), 160-165.

31. Nunes, P.; Fortunato, E.; Martins, R., Influence of the post-treatment on the properties of ZnO thin films. *Thin Solid Films* **2001,** 383, (1-2), 277-280.

32. Nikitin, S. E.; Nikolaev, Y. A.; Polushina, I. K.; Rud, V. Y.; Rud, Y. V.; Terukov, E. I., Photoelectric phenomena in ZnO : Al-p-Si heterostructures. *Semiconductors* **2003,** 37, (11), 1291-1295.

33. Song, D. Y.; Aberle, A. G.; Xia, J., Optimisation of ZnO : Al films by change of sputter gas pressure for solar cell application. *Applied Surface Science* **2002,** 195, (1-4), 291-296.

34. Jeong, M. C.; Oh, B. Y.; Nam, O. H.; Kim, T.; Myoung, J. M., Three-dimensional ZnO hybrid nanostructures for oxygen sensing application. *Nanotechnology* **2006,** 17, (2), 526-530.

35. Jeong, J. S.; Lee, J. Y.; Cho, J. H.; Suh, H. J.; Lee, C. J., Single-crystalline ZnO microtubes formed by coalescence of ZnO nanowires using a simple metal-vapor deposition method. *Chemistry of Materials* **2005,** 17, (10), 2752-2756.

36. Suh, H. W.; Kim, G. Y.; Jung, Y. S.; Choi, W. K.; Byun, D., Growth and properties of ZnO nanoblade and nanoflower prepared by ultrasonic pyrolysis. *Journal of Applied Physics* **2005,** 97, (4).

37. Chang, J. F.; Lin, W. C.; Hon, M. H., Effects of post-annealing on the structure and properties of Al-doped zinc oxide films. *Applied Surface Science* **2001,** 183, (1-2), 18-25.

38. Chang, J. F.; Hon, M. H., The effect of deposition temperature on the properties of Al-doped zinc oxide thin films. *Thin Solid Films* **2001,** 386, (1), 79-86.

39. El Hichou, A.; Addou, M.; Bougrine, A.; Dounia, R.; Ebothe, J.; Troyon, M.; Amrani, M., Cathodoluminescence properties of undoped and Al-doped ZnO thin films deposited on glass substrate by spray pyrolysis. *Materials Chemistry and Physics* **2004,** 83, (1), 43-47.

40. El Hichou, A.; Addou, M.; Ebothe, J.; Troyon, M., Influence of deposition temperature (T-s), air flow rate (f) and precursors on cathodoluminescence properties of ZnO thin films prepared by spray pyrolysis. *Journal of Luminescence* **2005,** 113, (3-4), 183-190.

41. Paul, G. K.; Bandyopadhyay, S.; Sen, S. K.; Sen, S., Structural, optical and electrical studies on sol-gel deposited Zr doped ZnO films. *Materials Chemistry and Physics* **2003,** 79, (1), 71-75.

42. Das, R.; Ray, S., Zinc oxide - a transparent, conducting IR-reflector prepared by rf-magnetron sputtering. *Journal of Physics D-Applied Physics* **2003,** 36, (2), 152-155.

43. Kelly, P. J.; Hisek, J.; Zhou, Y.; Pilkington, R. D.; Arnell, R. D., Advanced coatings through pulsed magnetron sputtering. *Surface Engineering* **2004,** 20, (3), 157-162.

44. Hong, R. J.; Helming, K.; Jiang, X.; Szyszka, B., Texture analysis of Al-doped ZnO thin films prepared by in-line reactive MF magnetron sputtering. *Applied Surface Science* **2004,** 226, (4), 378-386.

45. Hong, R. J.; Jiang, X.; Szyszka, B.; Sittinger, V.; Xu, S. H.; Werner, W.; Heide, G., Comparison of the ZnO : Al films deposited in static and dynamic modes by reactive mid-frequency magnetron sputtering (vol 253, pg 117, 2003). *Journal of Crystal Growth* **2004,** 260, (3-4), 606-606.

46. Czternastek, H., ZnO thin films prepared by high pressure magnetron sputtering. *Opto-Electronics Review* **2004,** 12, (1), 49-52.

47. Rhodes, C. L. W., S.; Maria, J.P.; Losego, M.; Leonard, D.N.; Laughlin, B.; Duscher, G.; Franzen, S., Surface Plasmon Resonance in Conducting Metal Oxides. *Journal of Applied Physics* **Accepted**.

48. Tominaga, M.; Hirata, N.; Taniguchi, I., UV-ozone dry-cleaning process for indium oxide electrodes for protein electrochemistry. *Electrochemistry Communications* **2005,** 7, (12), 1423-1428.

49. Furukawa, M.; Fujisawa, H.; Katano, S.; Ogasawara, H.; Kim, Y.; Komeda, T.; Nilsson, A.; Kawai, M., Geometrical characterization of pyrimidine base molecules adsorbed on Cu(110) surfaces: XPS and NEXAFS studies. *Surface Science* **2003,** 532, 261-266.

50. Stohr, J., *NEXAFS Spectroscopy*. Springer: Berlin, 1992.

51. Outka, D. A.; Stohr, J.; Rabe, J. P.; Swalen, J. D., The Orientation of Langmuir-Blodgett Monolayers Using Nexafs. *Journal of Chemical Physics* **1988,** 88, (6), 4076-4087.

52. Stohr, J.; Outka, D. A., Determination of Molecular Orientations on Surfaces from the Angular-Dependence of near-Edge X-Ray-Absorption Fine-Structure Spectra. *Physical Review B* **1987,** 36, (15), 7891-7905.

53. Delley, B., An all-electron numerical-method for solving the local density functional for polyatomic molecules. *Journal of Chemical Physics* **1990,** 92, (1), 508-517.

54. Perdew, J. P.; Chevary, J. A.; Vosko, S. H.; Jackson, K. A.; Pederson, M. R.; Singh, D. J.; Fiolhais, C., Atoms, molecules, solids and surfaces - Applications of the generalized gradient approximation for exchange and correlation. *Phys. Rev. B* **1992,** 46, 6671-6687.

55. Mermin, D., *Phys. Rev. A* **1965,** 137, 1441-1443.

56. Wooten, F., *Optical Properties of Solids*. Academic Press, Inc.: San Diego, 1972.

57. *Semiconductors-Basic Data*. 2nd revised edition ed.; Springer: Berlin, 1996.

58. Hansen, W., Electric Fields Produced by the Propagation of Plane Coherent Electromagnetic Radiation in a Stratified Medium. *Journal of the Optical Society of America* **1968,** 58, (3), 380-390.

59. Qiao, Z. H.; Agashe, C.; Mergel, D., Dielectric modeling of transmittance spectra of thin ZnO : Al films. *Thin Solid Films* **2006,** 496, (2), 520-525.

60. Laibinis, P. E.; Whitesides, G. M.; Allara, D. L.; Tao, Y. T.; Parikh, A. N.; Nuzzo, R. G., Comparison of the Structures and Wetting Properties of Self-Assembled Monolayers of Normal-Alkanethiols on the Coinage Metal-Surfaces, Cu, Ag, Au. *Journal of the American Chemical Society* **1991,** 113, (19), 7152-7167.

61. Bain, C. D.; Evall, J.; Whitesides, G. M., Formation of Monolayers by the Coadsorption of Thiols on Gold - Variation in the Head Group, Tail Group, and Solvent. *Journal of the American Chemical Society* **1989**, 7155-7164.

62. Brewer, S. H.; Wicaksana, D.; Maria, J. P.; Kingon, A. I.; Franzen, S., Investigation of the electrical and optical properties of iridium oxide by reflectance FTIR spectroscopy and density functional theory calculations. *Chemical Physics* **2005,** 313, (1-3), 25-31.

63. Inman, C. E.; Reed, S. M.; Hutchison, J. E., In situ deprotection and assembly of S-tritylalkanethiols on gold yields monolayers comparable to those prepared directly from alkanethiols. *Langmuir* **2004,** 20, (21), 9144-9150.

64. Cerruti, M. R., C.;Efremenko, A.;Losego, M.;Maria, J.P.;Genzer, J.;Fischer, D.;Feldheim, D.;Franzen, S.; , Influence of Indium-Tin Oxide surface structure on the ordering and coverage of organosilane, carboxylic acid and thiol monolayers. *Submitted*.

65. Rhodes, C. L. B., S.H.; Folmer, J.; Li, X.; Coutts, T.J.; Franzen, S. , Investigation of an Hexadecanethiol Self-Assembled Monolayers on Cadmium Tin Oxide Thin Films. *Thin Solid Films* **submitted**.

66. Ade, H. U., S.G.; , *Chemical Applications of Synchrotron Radiation*. World Scientific Publishing: Singapore, 2002; Vol. 12, p 285-355.

67. Fischer, D.; Efimenko, K.; Bhat, R.; Sambasivan, S.; Genzer, J., Mapping Surface Chemistry and Molecular Orientation with Combinatorial Near-Edge X-Ray Absorption Fine Structure Spectroscopy. *Macromolecular Rapid Communications* **2004,** 25, 141-149.

68. Bagus, P. S.; Weiss, K.; Schertel, A.; Woll, C.; Braun, W.; Hellwig, C.; Jung, C., Identification of transitions into Rydberg states in the X-ray absorption spectra of condensed long-chain alkanes. *Chemical Physics Letters* **1996,** 248, (3-4), 129-135.

69. Stohr, J.; Outka, D. A.; Baberschke, K.; Arvanitis, D.; Horsley, J. A., Identification of C-H Resonances in the K-Shell Excitation-Spectra of Gas-Phase, Chemisorbed, and Polymeric Hydrocarbons. *Physical Review B* **1987,** 36, (5), 2976-2979.

70. Yan, C.; Golzhauser, A.; Grunze, M.; Woll, C., Formation of alkanethiolate self-assembled monolayers on oxidized gold surfaces. *Langmuir* **1999,** 15, (7), 2414-2419.

71. Franzen, S., Density functional calculation of a potential energy surface for alkane thiols on Au(111) as function of alkane chain length. *Chemical Physics Letters* **2003,** 381, (3-4), 315-321.

72. Brewer, S. H.; Franzen, S., Optical properties of indium tin oxide and fluorine-doped tin oxide surfaces: correlation of reflectivity, skin depth, and plasmon frequency with conductivity (vol 338, pg 73, 2002). *Journal of Alloys and Compounds* **2002,** 343, (1-2), 244-244.

73. Lu, Y.; Sathitsuksanoh, N.; Yang, H. Y.; Chang, B. K.; Queen, A. P.; Tatarchuk, B. J., Microfibrous entrapped ZnO-support sorbents for high contacting efficiency H2S removal from reformate streams in PEMFC applications. In *Microreactor Technology and Process Intensification*, 2005; Vol. 914, pp 406-422.

74. Flores, J. F.; Fisher, C. R.; Carney, S. L.; Green, B. N.; Freytag, J. K.; Schaeffer, S. W.; Royer, W. E., Sulfide binding is mediated by zinc ions discovered in the crystal structure of a

hydrothermal vent tubeworm hemoglobin. *Proceedings of the National Academy of Sciences of the United States of America* **2005,** 102, (8), 2713-2718.

75. Kale, S. S.; Mane, R. S.; Lokhande, C. D.; Nandi, K. C.; Han, S. H., A comparative photo-electrochemical study of compact In2O3/In2S3 multilayer thin films. *Materials Science and Engineering B-Solid State Materials for Advanced Technology* **2006,** 133, (1-3), 222-225.

76. Kumar, P. M. R.; John, T. T.; Kartha, C. S.; Vijayakumar, K. P.; Abe, T.; Kashiwaba, Y., Effects of thickness and post deposition annealing on the properties of evaporated In2S3 thin films. *Journal of Materials Science* **2006,** 41, (17), 5519-5525.

Chapter 8

Additional NEXAFS spectra of Aluminum-doped Zinc Oxide

8.1. Introduction

Aluminum-doped (2%) zinc oxide (AZO) thin films have been the focus of intense study for my dissertation research. The optical and electronic properties of this n-type semiconducting thin film were examined and frequently compared to indium tin oxide (ITO). It has been suggested that AZO could possibly provide a low cost, environmentally friendly alternative to ITO as detailed in chapter 7. As much of the SAM deposition and material properties of this substrate was discussed in this chapter for a subsequent publication, this chapter will deal solely with the SAM deposition not discussed previously. I am of the opinion that the following results do not display results sufficient for publication but rather extend our knowledge of this substrate for future studies.

8.2. Results

After the successful deposition of hexadecanethiol and octadecanethiol SAMs that were discussed previously, I began to examine other possible chemistries for surface attachment. The initial studies focused on the deposition of silanes and carboxylates for possible use in later DNA deposition studies. The recipes and deposition procedures for these substrates are given in chapter 2. Shown in Figure 8.1A,B below is the results for attempt of a trimethoxyaminopropyl silane SAM.

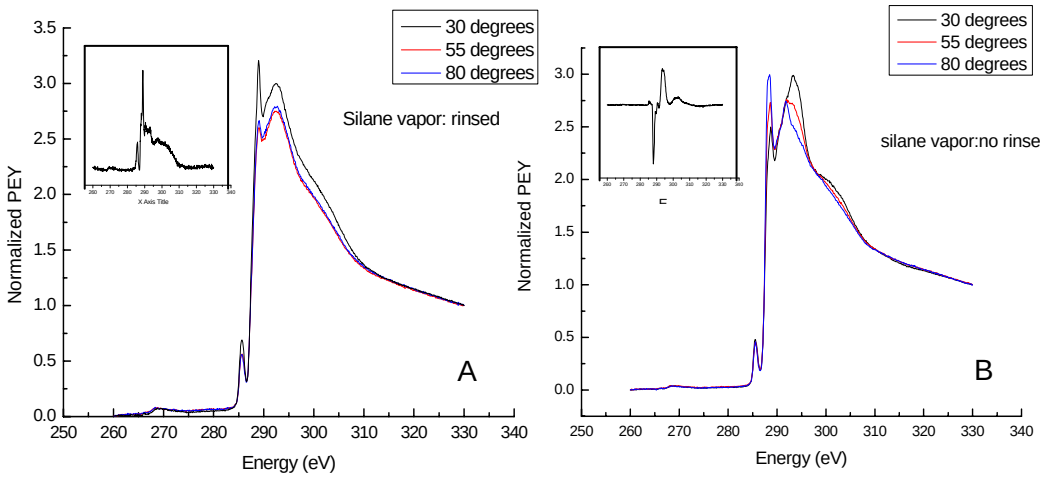

Figure 8.1A,B. Normalized carbon K edge PEY NEXAFS spectra of a monolayer of tirmethoxyaminopropyl silane (1% in absolute ethanol) deposited by vapor deposition on AZO collected at θ of 30, 55, 80 degrees where θ is the incident angle between the sample and X-ray beam. The inset is the difference spectra obtained from subtracting the intensity of the 30 degree angle spectrum from the spectrum taken at 80 degrees.

As shown in the insets of Figure 8.1, the first attempt of the vapor deposition of trimethoxyaminopropyl silane formed a nonordered adlayer on the AZO thin film that was rinsed, while an ordered adlayer was produced from a silane deposition that was not rinsed from the film. Further repetitions of this procedure did not produce similar results, all obtained were nonordered. Thus, it was suggested that more than likely the one ordered adlayer obtained from the nonrinsed silane AZO substrate was due to a multilayer rather than a nicely ordered SAM.

Figure 8.2 reveals a representative sample of an attempt for liquid deposition of the trimethoxyaminopropyl silane.

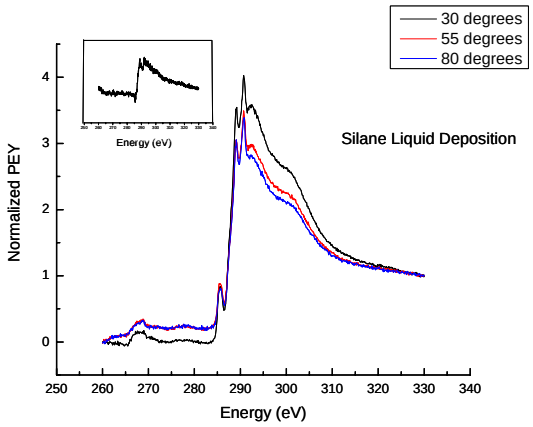

Figure 8.2. Normalized carbon K edge PEY NEXAFS spectra of a monolayer of tirmethoxyaminopropyl silane deposited by liquid submersion on AZO collected at θ of 30, 55, 80 degrees where θ is the incident angle between the sample and X-ray beam. The inset is the difference spectra obtained from subtracting the intensity of the 30 degree angle spectrum from the spectrum taken at 80 degrees.

Repetitions as well as several different deposition times were attempted, all with similar results of nonordered monolayers.

Next, another molecule, PEG (polyethylene glycol), was liquid deposited subsequent to a vapor-deposited silane SAM. It was hypothesized that the PEG adlayer could intercalate between the trimethoxyaminopropyl silane adlayers and thus, produce more ordered adlayers. Again, several repetitions of this were attempted, one of which is shown below in Figure 8.3.

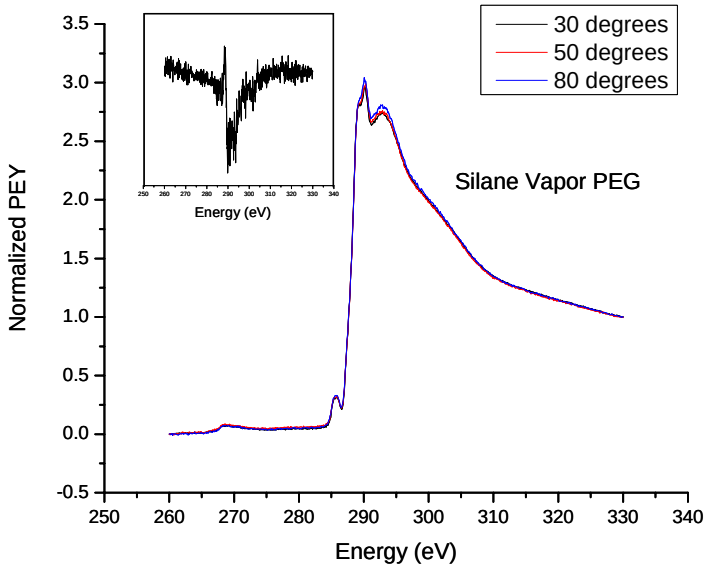

Figure 8.3. Normalized carbon K edge PEY NEXAFS spectra of a monolayer of tirmethoxyaminopropyl silane with PEG (polyethylene glycol) on AZO collected at θ of 30, 55, 80 degrees where θ is the incident angle between the sample and X-ray beam. The inset is the difference spectra obtained from subtracting the intensity of the 30 degree angle spectrum from the spectrum taken at 80 degrees.

As revealed in Figure 8.3, this molecule did not produce ordered adlayers; therefore, most likely it is positioned horizontally in a disordered array on the surface of the ITO and silane adlayer.

The subsequent steps involved the attempt at DNA deposition by the method of crosslinking the DNA with the silane monolayer as detailed in Chapter 1. The first attempt utilized an adlayer of vapor-deposited silane with the commercially available linker, sulfosuccinimidyl-4-(*N*-maleimidomethyl)cyclohexane-1-carboxylate (Sulfo-SMCC). As shown in figure 8.4, the addition of the crosslinker SSMCC does not produce the silane adlayer to become ordered, although as shown in the inset of

Figure 8.4B, a slightly more ordered system was apparent on the combined silane/PEG adlayer followed by the SSMCC deposition. This lack of ordering was the anticipated result as the SSMCC linker is short chain bulky molecule as described in chapter 1.

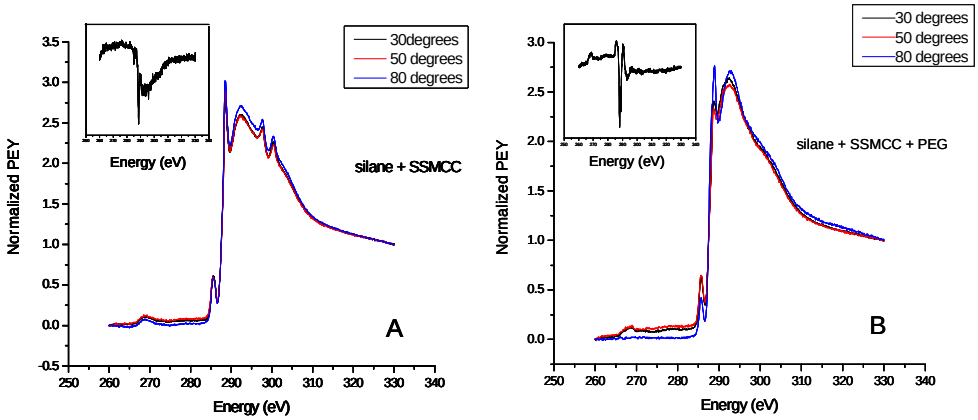

Figure 8.4 A,B. Normalized carbon K edge PEY NEXAFS spectra of a monolayer of tirmethoxyaminopropyl silane (vapor deposition) with the crosslinker SSMCC (A) and with a combined silane/PEG adlayer with subsequent SSMCC deposition (B) on AZO collected at θ of 30, 55, 80 degrees where θ is the incident angle between the sample and X-ray beam. The inset is the difference spectra obtained from subtracting the intensity of the 30 degree angle spectrum from the spectrum taken at 80 degrees.

For a more comprehensive study, the equivalent study was performed on ITO thin film with liquid-deposited silane adlayer with the PEG addition followed by deposition with the commercially available crosslinker SSMCC. Due to time constraints, it was chosen to only perform this deposition with the silane/PEG dual adlayer as this appeared to the more ordered system in the vapor-deposited silane trial above shown in figure 8.4. Figure 8.5 displays these results.

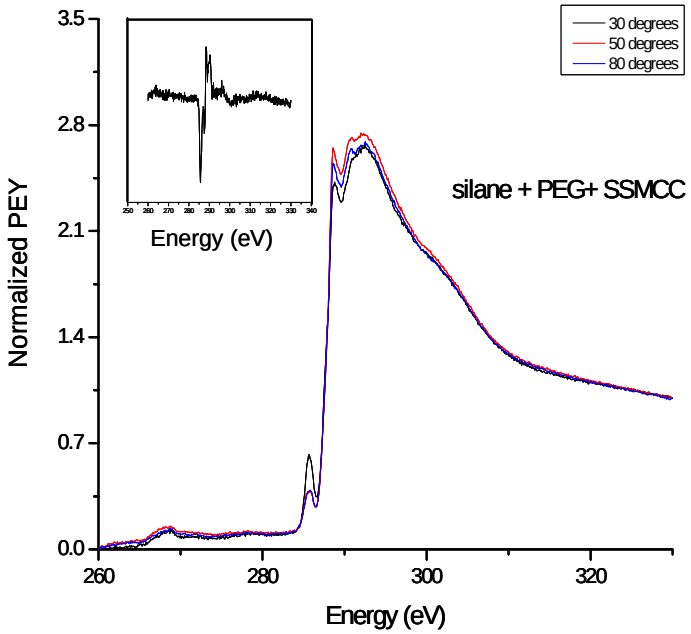

Figure 8.5. Normalized carbon K edge PEY NEXAFS spectra of a combined silane/PEG adlayer with subsequent SSMCC deposition on AZO collected at θ of 30, 55, 80 degrees where θ is the incident angle between the sample and X-ray beam. The inset is the difference spectra obtained from subtracting the intensity of the 30 degree angle spectrum from the spectrum taken at 80 degrees.

The AZO samples were prepared for nucleic acid deposition by the methodology described in Chapter 1, with a silane base crosslinked to ssDNA. These attempts were not very successful although they did provide insight into the deposition strategy as shown in Figure 8.6.

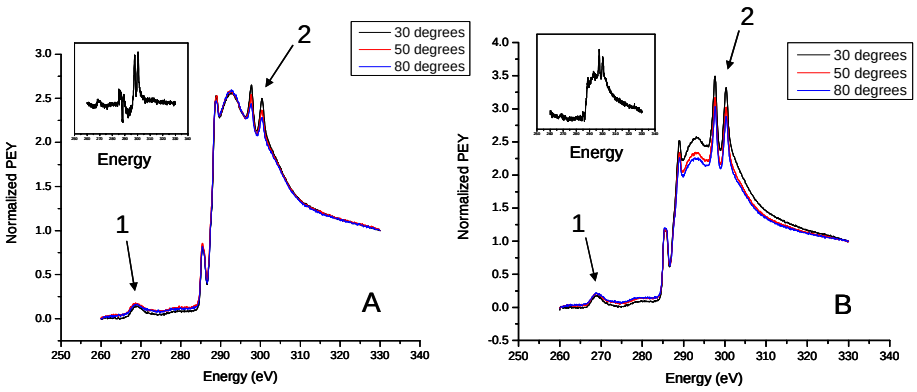

Figure 8.6 A,B. Normalized carbon K edge PEY NEXAFS spectra of a ssDNA deposition on AZO thin films with both a vapor deposited silane (A) and liquid deposited silane (B) collected at θ of 30, 55, 80 degrees where θ is the incident angle between the sample and X-ray beam. The inset is the difference spectra obtained from subtracting the intensity of the 30 degree angle spectrum from the spectrum taken at 80 degrees.

As shown in the above figure, neither of the attempted methodologies produced ordered monolayers, although both revealed spectral features to advance our understanding. At point 1 at ~268 eV, a distinct peak attributed to a oxygen harmonic is clearly visible, indicative of the presence of oxygen from either the nucleic acid base pairs of the oligmer or else insufficient coverage of the indium tin oxide film surface. The second point 2, reveals 2 peaks that are indicative of potassium. We reexamined our methodology and concluded that the potassium phosphate buffer is not rinsing away as assumed and may indeed be another contributing factor to the lack of success of this method.

The next set of surface chemistries attempted was carboxylates. The recipe for these liquid depositions was the standard 10 mM substrate into 100% absolute

ethanol. The dicarboxylatic acids examined were adipic acid (6 carbons) and dodecanedioic acid (12 carbons). Figure 8.7 details the results of this attempt at surface chemistry modification.

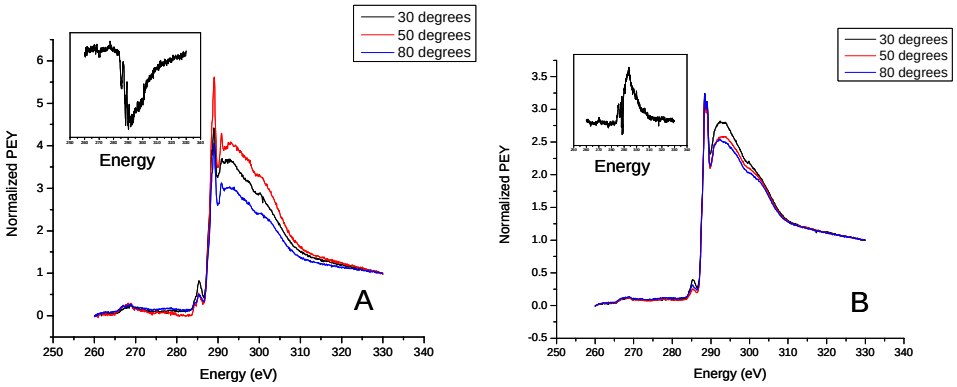

Figure 8.7 A,B. Normalized carbon K edge PEY NEXAFS spectra of a 10mM adipic acid deposition (A) and a dodecanioic acid deposition (B) on AZO thin films collected at θ of 30, 55, 90 degrees where θ is the incident angle between the sample and X-ray beam. The inset is the difference spectra obtained from subtracting the intensity of the 30 degree angle spectrum from the spectrum taken at 90 degrees.

From examination of Figure 8.7, it was concluded that the carboxylates we were attempting to use also did not produce ordered monolayers, possibly due to the bulkiness of the double carboxylic acids groups or even a bridged loop effect from these moieties.

A subsequent visit to Brookhaven National Laboratory allowed for further examination of the surface chemistries. We examined each of the previous trials and tried to account for possible factors contributing to the disordered adlayer produced. Our initial study focused on silanes with similar deposition techniques as mentioned before-a 1% solution in absolute ethanol. It was decided that longer chain silanes

may produce more ordered monolayers, thus, a 16-carbon silane (hexadecylsilane) and a 18-carbon silane (octyldecylsilane) were chosen as shown in Figure 8.8.

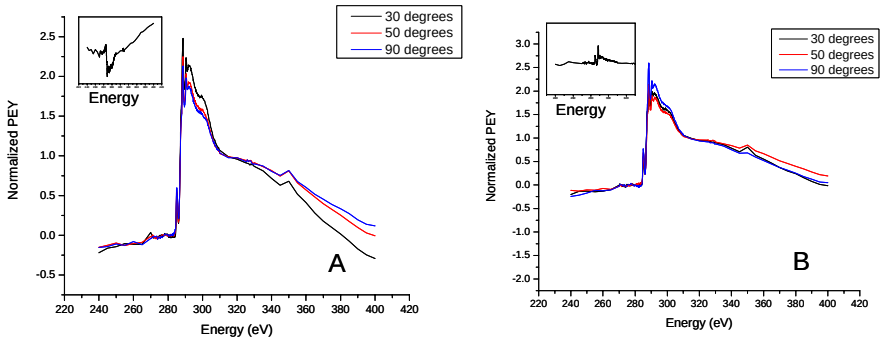

Figure 8.8 A,B. Normalized carbon K edge PEY NEXAFS spectra of a hexadecylsilane deposition (A) and a octyldecylsilane deposition (B) on AZO thin films collected at θ of 30, 55, 90 degrees where θ is the incident angle between the sample and X-ray beam. The inset is the difference spectra obtained from subtracting the intensity of the 30 degree angle spectrum from the spectrum taken at 90 degrees.

As shown in the above figure, ordered monolayers were not produced even with the long chain silane chains, thus, it was concluded that silane surface chemistry is not a viable route for AZO. In addition, the figure above reveals changes we made to the methodology during this trip. We extended the runs to 400 eV with only high resolution within the region of interest resulting in shorter run times while giving both a more informative range and allowing the instrument to equilibrate between runs.

Next other long chain carboxylates were examined. These molecules only contained one carboxylic acid, eliminating possible issues with the dicarboxylic moiety. The two examined were Stearic acid (C-18) and Palmitic acid (C-16). Initial studies focused on stearic acid as preliminary data with Indium Tin Oxide showed

promising results [1]. Results from a typical deposition on AZO are shown below in Figure 8.9.

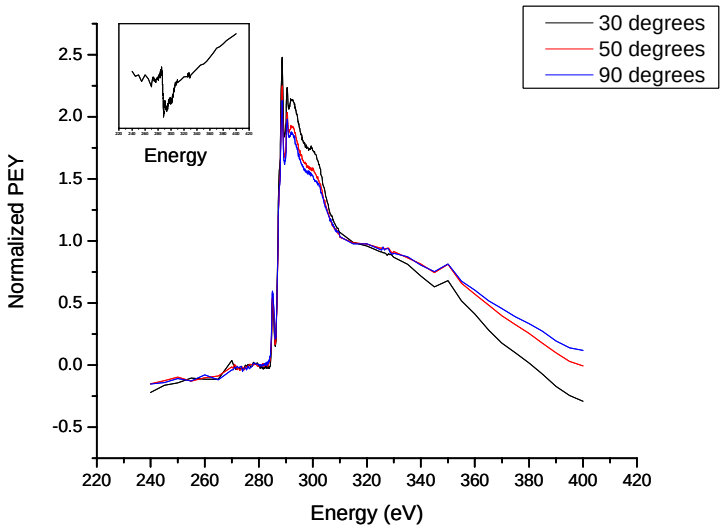

Figure 8.9. Normalized carbon K edge PEY NEXAFS spectra of a 10mM Stearic acid deposition on AZO thin films collected at θ of 30, 55, 90 degrees where θ is the incident angle between the sample and X-ray beam. The inset is the difference spectra obtained from subtracting the intensity of the 30 degree angle spectrum from the spectrum taken at 90 degrees.

All efforts with this substrate resulted in nonordered monolayers, thus, we changed substrates and attempted another carboxylate.

Palmitic acid deposition was the final trial with the aluminum-doped zinc oxide due to the lack of a suitable supplier. (To date, we still do not have a supplier and should consider that as a research route as well). Regardless of the shortage, we were able to perform 3 trials with the 10mM Palmitic acid. Two of the repetitions were shown below.

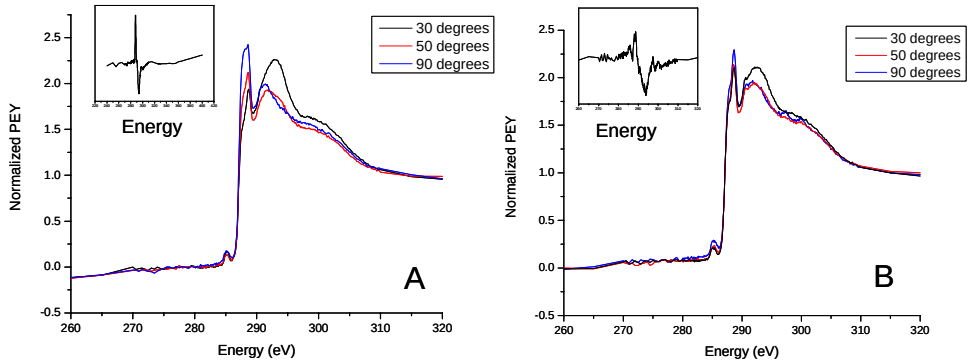

Figure 8.10 A,B. Normalized carbon K edge PEY NEXAFS spectra of two repetitions of a 10mM Stearic acid deposition (A and B) on AZO thin films collected at θ of 30, 55, 90 degrees where θ is the incident angle between the sample and X-ray beam. The inset is the difference spectra obtained from subtracting the intensity of the 30 degree angle spectrum from the spectrum taken at 90 degrees.

As shown in the figure above, the first trial (A) with Palmitic acid produced an ordered monolayer similar to those formed by hexa- and octadecanethiols. [2] The subsequent two additional trials revealed monolayers with less order although some is still present (B). Thus, it appears that carboxylate chemistry is a possibility with the AZO thin films, although further research is definitely required.

In conclusion, these results show the vast accessibility of AZO for SAM deposition and thus, necessitate the need for further examination. Unfortunately, up to this point, we do not have a readily accessible route for the production of this thin film as our previous collaborators are no longer involved in the development of the n-type AZO but rather the elusive p-type substrate. I personally believe that if another collaborative effort with the Material Science and Engineering department at NC

State could be achieved with the development of this substrate, then further studies should be performed.

8.3. References

1. Cerruti, M. R., C.;Efremenko, A.;Losego, M.;Maria, J.P.;Genzer, J.;Fischer, D.;Feldheim, D.;Franzen, S.; , Influence of Indium-Tin Oxide surface structure on the ordering and coverage of organosilane, carboxylic acid and thiol monolayers. *Submitted*.

2. Rhodes, C. L., Lappi, S. E., Fischer, D., Sambasivan, S., Genzer, J., Franzen, S., Characterization of Monolayer Formation on Aluminum-doped Zinc Oxide Thin Films. **In preparation**.

Chapter 9

Investigation of Hexadecanethiol Self-Assembled Monolayers on Cadmium Tin Oxide Thin Films

(In preparation for publication)

9.1. Abstract

This study reports the use of variable angle reflectance Fourier transform infrared spectroscopy and X-ray photoelectron spectroscopy to investigate the formation of a 1-hexadecanethiol adlayer on cadmium tin oxide (CTO) thin film surfaces. These adlayers appear to be robust, ordered monolayers. The optical and electronic properties of CTO thin films chemically vapor deposited onto glass substrates were also investigated. The reflectance of the CTO films was dependent upon the incident angle of the impinging radiation and revealed a reflectance decrease indicative of a plasma frequency in the mid-IR using p-polarized radiation. These studies were complemented by density functional theory calculations to determine the theoretical Fermi energy, charge carrier density, and plasma frequency for bulk CTO with a variety of oxygen deficiencies.

9.2. Introduction

Self-assembled monolayer (SAM) technology has been primarily used on gold surfaces for biosensing applications ranging from atomic force microscopy to electrochemistry. [1] The gold-sulfur bond is not extremely strong, but stable and reproducible monolayers have been formed on Au using an enormous variety of alkane thiolates. [1-7] Recently, alternative thin film materials such as metal oxides have been investigated as substrates for self-assembled monolayer technology. Indium tin oxide (ITO) has been shown to support SAMs based on thiolate, carboxylate and phosphonate interactions. [8-11] Although the preparation conditions for alkane thiolate monolayers on indium tin oxide surfaces require neat alkane thiolates, the SAMs produced on these surfaces appear robust. [8, 12] ITO belongs to the family of transparent conducting oxides (TCOs) and is an infrared reflecting material. This combination of properties has provided novel applications for thin film technology such as thermographic sensing, photothermal electrochemistry, and photoelectrochemistry. [13-16] The success of SAM technology on ITO leads to the consideration of other conducting metal oxides (CMO) both for comparison and for the development of novel applications for sensing and energy conversion technology.

As a class of materials, transparent conducting metal oxides have a variety of commercial applications including flat-panel displays and thin-film photovoltaics. [17] Indium tin oxide (ITO), zinc oxide (ZnO), and tin oxide (SnO_2) have traditionally been used for these applications, [18, 19] yet, due to the cost, availability, and environmental concerns of some of these TCO's, new materials are being

investigated. [18, 20] In fact, indium is relatively scarce in the earth's crust [21], and produced primarily as a by-product of zinc refining; therefore, as the rate of consumption of indium-based products continues to increase, other materials should be considered.

Cadmium is derived from zinc ores as well as indium although it is much more abundant. [21] Historically, one cadmium containing compound in particular, cadmium tin oxide, has high mobility and high charge carrier concentration while still maintaining a transparent appearance in the visible. [22] Therefore, cadmium tin oxide (Cd_2SnO_4) also known as cadmium stannate or CTO (a ternary TCO material) is the focus of this study. It combines the beneficial characteristics of SnO_2 and CdO in that it has low emissivity coupled to high electron mobility. [20] In fact, the conductivity and bandgap obtained by metal-organic chemical vapor deposition [23] is comparable to commercially available ITO and can be improved upon by changing the deposition precursor. [23] CTO is an n-type semiconductor typically with an orthorhombic or cubic crystal structure, high carrier concentration, high electrical conductivity, and low visible absorption. [20] The crystal structure is highly dependent on the fabrication method with orthorhombic unit cells created by sputtering targets [20] or by sol gel preparation, [24] spinel or cubic spinel unit cells created upon annealing of the thin films or high temperature deposition, [17, 20] and cubic unit cells observed with sol-gel nanocrystalline cadmium tin oxide. [25] The orthorhombic unit cell is more thermodynamically stable although the larger spinel unit cell was determined by X-ray diffraction (XRD) to be the form used in the present study. This spinel form may

be surface stabilized by the high temperatures used in the metal-organic chemical vapor process and therefore was the form chosen for the density functional theory (DFT) calculations carried out as part of this study. This cubic spinel unit cell contains octahedrally coordinated cadmium ions surrounded by six oxygen atoms, while the tin atoms in the molecule are found, in principal, in the center of oxygen tetrahedra. The high carrier concentration of CTO has been proposed by one group to be a function of cadmium vacancies in the unit cell [20], while the observed conductivity is thought to be function of Sn-on-Cd antisite defects within the CTO thin films. [26] With the nonstoichemetric ratios of cadmium and tin in our samples, the applicable theory was antisite defects.

The formation of alkane thiolate self-assembled monolayers on CTO was studied for comparison with monolayers formed on other conducting metal oxides. [8, 27] Hexadecanethiol monolayers were studied since it has been shown that thiolate adlayers do not form on ITO unless the chain length is greater than 12 methylene groups. [8] The observation of the deposition of thiolate monolayers onto cadmium tin oxide thin film supports the contention that metal oxide surfaces as a class of materials are suitable for self-assembled monolayer formation. The present study combines both variable angle reflectance FTIR spectroscopy and density functional theory (DFT) for characterization of the optical and electronic properties of cadmium tin oxide thin films. These properties, including the plasma frequency of CTO, were investigated in the mid-IR spectral region. DFT calculations empirically determined the Fermi energy, charge carrier concentration, and plasma frequency of a variety of

stoichiometries ranging from $Cd_{16}Sn_8O_{32}$ to $Cd_{16}Sn_8O_{26}$. Herein, we combine these methods to understand the formation of self-assembled monolayers and the optical properties of CTO for potential applications in sensing and energy production.

9.3. Materials and Methods

9.3.1. Chemicals and Substrates.

1-Hexadecanethiol was used as received from Sigma Aldrich. 95% Ethanol was used as received from Aaper Alcohol and Chemical Co. The gold electrodes were obtained from Evaporated Metal Films, Inc.

9.3.2. Cadmium Tin Oxide Film Preparation.

CTO electrodes were fabricated by Coutts et.al. at the National Renewable Energy Laboratory (NREL) using a low-pressure metal-organic chemical vapor deposition system made by CVD Equipment Co. (Ronkonkoma, NY). Ultrahigh-purity tetramethyltin (Morton International) and dimethylcadmium (Morton International) were used for the Sn and Cd precursors. The growth temperature of CTO film was varied between 500°C to 550°C. The Cd-to-Sn ratio in CTO films was approximately 1.5 to 2. A stylus profilometer (Dektak^3) was used to measure the film thickness. The carrier concentration and electron mobility were determined using Hall effect measurements (van der Pauw technique, BioRad Model HL5500). The composition of the films was analyzed by an electron probe microanalysis (JEOL 8900 Electron Microprobe), and crystal properties were assessed using

X-ray diffraction (Sintag Model PTS). The CTO thin films had thickness of either 3700 Å or 2900 Å with a sheet resistance of either 30.1 Ω/sq or 36.3 Ω/sq, respectively. The substrate for the Cd_2SnO_4 electrodes was 1-mm-thick 102 x 102-mm Corning 7059 borosilicate glass.

9.3.3. Deposition on Cadmium Tin Oxide Thin Films.

The CTO electrodes were cleaned by ozonolysis (UV/O_3) for 20 minutes. (UVO-60, model number 42, Jelight Co. Inc.) to yield a clean hydrophilic surface and remove any adventitious carbon present. [28] The clean Cd_2SnO_4 electrode was immersed in the deposition solution for 30 minutes. The 1-hexadecanethiol deposition solution was a 50/50 (v/v) 95% ethanol/1-hexadecanethiol. The electrodes were rinsed with 95% ethanol followed by drying the electrodes with N_2 gas.

9.3.4. Reflectance FTIR Spectroscopy.

The variable angle reflectance FTIR spectra were recorded by both Digilab FTS3000 and FTS6000 spectrometers using p-(vertically) polarized IR radiation and a Varian Universal Sampling Accessory attachment. The angle of incidence ranged from 60 to 75 degrees relative to the surface normal. A globar source, potassium bromide (KBr) beamsplitter, and liquid nitrogen cooled mercury-cadmium-telluride/A linearized detector were used in the spectral range of 650-5000 cm^{-1}. To obtain the CTO thin film reflectance spectra, a ratio of the single beam spectra of the metal oxide thin film on the glass substrate to the single beam spectra of a gold surface was

made. The reflectance IR spectra were averaged over 1024 scans at a resolution of 4 cm^{-1} and were performed at room temperature. The spectra of the 1-hexadecanethiol adlayer on the CTO electrode was obtained by taking a ratio of the single beam spectra of the p-polarized spectra of the deposited material (1-hexadecanethiol) on CTO to the s-polarized spectra of the same cadmium tin oxide thin film at an incidence angle of 70º. The absorption IR spectra were averaged over 256 scans at a resolution of 2 cm^{-1} and were performed at room temperature.

9.3.5. X-ray Photoelectron Spectroscopy.

XPS spectra were recorded on a Riber LAS3000 surface analysis system equipped with a MAC2 analyzer with MgK α X-rays (model CX 700 (Riber source)) ($h\upsilon$ = 1253.6 eV, takeoff angle = 75°). The elemental scans had a resolution of 0.5 eV with 20 scans for cadmium and 10 scans for tin and sulfur. XPS spectra were baseline corrected by selecting a point within a relatively stable region as the zero point and shifting the remaining spectral points in relation. The sulfur peaks were fitted using Gaussian line shape with the equation $y= y_o + A\exp [-(x-x_{o/}\text{width})^2]$ where x and y are plotted spectral points and A is a fitting constant. The sulfur $2p_{3/2}$ and $_{1/2}$ angular momentum components were fitted with a fixed 2:1 peak area ratio as reported for sulfur.[8]

9.3.6. Density Functional Theory Calculations.

The single point energy calculations of the unit cell were carried out with the use of the quantum chemical software DMol3 (Accelrys, Inc.). [29] The calculations were performed on a structure of cadmium tin oxide cell containing 8 formula units of Cd_2SnO_4 (56 atoms) with a cubic spinel structure. [20] The elemental cadmium and tin structures were alternated since crystallographic data has shown that 16 of the sites are randomly occupied by either cadmium or tin. [30] This $Cd_{16}Sn_8O_{32}$ cubic cell was used in order to study oxygen depletion as the mechanism of n-type conduction in CTO and was optimized by calculation of the energies of expansions and contractions of the cubic cell (a = 9.177 Å). The range from 0.98a to 1.06a was tested and the optimum unit cell was found to be 1.04a or 9.544 Å (see Supporting Information). Oxygen depletion stoichiometries ranging from $Cd_{16}Sn_8O_{32}$ to $Cd_{16}Sn_8O_{26}$ were studied by removal of oxygen atoms from random positions in the lattice without any further geometry optimization. Periodic boundary conditions were used to determine the bulk electronic and optical properties of the metal oxide thin film. The double numerical polarized function (DNP) basis set used was O(1s),2(2s),2(2p),2(3d), Cd(4s),(4p),2(4d),2(5s),(5p),(5d) and Sn2(5s),2(5p),(5d) for the three atoms with an atomic cutoff at 5.49Å. The Perdew and Wang GGA functional was used for the DFT calculations. [31] The DFT calculations utilized the grand canonical ensemble approach which

allows for partial electron occupation which is needed for the charge carrier calculations. [32]

The number of conduction electrons was determined from the energy bands of the Fermi energy at an electronic temperature of 300 K using a phenomenological model. The Fermi-Dirac distribution function was calculated based on the energy levels (bands) obtained from DFT. In all cases the Fermi energy, ε_F, is below the conduction band. The electron populations can modeled using the Fermi-Dirac distribution function $f(\varepsilon_i) = 1/(1 + \exp\{(\varepsilon_i - \varepsilon_F)/k_BT\}$,[1] where the ε_i are the discrete energies of bands with index i above ε_F. The charge carrier density value was determined by summing the electrons in the conduction band of cadmium tin oxide divided by the unit cell volume calculated from the lattice constants.

$$n = \frac{\sum_{i=n_{Fermi}}^{\infty} f(\varepsilon_i)}{V_{cell}} \qquad (2)$$

where n_{Fermi} is the quantum number of the energy level corresponding to the Fermi energy. This approach to determining the charge carrier density is a phenomenological method used to estimating the effects of doping, which is accomplished in CTO by depletion of oxygen atoms. The plasma frequency was determined using equation 3 [33]

$$\omega_p^2 = \frac{ne^2}{m^*\varepsilon_o} \qquad (3)$$

where ω_p is the plasma frequency, n is the charge carrier concentration, e is the charge of a conduction electron, ε_o is the permittivity of space, and m^* is the effective mass of cadmium tin oxide of approximately 0.3. [34] Thus, the plasma frequency is directly calculated from first principles using the Drude free-electron model. All of the DFT calculations were performed at the High Performance Computing center at the North Carolina State University Linux cluster.

9.4. Results and Discussion

Experimental variable angle reflectance FTIR spectroscopy was utilized to study the reflectance of a 370 nm CTO thin film. At an incident angle of 70 degrees, the reflectance below 3500 cm^{-1} is nearly 40% while above 3500 cm^{-1}, the reflectance drops to approximately 15%. This observed change in reflectance is similar to observed changes in other conducting metal oxides (CMO) such as ITO, IrO_2, and aluminum-doped zinc oxide (AZO). [14, 35-37] A sharp change in the optical reflectivity such as this is indicative of the transition to the plasma resonance frequency, which is the resonant frequency for the conduction electrons in a Drude model. When incident radiation is matched to the resonant plasma frequency the light is absorbed leading to a sharp decrease in the reflectivity of the film. Above the plasma frequency, electromagnetic radiation is no longer efficiently reflected leading to an increase in optical transparency of the film. As seen in Figure 9.1, the reflectance of the material is also dependent upon the angle at which the radiation impinges upon the surface.

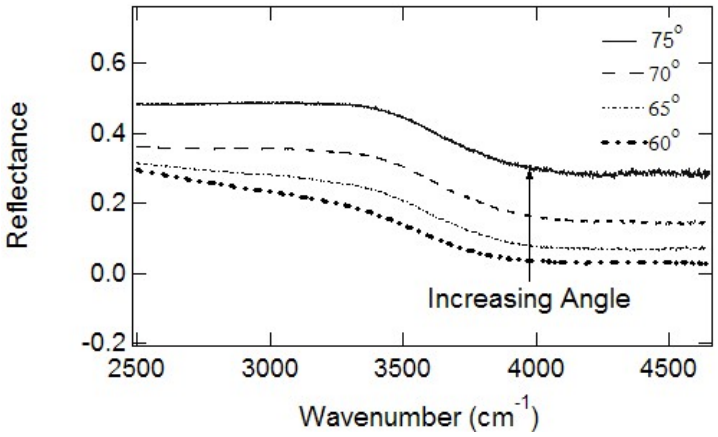

Figure 9.1. Experimental variable angle reflectance FTIR spectra of a thin film of CTO (30.1 Ω/□, 1.1 x 10^{20}/cm) on a glass substrate relative to a gold surface in the mid-IR region. These spectra were measured for incident angles ranging from 60 to 75° with p-polarized radiation with 5° increments.

As a function of angle, the decrease in reflectance at the plasma frequency, ω_p, at ~3,500 cm^{-1}, significantly changes in intensity while remaining in a relatively stable position. The reflectance spectra can be theoretically calculated from a Drude free-electron model [33] to determine the dielectric function of CTO and the three-phase Fresnel equation (air/glass/CTO) for reflection. [38] (see Supporting Information). In addition, as shown for other CMO's deposited on glass substrates [8, 35, 39], these spectra also displayed bands from the glass substrate onto which the cadmium tin oxide was deposited with the longitudinal optical and transverse optical Si-O-Si stretching modes observed at 1248 and 1064 cm^{-1} (data not shown).

Figure 9.2 displays the density functional theory (DFT) calculation of the Fermi level and plasma frequency of CTO and oxygen-depleted CTO.

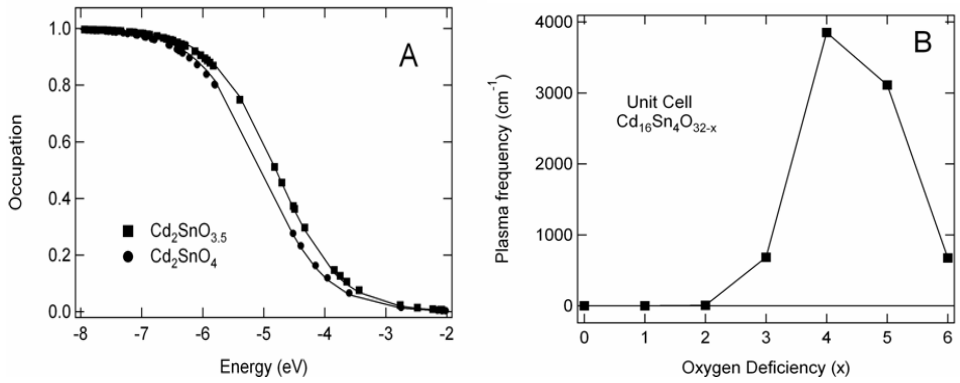

Figure 9.2A,B. Density functional theory calculation of the Fermi level and plasma frequency of CTO and oxygen-depleted CTO. A. The calculated bands and Fermi distribution function for CTO and one of the oxygen depleted models of conducting CTO thin films. B. Calculated plasma frequency using the Drude model and an effective mass of m* = 0. 3 m_e, where m_e is the mass of the electron.

The calculated band gap of $Cd_{16}Sn_8O_{32}$ is 1.5 eV, which is a factor of two smaller than the experimentally reported values of ~3 eV. [23, 40] The discrepancy of roughly a factor of two between DFT calculations and experiment is well known in the semi-conductor literature. [41-44] As oxygen is depleted there are trapped states that effectively decrease the band gap as indicated in Table 9.1. Figure 9.2A shows the Fermi-Dirac distribution function for two of the calculated models. The Fermi-Dirac distribution function was applied as indicated in Eqn. 2 to obtain an estimate for the occupation of energy levels above the Fermi level, ε_F. The occupied levels above ε_F are summed and divided by the unit cell volume to obtain an estimate for the charge carrier concentration. The CTO model calculation is consistent with the properties of a semi-metal when the oxygen depletion is ~12.5%. The Fermi energy, approximate band gap, ε_G, charge carrier concentration, n, are given in Table 9.1.

Table 9.1 Calculated Fermi level, Band gap and charge carrier density using DFT methods as a function of the stoichiometries of oxygen-depleted CTO.

Stoichiometry	Fermi level	Band Gap	Charge carrier concentration
	ε_F (eV)	ε_G (eV)	n (elec./cm^3) at 300 K
$Cd_{16}Sn_8O_{32}$	-5.03	1.28	3.11×10^{12}
$Cd_{16}Sn_8O_{31}$	-4.93	0.65	9.36×10^{12}
$Cd_{16}Sn_8O_{30}$	-4.78	0.69	2.49×10^{14}
$Cd_{16}Sn_8O_{29}$	-4.81	0.69	1.53×10^{18}
$Cd_{16}Sn_8O_{28}$	-4.80	0.57	4.83×10^{19}
$Cd_{16}Sn_8O_{27}$	-4.68	0.42	3.15×10^{19}
$Cd_{16}Sn_8O_{26}$	-4.71	0.22	1.49×10^{18}

In the oxygen-depleted species $Cd_{16}Sn_8O_{28}$, the calculated charge carrier density of 4.8×10^{19} electrons/cm^3 is in reasonable agreement with the experimentally determined value of 1.1×10^{20} electrons/cm^3 and is similar to previous theoretical work on a variety of metal oxides. [44-47] Based on the calculated charge carrier concentrations, the plasma frequencies shown in Figure 9.2B indicate agreement with our experimental observations in Figure 9.1. The species $Cd_{16}Sn_8O_{28}$ has a calculated plasma frequency of 3,850 cm^{-1} (Figure 9.2B) compared to 3,500 cm^{-1} determined experimentally.

Figure 9.3 shows the experimental variable angle reflectance FTIR reflectance spectra for a bare CTO thin film and a CTO thin film with a thiolate adlayer.

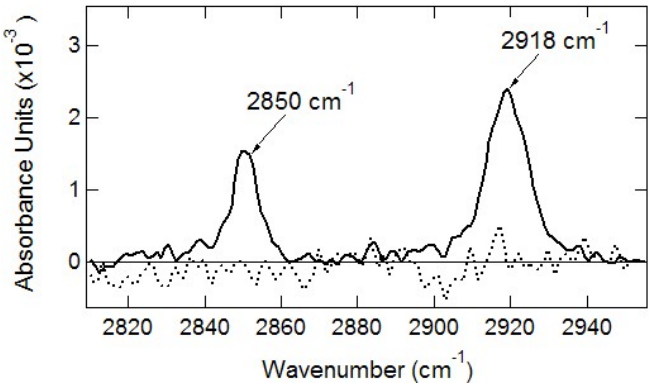

Figure 9.3. Baseline corrected reflectance FTIR spectra obtained from a ratio of p-polarized light of 1-hexadecanethiol on CTO to s-polarized light of the same CTO slide. The spectra shown are for an incident angle of 70° and p-polarized mid-IR light. The adlayer deposition time was 30 minutes for the hexadecanethiol solution.

The dashed line (---) displays the bare cadmium tin oxide thin film while the solid line reveals the spectrum of the cadmium tin oxide with a hexadecanethiol adlayer. Figure 3 displays two peaks indicative of an alkane adlayer. The observed peaks at 2918 cm^{-1}, and 2850 cm^{-1} correspond to the vibrational asymmetric and symmetric stretching modes of -CH_2-, respectively. The symmetric peak centered at 2850 cm^{-1} is lower than the peak corresponding to the vibrational stretching mode in neat liquid found at 2951 cm^{-1}. [2, 6, 8, 48] Thus, this shift is indicative of an ordered adlayer on the surface.

In previous studies with indium tin oxide, hexadecanethiol ($CH_3(CH_2)_{15}SH$) monolayers were examined by FTIR reflectance spectroscopy and XPS spectroscopy. [8] The positions of peaks revealed in the FTIR spectra are analogous to those shown for ITO, [8] although the intensities were more similar to those reported for alkanethiolate monolayers on gold. [6, 49] Specifically, the absorbance units of a SAM

on an ITO substrate are typically less than 0.001 a.u., [8] while thiolate monolayers on gold range from 0.002 to 0.006 a.u. [6, 39, 49] For the hexadecanethiol monolayer on CTO, the absorbance units were 0.002 to 0.003. This is indicative of a thiolate adlayer on CTO that more closely resembles a gold thiolate adlayer rather than an adlayer on ITO. Near edge X-ray absorption fine structure spectroscopy data collected on ITO and gold substrates [50] have also shown a difference in the surfaces with thiolate SAMs forming well-ordered structures on the gold substrates with only moderate ordering of adlayers on the conducting metal oxide. In addition, the ITO required a neat thiolate overnight deposition whereas the CTO minimum deposition concentration was a 50/50 v/v (hexadecanethiol/ethanol) with a 30 minute deposition time. Therefore, it can be construed that the hexadecanethiol monolayer on CTO is more ordered than on ITO and thus, giving the conclusion that the surface chemistries of each conducting metal oxides are each distinctive. Additionally, experimental evidence suggests a robust adlayer is formed on the cadmium tin oxide thin film since FTIR spectroscopy performed on previously deposited samples, up to 18 months previous, still reveal shifted methylene stretching vibrational modes indicative of an ordered monolayer.

Figure 4A shows the XPS spectra of cadmium $3d_{5/2,3/2}$ of bare cadmium tin oxide (dotted line) and an adlayer of 1-hexadecanethiol (solid line) on CTO.

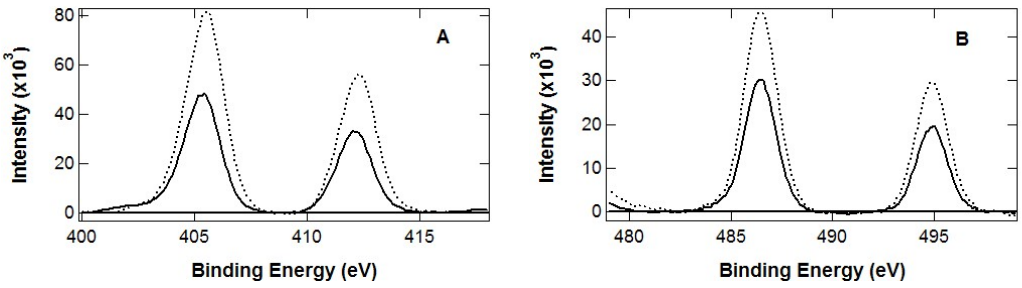

Figure 9.4A, B. Cadmium $3d_{5/2,3/2}$ (A) and Tin $3d_{5/2,3/2}$ (B) XPS spectra of bare CTO (dashed line) and 1-hexadecanethiol (solid line) on CTO.

The positions of the cadmium (405.5, 412.3 eV) correspond to Cd^{2+} oxidation state. [51, 52] The figure shows an attenuation of approximately 41% of the signal indicative of adlayer formation. Similarly, Figure 4B shows the XPS spectra of tin $3d_{5/2,3/2}$ of the bare cadmium tin oxide (dotted line) and an adlayer of 1-hexadecanethiol (solid line) with the XPS line positions of the tin (486.4, 494.8 eV) corresponding to a Sn^{4+} oxidation state. [28] A 33% attenuation in the Sn $3d_{5/2,3/2}$ signal is an additional indicator of adlayer formation.

With the addition of a thiolated alkane (hexadecanethiol), sulfur is integrated into the XPS spectrum of the thin film. Figure 5 shows the sulfur $2p_{3/2,1/2}$ XPS spectra of the adlayer of 1-hexadecanethiol on CTO with the raw data indicated by markers and the Gaussian fits of the $2p_{3/2,1/2}$ sulfur peaks as solid lines.

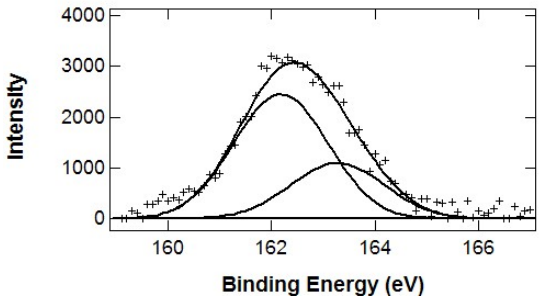

Figure 9.5. Sulfur $2p_{3/2,1/2}$ XPS spectra corresponding to an adlayer of 1-hexadecanethiol on CTO. The raw data (markers) and the individual Gaussian fits (solid lines) are shown.

These peak positions occur at 162 and 163.7 eV and are in good agreement with previously reported alkanethiolate monolayers on metallic surfaces. [2, 5, 39, 48]

9.5. Conclusions

The presence of ordered 1-Hexadecanethiol adlayers on CTO surfaces was confirmed by reflectance FTIR spectroscopy and XPS. These techniques showed the presence of the symmetric and asymmetric methylene stretching modes and the presence of a sulfur signal, respectively indicative of adlayer formation. In comparison with other metal oxide thin films such as indium tin oxide (ITO) and fluorinated tin oxide (SFO) [8], cadmium stannate forms thiolate adlayers at concentrations ½ of those used for ITO and SFO and at approximately 5% of the deposition time, indicative of stronger binding on CTO films relative to the previously studied metal oxides. Therefore, understanding the intrinsic electronic and optical properties of the thin film is an essential task of this study.

These intrinsic properties of the cadmium tin oxide thin films were characterized with the use of variable angle FTIR spectroscopy and X-ray

photoelectron spectroscopy. Reflectance FTIR spectroscopy revealed a sharp decrease in the optical reflectivity in the mid-IR of CTO suggestive of a surface plasmon resonance condition. The observed frequency dip in CTO at ~3,500 cm^{-1} is comparable to the experimentally observed plasma frequencies of other metal oxide thin films such as ITO and AZO at ~8,500 cm^{-1} [36, 37], IrO_2 at ~6500 cm^{-1} [35], and RuO_2 at ~4500 cm^{-1} (unpublished data) using analogous reflectance FTIR spectroscopy. As shown in previous work on ITO [37], the deposition of an adlayer also affects the optical and electronic properties of the CTO thin film by changing both the position and slope of the plasma frequency. DFT calculations of oxygen depletion studies revealed theoretical charge carrier densities and plasma frequencies consistent with experimental results. These studies were performed by removal of up to 8 oxygen atoms from random positions. Although the model is simple, in that it ignores the true band structure of the conducting metal oxide, it provides a means to examine doping and oxygen depletion that is not possible in a single unit cell calculation. Based on the calculations presented and in other studies on conducting metal oxides, we see the importance of oxygen depletion as an emerging trend in the calculations. The calculations are in agreement with well-known deposition procedures of oxygen removal for increased conductivity. Moreover, the calculation indicates that there is an optimum value for oxygen depletion. CTO is a novel system for thin film study that provides a combination of the both robust surface chemistry and substantial potential for development as a conducting material that has plasma resonance. [54]

Acknowledgements
The authors would like to thank Dr. Simon Lappi for assistance on the infrared spectroscopy and Accelrys, Inc. for access to the DFT computing program DMol3.

9.6. Supporting Information

Figure 9.6 shows the methodology for optimization of the unit cell.

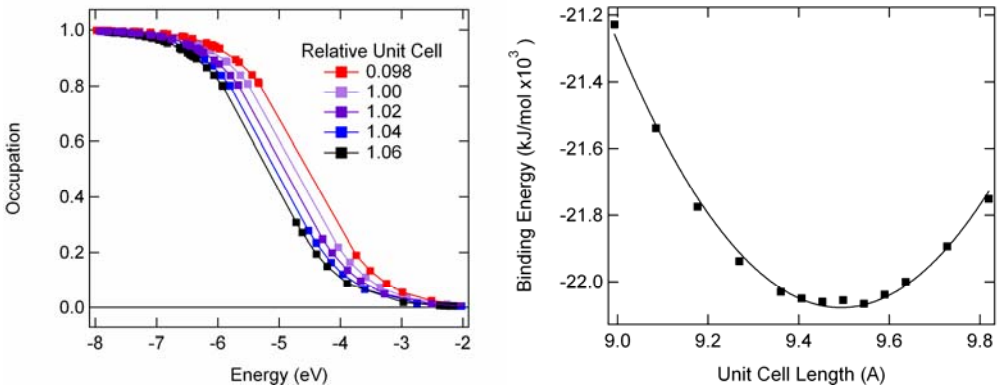

A. B.

Figure 9.6 Optimization of the unit cell. The experimentally determined cubic unit cell corresponds to a dimension of a = 9.177 Å. A.) The energy levels in the vicinity of the Fermi energy are shown for the range from 0.98a to 1.06a B.) The binding energy as a function of unit cell length is plotted for the range from 0.98a to 1.06a.

The unit cell was expanded or contracted for a stoichiometric ratio of 0.98a to 1.06a, where "a" is the lattice constant. Figure 9.6 relates the electronic occupation of the unit cells revealing an appromixate band gap for each of the CTO stoichiometries. This figure displays the binding energy as a function of unit cell length with a minimum binding energy revealing the optimum unit cell to be 1.04a or 9.544 Å

Figure 9.7 displays the experimental reflectance FTIR spectra for the Cd_2SnO_4 thin film at the 65 degree incident angle for p-polarized light.

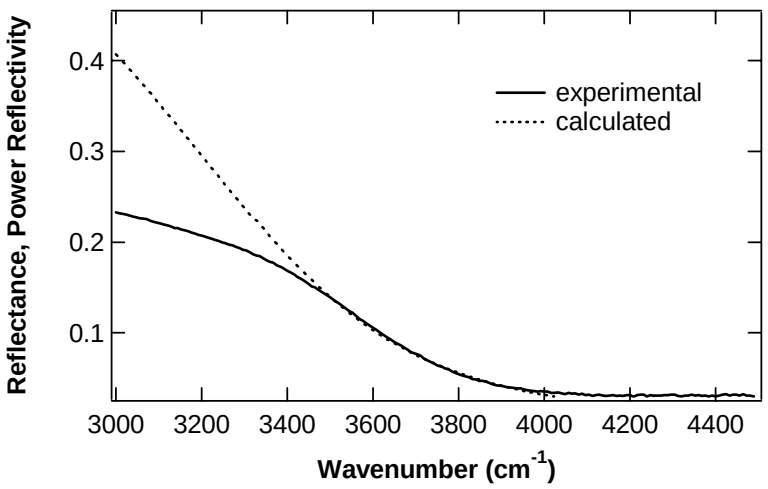

Figure 9.7. Experimental (solid line) and calculated (dashed line) reflectance spectra for an incident angle of 65° for CTO on a glass substrate with p-polarized radiation in the mid-IR region. The calculated spectra used the three-phase (air/glass/CTO) Fresnel equations of reflection.

The figure illustrates the calculated reflectance spectra as obtained from a Drude free-electron model [33] to determine the dielectric function of CTO and the three-phase Fresnel equation (air/glass/CTO) for reflection. [38] The reflectance spectrum of the cadmium tin oxide thin film is adequately modeled in the region of the reflectance decrease at ~3500 cm^{-1}; however, the reflectance calculated is higher than the experimental value for wavenumbers less than the plasma frequency and slightly lower than the experimental value for those wavenumbers higher than the frequency.

Theoretically, the Drude free-electron model describes the dielectric function ($\varepsilon(\omega)$) as a function of the plasma frequency (ω_p) and the scattering time (τ)

$$\varepsilon(\omega) = \varepsilon_\infty - \omega_p^2 \frac{1}{\omega^2 + \frac{i\omega}{\tau}} \qquad (4)$$

where ε_∞ is the high-frequency dielectric constant, ω_p is the plasma frequency as previously defined in equation 1, ω is the frequency, and τ is the electronic scattering time. Using the high frequency dielectric constant of the CTO substrate as 6.76 [20], an empirical scattering time of 4.1×10^{-15} s and a plasma frequency of 9,370 cm^{-1} were determined. These values were used in three-phase Fresnel equation of reflection to model a system comprised of two dielectric interfaces. Only the real components of the refractive index of air (η=1,κ=0) were included in the model. The complex refractive index for the CTO films was determined from the Drude free electron model as expressed in equation 5

$$\varepsilon(\omega)^{\frac{1}{2}} = N(\omega) = n(\omega) + ik(\omega) \qquad (5)$$

where N is the complex refractive index, n is the real, dispersive component and k is the imaginary, absorptive component of the refractive index. These equations relate the plasma frequency (ω_p) to both the charge carrier density (n) and the effective electron mass (m). Therefore, modeling of the plasma frequency is of interest although apparent disparities indicate that using the Drude free electron model reveals that CTO is non-ideal in certain spectral regions. This implies that the reflectance in the mid-IR is dependent on film preparation.

Table 9.2 reveals the DFT calculated electronic properties of Fermi energy, charge carrier density, and plasma frequency of cadmium tin oxide at a temperatures ranging from ~300 K (room temperature) to ~15,000 K.

Table 9.2. The calculated electronic properties of Fermi energy, and charge carrier concentration, and plasma frequency.

Temperature (K)	**Fermi Energy** (eV)	**Charge Carrier Density (n)** (electrons/cm^3**)**	**Plasma Frequency** (cm^{-1})
299.7	-5.820	3.8×10^{20}	10707.4
473.6	-5.798	6.4×10^{20}	13851.0
789.4	-5.768	3.1×10^{20}	9585.0
3947.0	-5.251	1.0×10^{19}	1757.3
4736.4	-5.086	5.2×10^{19}	3929.5
5525.7	-4.930	1.6×10^{20}	6974.1
6315.1	-4.798	3.8×10^{20}	10689.3
7893.9	-4.606	1.1×10^{21}	18451.8
11051.5	-4.382	3.6×10^{21}	32782.2
15787.8	-4.206	9.0×10^{21}	51721.4

9.7. References

1. Davis, F.; Higson, S. P. J., Structured thin films as functional components within biosensors. *Biosensors & Bioelectronics* **2005,** 21, 1-20.

2. Bain, C. D.; Biebuyck, H. A.; Whitesides, G. M., Comparison of Self-Assembled Monolayers on Gold - Coadsorption of Thiols and Disulfides. *Langmuir* **1989,** 5, (3), 723-727.

3. Bain, C. D.; Evall, J.; Whitesides, G. M., Formation of Monolayers by the Coadsorption of Thiols on Gold - Variation in the Head Group, Tail Group, and Solvent. *Journal of the American Chemical Society* **1989,** 111, 7155-7164.

4. Bain, C. D.; Troughton, E. B.; Tao, Y. T.; Evall, J.; Whitesides, G. M.; Nuzzo, R. G., Formation of Monolayer Films by the SponStaneous Assembly of Organic Thiols from Solution onto Gold. *Journal of the American Chemical Society* **1989,** 111, 321-335.

5. Bain, C. D.; Whitesides, G. M., Formation of Monolayers by the Coadsorption of Thiols on Gold - Variation in the Length of the Alkyl Chain. *Journal of the American Chemical Society* **1989,** 111, 7164-7175.

6. Nuzzo, R. G.; Zegarski, B. R.; Dubois, L. H., Fundamental-Studies of the Chemisorption of Adsorbates on Well-Defined Organic-Surfaces. *Journal of the Electrochemical Society* **1987,** 134, (3), C110-C110.

7. Ulman, A., *Thin Films: Self-assembled Monolayers of Thiols (Thin Films).* Academic Press: 1998.

8. Brewer, S. H.; Brown, D. A.; Franzen, S., Formation of thiolate and phosphonate adlayers on indium-tin oxide: Optical and electronic characterization. *Langmuir* **2002,** 18, (18), 6857-6865.

9. Gardner, T.; Frisbie, C.; Wrighton, M., Systems for Orthogonal Self-Assembly of Electroactive Monolayers on Au and ITO: An Approach to Molecular Electronics. *The Journal of the American Chemical Society* **1995,** 117, 6927-6933.

10. Guo, J.; Koch, N.; Bernasek, S.; Schwartz, J., Enhanced hole injection in a polymer light emitting diode using a small molecule monolayer bound of the anode. *Chemical Physics Letters* **2006,** 426, (4-6), 370-373.

11. Hanson, E.; Guo, J.; Koch, N.; Schwartz, J.; Bernasek, S., Advanced Surface Modification of Indium Tin Oxide for Improved Charge Injection in Organic Devices. *Journal of the American Chemical Society* **2005,** 127, (28), 10058-10062.

12. Sato, Y.; Uosaki, K., Electrochemical and Electrogenerated Chemiluminescence Properties of Tris(2,2'-Bipyridine)Ruthenium(Ii)-Tridecanethiol Derivative on Ito and Gold Electrodes. *Journal of Electroanalytical Chemistry* **1995,** 384, (1-2), 57-66.

13. Appleyard, S.; Day, S.; Pickford, R.; Willis, M., Organic electroluminescent devices: enhanced carrier injection using SAM derivatized ITO electrodes. *Journal of Material Chemistry* **2000,** 10, 169-173.

14. Brewer, S.; Franzen, S., Optical properties of indium tin oxide and fluorine doped tin oxide surfaces: correlation of plasmon frequency, reflectivity and skin depth with conductivity. *Journal of Alloys and Compounds* **2002,** 343, (1-2), 244-244

15. Lowe, L. B.; Brewer, S. H.; Kramer, S.; Fuierer, R. R.; Qian, G. G.; Agbasi-Porter, C. O.; Moses, S.; Franzen, S.; Feldheim, D. L., Laser-induced temperature jump electrochemistry on gold nanoparticle-coated electrodes. **2003,** 125, (47), 14258-14259.

16. Zotti, G.; Schiavon, G.; Zecchin, S.; Berlin, A.; Pagani, G., Adsorption of Ferrocene Compounds on Indium-TIn-Oxide Electrodes. Enhancement of Adsorption by Decomposition of Ferrocenium Molecules by Oxygen. *Langmuir* **1998,** 14, 1728-1733.

17. Li, X. A.; Gessert, T. A.; Coutts, T., The properties of cadmium tin oxide thin-film compounds prepared by linear combinatorial synthesis. *Applied Surface Science* **2004,** 223, (1-3), 138-143.

18. Ginley, D.; Roy, B.; Ode, A.; Warmsingh, C.; Yoshida, Y.; Parilla, P.; Teplin, C.; Kaydanova, T.; Miedaner, A.; Curtis, C.; Martinson, A.; Coutts, T.; Readey, D.; Hosono, H.; Perkins, J., Non-vacuum and PLD growth of next generation TCO materials. *Thin Solid Films* **2003,** 445, (2), 193-198.

19. Wu, X.; Mulligan, W. P.; Coutts, T. J., Recent developments in RF sputtered cadmium stannate films. *Thin Solid Films* **1996,** 286, (1-2), 274-276.

20. Coutts, T. J.; Young, D. L.; Li, X.; Mulligan, W. P.; Wu, X., Search for improved transparent conducting oxides: A fundamental investigation of CdO, Cd2SnO4, and Zn2SnO4. *Journal of Vacuum Science & Technology a-Vacuum Surfaces and Films* **2000,** 18, (6), 2646-2660.

21. Coutts, T. J., A Review of and Impressions from the 3rd European-Communities Conference on Photo-Voltaic Solar-Energy, Cannes, October 27-31, 1980. *Solar Cells* **1981,** 3, (4), 375-386.

22. Nozik, A. J., Optical and Electrical Properties of Cd2sno4 - a Defect Semiconductor. *Physical Review B* **1972,** 6, (2), 453-459.

23. Metz, A. W.; Ireland, J. R.; Zheng, J. G.; Lobo, R.; Yang, Y.; Ni, J.; Stern, C. L.; Dravid, V. P.; Bontemps, N.; Kannewurf, C. R.; Poeppelmeier, K. R.; Marks, T. J., Transparent conducting oxides: Texture and microstructure effects on charge carrier mobility in MOCVD-derived CdO thin films grown with a thermally stable, low-melting precursor. *Journal of the American Chemical Society* **2004,** 126, (27), 8477-8492.

24. Jayachandran, M.; Subramanian, B.; Chockalingam, M. J.; Lakshmanan, A. S., Cd2sno4 - Its Sol-Gel Preparation and Materials Properties. *Bulletin of Materials Science* **1994,** 17, (6), 989-997.

25. Valincius, G. R., V; Viler, V; Woodward, TJ; Vaudin, M, Electrochemical Properties of Nanocrystalline Cadmium Stannate Films. *Jounral of the Electrochemical Society* **2001,** 148, (8), E341-E347.

26. Zhang, S. B.; Wei, S. H., Self-doping of cadmium stannate in the inverse spinel structure. *Applied Physics Letters* **2002,** 80, (8), 1376-1378.

27. Noble-Luginbuhl, A. R.; Nuzzo, R. G., Assembly and characterization of SAMs formed by the adsorption of alkanethiols on zinc selenide substrates. *Langmuir* **2001,** 17, (13), 3937-3944.

28. Yan, C.; Zharnikov, M.; Golzhauser, A.; Grunze, M., Preparation and characterization of self-assembled monolayers on indium tin oxide. *Langmuir* **2000,** 16, (15), 6208-6215.

29. Delley, B., An all-electron numerical-method for solving the local density functional for polyatomic molecules. *Journal of Chemical Physics* **1990,** 92, (1), 508-517.

30. Bowden, M. E., Cardiley, C. M., Structures of orthorhombic and cubic dicadmium stannate by Rietveld refinement. *Powder Diffraction* **1990**, (1), 36-40.

31. Perdew, J. P.; Chevary, J. A.; Vosko, S. H.; Jackson, K. A.; Pederson, M. R.; Singh, D. J.; Fiolhais, C., Atoms, molecules, solids and surfaces - Applications of the generalized gradient approximation for exchange and correlation. *Phys. Rev. B* **1992,** 46, 6671-6687.

32. Mermin, D., *Phys. Rev. A* **1965,** 137, 1441-1443.

33. Wooten, F., *Optical Properties of Solids*. Academic Press, Inc.: San Diego, 1972.

34. Wu, X.; Coutts, T. J.; Mulligan, W. P., Properties of transparent conducting oxides formed from CdO and ZnO alloyed with SnO2 and In2O3. *Journal of Vacuum Science & Technology a-Vacuum Surfaces and Films* **1997,** 15, (3), 1057-1062.

35. Brewer, S. H.; Wicaksana, D.; Maria, J. P.; Kingon, A. I.; Franzen, S., Investigation of the electrical and optical properties of iridium oxide by reflectance FTIR spectroscopy and density functional theory calculations. *Chemical Physics* **2005,** 313, (1-3), 25-31.

36. Rhodes, C., Lappi, S., Fischer, D., Genzer, J., Keane, J., Li, X., Coutts, T., Drapcho, D., Franzen, S., Characterization of Monolayer Formation on Aluminun-doped Zinc Oxide Thin Films. **In preparation**.

37. Brewer, S. H.; Franzen, S., Indium tin oxide plasma frequency dependence on sheet resistance and surface adlayers determined by reflectance FTIR spectroscopy. *Journal of Physical Chemistry B* **2002,** 106, (50), 12986-12992.

38. Hansen, W., Electric Fields Produced by the Propagation of Plane Coherent Electromagnetic Radiation in a Stratified Medium. *Journal of the Optical Society of America* **1968,** 58, (3), 380-390.

39. Laibinis, P. E.; Whitesides, G. M.; Allara, D. L.; Tao, Y. T.; Parikh, A. N.; Nuzzo, R. G., Comparison of the Structures and Wetting Properties of Self-Assembled Monolayers of Normal-Alkanethiols on the Coinage Metal-Surfaces, Cu, Ag, Au. *Journal of the American Chemical Society* **1991,** 113, (19), 7152-7167.

40. Mamazza, R.; Morel, D.; Ferekides, C., Transparent conducting oxide thin films of Cd2SnO4 prepared by RF magnetron co-sputtering binary oxides. *Thin Solid Films* **2005,** 484, (1-2), 26-33.

41. Sham, L. J.; Kohn, W., 1-Particle Properties of an Inhomogeneous Interacting Electron Gas. *Physical Review* **1966,** 145, (2), 561-&.

42. Kohn, W.; Sham, L. J., Self-Consistent Equations Including Exchange and Correlation Effects. *Physical Review* **1965,** 140, (4A), 1133-&.

43. Hohenberg, P.; Kohn, W., Inhomogeneous Electron Gas. *Physical Review B* **1964,** 136, (3B), B864-&.

44. Brewer, S. H.; Franzen, S., Calculation of the electronic and optical properties of indium tin oxide by density functional theory. *Chemical Physics* **2004,** 300, (1-3), 285-293.

45. Mi, Y. M.; Odaka, H.; Iwata, S., Electronic structures and optical properties of ZnO, SnO2 and In2O3. *Japanese Journal of Applied Physics Part 1-Regular Papers Short Notes & Review Papers* **1999,** 38, (6A), 3453-3458.

46. Mryasov, O. N.; Freeman, A. J., Electronic band structure of indium tin oxide and criteria for transparent conducting behavior. *Physical Review B* **2001,** 64, (23), art. no.-233111.

47. Odaka, H.; Shigesato, Y.; Murakami, T.; Iwata, S., Electronic structure analyses of Sn-doped In2O3. *Japanese Journal of Applied Physics Part 1-Regular Papers Short Notes & Review Papers* **2001,** 40, (5A), 3231-3235.

48. Heinz, B.; Morgner, H., MIES investigation of alkanethiol monolayers self-assembled on Au(111) and Ag(111) surfaces. *Surface Science* **1997,** 372, (1-3), 100-116.

49. Inman, C. E.; Reed, S. M.; Hutchison, J. E., In situ deprotection and assembly of S-tritylalkanethiols on gold yields monolayers comparable to those prepared directly from alkanethiols. *Langmuir* **2004,** 20, (21), 9144-9150.

50. Cerruti, M. R., C.;Efremenko, A.;Losego, M.;Maria, J.P.;Genzer, J.;Fischer, D.;Feldheim, D.;Franzen, S.; , Influence of Indium-Tin Oxide surface structure on the ordering and coverage of organosilane, carboxylic acid and thiol monolayers. *Submitted*.

51. Lu, G. X.; Li, S. B., Effects of surface etching on the structure and performance of Rh2O3/CdS catalyst. *Journal of Photochemistry and Photobiology a-Chemistry* **1996,** 97, (1-2), 65-72.

52. Pavageau, M. P.; Morin, A.; Seby, F.; Guimon, C.; Krupp, E.; Pecheyran, C.; Poulleau, J.; Donard, F. X., Partitioning of metal species during an enriched fuel combustion experiment. Speciation in the gaseous and particulate phases. *Environmental Science & Technology* **2004,** 38, (7), 2252-2263.

Chapter 10

D Type Conductors: Iridium Oxide and Ruthenium Oxide

10.1. Introduction

Conducting metal oxides are generally in two categories, those with d-band conducting electrons and those with s and p band conducting electrons. [1] Iridium oxide (IrO_2) and ruthenium oxide (RuO_2) are examples of d-electron conductors. The experiments in this chapter build on previous work in the laboratory on s-p band conductors such as indium tin oxide (ITO) [2], aluminum-doped zinc oxide (AZO) presented in Chapter 7 and other d-electron conductors such as iridium oxide. [3] In all of these studies, the plasma frequency was observed in the near-IR spectral region regardless of the type of conduction band electron orbital character. [4-6] This plasma frequency is dependent on the charge carrier density and is therefore also related to the electronic conductivity of the thin film. [1] As observed for ITO, [7-11] and other sp-type conducting metal oxides the electrical and optical properties of iridium oxide and ruthenium oxide are strongly dependent on the deposition process used to form these thin films. [4, 12-15] Attempts have been made to understand the effects of this orbital change upon the electronic and optical properties of the thin films. For the studies, two d-type conducting substrates were chosen, iridium oxide and ruthenium oxide. This chapter details my attempted preparative methods of iridium oxide and computational trials of a ruthenium oxide unit cell, neither of which were very successful research studies.

10.2 Iridium Oxide

Iridium Oxide (IrO_2) is an opaque conducting metal oxide whose conduction band is filled with d electrons primarily arising from the iridium metal. [5] Due to its conductive nature, this material has been used for a variety of applications including light emitting diodes, pH biosensing, and electrocatalysis [16-18] and has been successfully deposited as a thin film onto glass substrates by a variety of techniques including spray pyrolysis, electrodeposition, sol-gel deposition, and reactive magnetron sputtering. [14, 15, 19, 20] Although the conduction electrons emanate from different orbitals, previous studies [3] have shown reflectivity changes indicative of a plasmon frequency apparent in the infrared region of the spectrum; therefore, this material was of great interest to me as another possible substrate for biosensing applications.

Initially, I needed to prepare more substrate for my studies as it was not commercially available and the previous research had been conducted on one thin film substrate. I contacted the Materials Science Department at NC State University since they had produced the initial IrO_2 thin film substrates. The deposition parameters used on both the silica and glass substrates in 2002 are identical and are outlined in the table below.

Table 10.1-Substrate depositions conditions of Iridium Oxide.

Substrates	-n type Si (001), resistivity 1-5 ohm cm (doping density ~10^{15} cm-^{3}) -Corning glass slide		
Pre-Treatment	-Si substrates were dipped into JT Baker 111-H_2O_2-H_2O solution for 10 minutes and rinsed with DI water for 10 minutes. (This is done to strip the native oxide layer and to grow a 0.8-1.2 nm-thick chemical layer. -Corning glass slides were ultrasonic bath cleaned in Methanol		
Deposition	DC Magnetron Reactive Sputtering -Target: Iridium -Gases: Ar:O_2 = 7:3 (argon to oxygen ratio) -Total Pressure: 30 mTorr -DC power: 150 W -Deposition rate ~ 1nm/s		
Thickness	Determined by the Alphastep profilometry for the samples thicker than 30nm		
	Sample Label	Deposition Time (s)	Thickness (nm)
	A	120	110
	B	60	70
	C	30	30
	D	20	20*
	E	10	10*
	*estimated thickness Note: There are 3 samples for each thickness-2 SiO_2/Si and 1 glass		
Post-Deposition Treatment	Annealed in a standard furnace with fast-fire technique 700°C, air atmosphere for 10 minutes		
XRD	As deposited: Amorphous After anneal: IrO_2 predominant, Ir exist		

My first attempt at magnetron DC reactive sputtering was unsuccessful due to the precleaning of the slides. I precleaned them in my laboratory with UVO and ultrasonic bath but I did not rinse them again before deposition. No usuable films were produced. I have since learned that an isopropanol rinse, rather than methanol, is the standard procedure for most deposition materials. Additionally, rinsing

immediately before deposition is the suggested method to use. Without proper cleaning, the deposition is not uniform, with areas of bare glass substrate. Another attempt at the deposition procedure produced slides of both glass and silica substrates. For each different optimization condition attempted, the substrate was analyzed by an X-ray diffractometer. This X-ray diffraction data was gathered on a Bruker AXS D-5000 X-ray diffractometer equipped with a GADDS area detector. The Cu anode was set at 30k kV and 20 mA and scans were 15 minutes in length. We did a θ-2θ scan ranging from 24 to 56 degrees for the initial trials and then 16 to 46 degrees for the subsequent preparations. The three graphs below depict the X-ray diffraction data of the various conditions tried on this attempt.

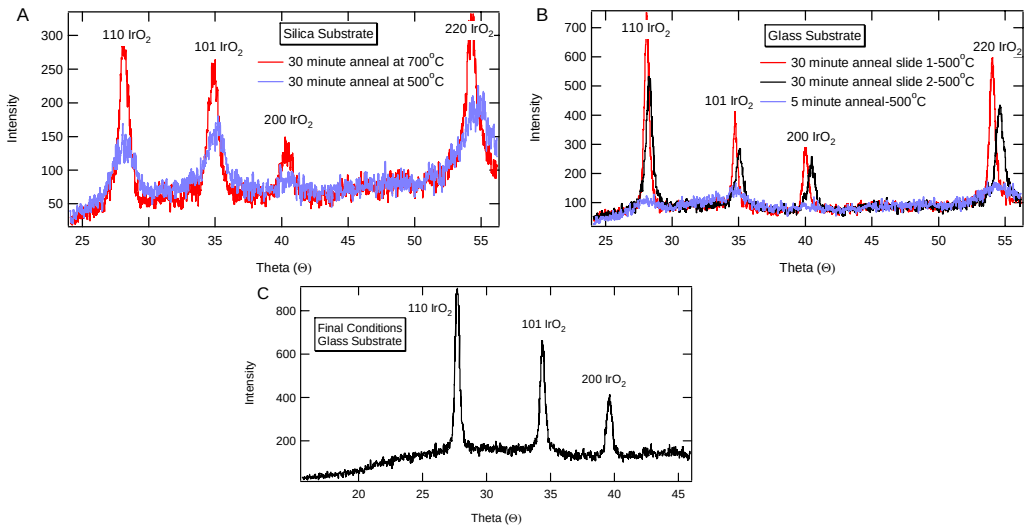

Figure 10.1A,B,C- X-ray diffraction spectra revealing development of optimal deposition parameters. Figure A depicts a silica substrate at two different annealing temperatures. Figure B reveals two different annealing times with a duplicate sample indicating the reproducibility of the results. Figure C shows the XRD of a glass substrate with the optimized conditions.

The figures above display the X-ray diffraction spectrums of different conditions attempted while optimizing the deposition procedure. The table below details the XRD peaks we observed.

Table 10.2. XRD Peaks of Irdium Oxide

Peak	Crystallographic Face	Diffraction Angle	Relative Intensity
IrO_2	110	28.05°	100
IrO_2	101	34.71°	90
IrO_2	200	40.06°	25
IrO_2	211	54.02°	55
IrO_2	220	57.94°	--

The final conditions we determined were as follows, with the changes from the original conditions highlighted. I used the same deposition instrumentation and target as previously employed.

Table 10.3. Revised substrate deposition conditions for Iridium Oxide

Substrates	-Corning glass slide		
Pre-Treatment	-Corning glass slides were cleaned in **Isopropanol**		
Deposition	DC Magnetron Reactive Sputtering -Target: Iridium -Gases: Ar:O_2 = **10:1** (argon to oxygen ratio) -Total Pressure: 30 mTorr -DC power: 150 W -Deposition rate ~ 1nm/s		
Thickness	Determined by the Alphastep profilometry for the samples thicker than 30nm		
	Sample Label	Deposition Time (s)	Thickness (nm)
	A	120	110
Post-Deposition Treatment	Annealed in a standard furnace with fast-fire technique **500°C**, air atmosphere for **30 minutes**		
XRD	After anneal: IrO_2 predominant, Ir exist		

Although a smooth opaque color matching the initial slides of 2002 was achieved, the FTIR data of these samples did not reveal a reflectivity change as shown below in Figure 10.2.

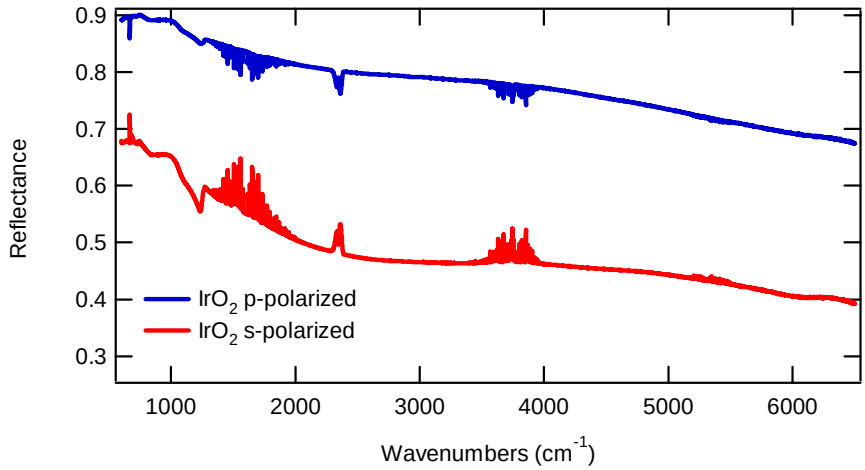

Figure 10.2. Reflectance FTIR spectrum of a 110 nm thick iridium oxide thin film deposited on a glass substrate. The spectrum was recorded with an incident angle of 70 degrees from the surface normal with p-polarized radiation.

Another attempt at IrO_2 substrate development was made. The X-ray diffraction data can be seen below. The same instrumentation was employed with an attempt at further optimization of the conditions.

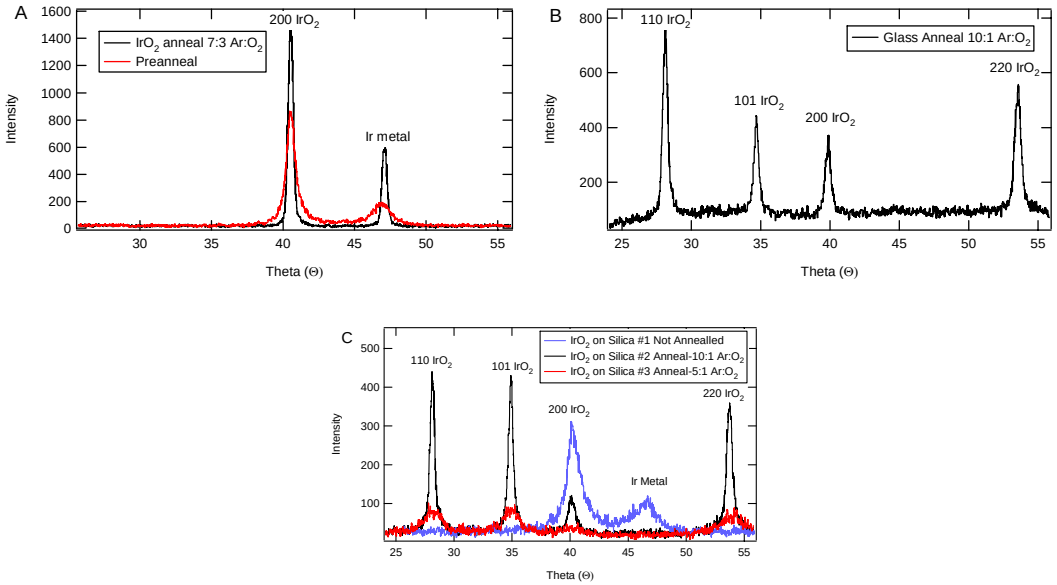

Figure 10.3A,B,C: The X-ray diffraction spectra of DC magnetron sputtering of 110 nm IrO_2 thin films. Figure 3A details differences between a thin film before annealing and the film after annealing at 500ºC for 10 minutes, sputtering with a carrier gas ratio of argon to oxygen ($Ar:O_2$) of 7:3 while figure 3B reveals the effect of changing the $Ar:O_2$ to 10:1. Figure 3C shows an IrO_2 thin film deposited on a silica wafer with both a $Ar:O_2$ gas ratio of 10:1 and 5:1.

Figures 10.3A,B, and C detail the X-ray diffraction spectra of IrO_2 deposition onto both glass and silica substrates. For optimization purposes, the $Ar:O_2$ gas ratio was changed thereby changing the oxide layer of the iridium oxide. The annealing temperature was not varied from 500°C and the time was a constant 30 minutes. Figure 10.3A shows the differences of a film before and after annealing with the conditions tried previously (7:3 $Ar:O_2$). Not all of the crystallographic faces were formed as before. The ratio of the carrier gas was changed to 10:1 argon to oxygen. This resultant X-ray diffraction spectrum is seen in figure 10.3B. This figure shows that many of the crystallographic faces were observed as before although the slides did not produce an even distribution. The final figure reveals our further attempts at

silica wafer deposition. The blue trace is the IrO_2 prior to annealing. The red and black traces reveal two different carrier gas ratios of 10:1 and 5:1. Neither of these produced ideal crystal structures. The black trace revealing the 10:1 ratio showed a thin film containing all of the required crystallographic faces but without the correct relative intensities. As the one glass film that did diffract correct was not evenly distributed, analysis was not performed on it. Yet, these experiments confirmed the ideal deposition conditions of IrO_2 film deposition as shown in the table above. In summary, the carrier gas ratio of argon to oxygen was kept at 10:1 and the annealing temperature of 500°C for 30 minutes become standard for iridium oxide deposition.

At a later date, the materials science department produced for me a thickness series with iridium oxide on glass substrates using the conditions listed above. The thickness ranged from ~10 nm to ~200 nm with thickness being determined from deposition time rather than a profilometry measurement. One sample was made in duplicate to examine the reproducibility of the deposition. These thin films shared the opaque color indicative of iridium oxide thin films and were evenly distributed. But yet, again, the FTIR results were not promising for a reflectivity change.

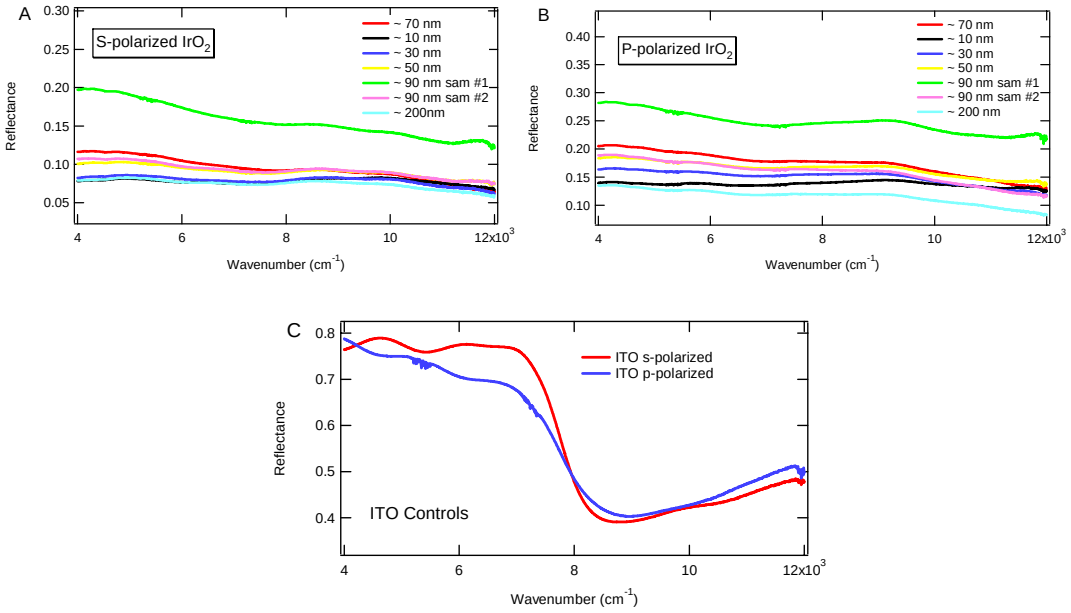

Figure 10.4A,B,C: The FT-IR reflectance data for 5 different thicknesses of IrO_2 ranging from ~10nm to ~200nm with a repetition at ~90nm. Figure 10.4A reveals the spectra with s-polarized light while 4B displays the spectra using p-polarized light. Figure 10.4C is a control with ITO that is known to have a reflectivity change in this region with p-polarized light.

Figure 10.4 reveals the FTIR reflectance spectra of 5 different thicknesses of IrO_2 thin films deposited onto glass substrates. Of all the thicknesses ranging from ~10nm to ~200nm, none revealed a reflectance changed either with s- or p-polarized light. In addition, the duplicate sample at ~90 nm did not show much reproducibility within the two films, indicating an additional problematic feature of iridium oxide deposition.

The detection of the surface plasmon resonance (SPR) effect was attempted on a typical iridium oxide thin film on glass substrate similar to BK7 using GWC

SPR instrumentation described in the methods section. The following figure was obtained using this instrumentation.

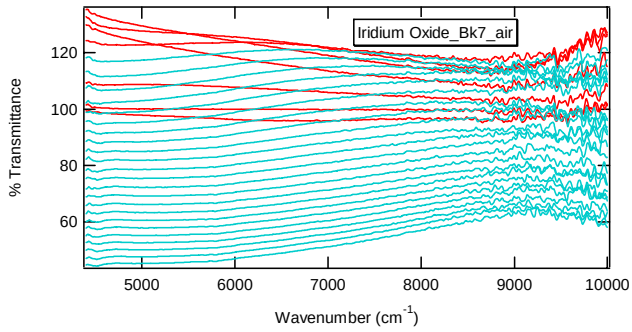

Figure 10.5: SPR spectra of a 110 nm iridium oxide thin film deposited onto a glass substrate using standard conditions of 10:1 Ar:O_2 and 500°C annealing for 30 minutes. Incident angles of 40 to 80 degrees increasing by 1 degree were examined for SPR effect with the red spectra indicative of angles 40-47 degrees.

The lack of any SPR effect confirmed our results with the FT-IR reflectance spectroscopy. It was at this point that I concluded that the development of the iridium oxide thin films would be more difficult than initially anticipated. Additionally, I hypothesize that the original conditions could not be replicated whether because of instrumentation issues with the sputtering, target degradation, or simply the wrong conditions were recorded. I did not see any promise in pursuing this substrate since ITO and AZO appeared so promising. Maybe at a later date, this conducting metal oxide could be revisited.

10.3. Ruthenium Oxide

10.3.1. Introduction

Theoretical studies on the electrical and optical properties of conducting metal oxides such as indium oxide, tin oxide, indium tin oxide, and zinc oxide have been performed; [21-25] yet, very few theoretical studies

have been performed on ruthenium oxide. [5, 6] Density functional theory calculations are useful in describing the ground state properties of these metal oxides by examining the fermion interactions using a density model of the conductor. These properties then allow for an understanding of the observed experimental spectrum of a conductor in terms of the DFT calculated electrical and optical properties of the conducting metal oxide

The present study combines density functional theory (DFT) calculations for the electrical and optical properties with optical measurements of ruthenium oxide thin films. Reflectance FTIR was used to determine the plasma frequency of ruthenium oxide thin films on a glass substrate. Reflectance spectra of the metal oxide thin film were observed with a 50-degree incident angle to the surface normal and of p-polarized IR radiation in the near-IR spectral region. DFT calculations yielded the optical band gap, Fermi energy, charge carrier concentration, effective electron mass, and the plasma frequency. All the parameters, with the exception of the effective electron mass, were studied as a function of temperature and the compression or the expansion of the ruthenium oxide unit cell. In addition, the conduction band orbital character was also calculated for ruthenium oxide. All of the calculations utilized the bulk crystal structure of the ruthenium oxide. These calculations revealing properties such as the optical band gap and charge carrier concentration are similar to previous theoretical work on a variety of metal oxides [2, 21, 23, 24] and are relevant to the overall properties of thin films of

metal oxides. The DFT calculations provided insight into the experimentally observed properties of ruthenium oxide thin films.

10.3.2. Materials and Methods

A. Ruthenium Oxide Thin Film Preparation.

Ruthenium oxide (RuO_2) thin films were formed on glass substrates cleaned in methanol using an ultrasonic bath. The RuO_2 thin films were deposited using ion beam reactive sputtering with a Ru target. The $Ar:O_2$ mix was 7:3 with a total pressure of 0.14 m Torr with an ion beam power of 500 V and 15 mA. The deposition rate was ~3-4 nm/min with the film thickness determined by Alphastep profilometry. The RuO_2 thin films were 360 nm thick on the glass substrate and were annealed in a standard furnace with a fast-fire technique at 700°C in air atmosphere for 10 minutes. After annealing, XRD analysis revealed that the predominant product was RuO_2 although some Ru was still present (data not shown).

B. Reflectance FTIR Spectroscopy.

The variable angle reflectance FTIR spectra were recorded by a Digilab FTS3000 spectrometer using p-polarized IR radiation and a Pike Technologies variable angle reflectance attachment (VeeMAXII). The angle of incidence was 50 degrees relative to the surface normal. A tungsten lamp source, quartz beamsplitter, and liquid nitrogen cooled InSb detector were all operated in the spectral range of 3,000-12,500 cm^{-1}. All of the IR spectra were averaged over 128 scans at a resolution of 8 cm^{-1}

and were performed at room temperature. To obtain the RuO_2 thin film reflectance spectra, a ratio of the single beam spectra of the metal oxide thin film on the glass substrate to the single beam spectra of a gold surface was made.

10.3.3. Computational Methods.

A. Density Functional Theory Calculations.

The density functional theory (DFT) calculations were carried out with the use of the quantum chemical software DMol3 (Accelrys, Inc.). [26] The calculations were performed on a ruthenium oxide unit cell containing 2 RuO_2 formula units with a rutile-type structure. [27] The lattice parameters of the unit cell were 8.4977, 8.4977, and 5.867 Å. Periodic boundary conditions were used to determine the bulk electronic and optical properties of the metal oxide thin film. The double numerical plus polarization function (DNP) basis set was utilized with the effective core potentials below the 4s orbital for ruthenium. The basis set used was O(1s),2(2s),2(2p),2(3d) and Ru(4s),(4p),2(4d),2(5s),(5p) for the two atoms with an atomic cutoff at 5.49Å. The Perdew and Wang GGA functional was used for the DFT calculations. [28] The optical band gap structure calculations at multiple k-points were computed with the canonical ensemble approach at T = 0 K (known as the FERMI option), [29] while the remainder of the DFT calculations utilized the grand canonical ensemble approach which allows for partial electron occupation which is needed for

the charge carrier calculations (known as the THERMAL option). [30] In these THERMAL calculations, the effective electronic temperature is 0.02 Hartrees or ~ 6,300 K. [30] This high temperature allows for a self-consistent field (SCF) convergence with the THERMAL option. [30] Yet, for validation purposes, the dependence of the optical band gap, Fermi energy, charge carrier concentration, and plasma frequency on the temperature was also examined. The molecular visualization program InsightII (Accelrys, Inc.) was utilized to envision the DMol3 calculated models and orbitals. All of the DFT calculations were performed at the North Carolina Supercomputing Center (NCSC) on the IBM RS/6000 SP.

For the determination of the Fermi energy and charge carrier concentration, a single point energy calculation at the Γ point in the Brillouin zone was performed. Additional points in k-space along high-symmetry lines in the Brillouin zone were utilized for the band structure calculation of ruthenium oxide. A charge carrier concentration value was determined by summing the electrons in the conduction band of ruthenium oxide divided by the unit cell volume calculated from the lattice constants. The multiple k-point calculation of the electronic band structure used a primitive cell structure. Additionally, the curvature in the conduction band was fit to Eqn. 1: [1, 31]

$$E(k) = E_o + \frac{h^2 k^2}{8\pi^2 m^*} \qquad (1)$$

where E is the energy in eV, E_o is the energy offset depending on where the zero value was chosen, k is the reciprocal wave vector and m^* is the effective free electron mass. This equation permitted for the determination of m^* for ruthenium oxide. This value was used in Eqn. 2: [1]

$$\omega_p^2 = \frac{ne^2}{m^* \varepsilon_o} \qquad (2)$$

where ω_p is the plasma frequency and n is the charge carrier concentration to calculate the plasma frequency of ruthenium oxide from first principles.

10.3.4. Results and Discussion

In this study, the electrical and optical properties of ruthenium oxide were investigated by the use of both reflectance FTIR spectroscopy and density functional theory (DFT). The wavenumber dependence of the reflectance of the films for p-polarized radiation in the near-IR spectral region was examined. The goal of computation state studies is to compare the calculated properties of this metal oxide with experiment. As in previous studies with ITO and iridium oxide [2, 4], DFT calculations of the optical band gap, charge carrier concentration and plasma frequency were examined for their agreement with the observed experimental spectra. The results presented here are in agreement with previous experimental and theoretical work on ruthenium oxide. [5, 6]

A. Reflectance FTIR Spectroscopy of Ruthenium Oxide Thin Films

Figure 10.6 shows the FTIR reflectance spectra of a 360 nm thick ruthenium oxide thin film on a glass substrate using p-polarized IR radiation.

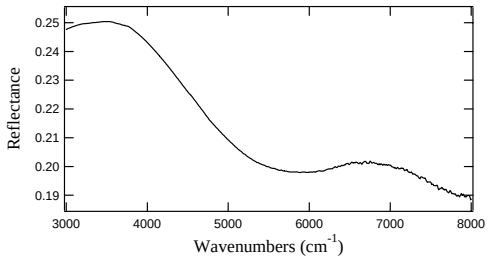

Figure 10.6. Reflectance FTIR spectrum of a 360 nm thick ruthenium oxide thin film deposited on a glass substrate. The spectrum was recorded with an incident angle of 50 degrees from the surface normal with p-polarized radiation.

The spectrum was recorded using an incident angle of 50 degrees from the surface normal. A considerable decrease in the observed reflectance occurs around 4,500 cm^{-1} due to the onset of the plasma frequency of RuO_2. The reflectance is high at frequencies lower than the plasma frequency and significantly less at greater frequencies. The position of the plasma frequency is related to the free electrons in the conduction band (charge carriers) and effective electron mass in the material (Eqn. 2). The decrease in the reflectance spectrum seen at approximately 6,000 cm^{-1} has been suggested previously to be due to the d-d intraband transitions in ruthenium oxide. [5, 6] Thus, there may strong mixing of the d-d transitions in the plasma resonance frequency band.

B. DFT Calculated Optical and Electronic Properties of Ruthenium Oxide

In order to calculate the electronic and optical properties of ruthenium oxide, a thermal population of electrons in the conduction band is used to determine the charge carrier density. This charge carrier concentration is calculated at an elevated electronic temperature to ensure a uniform electron density known as convergence of a self-consistent field (SCF). Therefore, the theoretical values obtained from the calculations are not directly comparable to the room temperature experimental data.

Recently, our methodology for DFT calculations has changed. The calculations performed on the ruthenium oxide were carried out by changing the input value for the electronic temperature in the THERMAL option in DMol3. The nuclear temperature is absolute zero in this option, thus, it is only the electron populations that are affected. However, the current DFT method applies the Fermi-Dirac distribution function to the energy levels obtained from the calculation. This approach was used for another CMO, cadmium tin oxide, and seemed to better correlate the theory with the experimental data [32]. The new approach was later applied to ruthenium oxide and compared to the original calculations.

Previous studies show that oxygen atom vacancies play a key role in the conductivity of a metal oxide possibly by increasing the n-type electrical conductivity. [33, 34] Therefore, the DFT calculations also

investigated how oxygen deficiency in ruthenium oxide related to the conductivity of this metal oxide.

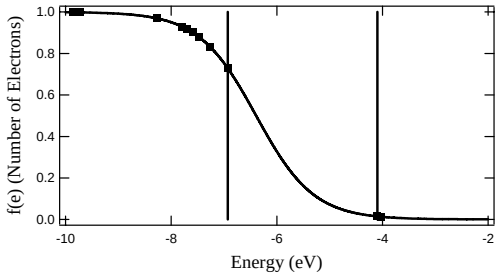

Figure 10.7. DFT calculated electron distribution in the Fermi energy vicinity for ruthenium oxide (markers) fit with a Fermi-Dirac distribution (solid line). The two vertical lines indicate the optical band gap.

Figure 10.7 shows the calculated electron distribution (markers) near the Fermi energy using density functional theory (DFT) with periodic boundary conditions for the experimental crystal structure of ruthenium oxide at point Γ in the Brilluoin zone. Near the band gap at point Γ, the distribution of the electrons was fitted to the Fermi-Dirac distribution (solid curve) using Eqn. 3:[35]

$$f(e) = \frac{1}{1 + e^{-\beta(\varepsilon_f - \varepsilon)}} \qquad (3)$$

where ε_f is the Fermi energy. The vertical lines illustrate the calculated optical band gap of 2.8 eV. The Fermi energy of ruthenium oxide was calculated to be –6.4 eV, while the charge carrier concentration was found to be 8.9×10^{20} electrons/cm^3 at 6300 K. The charge carrier concentration and the conductivity of the metal are related by Eqn. 4:[1]

$$\sigma = \frac{ne^2\tau}{m^*}\frac{1}{1-i\omega\tau} \qquad (4)$$

where σ is the conductivity and τ is the scattering time. Since these DFT calculations do not provide an estimate for the electronic scattering time, the exact conductivity cannot be determined. Further examination of the impurity scattering could be accomplished by applying more complex theories such as Erginsoy's [36]. This theory models scattering by impurities in semi-conductors by assuming an empty impurity band at absolute zero and partially filling it with increasing temperature. This has not been done for RuO_2 but may be a logical next step.

For correlations of the calculated charge carrier concentration with the plasma frequency of ruthenium oxide, the conduction band in the Δ (Γ→X) direction of the Brilluoin zone that is equivalent to the (0,0,0)→(1/2,0,0) wave vector was fitted to Eqn. 1 to calculate the effective electron mass. This mass (m^*) in the Δ(Γ→X) direction was determined to be 0.75 m_e, where m_e is the mass of an electron that is in agreement with experimental and theoretical effective masses of other conducting metal oxides. [23, 24] Using this value, the plasma frequency for ruthenium oxide was calculated to be 10,289 cm^{-1}. These values were all calculated at ~ 6,300 K.

In agreement with previous theoretical studies, these DFT calculations predicted the d character of the conduction band of RuO_2. [5, 6] Figure 3 shows the d type calculated conduction band of ruthenium oxide.

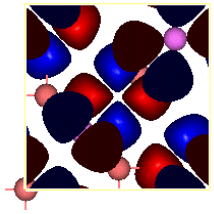

Figure 10.8. The DFT calculated orbital character of the conduction band orbital of ruthenium oxide.

Therefore, based on the DFT calculations, ruthenium oxide can be classified as a d-band conductor as opposed to sp-band metal oxide conductors such as ITO. [4] However, the plasma frequency of both the sp and d-band metal oxide conductors was found in the near IR spectral region. The primary observed difference between these two types of metal oxide conductors is the increase in the reflectance observed above the plasma frequency in d-band conductors such as ruthenium oxide. These DFT calculations cannot calculate d-d intraband transitions therefore these calculations are unable to confirm the origin of the dip in reflectance seen experimentally at ~ 6,000 cm^{-1}.

In order to validate the calculations performed at T~ 6,300 K, the optical band gap, charge carrier concentration, and plasma frequency were calculated as a function of electronic temperature. These plots for RuO_2 are shown in Figures 4A-4C.

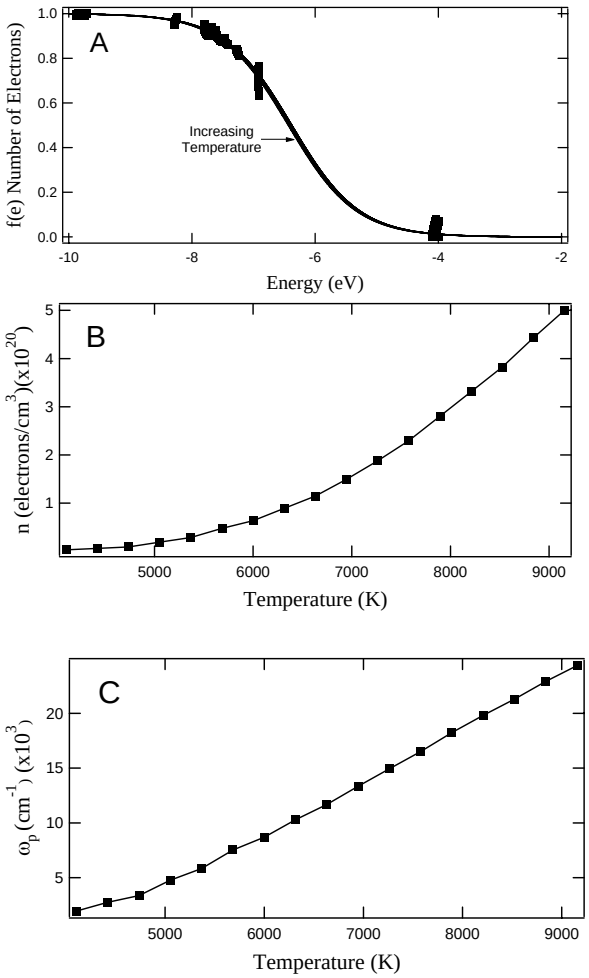

Figure 10.9. DFT calculated dependence of the optical band gap (A), charge carrier concentration (B), and plasma frequency (C) of ruthenium oxide on temperature.

Figure 10.9A displays the Fermi-Dirac electron occupations near the Fermi energy as a function of temperature at point Γ. The temperature ranged from ~ 4,100K to ~ 9,100K. Throughout this range, the calculated optical band gap was ~ 2.84±0.04 eV. Figure 10.9B shows the dependence of the calculated charge carrier concentration of ruthenium oxide on the temperature. The charge carrier concentration ranged from

$3.2x10^{19}$ cm^{-3} to $5.0x10^{21}$ cm^{-3} with increasing temperature. Since the charge carrier concentration is directly proportional to the electrical conductivity (Eqn. 4), Figure 10.9B demonstrates that the conductivity of RuO_2 also increases with increasing temperature assuming that the electronic scattering time does not change significantly. Using the effective mass of ruthenium oxide determined at T = 0 K, the dependence of the plasma frequency on the temperature is shown in Figure 10.9C. Similar to the charge carrier concentration and the electrical conductivity, the plasma frequency increases with an increase in the temperature. The plasma frequency values varied from 1,944 cm^{-1} to 24,364 cm^{-1} for the temperature range of ~ 4,100 K to ~ 9,100 K. Due to poor SCF convergence of the energy levels, calculations on temperatures below ~ 4,100 K were not obtainable.

Even at ~ 4,100 K, the calculated plasma frequency is much lower than the experimentally observed plasma frequency of ruthenium oxide thin films. We hypothesize that oxygen deficiency could be a contributing factor to the observed conductivity of these metal thin films that is not accounted for in the above calculations on RuO_2. To test this hypothesis, two non-stoichiometric ratios of ruthenium-to-oxygen in the ruthenium oxide unit cell were investigated. The results of the DFT calculated charge carrier concentration and plasma frequency are given in Table 1 calculated at ~ 6,300 K for the oxygen deficient models.

Table10.4. DFT calculated values of the charge carrier concentration and plasma frequency of oxygen deficient ruthenium oxide models.

Model	Charge Carrier Concentration (cm^{-3})	Plasma Frequency (cm^{-1})
Ru_2O_4	$8.92x10^{20}$	10,289
Ru_2O_3	$1.37x10^{21}$	12,751
Ru_2O_2	$7.10x10^{21}$	29,037

These results show that as oxygen is removed from the unit cell of ruthenium oxide, the charge carrier concentration and thus the conductivity and plasma frequency of ruthenium oxide increases significantly (maximum of 35 % increase) presenting some evidence for the role of oxygen deficiency in the observed conductivity of ruthenium oxide thin films.

To test the validity of the basis set employed in these calculations, the optical and electrical properties of ruthenium oxide as a function of the compression or expansion of the unit cell was investigated and the results are given in Figures 5A to 5D.

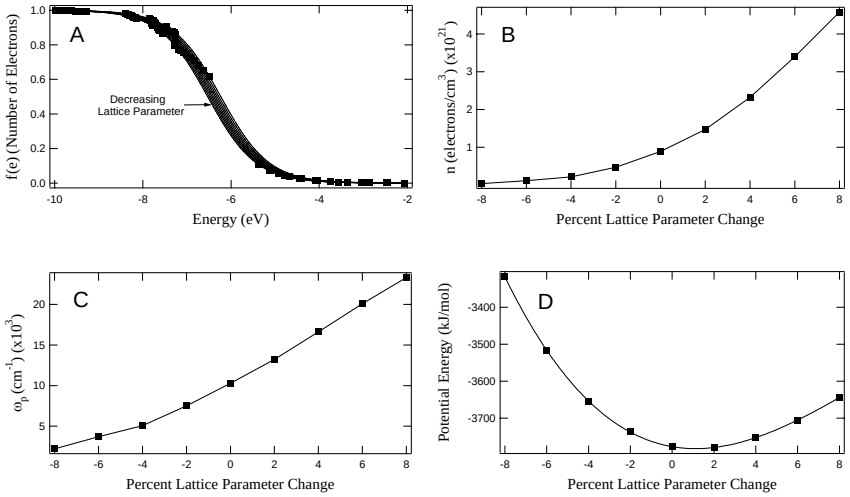

Figure 10.10. DFT calculated dependence of the optical band gap (A), charge carrier concentration (B), plasma frequency (C), and potential energy (D) of ruthenium oxide on the compression or expansion of the ruthenium oxide unit cell.

These figures reveal an agreement between the theoretical minimized energy structure and the experimentally determined crystal lattice parameters. Figure 10.10A shows the dependence of the electrons near the Fermi energy on the orbital energy. The graph reveals that the Fermi energy increases as the unit cell is expanded and decreases as the unit cell is compressed. Similarly, Figures 10.10B and 10.10C illustrate that the charge carrier concentration and the plasma frequency both increase with an expansion of the ruthenium oxide unit cell and decrease with the compression. The energy minimum for this structure was found to be at an expansion of the unit cell of 1.1% as seen in Figure 10.10D. This small deviation from the experimental lattice parameters for ruthenium oxide illustrates the validity of the basis set used in these calculations.

The two DFT methods were compared after performing the room temperature oxygen depletion calculations on an identical ruthenium oxide unit cell structure. The results are shown in the following table.

Table 10.5. The DFT calculated electronic properties of electrons/unit cell and charge carrier concentration as a function of the stoichiometry of the oxygen-depleted ruthenium oxide species.

Stoichiometry	Electrons Per unit cell	Charge carrier density Electrons/cm^3
RuO_2	$6.35x10^{-41}$	$1.01x10^{-18}$
Ru_2O_3	$7.68x10^{-33}$	$1.22x10^{-10}$
Ru_2O_2	$3.22x10^{-14}$	$5.12x10^{8}$

However, as shown in table 10.5, application of the revised DFT method did not this result in charge carrier densities that are in agreement with experiment. Yet, the overall trend corresponds with previous calculations since as oxygen atoms are removed the charge carrier density increases dramatically.

10.3.5. Conclusions

The electrical and optical properties of ruthenium oxide were investigated using both reflectance FTIR and density functional theory calculations (DFT). The reflectance FTIR spectroscopy revealed a sharp decrease in the reflectance at approximately 4,500 cm^{-1}. This decrease in reflectance is indicative of the plasma frequency of this ruthenium oxide thin film deposited onto a glass substrate. The charge carrier concentration and plasma frequency of ruthenium oxide were determined

from DFT calculations to be 8.19×10^{20} electrons/cm^3 and 10,289 cm^{-1} at ~ 6,300 K, respectively. However, at room temperature, SCF convergence was not possible preventing the charge carrier concentration from being calculated. Both the calculated charge carrier concentration and the plasma frequency of ruthenium oxide increased as the temperature increased as expected. The optimal unit cell was determined to be at an expansion of 1.1% compared to the experimental lattice constants of the unit cell validating the basis set used in these calculations. The optical band gap was determined to be 2.8 eV and the effective electron mass was found to be 0.75 m_e in the $\Delta(\Gamma \rightarrow X)$ direction. The ruthenium oxide conduction band was found to have d-character.

This d-band orbital character distinguishes it from other conducting metal oxide thin films such as indium tin oxide (ITO) that have s and p orbital character in the conduction band. Yet, both types of conducting thin films have plasma frequencies in the near-IR spectral region. This d-type conduction band may be responsible for the d-d intraband transitions proposed in the ruthenium oxide reflectance spectrum that would have effects on the optical properties in a manner different from ITO while oxygen deficiency could explain the experimental optical and electronic properties of ruthenium oxide thin films.

10.4. References

1. Wooten, F., *Optical Properties of Solids*. Academic Press, Inc.: San Diego, 1972.

2. Brewer, S., Wicaksana, D., Maria, J., Kingon, A., Franzen, S., Investigation of the Electrical and Optical of Iridium Oxide by Reflectance FTIR Spectroscopy and Density Functional Theory Calculations. *In Press* **2003**.

3. Brewer, S. H.; Wicaksana, D.; Maria, J. P.; Kingon, A. I.; Franzen, S., Investigation of the electrical and optical properties of iridium oxide by reflectance FTIR spectroscopy and density functional theory calculations. *Chemical Physics* **2005,** 313, (1-3), 25-31.

4. Brewer, S. H.; Franzen, S., Optical properties of indium tin oxide and fluorine-doped tin oxide surfaces: correlation of reflectivity, skin depth, and plasmon frequency with conductivity. *Journal of Alloys and Compounds* **2002,** 338, (1-2), 73-79.

5. Goel, A. K.; Skorinko, G.; Pollak, F. H., Optical-Properties of Single-Crystal Rutile Ruo2 and Iro2 in the Range 0.5 to 9.5 Ev. *Physical Review B* **1981,** 24, (12), 7342-7350.

6. Mattheiss, L. F., Electronic-Structure of Ruo-2, Oso-2, and Iro-2. *Physical Review B* **1976,** 13, (6), 2433-2450.

7. Hjortsberg, A.; Hamberg, I.; Granqvist, C., Transparent and Heat-Reflecting Indium Tin Oxide Films Prepared by Reactive Electron Beam Evaporation. *Thin Solid Films* **1982,** 90, 323-326.

8. Hamberg, I.; Hjortsberg, A.; Granqvist, C., High Quality Transparent Heat Reflectors of Reactively Evaporated Indium Tin Oxide. *Applied Physics Letters* **1982,** 40, (5), 362-364.

9. Shin, J.; Shin, S.; Park, J.; Kim, H., Properties of DC Magnetron Sputtered Indium Tin Oxide Films on Polymeric Substrates at Room Temperature. *Journal of Applied Physics* **2001,** 89, (9), 5199-5203.

10. Fan, J.; Bachner, F.; Foley, G., Effect of Oxygen Partial Pressure During Deposition on Properties of r.f. Sputtered Sn-Doped In2O3 Films. *Applied Physics Letters* **1977,** 31, (11), 773-775.

11. Bregman, J.; Shapira, Y.; Aharoni, H., Effects of oxygen partial pressure during deposition on the properties of ion-beam-sputtered indium-tin oxide thin films. *Journal of Applied Physics* **1990,** 67, (8), 3750-3753.

12. Kawar, R. K.; Chigare, P. S.; Patil, P. S., Substrate temperature dependent structural, optical and electrical properties of spray deposited iridium oxide thin films. *Applied Surface Science* **2003,** 206, (1-4), 90-101.

13. Hackwood, S.; Dayem, A. H.; Beni, G., Amorphous-Nonmetal to Crystalline-Metal Transition in Electrochromic Iridium Oxide-Films. *Physical Review B* **1982,** 26, (2), 471-478.

14. Patil, P. S.; Kawar, R. K.; Sadale, S. B., Effect of substrate temperature on electrochromic properties of spray-deposited Ir-oxide thin films. *Applied Surface Science* **2005,** 249, (1-4), 367-374.

15. Lee, I. S.; Park, J. M.; Son, H. J.; Park, J. C.; Lee, G. H.; Lee, Y. H.; Ciu, F. Z., Iridium oxide as a stimulating neural electrode formed by reactive magnetron sputtering. In *Asbm6: Advanced Biomaterials Vi*, 2005; Vol. 288-289, pp 307-310.

16. Satoh, W.; Hosono, H.; Suzuki, H., On-chip microfluidic transport and mixing using electrowetting and incorporation of sensing functions. *Analytical Chemistry* **2005,** 77, (21), 6857-6863.

17. Yagi, M.; Tomita, E.; Sakita, S.; Kuwabara, T.; Nagai, K., Self-assembly of active IrO2 colloid catalyst on an ITO electrode for efficient electrochemical water oxidation. *Journal of Physical Chemistry B* **2005,** 109, (46), 21489-21491.

18. Kim, S. Y.; Lee, J. L., Effect of thin iridium oxide on the formation of interface dipole in organic light-emitting diodes. *Applied Physics Letters* **2005,** 87, (23).

19. Elzanowska, H.; Abu-Irhayem, E.; Skrzynecka, B.; Birss, V. I., Hydrogen peroxide detection at electrochemically and sol-gel derived Ir oxide films. *Electroanalysis* **2004,** 16, (6), 478-490.

20. Mo, Y. B.; Stefan, I. C.; Cai, W. B.; Dong, J.; Carey, P.; Scherson, D. A., In situ iridium L-III-edge X-ray absorption and surface enhanced Raman spectroscopy of electrodeposited iridium oxide films in aqueous electrolytes. *Journal of Physical Chemistry B* **2002,** 106, (14), 3681-3686.

21. Mryasov, O. N.; Freeman, A. J., Electronic band structure of indium tin oxide and criteria for transparent conducting behavior. *Physical Review B* **2001,** 64, (23), art. no.-233111.

22. Odaka, H.; Iwata, S.; Taga, N.; Ohnishi, S.; Kaneta, Y.; Shigesato, Y., Study on electronic structure and optoelectronic properties of indium oxide by first-principles calculations. *Japanese Journal of Applied Physics Part 1-Regular Papers Short Notes & Review Papers* **1997,** 36, (9A), 5551-5554.

23. Odaka, H.; Shigesato, Y.; Murakami, T.; Iwata, S., Electronic structure analyses of Sn-doped In2O3. *Japanese Journal of Applied Physics Part 1-Regular Papers Short Notes & Review Papers* **2001,** 40, (5A), 3231-3235.

24. Mi, Y. M.; Odaka, H.; Iwata, S., Electronic structures and optical properties of ZnO, SnO2 and In2O3. *Japanese Journal of Applied Physics Part 1-Regular Papers Short Notes & Review Papers* **1999,** 38, (6A), 3453-3458.

25. Maki-Jaskari, M. A.; Rantala, T. T., Band structure and optical parameters of the SnO2(110) surface. *Physical Review B* **2001,** 64, (7), art. no.-075407.

26. Delley, B., *Journal of Chemical Physics* **1990,** 92, 508-517.

27. Bolzan, A. A.; Fong, C.; Kennedy, B. J.; Howard, C. J., Structural studies of rutile-type metal dioxides. *Acta Crystallographica Section B-Structural Science* **1997,** 53, 373-380.

28. Perdew, J. P.; Chevary, J. A.; Vosko, S. H.; Jackson, K. A.; Pederson, M. R.; Singh, D. J.; Fiolhais, C., Atoms, molecules, solids and surfaces - Applications of the generalized gradient approximation for exchange and correlation. *Physical Review B* **1992,** 46, 6671-6687.

29. Kohn, W.; Sham, L., *Phys. Rev. A* **1965,** 137, 1697-1699.

30. Mermin, D., *Phys. Rev. A* **1965,** 137, 1441-1443.

31. Hamberg, I.; Granqvist, C. G.; Berggren, K. F.; Sernelius, B. E.; Engstrom, L., Band-Gap Widening in Heavily Sn-Doped In2o3. *Physical Review B* **1984,** 30, (6), 3240-3249.

32. Rhodes, C. L. B., S.H.; Folmer, J.; Li, X.; Coutts, T.J.; Franzen, S. , Investigation of an Hexadecanethiol Self-Assembled Monolayers on Cadmium Tin Oxide Thin Films. *Thin Solid Films* **submitted**.

33. Tikhonovich, V. N.; Naumovich, E. N.; Kharton, V. V.; Yaremchenko, A. A.; Kovalevsky, A. V.; Vecher, A. A., Oxygen nonstoichiometry of Bi2V0.9Cu0.1O5.5-delta solid electrolyte by coulometric titration technique. *Electrochimica Acta* **2002,** 47, (24), 3957-3964.

34. Maeder, T.; Bednorz, J. G., Influence of oxygen stoichiometry on electrical transport and magnetic properties of doped perovskite-type ferrate and manganate single crystals. *Journal of the European Ceramic Society* **1999,** 19, (6-7), 1507-1510.

35. McQuarrie, D. A., *Statistical Mechanics*. Harper Collins Publishers Inc.: New York, 1976.

36. Erginsoy, C., On the Mechanism of Impurity Band Conduction in Semiconductors. *Physical Review* **1950,** 80, (6), 1104-1105.

APPENDICES

Appendix 1 - Further Explanation of the Drude Free Electron Model Equations

Historically, in 1900 after the wave-particle dual nature of an electron had been established, Drude developed the classical theory of conductivity. In this theory, he applied the kinetic theory of gases to electrons. In 1905, Lorentz elaborated on the theory by applying Maxwell-Boltzmann statistics to the theory. A difficulty arose with the theoretical prediction of the electronic specific heat that was not resolved until Sommerfeld applied a quantum mechanical treatment to the model in 1928. Sommerfeld still retained the concepts of the free electron gas that Drude had originally proposed, therefore, the final version of the model was named the Drude-Lorentz-Sommerfeld Model.

Nearly a hundred years later, this model is still routinely used to model the free electron optical responses in various types of spectroscopy. The following discussion relates this model in its role of modeling the plasmon resonance frequency. A few basic assumptions made with this modeling are that external forces are determined for one electron and then multiplied by the number electrons in the material, all the electrons are in phase, and that the perturbation of the electric field does not contain local field corrections.

Assuming an electric field exists such that

$$\mathbf{E} = \mathbf{E_0} e^{-i\omega t}$$

The mass of a free electron (m_e) and charge of the electron (e) can then be described by the drift motion superimposed onto the motion if the case were field-free.

$$m_e \frac{\partial^2 \boldsymbol{r}}{\partial t^2} + m_e \Gamma \frac{\partial \boldsymbol{r}}{\partial t} = e\boldsymbol{E_0} e^{-i\omega t}$$

The phenomenological damping constant Γ is added since in reality, energy dissipation by damping is unavoidable. This equation is solved to yield two defined physical entities. The dipole moment

$$\mathbf{p} = e\mathbf{r}_0$$

and the polarization where n is the number of electrons per unit volume.

$$\mathbf{P} = np = ner_0$$

In an isotropic media, the polarization is parallel to the external electric field, therefore,

$$P = \chi(\omega)\varepsilon_0 E$$

where $\chi(\omega)$ is the dielectric susceptibility that is frequency dependent and ε_0 is the permittivity of vacuum. Since the polarization P is related to the dielectric function, $\varepsilon(\omega)$, by the following equation

$$\chi(\omega) = \varepsilon(\omega) - 1 \text{ thus } P = (\varepsilon(\omega) - 1)\varepsilon_0 E .$$

Therefore, an expression for the motion of the field expressed in terms of the polarization is as follows.

$$\frac{\partial^2 \boldsymbol{P}}{\partial t^2} + \Gamma\frac{\partial \boldsymbol{P}}{\partial t} = \frac{ne^2}{m_e}\boldsymbol{E}_0 e^{-i\omega t}$$

Using the above definitions, the perturbation of the electric field can be expressed

$$\varepsilon_0\chi(\omega)\left(\frac{\partial^2 \boldsymbol{E}}{\partial t^2} + \Gamma\frac{\partial \boldsymbol{E}}{\partial t}\right) = \frac{ne^2}{m_e}\boldsymbol{E}_0 e^{-i\omega t}$$

such that the frequency-dependence of the perturbation is related solely by the dielectric susceptibility. If $E=\mathbf{E_0}e^{-i\omega t}$, then the equation can be solved to yield the following relationship.

If we next cancel the electric field term ($E=\mathbf{E_0}e^{-i\omega t}$) and solve for $\chi(\omega)$, then the following

$$\varepsilon_0\chi(\omega)\left(-\omega^2 - i\omega\Gamma\right)\boldsymbol{E_0}e^{-i\omega t} = \frac{ne^2}{m_e}\boldsymbol{E_0}e^{-i\omega t}$$

equation arises.

$$\chi(\omega) = \frac{-1}{\omega^2 + i\omega\Gamma}\frac{ne^2}{m_e\varepsilon_0}$$

This equation can be rearranged to yield the following relationship.

$$\chi(\omega) = \left(\frac{ne^2}{m_e\varepsilon_0}\right)\frac{-1}{\omega^2 + i\omega\Gamma}\frac{\omega^2 - i\omega\Gamma}{\omega^2 - i\omega\Gamma}$$
$$= \left(\frac{ne^2}{m_e\varepsilon_0}\right)\left(\frac{-1}{\omega^2 + \Gamma^2} + i\frac{\Gamma}{\omega\left(\omega^2 + \Gamma^2\right)}\right)$$

With the definition

$$\chi(\omega) = \varepsilon(\omega) - 1$$

and the Drude defition of the plasmon resonance frequency

$$\omega_p = \left(\frac{ne^2}{m_e\varepsilon_0}\right)^{1/2}$$

the equation can be rearranged to yield the following correlation.

$$\varepsilon(\omega) = 1 - \frac{\omega_p^2}{\omega^2 + \Gamma^2} + i\frac{\Gamma\,\omega_p^2}{\omega\left(\omega^2 + \Gamma^2\right)}$$

The afore-mentioned phenomenological damping constant Γ, also known as the relaxation constant can be related to the electron mean free path, l, and the Fermi velocity, V_F, by the following definition.

$$\Gamma = v_F/l$$

The dielectric function, ε, has both a real and imaginary component.

$$\varepsilon(\omega) = \varepsilon_1(\omega) + i\varepsilon_2(\omega)$$

In the realm of frequency dependence of the dielectric function, the following relationships exist.

In the limit that ω>>Γ, then

$$\varepsilon_1(\omega) \approx 1 - \frac{\omega_P^2}{\omega^2} \ , \ \varepsilon_2(\omega) \approx \frac{\omega_P^2}{\omega^3}\Gamma$$

If the radius of a sphere is much greater than the wavelength of light impinging upon it, R<<λ, then the response to an applied electric field can be assumed to be a quasi-static regime. Therefore, the assumption is that the electric field is spatially constant but time-dependent. Thus, the Onsager local field approximation is

$$E_i = E_0 \frac{3\varepsilon_m}{\varepsilon + 2\varepsilon_m}$$

where ε_m is the dielectric constant of the surrounding medium. And from this local field approximation, the static polarizability is given by the following equation.

$$\alpha = 4\pi\varepsilon_0 R^3 \frac{\varepsilon - \varepsilon_m}{\varepsilon + 2\varepsilon_m}$$

Note that for metals, the zero frequency dielectric constant (ε(0)) is infinity (∞); therefore, the static polarizability equation simplifies for the sphere.

$$\alpha = 4\pi\varepsilon_0 R^3$$

Under examination of the frequency dependence of the applied electric field, one observation that arises is that the internal field and frequency both show resonance at the following minimum point of

$$\varepsilon(\omega) + 2\varepsilon_m(\omega) = \text{minimum}$$

Therefore at a resonance condition, utilizing the definition of the complex dielectric function, the following statements can be concluded.

$$\varepsilon_1(\omega) + i\varepsilon_2(\omega) + 2\varepsilon_m(\omega) = \text{minimum} \quad \text{or}$$

$$[\varepsilon_1(\omega) + 2\varepsilon_m(\omega)]^2 + \varepsilon_2(\omega)^2 = \text{minimum}$$

The physical meaning of these equations are that a negative $\varepsilon_1(\omega)$ is necessary for the phase relationship between the field and particle polarization to be accurate. Another conclusion from these statements is that for a small $\varepsilon_2(\omega)$ the resonance will be found at

$$\varepsilon_1(\omega) = -2\varepsilon_m(\omega)$$

Assuming that in vacuum, $\varepsilon_m = 1$, the resonance position can be calculated by the following approximation.

$$\omega \approx \frac{\omega_p}{\sqrt{3}}$$

Therefore, beginning with Drude's definition of a plamson frequency, the following equations can be substituted and rearranged in the following manner.

$$\omega_p = \left(\frac{ne^2}{m_e\varepsilon_0}\right)^{1/2}$$

$$\omega \approx \left(\frac{ne^2}{m_e 3\varepsilon_0}\right)^{1/2} = \left(\frac{Ne^2}{m_e 3V\varepsilon_0}\right)^{1/2} = \left(\frac{Ne^2}{m_e 4\pi R^3\varepsilon_0}\right)^{1/2} = \left(\frac{Ne^2}{m_e \alpha}\right)^{1/2}$$

Thus, the optical resonance frequency has an inverse relationship to the static polarizability.

Appendix 2

We will require the following sequences (all sequences are 5' to 3'):

R15A	(LINKER2)GGAGACTGTTATCCG
R15B	CTCACAATTCCACAC(LINKER1)
R15C	CTCACAATTCCACAC(LINKERF)
R15D	(LINKER2)
R30E	(LINKER2)GGAGACTGTTATCCGCTCAGAATTCCACAC(LINKER1)
R30F	(LINKER2)GGAGACTGTTATCCGCTCAGAATTCCACAC(LINKERF)
S30E	GTGTGGAATTCTGAGCGGATAACAGTCTCC
T30E	(LINKER2)GTGTGGAATTCTGAGCGGATAACAGTCTCC
U30E	(LINKER3)GTGTGGAATTCTGAGCGGATAACAGTCTCC
W30E	(LINKERF)GTGTGGAATTCTGAGCGGATAACAGTCTCC
R30	(LINKER2)GGAGACTGTTATCCGCTCACAATTCCACAC(LINKER1)
S30	GTGTGGAATTGTGAGCGGATAACAGTCTCC
T30	(LINKER2)GTGTGGAATTGTGAGCGGATAACAGTCTCC
U30	(LINKER3)GTGTGGAATTGTGAGCGGATAACAGTCTCC
W30	(LINKERF)GTGTGGAATTGTGAGCGGATAACAGTCTCC
R26	(LINKER2)AACCAGGATTATCCGCTCACAATTCC(LINKER1)
S26	GGAATTGTGAGCGGATAATCCTGGTT
T26	(LINKER2)GGAATTGTGAGCGGATAATCCTGGTT
U26	(LINKER3)GGAATTGTGAGCGGATAATCCTGGTT
W26	(LINKERF)GGAATTGTGAGCGGATAATCCTGGTT
B20	LINKERB-AACCAGGATTATCCGCTCAC
R20	(LINKER2)AACCAGGATTATCCGCTCAC(LINKER1)
S20	GTGAGCGGATAATCCTGGTT
T20	(LINKER2)GTGAGCGGATAATCCTGGTT
U20	(LINKER3)GTGAGCGGATAATCCTGGTT
W20	(LINKERF)GTGAGCGGATAATCCTGGTT
X20	(LINKER2)-AACCAGGATTATCCGCTCAC -> [5' thiol]
R15	(LINKER2)AACCAGGATTATCCG(LINKER1)
S15	CGGATAATCCTGGTT
T15	(LINKER2)CGGATAATCCTGGTT
U15	(LINKER3)CGGATAATCCTGGTT
W15	(LINKERF)CGGATAATCCTGGTT
P20	(LINKER AMINO) AACCAGGATTAT

Appendix 3

```
192  2.0
1    1.0
192  0.0

# Number of ions
80

# Number of species
4

# Number of k-points
2

# K-point and weights
0.25 0.25 0.25 0.25
-0.25 0.25 0.25 0.75


# Bravais lattice type
8

# Lattice constants in (x, y, z) directions
19.41, 1, 1, 0.0 0.0 0.0

# Energy cutoff parameter
1.35

# Mehrstellen pre/post smoothings counts and mehrstellen timestep
# orbital and hartree solvers
2 1 1.0 2 1 1.35

# Multigrid levels: orbital and hartree solvers
#  0 = global grid only
1 1

# 0=cell relative coordinates 1=absolute coordinates
0

# Ionic coordinates: species x y z movable-ion
#     Note: the species number is indexed from one (not zero)
#           can the ion move? yes/no = 1/0.
4     0.24999587  0.24999589  0.24999563  0
1     0.7499958   0.74999583  0.74999605  0
1     0.24999616  0.74999654  0.25000394  0
1     0.74999655  0.24999616  0.7499964   0
1     0.2499962   0.24999653  0.74999628  0
1     0.74999653  0.7499962   0.25000377  0
1     0.74999582  0.24999589  0.25000416  0
1     0.24999618  0.74999621  0.74999671  0
1     0.46685809  -0.00000068 0.24999601  0
1     0.96685808  0.49999927  0.74999654  0
1     0.24999644  0.46685762  -0.00000055 0
1     0.74999633  0.9668576   0.49999953  0
1     -0.0000005  0.24999639  0.46685792  0
1     0.49999934  0.74999627  0.96685811  0
1     0.24999603  0.53314146  0.49999998  0
1     0.74999613  0.03314167  0.0   0
1     -0.0000003  0.7499961   0.03314156  0
1     0.49999958  0.249996    0.53314155  0
1     0.03314106  -0.00000025 0.74999624  0
```

Appendix 3

```
# Orbital occupation flag, electron temperature (eV), occupartion mixing
#    0 = No fermi occupation
#    1 = Fermi-Dirac occupations
#    2 = Gaussian occupations
#    3 = Error-Function occupations
# +10 = Use Gillan free energy for forces (thus, 11 = FD + Gillan, etc)
1 0.02 0.1

# Diagonalization info:
#  Initial diag (0/1); Diag period
0 100  40

# MD method
#  0 = no ionic forces computed - quench electrons
#  1 = fast relax
#  2 = constant volume & energy
#  3 = constant temperature & energy
#  4 = constant pressure & energy (not working yet)
#  5 = constrained fast relax
#  8 = Band structure calculations only
#
#  second field is number of md step
#  third and fourth field are diagonalization flags for the scf steps
#
0   18    0  0.0   0.0   1.0


# Finite temperature control
#  0 = Nose-Hoover chains
#  1 = Anderson Rescaling
#
# the second field is the target temperature
# the third field is the number of Nose thermostats
# the fourth field is the Nose Frequency of the system in THz
# the fifth field is the random velocity flag (0=on/1=off)
#
0 1000.0 5 15.59 0

# Order of MD integration
# 0 = 2nd Order Velocity Verlet
# 1 = 3rd Order Beeman-Velocity Verlet
# 2 = 5th Order Beeman-Velocity Verlet
#
1

# Ionic motion timestep
40.0

# DX charge volume movie maker (0=off or # of steps between output)
# Second field is milliken population flag (0=off 1=do projections)
0 0

# rotmovie movie maker (0=off or # of steps between output)
4

# Number of states
385

# Occupations for the states in the format of a repeat count followed by
# the occupation.
```

Appendix 3

```
#
#   Input control file for md program. All items after a # are
#   treated as comments. Blank lines are ignored.
#

# Description of run. One line only!
ITO , assign 2 pseudopotential to Oxygen

# Input file name to get initial wavefunctions from
wave2.out

# output file name to write wavefunctions to
wave2.out

# Pseudopotential file name
pseudo.InOOSn

#
# Input control flag.
#     0 = random start
#     1 = restart file
#

1  0  0

# Boundary condition flag.
#    0 = periodic
#    1 = cluster (Does not work yet)
#    2 = surface (Does not work yet)
#
0

# Density mixing parameter and projector mixing parameter
0.75  0.8

# Exchange correlation flag
#   0 = LDA
#   1 = GGA
#   4 = PBE
0

# Number of steps
40

#  RMS and force convergence criteria
1.0e-6  0.0005

# Checkpoint count (Number of steps after which to save data to disk)
20000

# Output count (Number of steps after which to write results to stdout
0

# Sorting flag
#   0 = do not perform sort.
#   1 = perform sort of wavefunction by eigenvalue
1
```